UNIVERSITÀ DI PARMA

UNIVERSITÀ DEGLI STUDI DI PARMA

DOTTORATO DI RICERCA IN
"FISICA"

CICLO XXXVIII

Characterisation Of Different Tourmaline Species Using Raman Spectroscopy

Coordinatore:
Chiar.mo Prof. Raffaella Burioni
Tutore:
Chiar.mo Prof. Danilo Bersani

Dottorando: Lorenzo Pasetti

Anni Accademici 2022/2023 - 2024/2025

Summary

Chapter 1

Introduction

The term "tourmaline" derives from the Sinhalese word "*turmali*", used by gem traders from Serendib (present-day Sri Lanka) to refer to a variety of stones displaying several colours.

The primary property of tourmalines is their display of a wide range of colours, attributed to the incorporation of various elements within their crystal structure, leading to their use as jewels and decorative items. The early 18th-century imports of these gemstones to Europe permitted scientists to analyse their physical properties. Pyroelectricity was initially identified, followed by the exploration of piezoelectricity. However, earlier research on these minerals was recorded: the initial mention of tourmaline properties comes from the Greek philosopher Theophrastus (ca. 327–287 BC) in his treatise *De lapidibus*, which details “lyngurium”, a yellow stone capable of attracting dust and small items (including straw, leaves, copper, and iron) when heated.

As research on the physical characteristics of these minerals intensified, their chemical composition gained attention in the 19th century, partially due to the identification of the element boron in 1808. The broad variety of tourmaline species, currently classified into 44 types, leads to a complex overall chemical formula dependent on the occupancy of many sites that may vary within the same crystal. This trait resulted in considerable interest from a geological perspective, as tourmalines function as remarkable recorders of geological processes and as indicators of the composition of their host rocks, owing to their broad stability range and low diffusivity of chemical species within their structure. Establishing the chemical composition of these minerals is crucial for understanding the formation processes and the environmental makeup over time. However, this operation may be complex due to the wide spectrum of elements that natural tourmalines can comprise, even in minimal quantities, which complicates the clear identification of the many species.

Raman spectroscopy is an ideal approach for analysing tourmaline composition: it is a non-destructive technique that generally necessitates no specific sample preparation and does not damage the specimens, which is crucial in the gemmological domain. Furthermore, when combined with a microscope, it can achieve high spatial resolution, facilitating the examination of micrometric grains in sediments for geological provenance studies. Many studies of the Raman spectra of tourmalines have focused on clarifying the changes in peak parameters according to their group classification and the composition of the examined samples. However, a comprehensive model that correlates fluctuations in the Raman spectrum with changes in tourmaline's chemical makeup remains absent.

This thesis aims to examine a specific category of tourmalines, the alkali group, and to differentiate its three principal subspecies (dravite, schorl, and elbaite) through the analysis of their Raman spectrum characteristics. We will subsequently study the variation of spectral parameters and develop a method to determine the chemical composition of the studied samples, facilitating the quantitative determination of specific elements distinctive of these species.

> *-MARY: And what is [tourmaline] made of?*
>
> *-LECTURER: A little of everything; there's always flint, and clay, and magnesia in it; and the black is iron, according to its fancy; and there's boracic acid, [...] and there's potash, and soda; and, on the whole, the chemistry of it is more like a mediaeval doctor's prescription than the making of a respectable mineral: but it may, perhaps, be owing to the strange complexity of its make, that it has a notable habit which makes it, to me, one of the most interesting of minerals.*
>
> *(Ruskin, 1894)* [1]

Tourmaline

Tourmalines form a **supergroup** (a group of different mineral groups with the same structure and similar chemistry) of borosilicate minerals distinguished by a crystal structure exhibiting **rhombohedral symmetry**, categorised within the space group *R3m*[2]. The chemical formula of these minerals is complex due to the varied occupancy of the several crystal sites. It is frequently expressed as

$$XY_3Z_6(T_6O_{18})(BO_3)_3V_3W$$

with the various positions potentially occupied by the following cations and anions, listed in order of abundance[3,4]:

- X: Na^+, Ca^{2+}, □ (vacant site), K^+.
- Y: Fe^{2+}, Mg^{2+}, Mn^{2+}, Al^{3+}, Li^+, Fe^{3+}, Cr^{3+}, Ti^{4+}, Zn^{2+}, Cu^{2+}, V^{3+}.
- Z: Al^{3+}, Fe^{3+}, Mg^{2+}, Fe^{2+}, Cr^{3+}, V^{3+}.
- T: Si^{4+}, Al^{3+}, B^{3+}.
- B: B^{3+}.
- V: hydroxide ion $(OH)^-$, oxide ion (O^{2-}).
- W: F^-, $(OH)^-$, O^{2-}.

The configuration of the sites is usually represented as illustrated in Figure 1.

The **six TO_4 tetrahedra**, represented in brown, are arranged in a ring, as clearly shown in Figure 1A, with the apical oxygen orientated along the −c-axis. Typically, the T position is occupied by silicon, leading to the widespread designation of these units as SiO_4 tetrahedra.

The **ninefold-coordinated X-site** (purple) is located in the centre of the ring and is partially offset along the c-axis (Figure 1C).

The **three triangular BO_3 groups** (in pink) are orientated parallel to the (001) lattice plane and are slightly tilted along the negative c-axis relative to the ring plane. One of the three oxygen atoms at the vertices of the group is shared with two Y-type octahedra from neighbouring unit cells (not visible in this picture), while the remaining two are each shared with a Z-type octahedron. B-sites are typically solely filled by boron, facilitating the quantification of this element.

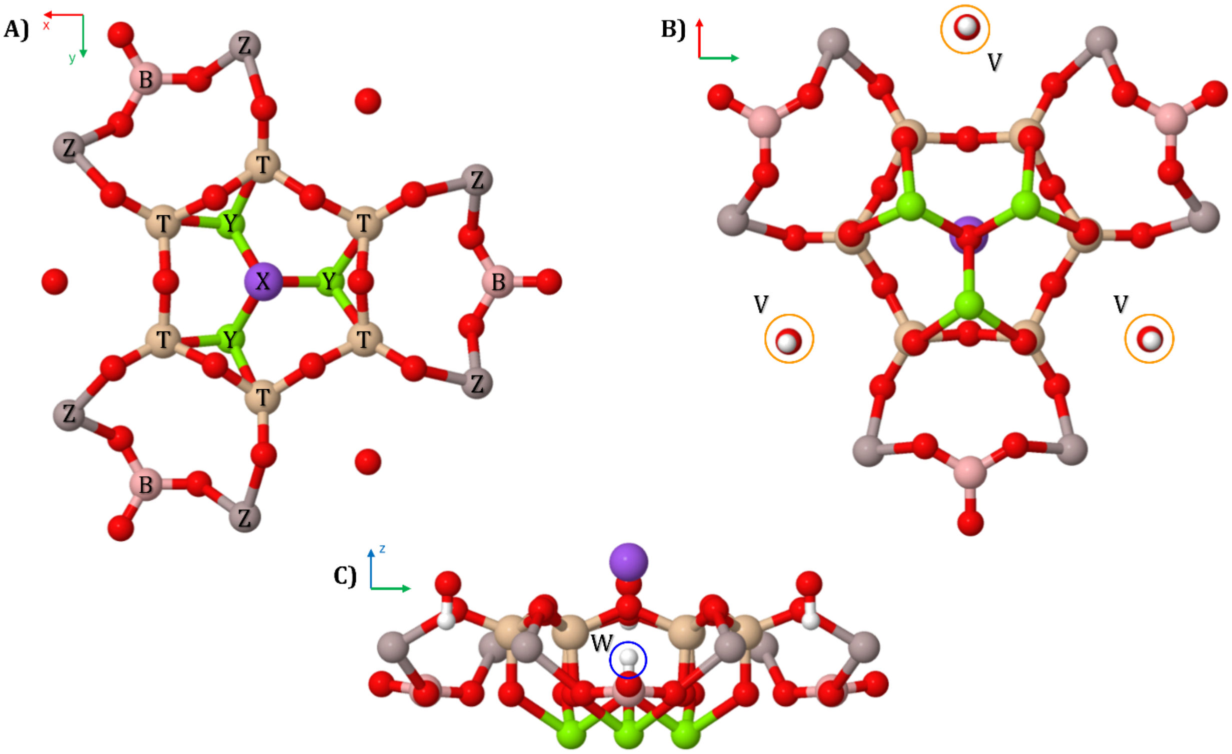

Figure 1: The representations of the tourmaline crystal structure from multiple orientations, with distinct crystal sites emphasised in various colours. Atoms in red are oxygen.

The **three YO_6 octahedra** (green) are arranged to share a single oxygen at the vertex beneath the X-site, while the opposite vertex is simultaneously shared with two Z-type octahedra from adjacent unit cells. The three octahedra form a more constricted ring than the TO_4 tetrahedra and are slightly inclined relative to the c-axis. The remaining oxygens of the YO_6 octahedra are also coordinated with BO_3 and TO_4 sites.

The **six ZO_6 octahedra** (in grey) are arranged in pairs, each sharing an oxygen atom that is also shared with a Y-type octahedron. The octahedra form a ring that is wider than that created by the TO_4 tetrahedra, and they are also slightly inclined relative to the c-axis. The remaining oxygens of the ZO_6 octahedra are coordinated with BO_3 and TO_4 sites.

The **three V-sites**, often denoted as O(3) and illustrated in orange in Figure 1B, correspond to one of the three distinct oxygens associated with a Y group and two Z groups of neighbouring unit cells. If these sites are filled by hydroxyl groups, as is often the case, the O-H bond is orientated parallel to the c-axis with the hydrogen in the negative direction, and the three hydrogen positions are often denoted as H(3).

One W-site (depicted in blue, Figure 1C), also referred to as O(1), is located along the axis of X-site (in the c direction) and is linked to the oxygen that is shared among the three YO_6 octahedra. If this site is occupied by a hydroxyl group, the O-H bond is aligned parallel to the c-axis, with the hydrogen atom orientated towards the X-site in the position indicated as H(1).

Tourmaline Species

There are a total of 44 species of tourmaline nowadays[5], differentiated by the occupation of diverse crystal sites determined by bond-valence constraints[6]; all of these species can be categorised into subgroups with similar compositions (Table 1)[7]. The primary classification among the many species is based on the occupation of the X-site: when occupied by Na^+ or, less commonly, by K^+, the tourmaline species belongs to the **alkali group**. Otherwise, if the main element in the X-site is Ca^{2+}, the species belongs to the **calcic group**. Finally, if the X-site is unoccupied, the tourmaline is part of the **X-vacant group** (Figure 2A).

A secondary classification of subgroups is based on the anions occupying the W-site (O(1)) and V-sites (O(3)). In particular, the name is assigned to the species with the end-member formula containing the OH^- group in the W-site (sometimes featuring the suffix *hydroxyl-*), whereas the suffixes *oxy-* or *fluor-* are appended if O^{2-} or F^- predominates in the W-site, respectively (Figure 2B).

This study will focus exclusively on hydroxyl species within the alkaline group, in particular, on those linked to the Li – Fe^{2+} – Mg – ^{Z}Al – $^{O(1)}(OH)$ subsystem (Figure 2C), namely **dravite**, **schorl**, and **elbaite**, which are some of the most abundant tourmaline species in nature[8].

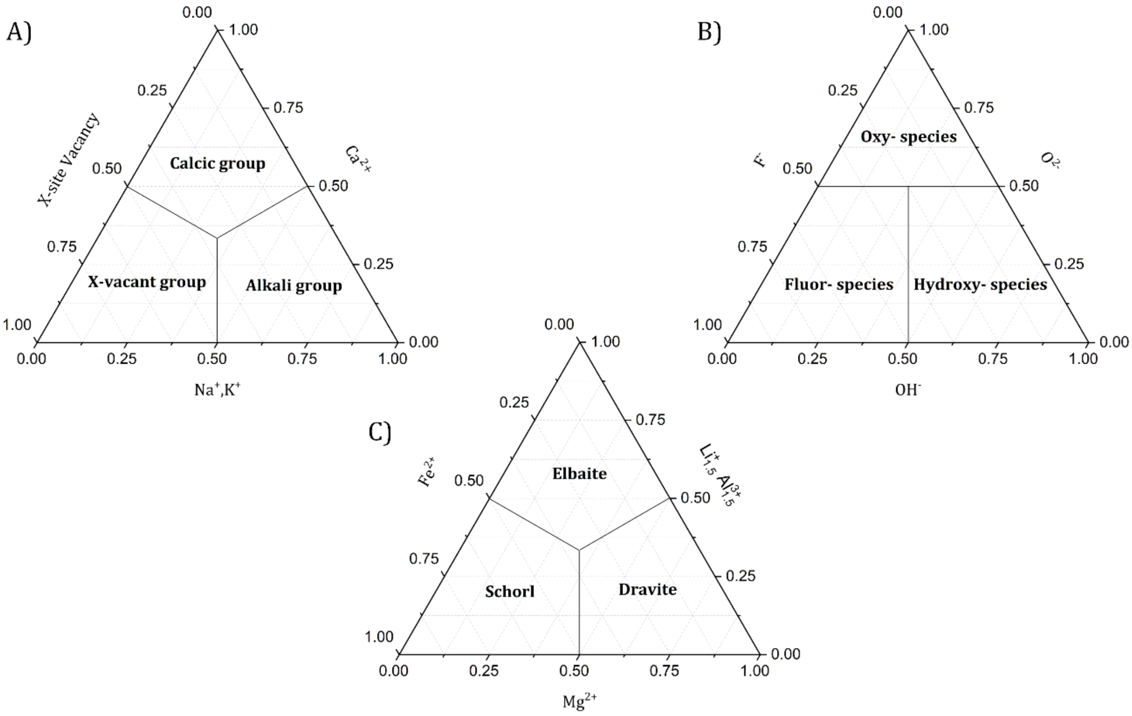

Figure 2: Ternary systems for different tourmaline classification based on the occupancy of the X-site (A), W-site (B) and Y-sites (C). In the case of the W-site, since there are two different valences for anions (2- for O and 1- for OH and F), oxy species must contain more than 50% of O^{2-} in the W-site.

Species Name	X	Y_3	Z_6	T_6O_{18}	$(BO_3)_3$	V_3	W
Alkali Group							
Dravite	Na	Mg_3	Al_6	Si_6O_{18}	$(BO_3)_3$	$(OH)_3$	OH
Fluor-Dravite	Na	Mg_3	Al_6	Si_6O_{18}	$(BO_3)_3$	$(OH)_3$	F
Schorl	Na	Fe^{2+}_3	Al_6	Si_6O_{18}	$(BO_3)_3$	$(OH)_3$	OH
Fluor-Schorl	Na	Fe^{2+}_3	Al_6	Si_6O_{18}	$(BO_3)_3$	$(OH)_3$	F
Tsilaisite	Na	Mn^{2+}_3	Al_6	Si_6O_{18}	$(BO_3)_3$	$(OH)_3$	OH
Fluor-Tsilaisite	Na	Mn^{2+}_3	Al_6	Si_6O_{18}	$(BO_3)_3$	$(OH)_3$	F
Chromium-Dravite	Na	Mg_3	Cr_6	Si_6O_{18}	$(BO_3)_3$	$(OH)_3$	OH
Vanadium-Dravite	Na	Mg_3	V_6	Si_6O_{18}	$(BO_3)_3$	$(OH)_3$	OH
Elbaite	Na	$Li_{1.5}Al_{1.5}$	Al_6	Si_6O_{18}	$(BO_3)_3$	$(OH)_3$	OH
Fluor-Elbaite	Na	$Li_{1.5}Al_{1.5}$	Al_6	Si_6O_{18}	$(BO_3)_3$	$(OH)_3$	F
Oxy-Dravite	Na	Al_2Mg	Al_5Mg	Si_6O_{18}	$(BO_3)_3$	$(OH)_3$	O
Oxy-Schorl	Na	Fe^{3+}_2Al	Al_6	Si_6O_{18}	$(BO_3)_3$	$(OH)_3$	O
Povondraite	Na	Fe^{3+}_3	$Fe^{3+}_4Mg_2$	Si_6O_{18}	$(BO_3)_3$	$(OH)_3$	O
Bosiite	Na	Fe^{3+}_3	Al_4Mg_2	Si_6O_{18}	$(BO_3)_3$	$(OH)_3$	O
Ferro-Bosiite	Na	Fe^{3+}_3	$Al_4Fe^{2+}_3$	Si_6O_{18}	$(BO_3)_3$	$(OH)_3$	O
Princivalleite	Na	Mn_2Al	Al_6	Si_6O_{18}	$(BO_3)_3$	$(OH)_3$	O
Chromo-Alumino-Povondraite	Na	Cr_3	Al_4Mg_2	Si_6O_{18}	$(BO_3)_3$	$(OH)_3$	O
Oxy-Chromium Dravite	Na	Cr_3	Cr_4Mg_2	Si_6O_{18}	$(BO_3)_3$	$(OH)_3$	O
Oxy-Vanadium Dravite	Na	V_3	V_4Mg_2	Si_6O_{18}	$(BO_3)_3$	$(OH)_3$	O
Vanadio-Oxy-Chromium Dravite	Na	V_3	Cr_4Mg_2	Si_6O_{18}	$(BO_3)_3$	$(OH)_3$	O
Vanadio-Oxy-Dravite	Na	V_3	Al_4Mg_2	Si_6O_{18}	$(BO_3)_3$	$(OH)_3$	O
Maruyamaite	K	Al_2Mg	Al_5Mg	Si_6O_{18}	$(BO_3)_3$	$(OH)_3$	O
Dutrowite	Na	$Fe^{2+}_{2.5}Ti_{0.5}$	Al_6	Si_6O_{18}	$(BO_3)_3$	$(OH)_3$	O
Magnesio-Dutrowite	Na	$Mg_{2.5}Ti_{0.5}$	Al_6	Si_6O_{18}	$(BO_3)_3$	$(OH)_3$	O
Darrellhenryite	Na	$LiAl_2$	Al_6	Si_6O_{18}	$(BO_3)_3$	$(OH)_3$	O
Olenite	Na	Al_3	Al_6	Si_6O_{18}	$(BO_3)_3$	$(O)_3$	OH
Fluor-Buergerite	Na	Fe^{3+}_3	Al_6	Si_6O_{18}	$(BO_3)_3$	$(O)_3$	F
Ertlite	Na	Al_3	Al_6	$Si_4B_2O_{18}$	$(BO_3)_3$	$(OH)_3$	O
Calcic Group							
Uvite	Ca	Mg_3	Al_5Mg	Si_6O_{18}	$(BO_3)_3$	$(OH)_3$	OH
Fluor-Uvite	Ca	Mg_3	Al_5Mg	Si_6O_{18}	$(BO_3)_3$	$(OH)_3$	F
Feruvite	Ca	Fe^{2+}_3	Al_5Mg	Si_6O_{18}	$(BO_3)_3$	$(OH)_3$	OH
Liddicoatite*	Ca	Li_2Al	Al_6	Si_6O_{18}	$(BO_3)_3$	$(OH)_3$	OH
Fluor-Liddicoatite	Ca	Li_2Al	Al_6	Si_6O_{18}	$(BO_3)_3$	$(OH)_3$	F
Lucchesiite	Ca	Fe^{2+}_3	Al_6	Si_6O_{18}	$(BO_3)_3$	$(OH)_3$	O
Magnesio-Lucchesiite	Ca	Mg_3	Al_6	Si_6O_{18}	$(BO_3)_3$	$(OH)_3$	O
Adachiite	Ca	Fe^{2+}_3	Al_6	$AlSi_5O_{18}$	$(BO_3)_3$	$(OH)_3$	OH
X-Vacant Group							
Magnesio-Foitite	□	Mg_2Al	Al_6	Si_6O_{18}	$(BO_3)_3$	$(OH)_3$	OH
Foitite	□	Fe^{2+}_2Al	Al_6	Si_6O_{18}	$(BO_3)_3$	$(OH)_3$	OH
Celleriite	□	Mn^{2+}_2Al	Al_6	Si_6O_{18}	$(BO_3)_3$	$(OH)_3$	OH
Rossmanite	□	$LiAl_2$	Al_6	Si_6O_{18}	$(BO_3)_3$	$(OH)_3$	OH
Fluor-Rossmanite	□	$LiAl_2$	Al_6	Si_6O_{18}	$(BO_3)_3$	$(OH)_3$	F
Oxy-Foitite	□	Fe^{2+}_2Al	Al_6	Si_6O_{18}	$(BO_3)_3$	$(OH)_3$	O
Alumino-Oxy-Rossmanite	□	Al_3	Al_6	$AlSi_5O_{18}$	$(BO_3)_3$	$(OH)_3$	O
Oxy-Rossmanite*	□	$Li_{0.5}A_{2.5}$	Al_6	Si_6O_{18}	$(BO_3)_3$	$(OH)_3$	O

Table 1: List of the 44 different tourmaline species with their end-member formula divided into the three main X-site-related groups. Horizontal lines denote the divisions into subgroups containing tourmaline species with similar charge distribution in each site.

---

* *The species is not recognised by the IMA (International Mineralogical Association).*

The first species, **dravite**, is predominantly occupied by magnesium (Mg^{2+}) in the Y-sites, resulting in the following end-member formula:

$$NaMg_3Al(Si_6O_{18})(BO_3)_3(OH)_3OH$$

The second species, **schorl**, has ferrous iron (Fe^{2+}) in the Y-sites and is thus represented by the general end-member formula:

$$NaFe_3^{2+}Al(Si_6O_{18})(BO_3)_3(OH)_3OH$$

Finally, **elbaite** shows a mixed occupancy of the Y-sites by lithium (Li^+) and aluminium (Al^{3+}), yielding the end-member formula:

$$NaLi_{1.5}Al_{1.5}Al(Si_6O_{18})(BO_3)_3(OH)_3OH$$

As visible, the chemical end-member formulas of the three species differ exclusively in their Y-sites compositions. However, natural tourmaline crystals exhibit varied chemical compositions that deviate from the end-member formula, leading to the ternary system of dravite-schorl-elbaite. Moreover, Y-Z-sites disorder may arise[9–11], with Al^{3+} ions occupying Y-sites and Fe and Mg situated in the Z-sites, particularly in oxy-species, or generally when certain W-sites are filled by O^{2-} anions, as illustrated in Table 1. Therefore, it is essential to develop a method for estimating the concentration of elements present in the Y-sites of the analysed samples to classify them into a specific species within the ternary system. Dravite, schorl, and elbaite crystals are typically distinguishable by their distinct colours; nonetheless, the quantification of mixed compositions remains challenging.

Tourmalines Properties And Applications

Tourmalines exhibit a **broad stability range** at diverse **temperature** and **pressure** conditions, encompassing most environments present in the Earth's crust and upper mantle. Tourmalines may maintain stability at temperatures ranging from 725 to 950°C, contingent upon pressure conditions, up to 7 GPa, and its composition[12,13]. This feature enabled tourmalines to be found in various geological environments. The stability is also influenced by fluid phases; they exhibit greater stability in acidic and neutral aqueous solutions, whereas their stability diminishes in alkaline aqueous solutions or in fluids lacking adequate boron concentration (0.5–9 wt% of B_2O_3)[14–16]. Tourmalines have a density ranging from 2.8 to 3.3 g/cm^3 and a hardness of approximately 7 to 7.5 on the Mohs scale, depending upon the species and its composition[17].

Another fundamental property related to tourmalines stability is the **low volume diffusion rate for major and trace elements** within their structure once the tourmaline crystal is formed, enabling them to retain chemical and textural information throughout different geological processes[18,19]. This property is highlighted by different colour zonation in some tourmaline crystals related to changes in external conditions (temperature, pressure and composition) during the crystal growth (Figure 3).

The point group symmetry of tourmalines (*3m*) is **non-centrosymmetric** and **polar**, indicating the absence of a centre of symmetry and the presence of a net electric dipole moment in their crystal structure. This leads to two of their physical properties: **piezoelectricity** and **pyroelectricity**. The non-centrosymmetric characteristic is emphasised by the **polar growth** of tourmaline crystals, wherein SiO_4 tetrahedra orient along the −c axis, exhibiting **hemimorphic** traits, specifically differing faces along the +c and −c axes, with preferential growth along the +c axis, particularly at lower temperatures[17,20].

Finally, tourmaline can contain a lot of different **minor** and **trace elements** which can act as **chromophores**, resulting in a wide range of colours that these mineral species can present even within the same crystal as described before.

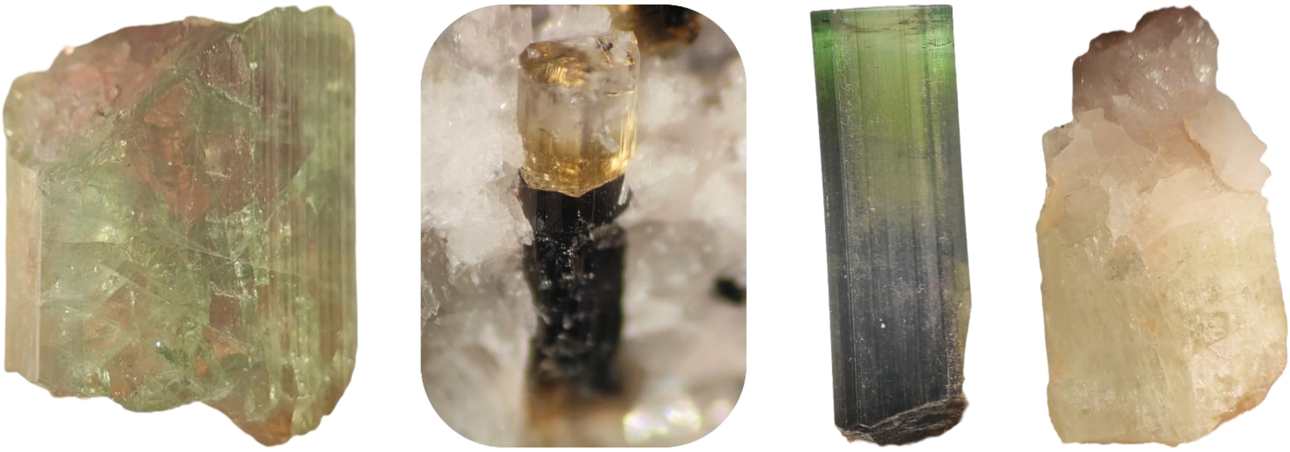

Figure 3: Illustration of several multicoloured tourmaline crystals. Diverse colourations correspond to varying elemental distributions within the crystal, attributed to fluctuations in external conditions during crystal formation, which are localised due to the low rate of volume diffusion for the elements.

Geological Applications

Tourmalines hold considerable importance in geology, as they preserve information about their **compositional makeup** and the **environmental conditions** during their formation. A single grain can encompass information regarding the complete formation cycle of tourmaline, enabling deductions about the **temperature**, **pressure**, and **rock composition** during the lithogenic process. Owing to their mechanical and chemical durability, chemical diversity, and prevalence in diverse geological contexts, they have emerged as a significant asset in numerous geological investigations.

Tourmalines have been documented in many lithologic contexts over the 20th and 21st centuries, encompassing **igneous**, **metamorphi**c, and **sedimentary rocks**, along with associated **diagenetic environments**[21–26]. This ubiquity is due largely to the great affinity of boron for tourmaline, which leads to its crystallisation in practically every **boron-rich** geologic environment[27].

Primarily, tourmalines are generated in **magmatic settings**, namely during the concluding phases of magma crystallisation, characterised by elevated residual concentrations of boron and water. The chemical composition is contingent upon the magmatic environment where fractional crystallisation transpires; varying degrees of fractionation yield distinct species of tourmaline. In the initial phases, intermediate igneous rocks emerge with elevated sodium concentrations, along with iron and magnesium, characteristic of schorl and dravite compositions. As fractionation intensifies, the lithium content correspondingly rises, resulting in the creation of elbaite. Variations in the magmatic environment during crystallisation might result in the manifestation of growth zoning in the formed crystals. Diagenetic processes ultimately facilitate the continued growth of detrital grains, typically occurring along the crystal's +c-axis in a monopolar fashion or with pronounced asymmetry due to the polar property of tourmaline. **Metamorphic** rocks represent the second most prevalent environment for tourmaline formation, following igneous rocks; however, the existence of pre-existing grains for their development is essential. The composition and structure are influenced by metamorphic reactions and fluctuations in pressure, temperature, and the composition of the surrounding environment. Ultimately, **hydrothermal processes** may facilitate the infiltration of fluids containing trace elements (< 1000 ppm) into the tourmaline[28].

Tourmaline's resilience to chemical and mechanical degradation allows grains to endure processes like weathering, erosion, and diagenesis, generally maintaining their original chemical fingerprints. This durability, along with complex internal zoning, enables tourmaline to function as an **information archive**, documenting alterations in its host rock's metamorphic, magmatic, or hydrothermal development. Furthermore, tourmaline's capacity to participate in chemical equilibria with surrounding minerals enables it to keep records of the evolution of its host rock system[29,30]. The chemical zoning may indicate several metamorphic or magmatic occurrences, offering an in-depth description of geological history[14,31].

As a common gangue mineral in many **hydrothermal ore deposits**, tourmaline’s chemical and isotopic characteristics help trace the evolution of ore-forming fluids and reconstruct the history of mineralization[32–34].

Tourmalines have been used in both bulk and *in situ* isotopic studies to infer **formation temperatures**, **fluid sources**, and **geochronological information**[30,35–39].

The use of tourmalines in **provenance studies** dates back to the discovery of detrital grains in sedimentary rocks using petrographic microscopes in the 19th century[40]. Tourmalines, together with zircon and rutile, were soon recognised as one of the most common and stable heavy minerals in clastic sediments[41–43]. The relative abundance of zircon, tourmaline, and rutile in sedimentary rocks, the so-called **ZTR index**, is used as a measure of sediment maturity[44]. High ZTR values indicate advanced sediment recycling and weathering, as only the most stable minerals persist.

Early provenance studies utilised the optical properties of detrital tourmalines to link grains to specific granites[45]. With advances in microanalysis, chemical compositions of tourmaline grains could be determined, providing powerful constraints on source lithologies. Henry and Guidotti[29] developed chemical diagrams (Al–Fe–Mg and Ca–Fe–Mg subsystems – see Figure 4) to distinguish tourmalines from different **source rocks**. Using these chemical fingerprints, the provenance of sedimentary deposits can be robustly constrained[36].

In addition to chemistry, **grain size**, **degree of rounding**, and **mineral inclusions** within tourmaline grains provide further evidence for interpreting sedimentary processes and source rocks[46,47]. These characteristics can reveal the transport history and depositional environment of the host sediment. The compositional and textural attributes of detrital tourmalines have also been utilised for stratigraphic correlation, linking sedimentary layers across regions based on their heavy mineral assemblages and tourmalines characteristics.

With the advent of high-resolution *in situ* analytical techniques, tourmaline's utility in provenance studies has expanded. Its trace elements and isotopic composition can now be precisely measured, linking individual grains to specific magmatic, metamorphic, or sedimentary source rocks with greater confidence[14,48,49].

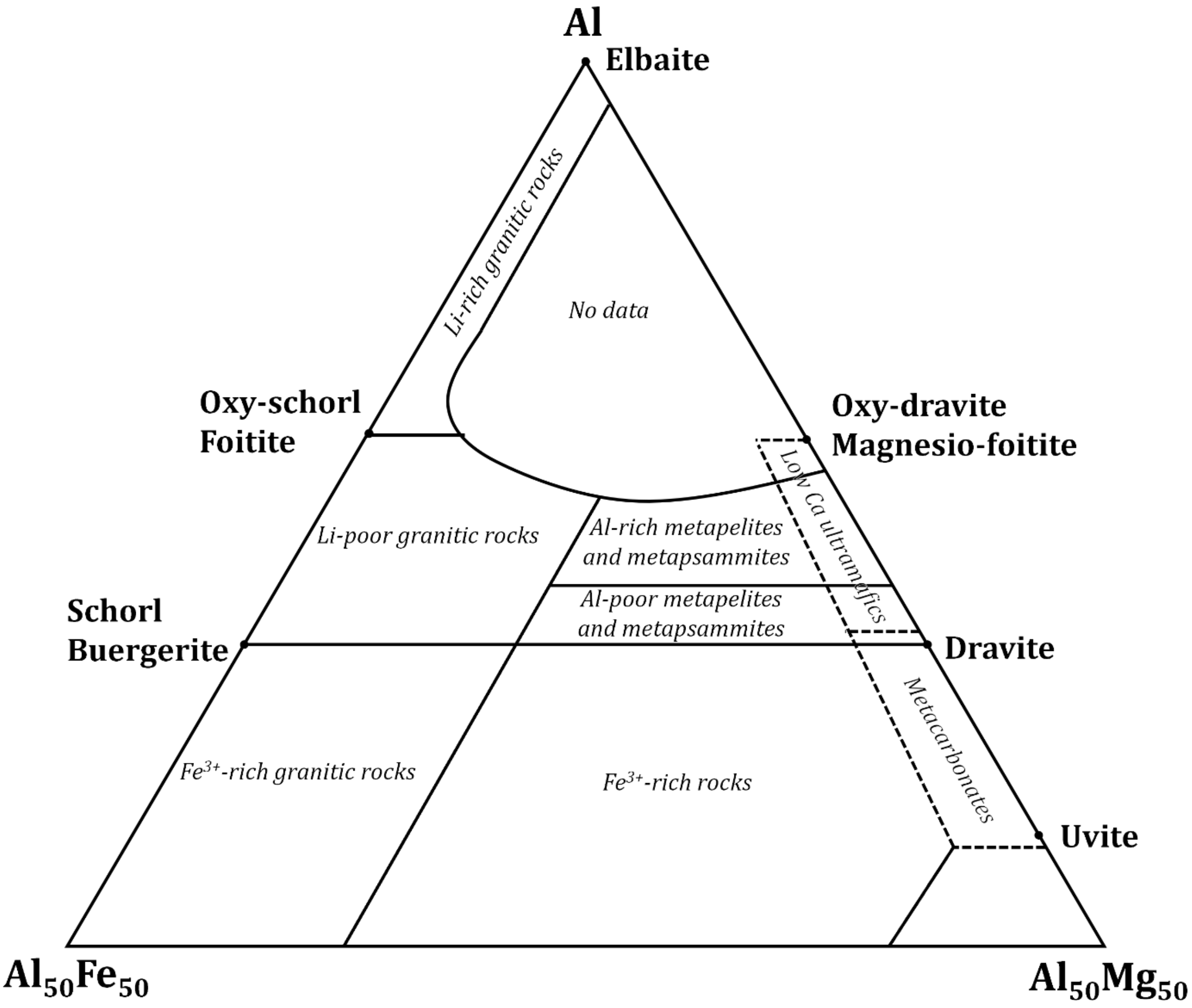

Figure 4: Al-Fe-Mg system proposed by Henry and Guidotti[29] for tourmalines host-rock identification.

Gemmological Applications

Tourmalines are highly esteemed **gem minerals**, valued for their remarkable variety of colours and durability. Tourmalines exhibit chemical and optical complexity, incorporating a wide array of transition elements (Fe^{2+}, Fe^{3+}, Mn^{2+}, Mn^{3+}, Ti^{4+}, Cu^{2+}, V^{3+}, Cr^{3+}) occupying the Y and Z octahedral sites and acting as **chromophores**. In addition, **colour centres**, generated by the interaction of natural or artificial irradiation with the crystal lattice, can further enhance colour expression[50]. The primary colour mechanisms in tourmalines comprise:

- **Crystal-Field Transitions** (CFT): Accountable for the absorption characteristics linked to Cu^{2+}, Fe^{2+}, Fe^{3+}, and Mn^{3+}.

- **Intervalence Charge Transfer** (IVCT): Especially pertinent in blue-green elbaite, involving Cu^{2+}–Mn^{3+} or Fe^{2+}–Ti^{4+} couples.
- **Colour Centres**: Radiation-induced defects that stabilise atypical colour states, particularly in pink/red and pale green tourmalines[51].

This complex nature contributes to the mineral's exceptional colour fluctuation, even within single crystals, thereby augmenting its market value[52]. Tourmalines possess a moderate refractive index (~1.61–1.67), exceptional hardness (7–7.5 on the Mohs scale), and a lack of cleavage, making them ideal for crafting resilient and aesthetically pleasing jewels[53]. These traits have garnered the interest of gemmologists, who have categorised tourmaline crystals and gems into several varieties based on their colour and, consequently, the concentration of chromophores.

- **Achroite**, commonly lacking colour, has no specific chromophores.
- **Rubellite**, exhibiting pink and red tones, is distinguished by a greater concentration of Mn^{3+}.
- **Canary**, varying from yellow to yellowish-green, could be linked to the presence of Mn^{2+} alone or to the coexistence of both Mn^{2+} and Ti^{4+}.
- **Verdelite**, the green variety, has a greater amount of iron in both oxidation states (Fe^{2+} and Fe^{3+}) or a concentration of both Fe^{2+} and Ti^{4+}.
- **Indicolite**, distinguished by its blue hue, is mostly associated with the presence of either Fe^{2+} alone or both Fe^{2+} and Fe^{3+}.
- The **Paraíba-type**, defined by its characteristic "neon" blue colour (lighter than indicolite), consists of Cu^{2+}-bearing tourmalines, representing the most sought-after and valuable type of tourmaline gemstones.

Among the different tourmaline varieties, our focus will be on **Paraíba-type** gemstones and on the particular **pink-green watermelon** tourmalines, characterised by a pink core and a concentric green rim with respect to the crystal c-axis**.**

The **Paraíba-type** variety was first discovered in the late 1980s in the state of **Paraíba, Brazil**, at the *Mina da Batalha*[54]. The electric blue-to-green colouration, defined as "neon" or "fluorescent" (see Figure 5), impacted on the coloured gemstone market, achieving values of up to US$25,000 per carat for the highest quality specimens[53–55]. Paraíba-type tourmalines typically belong to the **elbaite** and **fluor-elbaite** species; however, **fluor-liddicoatite** minerals have also been classified within this variety[56].

The unique hue of Paraíba-type tourmalines is primarily attributed to elevated levels of **Cu^{2+}** (0.37–2.38 wt.% CuO) and, to a lesser extent, the interaction with Mn and minor quantities of Fe and Ti[54,57,58]. The blue colour arises from strong d–d electronic transitions of Cu^{2+}, exhibiting absorption bands centred around 700 nm and 900 nm in the near-infrared (NIR) region of the absorption spectrum; in samples with minimal Fe and Ti, the lack of interfering absorption facilitates elevated colour saturation and "neon" effects[59]. Manganese occurs in both Mn^{2+} and Mn^{3+} oxidation states, with the latter producing pink to purple colours (typical of the so-called rubellite variety) by absorption at approximately 520 nm[60]. Consequently, **heat treatments** are frequently employed to reduce Mn^{3+} to Mn^{2+}, thus removing the violet-pink component and augmenting blue saturation[61]. The majority of Paraíba-type stones available in the market undergo heat treatment to enhance or increase the "neon" blue shade. Treatment temperatures span from 350 to 550°C, requiring meticulous regulation to prevent the damage of inclusions or the fracturing of crystals[62]. A green component may also arise, influenced by Fe^{2+}–Ti^{4+} intervalence charge transfer[53,54].

Figure 5: A Paraíba-type tourmaline gemstone from the Laboratoire Français de Gemmologie (LFG, Paris, France) collection.

Subsequent to the first finding in Brazil, analogous Cu-bearing elbaites were identified in **Nigeria** and **Mozambique**[58,63–65]. Paraíba-type elbaite is found in highly differentiated pegmatites, usually in association with quartz, feldspar, lepidolite, and other phosphate minerals. The remarkable concentration of Cu is geologically atypical, indicating localised fluid-rock interaction and distinct pegmatite development[55,66–68]. Due to the commercial significance of Paraíba-type tourmalines, precise provenance identification is essential. The **Laboratory Manual Harmonisation Committee** (LMHC) currently classifies "Paraíba tourmaline" as any tourmaline exhibiting "*a blue (electric blue, neon blue, violet blue), bluish green to greenish blue, green or yellowish green tourmaline, of medium-light to high saturation and tone (relative to this variety of tourmaline), mainly due to the presence of copper (Cu) and manganese (Mn) of whatever geographical origin*"[69]. Nonetheless, improved chemical fingerprinting is essential for customers demanding accurate source identification. Indeed, despite Paraíba-type tourmaline currently being located in multiple sites, chemical provenance analyses employing **Laser Ablation-Inductively Coupled Plasma-Mass Spectrometry** (LA-ICP-MS) have disclosed complex yet statistically significant variations in **trace element** compositions (Ga, Pb, Zn, Bi, Sb, Be, Sc)[70–73]. Nigerian tourmalines are abundant in Ga and Pb, whereas Brazilian stones have elevated levels of Mg, Zn, and Sb. Mozambique gemstones exhibit higher Be and Sc levels but are deficient in magnesium. These characteristics are crucial for ascertaining their origin, which is necessary in the high-value gemstones market.

On the other side, **watermelon tourmalines** are a specific variety of **elbaite** and **liddicoatite** species distinguished by concentric colour zoning perpendicular to the crystal c-axis, featuring a **pink core** and a **green or dark green outer rim** (Figure 6), which is clearly observable in slices cut perpendicular to the c-axis[74–78]. This zoning arises from alterations in pegmatitic fluid composition throughout crystal growth[79,80]. This is also evidenced by various shades of the same colour, particularly in the green rim, signifying numerous subsequent variations in the crystal growth conditions. The pink core is typically due to the presence of **Mn^{3+}** as a chromophore, while the green rim is associated with **Fe^{2+}**.

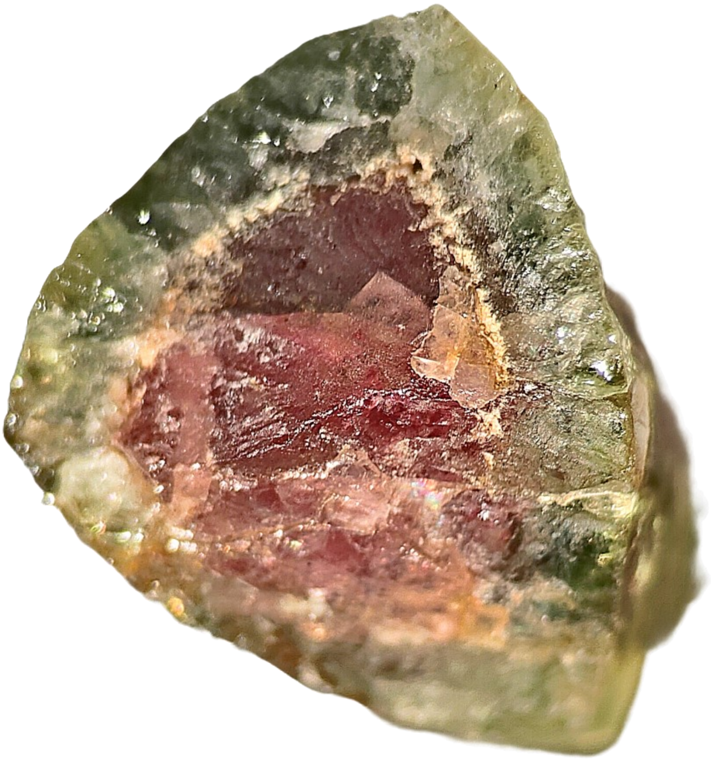

Figure 6: Example of watermelon tourmaline with a pink core and concentric green rim perpendicular to the crystal c-axis.

Watermelon tourmalines are esteemed by collectors and gem enthusiasts for their vivid appearance and the insights they offer into the crystal's growth history. Rare specimens that are large, transparent, and well-zoned possess considerable market value[53,79].

Other Applications

This thesis will mainly investigate the geological and gemmological applications of tourmalines. Nevertheless, numerous other applications, particularly in **environmental fields**[81], exist and have been researched with noteworthy advancements. This is a concise overview of the research that examined other tourmaline's applications.

Tourmalines exhibit a pronounced affinity for **heavy metals** in both acidic and alkaline aqueous environments, outperforming conventional adsorbents such as activated carbon, zeolite, and biochar, particularly in acidic conditions[82–85]. The adsorption mechanisms encompass **electrostatic adsorption**, **ion exchange**, **polarization-induced cation transfer**, and **hydroxide precipitation**[86,87]. Consequently, tourmalines have attracted considerable attention as a promising alternative due to their distinctive physicochemical and electrochemical characteristics for the remediation of heavy metals and organic contaminants in diverse environmental matrices[88–90,81]. These pollutants are well-known for their toxicity, persistence, and potential for bioaccumulation, presenting significant risks to ecosystems and human health. Traditional remediation technologies, encompassing physical, chemical, and biological approaches, frequently face constraints related to efficiency, cost, environmental compatibility, and the potential for secondary pollution[91]. Thus, there is an urgent requirement for novel, efficient, and sustainable materials for environmental recovery.

Electrostatic adsorption arises as the electric field on tourmaline's surface, generated by its persistent dipoles, attracts heavy metal cations. The phenomenon of **ion exchange** is evidenced by the proportional rise in cations, including Ca^{2+}, Mg^{2+}, and K^{+}, released from tourmaline corresponding to enhanced heavy metal absorption[86]. The **polarisation** of water by tourmaline enhances subsequent cation transfer, a process peculiar for this mineral[83,92]. Moreover, tourmalines possess the ability to independently **regulate solution pH**, which may result in **hydroxide precipitation** contingent upon the solubility product of the specific metal ion in question. Multiple parameters affect adsorption efficiency, including **temperature**[93], **solution pH**[94,95], **particle size**[86,96], and **tourmaline dose**. Smaller particle sizes significantly increase specific surface area and reveal additional reactive mineral sites, hence enhancing adsorption[87].

Soil amendment using tourmalines transforms harmful heavy metal components into more stable and less accessible forms, thereby diminishing toxicity and enhancing plant and microbial health[97]. In contrast to conventional amendments such as lime or fly ash, tourmaline does not induce excessive soil alkalinity or compaction[98]. The efficacy is further augmented by diminishing particle size and amalgamating with other substances such as biochar[99]. Furthermore, tourmalines augment soil **enzyme activity**, hence promoting soil fertility.

Tourmalines, owing to the intrinsic iron composition and electric surface field, facilitate **Fenton-like reactions** for the oxidative degradation of organic pollutants, expanding the applicable pH range and minimising secondary pollution relative to conventional Fenton reagents[100,101]. Applications involve the elimination of dyes and antibiotics from wastewater[102]. Tourmaline-based catalysts demonstrate significant reusability, and their catalytic performance can be augmented by ultrasound, which improves catalyst dispersion and the generation of active species[103,104]. Three mechanisms function in tourmaline-catalysed Fenton-like systems: physical adsorption of organic compounds, homogeneous Fenton-like reactions facilitated by leached iron ions, and heterogeneous catalysis occurring at surface iron sites. The prevailing mechanism is influenced by pH and iron ions concentration[105,106].

Tourmaline-TiO_2 composites mitigate the drawbacks of pure TiO_2 photocatalysts, including restricted light absorption and charge recombination[107,108]. The internal electric field of tourmaline suppresses electron-hole recombination, while its far-infrared (FIR) radiation enhances dissolved oxygen amounts, collectively augmenting the photocatalytic efficacy of TiO_2 in the breakdown of organic pollutants[109–111]. The composites exhibit significant stability and reusability[112]. Tourmalines also catalyse **persulfate** and **peroxymonosulfate** to produce highly reactive oxygen species (OH, SO_4^-), facilitating the accelerated oxidation of organic pollutants[113,114]. The iron in tourmaline functions as a catalyst, resulting in a system that exhibits great efficiency, stability, and a wide pH operating range. The effects of anion scavenging and appropriate dosages must be evaluated for maximum efficacy[115].

Tourmalines support bioremediation of soils contaminated with **persistent organic pollutants** (POPs) by releasing micronutrients and promoting microbial growth[116]. Combined applications with **fungi** such as *Phanerochaete chrysosporium* and *Aspergillus niger* significantly enhance pollutant removal compared to individual treatments[117–119]. Tourmaline reduces soil **humic acid** content, increasing the bioavailability of hydrophobic organics and facilitating microbial degradation. Moreover, tourmalines in tandem with **rhizosphere microorganisms**, like *F. solani*, are efficacious in soils simultaneously polluted with heavy metals and organic compounds, diminishing pollutant bioavailability and promoting plant growth[97,117,118].

The **piezoelectric** properties of tourmalines were significant in the 20th century, particularly for the detection and measurement of **explosive pressures**[120,121]. In World War II, the necessity for low-Fe tourmalines for underwater blast detection prompted substantial international endeavours to obtain high-quality crystals[122]. Following the war, the advancement of tourmaline-based piezoelectric sensors persisted for the detection of shockwaves and blasts, capable of functioning at extreme temperatures reaching 700°C[123,124]. The shortage of high-quality tourmalines during and after the war triggered advancements in **synthetic crystal growth**, leading to comprehensive experimental investigations aimed at regulating cation composition and enhancing crystal quality[125–127]. The synthesis of tourmalines with specific compositions is complex; it necessitates meticulous control of starting materials and conditions, along with rigorous post-synthetic characterisation. Despite stoichiometric starting mixtures, synthetic tourmalines frequently exhibit significant substitutions or deviations from the ideal formula, particularly with excess Al in the Y-site and alkali vacancies in the-X site. Furthermore, only dravite produced crystals sufficiently large for comprehensive optical characterisation, whereas other end-members, particularly those with transition metal substitutions, crystallise as fine spherulites or acicular aggregates, restricting the formation of large, single crystals appropriate for extensive physical or crystallographic analysis.

Raman Spectrum Of Tourmalines

Raman spectroscopy is an optimal analytical technique for tourmalines characterisation for several reasons. This method is **non-destructive**, essential for gemmological applications, and enables **rapid** analysis of **micrometre-sized** materials without prior preparation, hence facilitating the examination of micrometric grains in sediments for provenance investigations. Secondly, the spectrum's change is explained by **symmetry selection principles**, which confine the array of active Raman modes according to the analysed species. The position and width of the peaks depend on the occupation of the relevant sites for the specific mode, as the phonon wave number is affected by the masses and interatomic interactions of the atoms involved in that vibrational mode. The relative intensity of the peaks depends on the chemical abundance of the various atoms involved.

Group-Theory

Through investigations grounded in **group theory**[128], it has been established that the **phonon modes** of tourmalines are categorised as follows:

- 32 A_1 modes.
- 22 A_2 modes.
- 54 E modes.

Two modes, one A_1 and one E, are **acoustic**, whilst the remaining modes ($31A_1 + 22A_2 + 53E$) are **optical**. The acoustic modes represent the lowest-energy phonon states, thereby correlating with atoms of greater mass or those involved in the weakest interactions. In tourmalines, such atoms are the cations located at the X-site. However, X-site occupancy can influence the vibrational modes related to the neighbouring sites. A_2 modes are inactive in Raman spectroscopy, whereas A_1 and E modes are Raman active. The 31 A_1 modes are detectable in the $\bar{\boldsymbol{y}}(\boldsymbol{zz})\boldsymbol{y}$ configuration (in Porto's notation), the 53 E modes are identifiable in the $\bar{\boldsymbol{y}}(\boldsymbol{zx})\boldsymbol{y}$ configuration, while all 84 modes (A_1 + E) are predicted to contribute to the spectrum obtained in the $\bar{\boldsymbol{y}}(\boldsymbol{xx})\boldsymbol{y}$ configuration. The polar traits of tourmalines may result in varying intensities of **longitudinal** (LO) and **transverse** (TO) optical modes for both A_1 and E, contingent upon the analytical configuration employed. Consequently, the configuration, namely the orientation of polarisation of the input light relative to the crystal axes, must be constant across various samples to investigate chemically driven variations in peak intensities. Numerous investigations concentrated on the A_1 modes of tourmalines, employing the $\bar{y}(zz)y$ configuration to achieve the largest peak intensity[129–133].

Regions Of The Tourmaline Raman Spectrum

By examining the Raman shift region of the several peaks linked to the A_1 modes, it is possible to ascertain the origin of each distinct vibrational mode (Figure 7). Three primary sections can be delineated: the **low-frequency band** (LFB), ranging from 150 to 450 cm^{-1}; the **mid-frequency band** (MFB), spanning 450 to 1200 cm^{-1}; and the **OH stretching region**, located at higher wavenumbers between 3300 and 3800 cm^{-1}[134,135].

The average bond lengths for each tourmaline site and its surrounding oxygens are presented in Table X, which aids in clarifying the subsequent association between various frequency regions in the Raman spectrum and specific site vibrations. Vibrational modes associated with the Y- and Z-sites are found in the LFB. The peaks corresponding to the vibrational modes of the YO_6 octahedra are located between 200 and 315 cm^{-1} (depicted in green in Figure 7). Generally, three principal peaks are identified as P_1, P_2, and P_3. The P_3 peak, arising from the deformation of the YO_6 octahedron and, to a lesser degree, the effect of adjacent sites, is typically located at about 315 cm^{-1} and displays modest intensity. In contrast, peaks P_1

and P_2, resulting from the vibrations of the YO_6 octahedra, demonstrate increased intensity, with their position and intensity significantly varying depending on the examined tourmaline species and the elements occupying the Y-site. Peaks corresponding to the vibrational modes of the ZO_6 octahedra are identified within the range of 360 - 375 cm^{-1} (depicted in grey in Figure 7), featuring two predominant peaks: one markedly more intense at approximately 370 cm^{-1} and a less intense counterpart at a slightly elevated wavenumber, occasionally reaching up to 400 cm^{-1}. The position of the most intense peak depends on the aluminium concentration at the Z-site and generally shifts to lower wavenumbers when replaced by iron and magnesium[130].

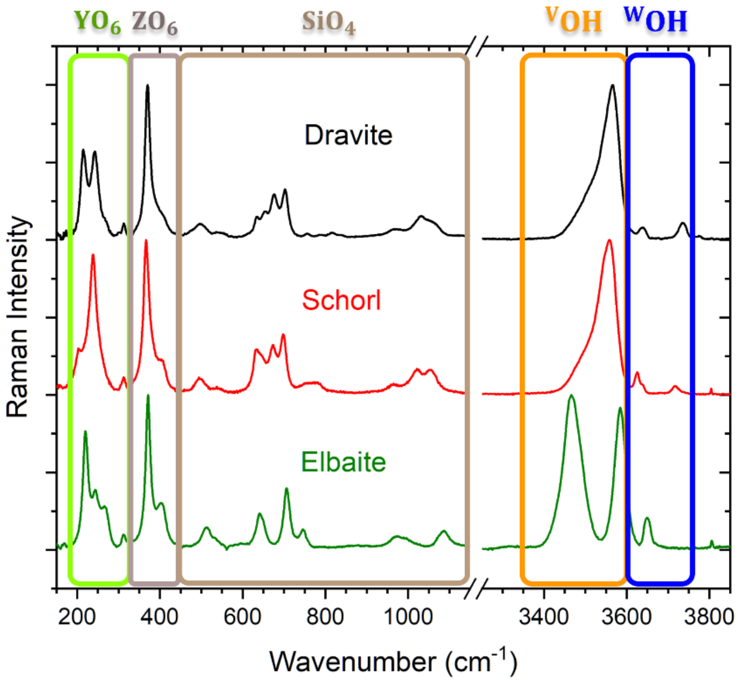

Figure 7: Different regions of the Raman spectrum of tourmaline (specifically for the dravite, schorl, and elbaite species) with distinct site-related vibrational modes highlighted.

Bond	Mean bond distance (Å)
<X–O>	2.683
<Y–O>	2.005
<Z–O>	1.9321
<T–O>	1.6206
<B–O>	1.3752
O3–H3 (^{V}OH)	0.972(2)
O1–H1 (^{W}OH)	0.958(8)

Table 2: Mean bond distance for each tourmaline site and its surrounding oxygens (data from Gatta et al.[136])

Vibrational modes associated with the TO_4 tetrahedral ring are identified in the MFB (highlighted in brown in Figure 7). The range of 600 to 750 cm^{-1} relates to the vibrational modes of the bridging oxygens inside the TO_4 tetrahedral configuration. Generally, it exhibits four different peaks; however, these may vary depending on the specific tourmaline species analysed, as the vibrational modes of the TO_4 tetrahedral rings are significantly affected by the adjacent non-tetrahedral cations, particularly those located at Y-sites[137]. Peaks at lower wavenumbers (460–560 cm^{-1}) may be observed, potentially ascribed to Fe^{3+} at the Z-site, influencing the stretching of the tetrahedral ring. The range of 960 - 1120 cm^{-1} is characterised by the stretching modes of the TO_4 tetrahedra, appearing as two to three broad bands of relatively low intensity.

At elevated wavenumbers, the peaks corresponding to the stretching of the OH groups situated in V- and W- sites are detected. The band of the ^{V}OH modes is often identifiable within the range of 3400 – 3615 cm^{-1} (depicted in orange in Figure 7), whereas the ^{W}OH modes are located between 3630 – 3770 cm^{-1} (shown in blue in Figure 7), attributable to the shorter (and thus weaker) bond length of O(1)-H(1) relative to O(3)-H(3).

Hydroxyl Groups

The analysis of the spectra related to the vibrational modes of hydroxyl groups at V-sites and W is significant for the classification of different tourmaline species; these stretching modes are detected at wavenumbers between 3400 and 3770 cm^{-1}. The vibrational modes of O-H bonds demonstrate significant sensitivity to the occupancy of neighbouring X-, Y-, and Z-sites, mostly due to their shared oxygen with Y- and Z-sites. From theoretical group analysis, it is anticipated that two unique Raman peaks will be observed in the $\bar{y}(zz)y$ configuration: one A_1 mode linked to the stretching of the O(1)-H(1) bond and the other A_1 mode related to the stretching of the O(3)-H(3) bond. However, the local composition of adjacent sites may vary across different unit cells, leading to the generation of **secondary peaks** due to various potential local compositions.

The attribution of the various peaks in the ^{W}HO modes is associated with changes in the composition of the three Y-sites that share the O(1) oxygen and the configuration of the adjacent X-site. The occupation of X-site can significantly modify the wavenumber of the ^{W}OH mode, resulting in several signals rather than a unique peak, depending on the different site composition. The presence of a positive charge at X-site causes repulsion with the H^+ ion of the OH group, leading to the modes related to the occupied X-site appearing at higher wavenumbers (3710 – 3810 cm^{-1}) compared to those connected with the X-vacant site (3615 – 3685 cm^{-1}). As an outcome, experimental results demonstrate that OH groups preferentially localise around an X-vacancy site, leading to a differential occupancy of the three Y-sites to sustain charge equilibrium. However, these peaks are often less pronounced than those linked to ^{V}OH modes, and in rapid observations, they may be obscured by noise.

The interpretation of peaks for the OH groups in the V-sites is controversial, with two different approaches documented in the literature to help explain the many ^{V}OH modes. Both agree that these stretching modes are significantly influenced by the composition of the Y-site and the two Z-sites associated with each O(3) oxygen. However, the two models differ in the attribution of the multiple peaks of the ^{V}OH bands. The first model, initially described by Hoang et al.[138] and derived from a prior model utilised for interpreting OH stretching modes in the infrared (IR) spectrum of tourmalines[139], examines the **YZZ triplet individually**, hence ascribing the emergence of secondary peaks to mixed composition triplets: in the example of dravite, the primary contribution arises from the $^{Y}Mg^{Z}Al^{Z}Al$ triplet, indicated by the principal peak at higher wavenumbers, whilst the lesser peaks at lower wavenumbers can be ascribed to the existence of alternative elements at the Y-sites, such as Fe^{3+} and Al^{3+}. The second model, proposed by Watenphul et al.[129], supports the consideration of the **entire set of three triplets configuration YZZ–YZZ–YZZ** within the unit cell, rather than solely a single YZZ group. The wavenumber of the vibrational mode is inversely correlated with the total charges of the cations in the octahedral sites that coordinate the OH group: as the cation charge grows, the bond strength between the cation and oxygen increases, leading to a reduction in the OH bond strength and a consequent shift of its stretching mode towards lower wavenumbers. The most prominent peak aligns with the most likely YZZ–YZZ–YZZ configuration; for dravite, the $3^{Y}Mg^{Z}Al^{Z}Al$ configuration predominates, resulting in a peak at about 3573 cm^{-1}. In this case, the presence of aluminium at Y-site, rather than magnesium, causes a shift towards lower wavenumbers, enabling the existence of two intermediate configurations that correspond to two additional peaks of lesser intensity than the primary peak (Figure 8): the $2^{Y}Mg^{Z}Al^{Z}AL$-$^{Y}Al^{Z}Al^{Z}Al$ configuration for the peak at approximately 3534 cm^{-1} and the $^{Y}Mg^{Z}Al^{Z}Al$-$2^{Y}Al^{Z}Al^{Z}Al$ configuration for the peak at around 3494 cm^{-1}.

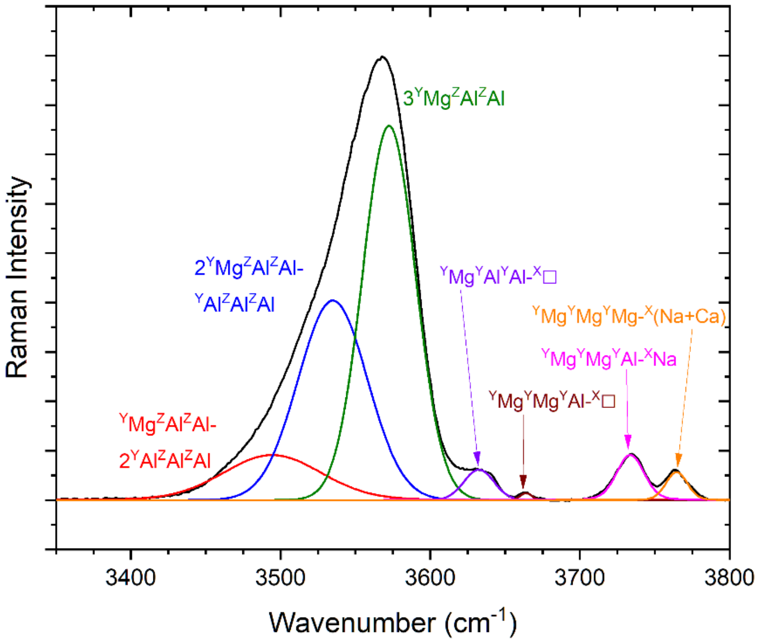

Figure 8: Example of OH peaks attribution for dravite based on the model proposed by Watenphul et al.[129]

Watenphul presented a formula to determine the concentration of the primary element in the Y-sites (C) based on the intensity of the three Raman peaks, $I_{V_{OH_1}}$, $I_{V_{OH_2}}$ and $I_{V_{OH_3}}$, convoluted within the ^{V}OH band:

$$\mathrm{C}(a.p.f.u.) = {\left(3I_{V_{OH_3}} + 2I_{V_{OH_2}} + I_{V_{OH_1}}\right)}\Big/{I_{V_{OH_{tot}}}}$$

Specifically, $^{V}OH_1$ corresponds to the $^{Y}C^{Z}Al^{Z}Al$+2 $^{Y}Al^{Z}Al^{Z}Al$ configuration, $^{V}OH_2$ to 2$^{Y}C^{Z}Al^{Z}Al$+ $^{Y}Al^{Z}Al^{Z}Al$, $^{V}OH_3$ to 3$^{Y}C^{Z}Al^{Z}Al$ and $I_{V_{OH_{tot}}}$ denotes the sum of the intensities of the three peaks.

The objective of this thesis is not to assess whether of the two proposed models is correct, as this remains a subject of ongoing dispute. However, as the Watenphul model is essential for resolving the previously presented formula, our results will mostly reference it.

Chapter 2

Characterisation Techniques

This thesis primarily focuses on characterising various tourmalines using **Raman spectroscopy**; however, additional techniques were employed to obtain information on the chemical composition of the analysed samples, which was subsequently utilised to examine the alterations in tourmaline chemistry associated with variations in the Raman spectra. We worked on various characterisation techniques for chemical composition, including **SEM-EDS** (Scanning Electron Microscopy with Energy Dispersive X-ray Spectroscopy), **μXANES** (Micro X-ray Absorption Near Edge Structure), **μXRF** (Micro X-ray Fluorescence), and **LIBS** (Laser-Induced Breakdown Spectroscopy). Moreover, in the case of tourmaline gemstones, variation in the **UV-VIS-NIR absorption spectrum** were studied compared to changes in chemical composition.

Raman Spectroscopy

Raman spectroscopy is an analytical technique that studies **inelastically scattered light**, enabling the identification of the vibrational frequencies of molecules inside the measured material. The Raman effect was initially documented by Indian physicists Sir Chandrasekhara Venkata **Raman**, who named the phenomenon and received the Nobel Prize in Physics in 1930 for this discovery, and Sir Kariamanikkam Srinivasa **Krishnan** in 1928, who noted **frequency shifts** in light scattered by liquids[140].

Initially, Raman spectroscopy had significant experimental constraints due to the low intensity of Raman scattering, with only one photon out of 10^7 experiencing inelastic scattering, whereas the rest of it goes through elastic scattering, also known as **Rayleigh scattering.** The advent of **lasers**, which serve as powerful monochromatic coherent light sources, together with more sensitive detectors and enhanced filters for elastically scattered light, had made Raman spectroscopy increasingly essential for material analysis across several research areas.

The inelastic scattering of light from near-infrared to near-ultraviolet, including the entire visible spectrum, is associated with the excitation and de-excitation of vibrational modes of atoms in the examined material. The incident monochromatic light consists of photons of energy $E_0=h\nu_0$, which, upon absorption, can elevate the molecule to a **virtual excited state**; subsequently, the molecule typically re-emits a photon with energy equal to the original, resulting in elastic scattering. Nonetheless, with a low probability, a molecule may shift from a virtual state to an **excited vibrational state**, emitting a photon of lesser energy than the incident photon, $E_f=E_0-h\nu_i$, where $h\nu_i$ represents the energy absorbed by the molecule to **excite a phonon**; this occurrence is known as **Raman Stokes scattering**, leading to the excitation of a molecular or lattice vibration. The molecule may initially occur in a vibrationally excited state and, upon transitioning to a virtual state, subsequently de-excites to the ground state, emitting a photon with energy exceeding that of the incident photon, $E_f=E_0+h\nu_i$; in this scenario, the **de-excitation of a phonon** is referred to as **Raman anti-Stokes scattering** and relates to the suppression of a molecular or lattice vibrational mode. Figure 9 depicts the several types of scattering that can be achieved.

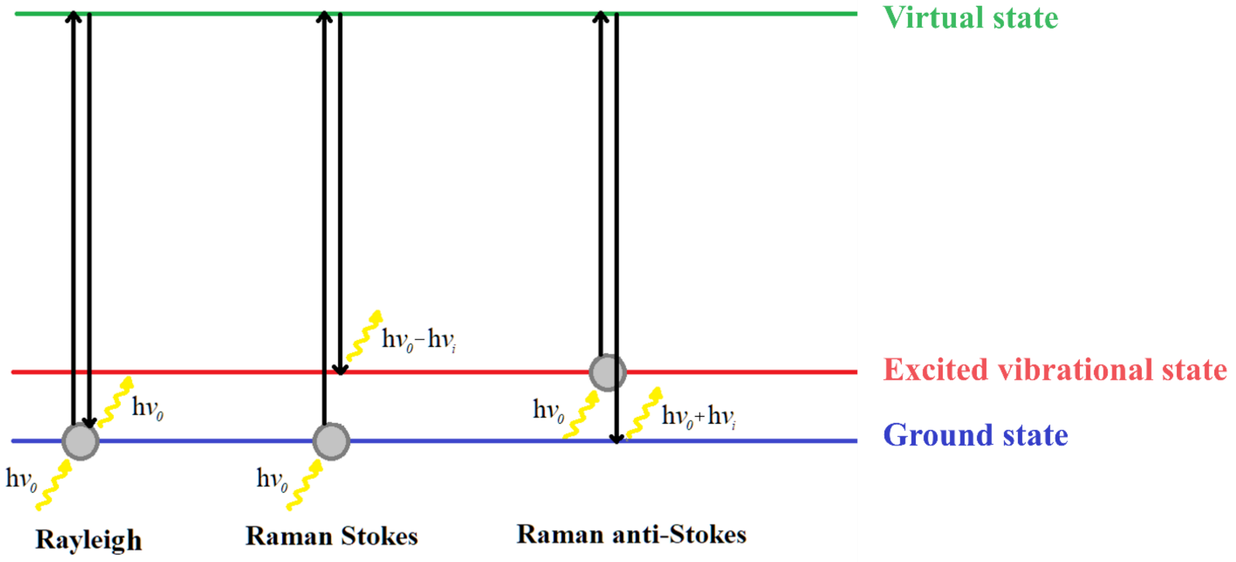

Figure 9: Different energy level transitions involved in the Raman scattering process.

A classical description of the Raman effect can be derived by examining **polarizability**. The incident electromagnetic radiation produces an **induced dipole moment** represented by

$$\mu_{ind}(t) = \alpha E(t) = \alpha E_0 cos(2\pi\nu_0 t)$$

where α denotes the polarizability. When α is constant, the induced dipole moment oscillates at the frequency ν_0, hence producing radiation at the same wavelength as the incident light, resulting in the Rayleigh scattering. If, conversely, the polarizability oscillates at its intrinsic frequency ν_k, depending on the changing distance between the nuclei, beats arise from the combination of three components:

- The induced dipole moment at frequency ν_0 (**Rayleigh scattering**).
- The induced dipole moment at frequency $\nu_0 - \nu_k$ (**Raman Stokes**).
- The induced dipole moment at frequency $\nu_0 + \nu_k$ (**Raman anti-Stokes**).

The polarizability can be articulated as a function of the **normal vibrational mode coordinate**.

$$Q_k = Q_k^0 \, cos(2\pi\nu_k t)$$

The Taylor series of the cos function truncated at the first order leads to the following expression:

$$\alpha = \alpha_0 + \left(\frac{\partial\alpha}{\partial Q_k}\right)_0 Q_k$$

Upon applying incident radiation characterised by the electric field $E(t) = E_0 cos(2\pi\nu_0 t)$, the resulting induced dipole moment is expressed as:

$$\mu_{ind}(t) = \alpha E(t) = \alpha_0 E_0 cos(2\pi\nu_0 t) + E_0 Q_k^0 \left(\frac{\partial\alpha}{\partial Q_k}\right)_0 cos(2\pi\nu_0 t)cos(2\pi\nu_k t)$$

The first term on the right side of the equation denotes elastic scattering, while the second term is related to inelastic scattering, which can be decomposed using the trigonometric identity $cos\alpha cos\beta = \frac{1}{2}[cos(\alpha+\beta) + cos(\alpha-\beta)]$. The following outcome is achieved:

$$\mu_{ind}(t) = \alpha_0 E_0 cos(2\pi\nu_0 t) + E_0 Q_k^0 \left(\frac{\partial\alpha}{\partial Q_k}\right)_0 [cos(2\pi(\nu_0+\nu_k)t) + cos(2\pi(\nu_0-\nu_k)t)]$$

The first part in square brackets denotes **Raman anti-Stokes scattering**, while the second term represents **Raman Stokes scattering**. This result indicates that the requisite condition for Raman scattering is

$$\left(\frac{\partial\alpha}{\partial Q_k}\right)_0 \neq 0$$

and the strength of the resulting peak will be contingent upon the magnitude of this derivative. If the molecule, or the crystal, considered has a centre of symmetry, the vibrations that fulfil these criteria primarily involve symmetric stretching of the molecules, where the derivative of the polarizability at equilibrium is non-zero, while in the case of asymmetric stretching, the derivative is zero. Generally, all vibrational modes exhibiting an **odd function of polarizability**, relative to the normal coordinates, are **Raman active**, while those demonstrating an even function are Raman inactive.

The vibrational modes associated with the peaks observed in the Raman spectrum are situated at specific positions on the x-axis, where the "**Raman shift**" is indicated; this "shift" represents the **difference** between the **wavenumber** of the incident light (determined by the source employed) and the wavenumber of the scattered light. Consequently, the x-axis of the Raman spectrum often displays the "wavenumber" label, measured in cm^{-1}, to denote the Raman shift. This method is useful, as it allows the position of the Raman peaks to remain independent of the excitation light wavelength.

Raman Stokes scattering is typically regarded with greater interest due to its increased intensity under standard conditions compared to anti-Stokes scattering. This is primarily attributable to **Boltzmann distribution,** which describes the predominance of atoms and molecules in the ground state prior to excitation by a laser source, with only a minority existing in an excited vibrational state:

$$\frac{I_{Stokes}}{I_{anti-Stokes}} = \left(\frac{\nu_0-\nu_k}{\nu_0+\nu_k}\right)^4 e^{\frac{h\nu_k}{kT}}$$

Raman anti-Stokes modes, although less intense, can provide significant information; specifically, the relative intensities of the corresponding Stokes and anti-Stokes modes relate to the **temperature** of the analysed sample. In this study, the examined tourmalines did not undergo specific heating treatments prior to or during the Raman observations; hence, we will concentrate exclusively on the Stokes component of the Raman spectrum.

Previously, our emphasis was on the one-dimensional characteristics of polarizability; however, particularly in the context of mineral studies, it is imperative to consider its three-dimensional behaviour. Consequently, polarizability can be written as a **3x3 tensor** describing the effects of the three components of the incident electric field on the three components of the induced dipole moment.

$$\begin{bmatrix} \mu_{ind,x} \\ \mu_{ind,y} \\ \mu_{ind,z} \end{bmatrix} = \begin{bmatrix} \alpha_{xx} & \alpha_{xy} & \alpha_{xz} \\ \alpha_{yx} & \alpha_{yy} & \alpha_{yz} \\ \alpha_{zx} & \alpha_{zy} & \alpha_{zz} \end{bmatrix} \begin{bmatrix} E_x \\ E_y \\ E_z \end{bmatrix}$$

The polarizability tensor is often symmetric, allowing for the identification of two distinct invariant components, which are the isotropic (α^{I}) and the anisotropic (α^{A}) parts:

$$\alpha = \alpha^I + \alpha^A \begin{cases} \alpha^I = \frac{1}{3}(\alpha_{xx} + \alpha_{yy} + \alpha_{zz}) \\ \alpha^A = \frac{1}{2}\left[(\alpha_{xx} - \alpha_{yy})^2 + (\alpha_{yy} - \alpha_{zz})^2 + (\alpha_{zz} - \alpha_{xx})^2 + 6(\alpha_{xy}^2 + \alpha_{yz}^2 + \alpha_{xz}^2)\right]^{1/2} \end{cases}$$

The derived polarizability tensor with respect to the three normal vibration coordinates is commonly defined as the "**Raman tensor"**. Each vibrational mode has a different polarizability tensor and thus a different Raman tensor. This results in varying scattered intensities across distinct polarisation directions, which may be analysed using the **depolarisation ratio**:

$$\rho(\theta) = \frac{I_{\perp}(\theta)}{I_{\parallel}(\theta)}$$

where $I_{\perp}$ and $I_{\parallel}$ are the intensities of the scattered line perpendicular and parallel to the scattering plane, respectively. θ represents the angle between the incident light direction and the scattered light direction; in our investigations, as well as in the majority of contemporary Raman instruments, the analytical geometry employed is the **backscattering** configuration, with θ=180°. The intensity can be computed (full calculations are provided in Keresztury[141] and Long[142]) for both parallel and perpendicular orientations, yielding the subsequent equation for the depolarisation ratio:

$$\rho = \frac{3{\alpha'^A}^2}{45{\alpha'^I}^2 + 4{\alpha'^A}^2}$$

where α'^I and α'^A are the analogues of α^I and α^A, respectively, obtained from Raman tensor components. Given that both α'^I and α'^{A} can equal 0, the range of potential values for ρ is:

$$0 \leq \rho \leq \frac{3}{4}$$

resulting in three distinct potential scenarios:

- Completely asymmetric vibrations, with $\alpha'^{\mathrm{I}} = 0$ and $\alpha'^{\mathrm{A}} \neq 0$, result in $\rho = \frac{3}{4}$, indicating that a variation in the orientation of the detected polarised scattered light yields only a minor alteration in Raman peak strength. Raman bands exhibiting this characteristic are known as "**depolarised**".

- Partially symmetric vibrations, characterised by both α'^{I} and α'^{A} being non-zero, result in $\rho < \frac{3}{4}$, indicating that variations in peak intensity associated with alterations in polarisation direction are more pronounced. In this scenario, the Raman bands are referred to as "**partially polarised**".
- Fully symmetric vibrations, characterised by $\alpha'^{\mathrm{I}} \neq 0$ and $\alpha'^{\mathrm{A}} = 0$, result in $\rho = 0$, indicating that altering the orientation of detection of the polarised scattered light causes the disappearance of the Raman peak, referred to as "**completely polarised**".

The alignment of the sample concerning the polarisation of incident light and the orientation for detecting the polarised scattered light is thus crucial for achieving comparable measurements across different samples without influencing peak intensity due to orientation.

The intensity of scattered light, and consequently the Raman peaks, is also influenced by the light source; specifically, the intensity of the scattered light is proportional to the fourth power of the frequency of the incident light[143]. Nevertheless, if the energy of the excitation light source aligns with a true excited electronic state of the investigated material, instead of a virtual state (Figure 10), a gain of up to six orders of magnitude in the intensity of the scattered light for specific Raman modes is observed, attributable to a **resonance effect**[144,145]. The **resonant Raman** signal can boost the intensity of weak Raman modes by adjusting the excitation light source. This technique may, however, generate complications, since the system can de-excite through non-radiative transitions after attaining an excited electronic state and before re-emitting a photon, leading to a **fluorescence** effect that is far more powerful and can obscure the Raman signal. Consequently, the excitation light must be chosen according to the system under investigation, and various spectral peaks can be analysed using different laser sources.

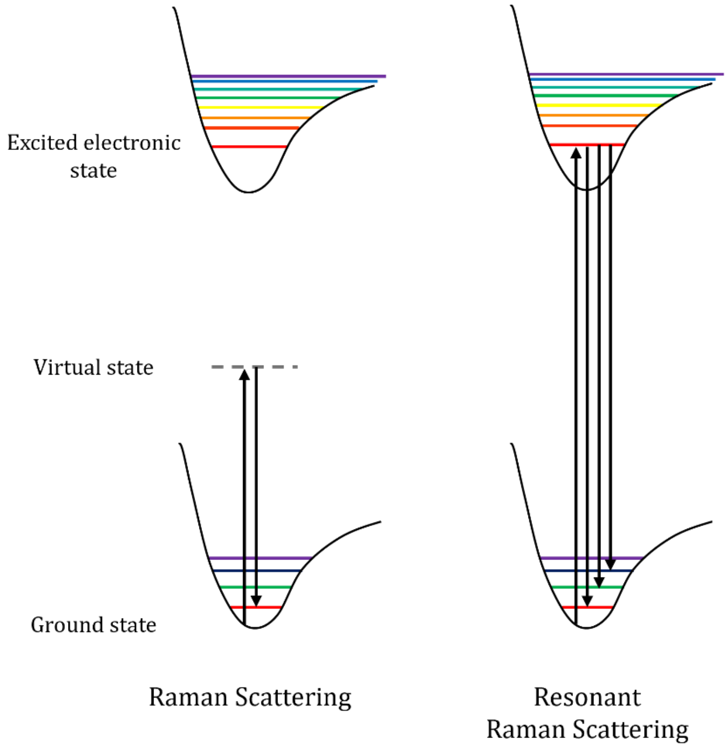

Figure 10: Representation of the difference between the "normal" Raman scattering and the resonant Raman scattering.

µRaman Spectroscopy

Nowadays, the majority of commercial benchtop Raman instruments are integrated with **optical microscope systems**, enabling the focusing of the incoming laser beam into a narrow area of the sample, up to a few micrometres. This configuration enhances the spatial resolution of the instrument and facilitates measurements on small samples or localised regions of heterogeneous specimens. The scattered light is subsequently gathered in a backscattering configuration by the same **objective** that focuses the laser on the sample and then cleaned using **notch filters** to eliminate Rayleigh scattering. A **confocal hole** is employed to remove scattered light from out-of-focus areas, thereby enhancing control over the depth of field in the analysis and mitigating background signals that may interfere with the resultant Raman spectrum. The different components of the filtered scattered light are dispersed by a **grating** and captured by a **detector**, typically a silicon **charge-coupled device** (CCD). Figure 11 presents a schematic of the **µRaman** equipment utilised in this study.

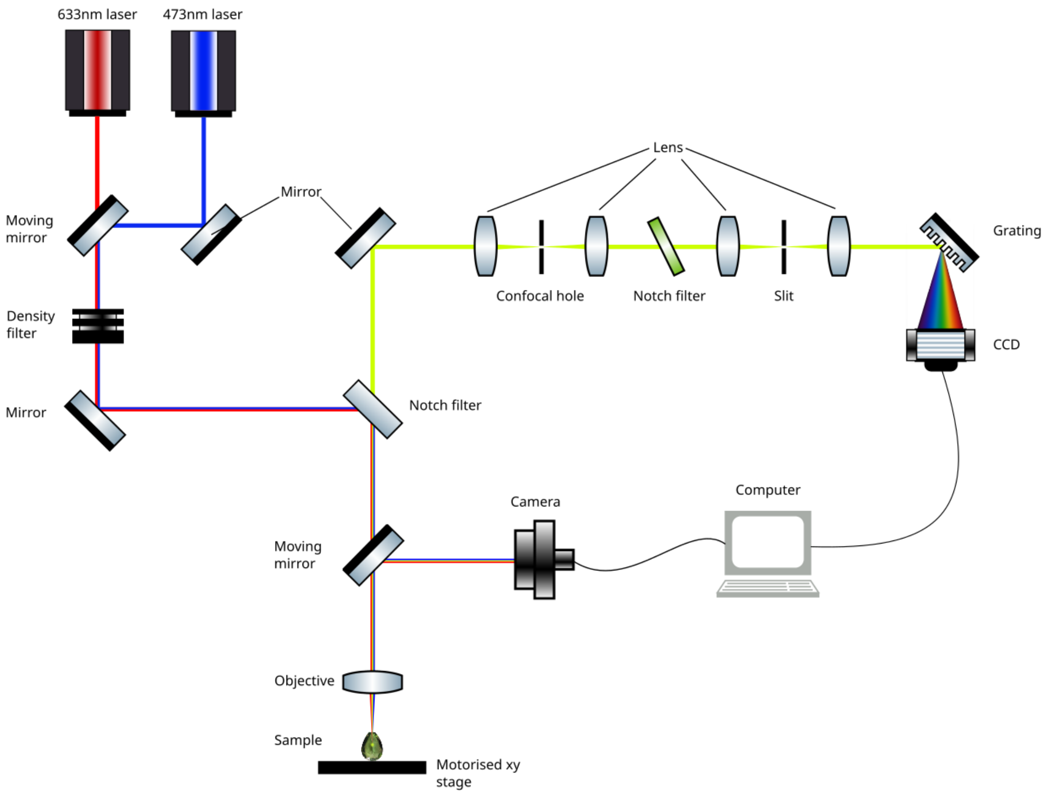

Figure 11: Scheme of the µRaman setup used in this work.

A *Horiba Jobin-Yvon LabRam micro-Raman spectrometer*, integrated with an *Olympus BH-4 confocal optical microscope*, was employed for the analysis presented in this thesis (Figure 12). The microscope features four objectives of varying magnification: 4x, 10x, ULWD50x (Ultra Long Working Distance), and 100x. The measurements were primarily conducted using the ULWD50x objective, while the 4x and 10x objectives were utilised to capture images of the sample surface, enabled by the instrument's **camera** (iDS, uEye UI-1460LE-C-BG), and to select the points for analysis. The 100x objective was not utilised, as it necessitates flat samples due to its short working distance, which made it unfeasible for natural tourmaline specimens that frequently exhibit irregular surfaces. The ULWD50x objective allows a spatial resolution of approximately 2 μm. The specimen is positioned on a **motorised XY stage**, enabling the selection of the analysis point with micrometric accuracy, while the Z-axis movement is adjusted manually to achieve the appropriate focal distance.

The Raman instrument features two distinct excitation lines: a *632.8 nm He-Ne* red laser, utilised for measuring the low-frequency spectrum region (150-750 cm^{-1}) to minimise fluorescence, and a *473.1 nm frequency-doubled Nd:YAG* blue laser, employed to induce a resonance effect in the OH stretching region (3400-3800 cm^{-1}). Both lasers pass through a tunable **density filter** that reduces the laser strength before reaching the sample. Nevertheless, as the heating effects of the focused laser, which operates at a power level of 10^{-1} to 10^{-2} watts, on the tourmaline samples are negligible, no density filter was employed during the measurements detailed in the following chapters. Each excitation line employs a grating to resolve the scattered light components on the **Peltier-cooled** silicon CCD detector: an 1800 lines/mm grating is employed for measurements with both lasers, allowing us to obtain at least a 3-4 cm^{-1} spectral resolution. In order to achieve low noise-to-signal ratio and thus a good precision n the determination of the parameters, Raman spectra were acquired for 60 seconds and 4 repetition for each measurement. However, 30 seconds measurements are sufficient to achieve good spectra for identification of different tourmaline species.

Measurements and parameter settings are conducted using Horiba's **LabSpec®** software, which also enables data analysis, including baseline subtraction and peak fitting.

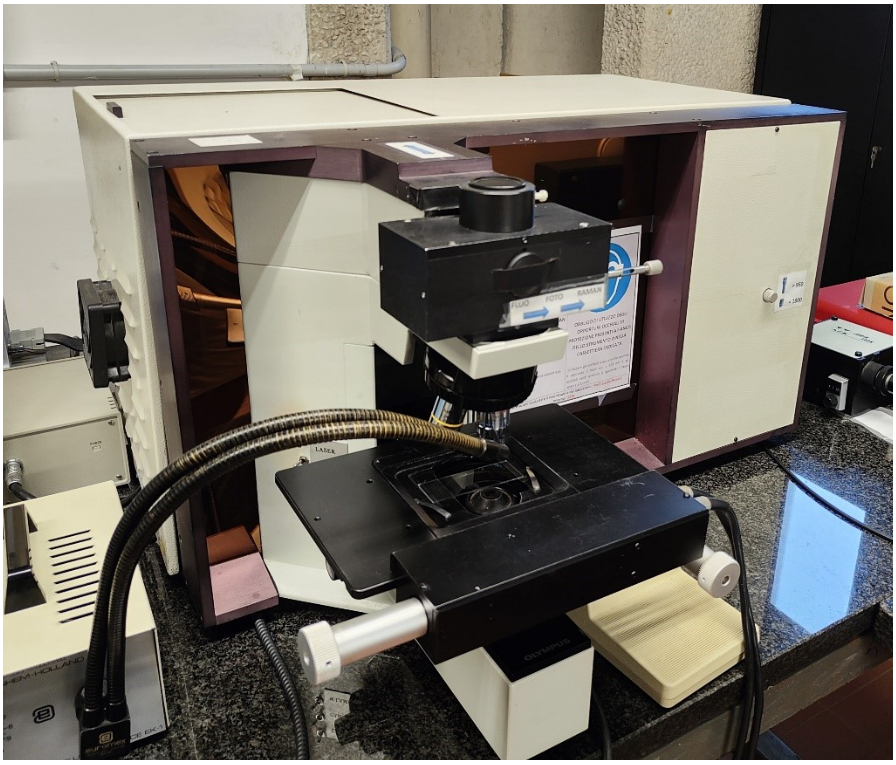

Figure 12: The Horiba Jobin-Yvon LabRam micro-Raman spectrometer used for μRaman analysis

Part of the Raman measurements, particularly on Paraíba-type tourmaline gemstones, were obtained using a *Renishaw inVia spectrometer* (Renishaw plc, Wotton-under-Edge, Gloucestershire, UK), integrated with an optical microscope and a 514 nm laser excitation (diode-pumped solid-state laser) at the Laboratoire Français de Gemmologie (LFG). The laser intensity applied to the material was 4 mW, and the spectral resolution was around 2 cm^{-1}. Raman spectra in the 100–1500 cm^{-1} range were obtained with 10 accumulations and a 30-second exposure time, whereas spectra in the 3000–3800 cm^{-1} range were collected with 20 accumulations and a 15-second exposure time. The spectrometer was calibrated using a diamond, namely its 1331.8 cm^{-1} Raman band. Measurements in three distinct crystallographic orientations were performed, aligning the samples with a polariser and a conoscope.

Portable Raman

Portable Raman devices are also increasingly popular; although they typically exhibit inferior spectrum resolution compared to benchtop equipment, their significant advantage of portability facilitates effective *in situ* observations. This study conducted portable Raman measurements to evaluate the feasibility of results obtained with μRaman also for *in situ* studies, comparing the spectra acquired from the two distinct types of systems (portable and bench-top). A handheld Raman instrument, the *EnSpectr RaPort* (Figure 13), was utilised with a *532 nm frequency-doubled Nd:YAG green laser,* serving as the excitation source across the 120-4000 cm^{-1} spectral region. The instrument possesses a modest spectral resolution of approximately 8-11 cm^{-1}, which yet facilitates the identification of various minerals. The equipment focuses the laser using a lens while simultaneously capturing the backscattered light from the sample, targeting a 0.5 mm spot, making it appropriate solely for sufficiently large samples or those with minimal heterogeneity.

Despite the foregoing deficiencies in the instrument hardware, testing has demonstrated that the RaPort handheld device produces high-quality Raman spectra, with peak positions consistent with those produced from the benchtop instrument[146], as also detailed in the data presented in this thesis.

Figure 13: The EnSpectr RaPort handheld Raman spectrometer.

Scanning Electron Microscopy (SEM) And Energy Dispersive X-Ray Spectroscopy (EDS)

Scanning electron microscopy (SEM) is an appropriate and adaptable technique for matching data acquired from Raman spectroscopy with information concerning the composition of the examined samples. Along with images that help to retrieve information on the sample surface morphology beyond the diffraction limit of visible light, thanks to the accelerated electron's wavelength, which is smaller than visible light, when integrated with an **energy-dispersive X-ray spectroscopy** (EDS) system, SEM can yield insights on the chemical composition of the analysed location.

SEM System

Electrons are employed as a source of excitation because they are more easily generated than heavier charged particles, hence aiding in the investigation of a sample's chemical composition. Electrons are generated by heating a filament, often made of tungsten (W) or lanthanum hexaboride (LaB_6), which is used as a cathode and conducts a current of approximately 2.7 A. When the thermal energy of the electrons exceeds the extraction energy of the filament material, emission occurs, and the electron beam is directed towards the anode by a potential difference. The SEM system typically operates with potential differences ranging from 0.3 to 30 keV; 25 keV is used for morphological observations, while 15 keV is employed for chemical analysis. From these potentials, one can ascertain the de Broglie wavelength of the electron beam, thus establishing the operational magnitude scale of the technique, which overcomes the diffraction limits of visible light.

$$\lambda = \frac{h}{mv} = \frac{h}{\sqrt{2eVm}}$$

The examined sample is located within a **vacuum chamber** alongside the electron source to prevent the generated beam from interacting with gas molecules throughout its path, hence improving the achieved resolution. The electron beam traverses a series of apertures and **magnetic and electrostatic lenses** that enable its collimation and focusing, whereas **scan coils** convey the beam to the designated location of the sample for analysis (Figure 14).

The incoming electrons on the sample can interact via two mechanisms: **elastic scattering** and **inelastic scattering**. Electrons that are elastically scattered by the nuclei of sample atoms or their outermost electrons, with corresponding energy, are referred to as **backscattered electrons** (BE) when their scattering angle exceeds 90°. An increase in an atom's atomic number corresponds with a higher probability of backscattered electrons, yielding a more robust signal. By utilising this dependence, one can obtain information on the distribution of various chemical elements inside the sample, therefore identifying the separate phases by studying changes in the intensity of the backscattered electrons.

On the other side, electrons undergoing inelastic scattering lose a fraction of their energy to the sample atoms, leading to ionisation and the release of inner shell electrons. These electrons, known as **secondary electrons** (SE), have minor energy; hence, only those produced on the sample surface escape reabsorption and may be detected. Secondary electrons show no association with atomic number, thereby providing information exclusively about the sample's morphology.

Backscattered electrons and secondary electrons can be observed using dedicated detectors, typically scintillators coupled with photomultiplier tubes or solid-state detectors, arranged at different angles.

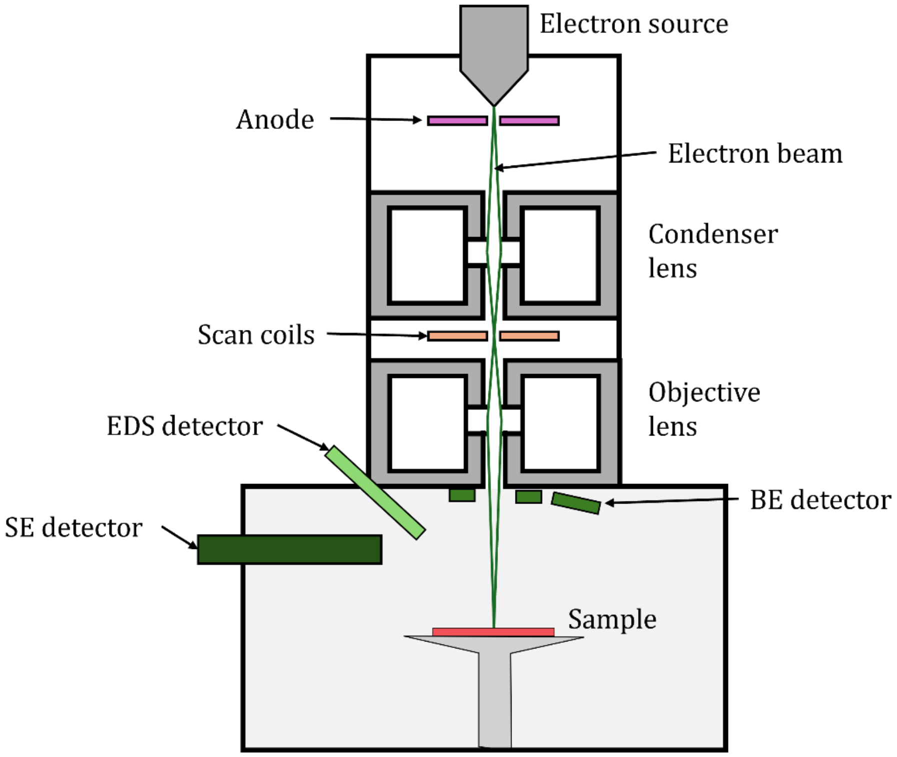

Figure 14: Scheme of the structure of a Scanning Electron Microscope.

In addition to these electrons, other products are present, including **X-rays** and **Auger electrons**. X-rays are produced when outer shell electrons transition to innermost atomic shells that have been vacated by the emission of secondary electrons; these transitions release X-radiation with energy that corresponds to the difference between the initial and final energy levels, dependent on the specific atom involved. X-rays have different energies depending on the atomic number of the emitting atom, facilitating the determination of sample composition through different acquiring methods such as **Wavelength Dispersive Spectroscopy** (WDS) and **Energy Dispersive Spectroscopy** (EDS). Auger electrons are emitted electrons resulting from the interaction with X-rays released by the same atom and can be employed to obtain compositional information through **Auger spectroscopy**.

The various results of electron microscopy arise from distinct depths inside the analysed material. The incident electron beam has a different interaction depth for each of the products; thus, modifying the beam energy allows for varying penetration depths into the sample (Figure 15).

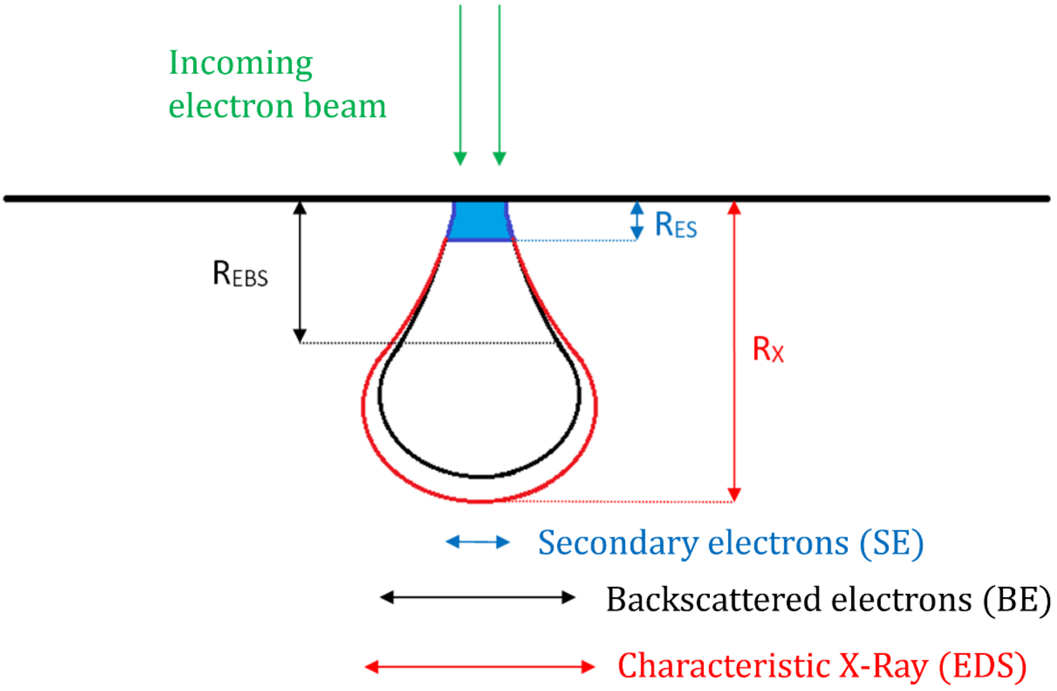

Figure 15: Scheme of the penetration depth of the electron beam with the highlighted areas where electrons and photons are produced.

EDS System

The analysis of characteristic X-rays generated by the material examined via SEM enables the reconstruction of the sample's composition at the specified location. An Energy Dispersive Spectroscopy (EDS) detector, typically a **Silicon Drift Detector** (SDD), is utilised; this detector consists of a semiconductor material (Si) that produces electron-hole pairs upon photon interaction. An anode attracts emitted electrons, and the energy of the incident photon can be determined from the quantity of electrons reaching it; however, the observable electron count is constrained by the necessity for periodic capacitor discharge. Extended measurement duration enhances accuracy and produces narrower peaks, but to avoid saturation, rapid observations are essential when photon flux increases, resulting in heightened noise in the recorded signal. The SSD is attached to a **cold finger condenser** that reduces shot noise, which arises from thermal energy generated during the formation of electron-hole pairs. An electron trap, consisting of a robust magnetic field and a beryllium window, is employed to remove low-energy electrons and photons, thus allowing only X-rays to reach the detector. The beryllium absorbs these X-rays and subsequently re-emits them at a reduced energy, appropriate for the formation of electron-hole pairs (Figure 16).

Artefacts exist that might distort the signal and lead to errors in the measured data: the absorption of X-rays by a non-active silicon layer (dead layer) may ionise silicon atoms, generating a signal in the spectrum associated with the detector material.

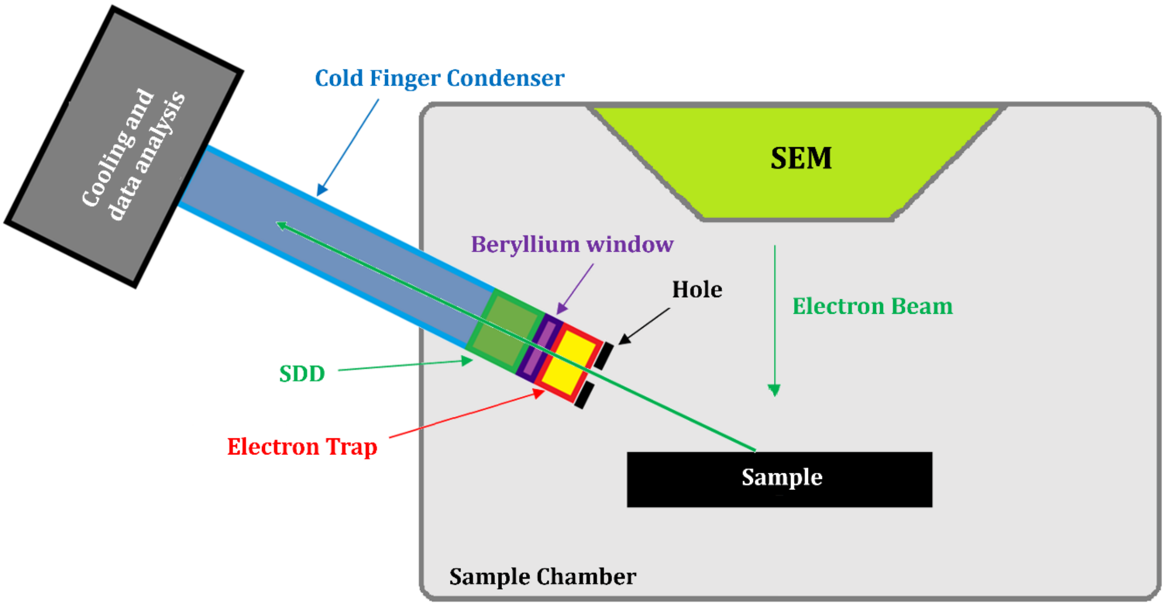

Figure 16: Scheme of the EDS detector used in the SEM instrument.

EDS has traditionally been perceived as a less accurate method compared to WDS for determining chemical composition; nevertheless, contemporary SDD can yield results with precision comparable to WDS, while offering the benefit of faster data acquisition. Nonetheless, EDS necessitates greater focus on the quantification of elements, particularly in peak identification and instrument calibration with appropriate standards, to prevent systematic errors[147].

This study utilised a *Jeol 6400 scanning electron microscope* equipped with an *Oxford energy-dispersive spectrometer microprobe*. The microprobe examination was conducted at 20 kV and 1.2 mA current, with an approximate beam width of 1 μm and a counting duration of 75 seconds. Approximately 15 analytical points per sample were averaged due to the absence of discernible chemical zoning in each sample. Certain samples were encapsulated in epoxy resin, polished to provide a flat surface, and coated with a high-conductivity thin graphite sheet to mitigate charging effects. Further samples, particularly larger crystals, were examined in their original state, positioned on a tape layer, and covered with graphite. SEM pictures were acquired utilising both secondary and back-scattered electron detectors to more effectively evaluate the existence of compositional heterogeneities.

X-Ray Absorption Near Edge Structure (XANES) Spectroscopy

The **X-Ray Absorption Near Edge Structure** (XANES) spectroscopy is a recognised technique that utilises synchrotron radiation to provide information on the electronic, structural, and magnetic characteristics of the examined samples. XANES is a component of the broader technique known as **X-ray Absorption Spectroscopy** (XAS), which also includes **Extended X-ray Absorption Fine Structure** (EXAFS) spectroscopy.

The XAS technique relies on **X-ray photons** which are absorbed by the material, promoting core-shell electrons to unoccupied energy levels. The absorption energy corresponds to the core-level energy characteristic of each element, resulting in a step-like feature in the absorption spectrum, known as the **absorption edge,** due to the increase in **photoabsorption cross-section** following the transition of a core electron, which can be derived from **Fermi's golden rule**:

$$\sigma = \frac{4\pi^2}{\omega} \sum_f \left| \langle f | \hat{\boldsymbol{\epsilon}} \cdot \boldsymbol{p} e^{i\boldsymbol{k}\cdot\boldsymbol{r}} | i \rangle \right|^2 \delta\left(E_i - E_f + \omega\right)$$

Where ω and $\hat{\boldsymbol{\epsilon}}$ are the frequency and the polarisation of the incident X-ray, $|i\rangle$ and $|f\rangle$ are the initial and the final states, while E_i and E_f are their energies, respectively.

XANES and EXAFS regions, though contiguous, probe different physical phenomena and require distinct theoretical treatments[148]. XANES covers the energy range from the edge to approximately 30–50 eV above the edge. In this domain, the photoelectron possesses low kinetic energy, yielding a relatively long de Broglie wavelength similar to interatomic distances. Consequently, many scattering events dominate the photoelectron's path, and strong final-state effects, including the existence of a core hole, are significant. XANES is particularly sensitive to the density of unoccupied states, oxidation state, and local symmetry, making it essential for investigating **valence**, **coordination geometry**, and **site symmetry**. EXAFS refers to the oscillating pattern observed at elevated energies (usually over 50 eV above the edge). In this region, the photoelectron possesses elevated kinetic energy, a reduced wavelength, and is minimally scattered by adjacent atoms. Single-scattering events predominate, and the absorption coefficient displays oscillations resulting from interference between outgoing and backscattered photoelectron waves. EXAFS oscillations give information regarding **interatomic distances**, **coordination numbers**, and **structural disorder** in close proximity of the analysed atomic species, as the mean free path of the photoelectron decreases with increasing energy due to inelastic losses, thereby constraining the range of structural information.

Since, in this thesis, we are mainly interested in the investigation of the iron oxidation states, we will focus on the XANES energy region, and, in this framework, we will examine excitations from the 1s core shell, commonly referred to as **K-edges**, which have been extensively studied for applications involving transition metals, within an energy range of 4-9 keV (Figure 17). Transitions from higher energy levels, such as 2s and 2p (L-edges) or 3s, 3p, and 3d (M-edges), are significantly more complicated to analyse due to "**multiplet effects**"[149] (interactions between core and valence electrons), which induce alterations in the edge profile, complicating the determination of the precise energy of the edge.

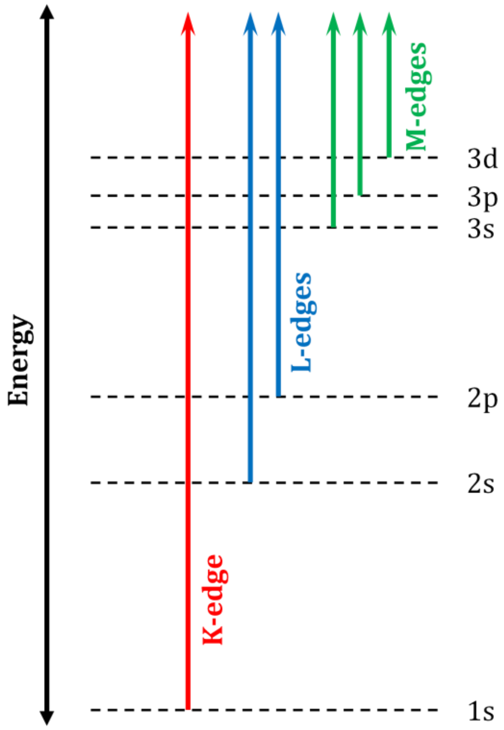

Figure 17: Scheme of the different electron transitions from each energy level in 3d transition metals.

A shift in the K-edge position, and hence in the 1s binding energy, corresponds with alterations in the valence of 3d transition metals, exemplified by iron, where the Fe^{3+} K-edge is situated at a higher energy than that of Fe^{2+}. Determining the precise edge energy is complex, particularly for elements with shoulder-like edge configurations. Consequently, the edge position can solely provide qualitative information regarding the valence of the examined metal, especially in the presence of mixed concentrations of multiple valences[150].

To quantify the concentration of various oxidation states of transition metals, the **pre-edge** peak, observed around 15-20 eV prior to the K-edge (Figure 18) in numerous 3d-metal systems due to the 1s→3d electron transition[151–154], can be analysed, as shifts in its position to higher energy have been shown to correlate strongly with increasing oxidation state[155,156].

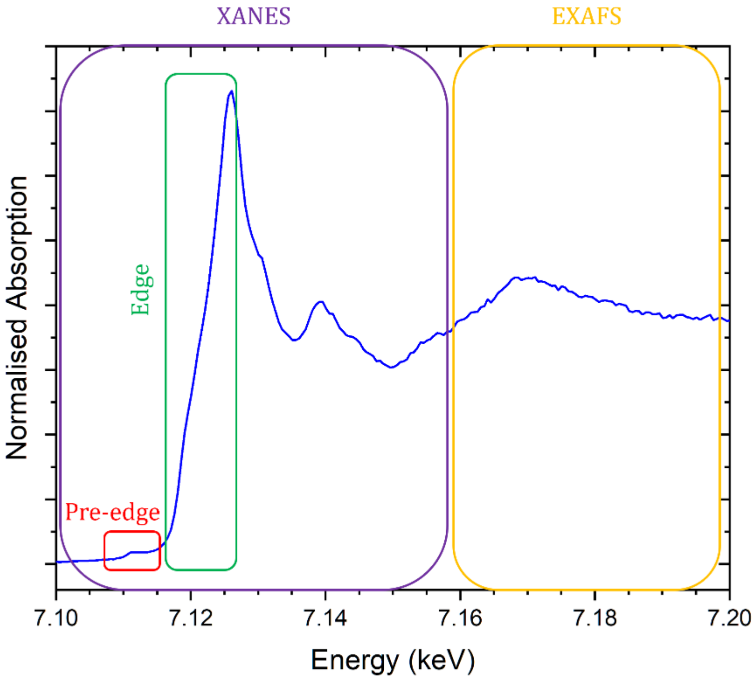

Figure 18: Example of XANES spectrum of olivine (Fe_2SiO_4) with edge and pre-edge in the XANES region highlighted. Additionally, the EXAFS domain, which extends to higher energies, is indicated.

Chapter 3 of this thesis provides a comprehensive explanation of the process for accurately interpolating the pre-edge peak to determine its centroid position, as outlined in the literature[157].

Synchrotron μXANES Instrument

XANES measurements reported in the following chapters were performed at *SOLEIL synchrotron* (Saint-Aubin, France) on the *PUMA (Photons Utilisés pour les Matériaux Anciens) beamline*[158], as part of experiment No. 20231463 titled "*Towards the Development of a Non-Destructive Compositional Tool for Tourmaline Studies: Correlation of XANES Data and Raman Parameters*".

The principal source of the beamline for XANES studies is a high-brightness 1.8 T **wiggler** featuring twenty 164.2 mm periods, providing a continuous X-ray spectrum with a critical energy of 8.98 keV. The extensive spectrum range (10-20 keV) with elevated photon flux (10^{10} photons/s) is especially beneficial for XANES, which necessitates accurate energy calibration near the absorption edge of the target element. A 300 μm **beryllium window** is situated at the beamline entry to exclude low-energy X-rays (<1 keV), thus minimising background noise and safeguarding downstream optics. **Primary slits** are employed to align the beam size with the optical apertures, thereby reducing beam divergence and enhancing energy resolution. The beam energy selection for XANES experiments is critical, facilitated by the **double crystal monochromator** (DCM), which ensures high spectral purity and accurate energy selection. The DCM employs two sets of crystals—Si(111) for 4–23 keV and Si(220) for 20–60 keV—configured in a fixed-exit geometry with horizontal beam deflection. Crystal switching is accomplished through vertical translation, facilitating fast adjustment to varying energy regimes. The monochromator is refrigerated with liquid nitrogen to preserve crystal stability under elevated thermal loads, hence ensuring minimum drift during data collection. The horizontal deflection geometry improves mechanical stability by avoiding gravitational influences on the rotation axis, which is essential for the extended scans necessary in XANES.

Located downstream of the monochromator, a pair of **Kirkpatrick–Baez (KB) mirrors** concentrate the monochromatic beam into a microspot at the sample location. These mirrors, including selectable coatings (B_4C for <10 keV and Rh for up to 22 keV), yield a focal spot size of 5 µm (vertical) x 7 µm (horizontal), thereby guaranteeing high spatial resolution for µXANES investigations. Encasing the optics in helium-filled chambers diminishes air absorption at lower energies. A diamond intensity monitor positioned near the mirror chamber's exit continually quantifies the incident photon flux, facilitating the normalisation of XANES spectra and the correction for variations in the incident beam.

Precise and consistent sample placement is essential for XANES. The beamline features an **8-axis high-precision goniometer**, enabling micron-level translation and sub-degree rotation. This approach facilitates accurate alignment of the region of interest with the X-ray microbeam and accommodates both point and mapping measurements. A high-resolution video microscope is incorporated into the sample environment, delivering real-time imaging of the sample surface at a 45° angle to the incident beam. This feature is crucial for aligning sensitive or heterogeneous samples and monitoring beam-induced effects during XANES studies.

XANES is acquired in fluorescence mode using a **silicon drift detector** (SDD) with an 80 mm^2 collimated area, orientated at 90° to the incident beam (Figure 19). This geometry reduces contributions from elastic and Compton scattering, hence improving the signal-to-noise ratio in the XANES region.

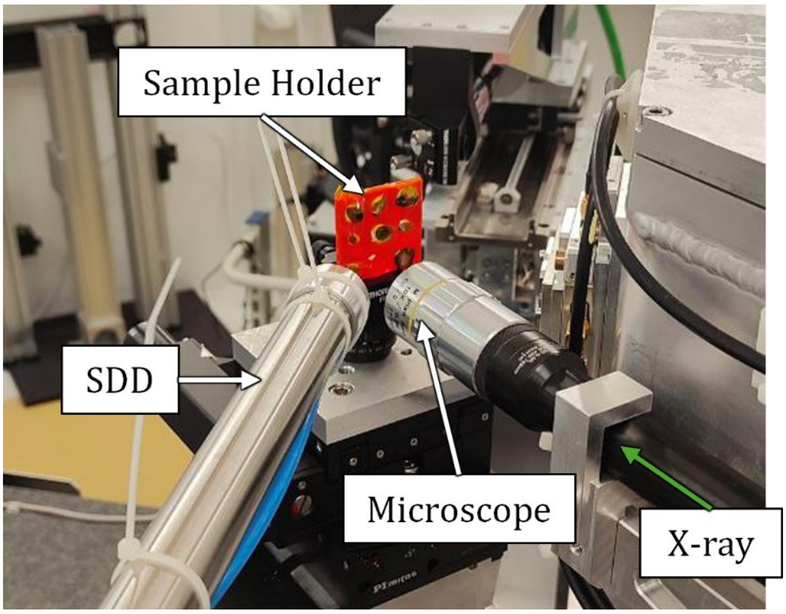

Figure 19: Configuration of the acquisition system for XANES measurements at the Puma beamline, synchrotron SOLEIL, with a 90° detector geometry.

XANES measurements were conducted on both the Fe and Mn K-edges to ascertain the concentration of various oxidation states in each tourmaline sample. Data concerning the Fe K-edge were obtained in the 7050–7400 eV range utilising varying resolution increments: a 2 eV step was employed for measurements in the 7050-7100 eV and 7220-7400 eV sectors, while a 0.5 eV step was utilised in the 7100-7220 eV region, encompassing both the pre-edge and K-edge. Analogously, analyses of the Mn K-edge were conducted within the 6510–6800 eV range, with 2 eV increments in the 6510–6534 eV and 6634–6800 eV regions, and a 0.5 eV resolution in the 6534–6634 eV region, where the pre-edge and K-edge are situated. In the XANES analysis of Fe, each data point was collected over 1 second, whereas for Mn, a 3-second acquisition was conducted per point to ensure a robust signal, even at low concentrations. The instrument was calibrated utilising Fe and Mn foils.

X-Ray Fluorescence (XRF)

X-ray fluorescence (XRF) spectroscopy is a prevalent analytical technique for ascertaining the elemental composition of materials. XRF is regarded for its rapidity, precision, and non-invasive analysis, making it essential in geology, materials science, environmental monitoring, and cultural heritage studies. The technique depends on the emission of characteristic secondary (fluorescent) X-rays from a sample exposed to a primary **X-ray source**, with each element generating a unique array of emission lines[159]. These secondary photons act as fingerprints of the elements present in the sample, allowing both qualitative and quantitative analysis across a wide concentration range, from trace levels to major constituents. The procedure employed is identical to that of SEM-EDS, utilising X-rays as the excitation source rather than electrons.

When a material is subjected to high-energy X-rays, the photons interact with atoms by three primary mechanisms: absorption (**fluorescence**), elastic (**Rayleigh**) scattering, and inelastic (**Compton**) scattering[160]. In fluorescence, an incident photon expels a core-shell electron, resulting in the atom reaching an excited state. The core-shell vacancy is subsequently filled by an electron from outer shells, which generates a distinctive X-ray photon during its transition to a lower energy level. The emissions are categorised as K-series, L-series, or M-series lines based on the electron transitions that take place[161,162] (Figure 20). Every element possesses a distinct array of emission lines, making XRF an unequivocal instrument for elemental identification. The energy of the n-emission line can be calculated from the semi-empirical model[163]:

$$E_n \approx R_\infty hc\frac{(Z-\sigma_n)^2}{n^2}$$

Where $R_\infty hc = 13.605693\ eV$ is the **Rydberg constant** and $Z_{eff} = Z - \sigma_n$ is the **effective charge** obtained from the difference between the atomic number of the analysed element (Z) and the screening constant of the n-shell (σ_n). The principal quantum number (n) is 1 for K shells and 2 for L shells, leading to the two formulas for the K and L edges:

$$E_K \approx 13.605693\ eV \times (Z-\sigma_K)^2$$

$$E_L \approx \frac{13.605693\ eV}{2^2} \times (Z-\sigma_L)^2 = 3.401423\ eV \times (Z-\sigma_L)^2$$

In both instances, the energy of the released photon is lower than that of the absorbed incoming X-ray, as it represents the disparity between the energies of the end and starting levels of the electronic transition. The positions of the peaks in the XRF are thus situated at lower energies compared to the absorption edge observed in XANES.

The probability of emission and the relative intensities of various lines are contingent upon the atomic number and transition probabilities, which delineate the spectral "fingerprint" of each element, whereas the intensity of lines from distinct elements in an XRF spectrum is influenced by their concentration within the matrix of the analysed sample. The **photoelectric cross section** can be generally expressed as

$$\sigma_{ph}(E,Z) = C\frac{Z^a}{E^b}$$

This equation highlights the dependence of the cross section on the atomic number of the analysed species (Z) and the energy of the incident photon (E)[164]. C is an empirical constant, while the a and b exponents depend on the electronic transition considered. In the case of K and L shells, the equation becomes:

$$\sigma_{ph,K}(E,Z) = C_K\frac{Z^4}{E^3}$$

$$\sigma_{ph,L}(E,Z) = C_L\frac{Z^{4.5}}{E^{2.7}}$$

Modern databases contain all the references for the cross sections and the energy levels for every atom, which can be used for accurate quantitative evaluation of sample composition[165,166].

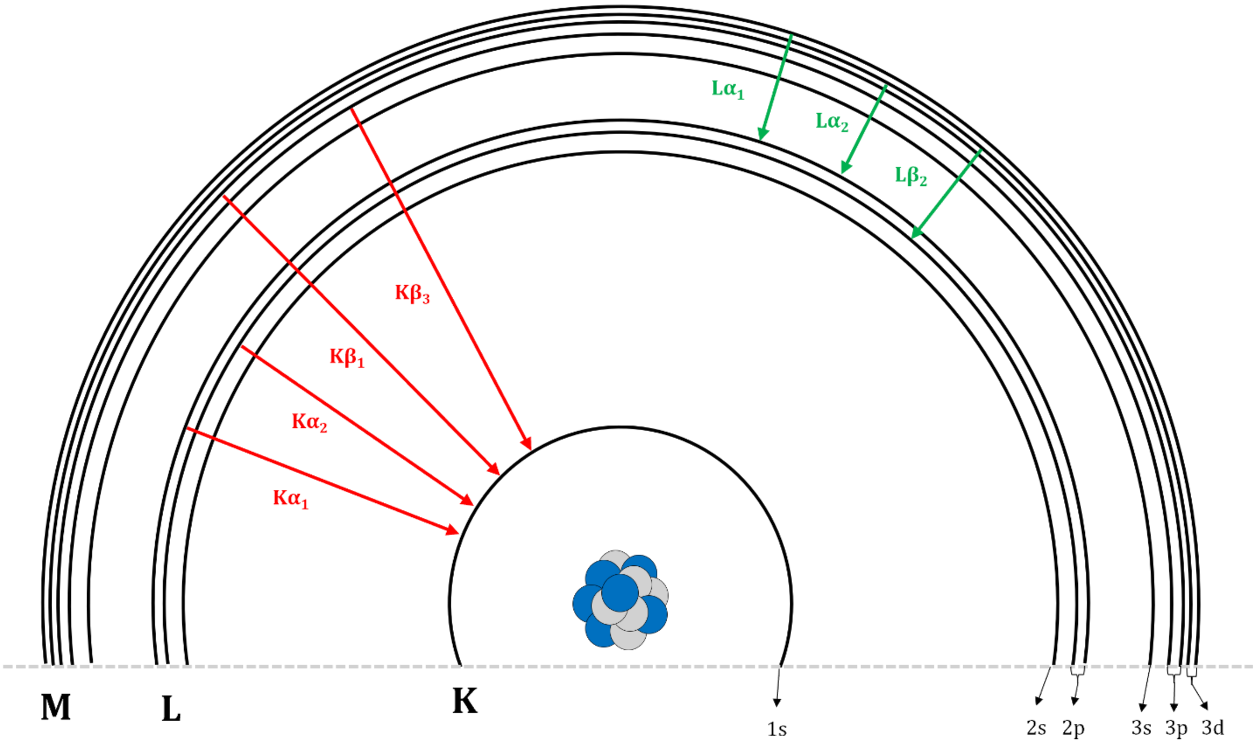

Figure 20: Energy level diagram for transition metals showing K, L, and M shell transitions and emission of characteristic X-rays (Kα, Kβ, etc.).

Most laboratory XRF systems employ **X-ray tubes**, in which electrons emitted from a heated cathode collide with a metallic anode, generating both continuous **bremsstrahlung** radiation and discrete **characteristic lines** associated with the anode's material. Alternative sources comprise **synchrotron radiation** and, to a lesser extent, **radioactive isotopes**. Synchrotron-based XRF provides significantly more brightness and tunability, resulting in enhanced detection limits and spatial resolution relative to conventional XRF equipment. The synchrotron source configuration employed for the XRF measurements is identical to that described for XANES in the preceding section. The sole distinction with respect to XANES is the chosen energy of the source, which is set at 18.5 keV, rather than scanning within the Fe and Mn K-edges, hence facilitating the emission of fluorescence X-rays for most of the elements expected in tourmalines. We may excite K-emissions for elements with K energy below 18.5 keV and L-emissions for elements with K energy above 18.5 keV. Nevertheless, for atoms exhibiting low K-emission energy, such as light elements like lithium and boron found in tourmalines, detection of their signal is unfeasible, making the quantification of light elements via XRF impossible.

XRF spectrometers are categorised into two primary categories, as described for X-rays emitted in SEM.

- **Energy Dispersive X-ray Fluorescence (EDXRF)**: Employs solid-state detectors to directly measure photon energy by counting the produced photoelectrons. It facilitates simultaneous multi-element detection, involving minimal sample preparation, and is frequently employed in portable devices. Its adaptability renders it ideal for *in situ* and non-destructive analysis.

- **Wavelength Dispersive X-ray Fluorescence (WDXRF)**: uses diffraction crystals for separating fluorescence X-rays based on wavelength prior to detection. It provides enhanced energy resolution and sensitivity relative to EDXRF, particularly for light elements, but generally necessitates sample preparation (e.g., pelletising or fusion beads). Consequently, WDXRF is regarded as a semi-destructive approach in numerous instances.

We opt for EDXRF for the same reasons outlined for SEM-EDS, seeking rapid and non-destructive analyses. The **SDD** utilised for XRF measurements on the PUMA beamline is identical to that mentioned for XANES.

XRF measurements reported in the following chapters, like XANES, were performed at *SOLEIL synchrotron* (Saint-Aubin, France) on the *PUMA (Photons Utilisés pour les Matériaux Anciens) beamline*[158], as part of experiment No. 20231463 titled "*Towards the Development of a Non-Destructive Compositional Tool for Tourmaline Studies: Correlation of XANES Data and Raman Parameters*".

Some measurements, particularly of Paraíba-type tourmaline gemstones, were obtained using an *EDXRF* (energy dispersive X-ray fluorescence; *Thermo Fisher Scientific Inc*., Waltham, MA, USA) at the Laboratoire Français de Gemmologie (LFG). A sample holder featuring a 5 mm aperture diameter was utilised, and particular parameter sets were optimised for the most precise examination of tourmaline. Multiple conditions were employed for filters and voltage (no filter/4 kV, cellulose/8 kV, aluminium/12 kV, thin palladium/16 kV, medium palladium/20 kV, thick palladium/28 kV, and thick copper/50 kV), with an acquisition duration of around 20 minutes per sample.

Laser-Induced Breakdown Spectroscopy (LIBS)

Laser-Induced Breakdown Spectroscopy (LIBS) is an analytical method that exploits the interaction of a low-energy, high-power, pulsed laser with matter to produce a transient plasma. Since its initial introduction in the 1980s by Radziemski and Loree[167,168], LIBS has developed into a versatile instrument for multi-elemental analysis across various fields, including material science, environmental monitoring, forensics, cultural heritage, and gemmology. The primary benefits of LIBS include minimal or no sample preparation, velocity, multi-elemental capability, and suitability for *in situ* and remote analyses.

When a focused laser pulse with sufficient irradiance reaches a material's surface, it ablates a minor portion of the sample, generating a heated, **ionised plasma** plume. The plasma comprises neutral atoms, ions, and free electrons, with temperatures exceeding several thousand Kelvin ($>10^4$ K). As the plasma cools, excited atoms and ions move to lower energy states, producing characteristic radiation. The recording and analysis of this optical emission spectrum provide both qualitative and quantitative elemental measurements.

The plasma production process is dependent upon the laser parameters (wavelength, power, and pulse duration) and the sample's physical characteristics. In solids, plasma is produced via laser ablation, whereas in gases and liquids, it is generated through laser-induced breakdown via multiphoton ionisation, which occurs at elevated irradiance compared to solids. Various ablation regimes—namely vaporisation, melt displacement, melt expulsion, and phase explosion—can appear based on the **laser fluence** (J/cm^2) and are associated with distinct plasma dynamics[169]. The LIBS signal is sensitive to fluence and matches with the behaviour of the ablated mass and the plasma electron temperature. Enhanced LIBS signals are achieved between vaporisation and melt displacement (fluence ~30 J/cm^2) and within the phase explosion regime (fluence >320 J/cm^2)[170].

When the radiative process associated with the de-excitation of atoms and ions in the plasma occurs more slowly than the period necessary for the plasma to attain thermal equilibrium, LIBS plasmas are considered to be in **local thermal equilibrium** (LTE), which allows their description using the **Boltzmann**

$$n_k^{I/II} = N^{I/II} g_k \frac{e^{-\frac{E_k}{k_B T}}}{U^{I/II}(T)}$$

and **Saha–Eggert** equations

$$\frac{N^{II}}{N^{I}} = \frac{1}{n_e} \frac{(2\pi m_e k_B T)^{3/2}}{h^3} \frac{2U^{II}(T)}{U^{I}(T)} e^{-\frac{E_{ion}}{k_B T}}$$

In the Boltzmann equation, E_k represents the electron energy of neutral (n_k^I) and ionised (n_k^{II}) atoms of the k-th element in the studied materials. g_k represents the degeneration of the upper level, N is the total number of the associated species, and U indicates the partition function for the species at temperature T. In the Saha–Eggert equation, h denotes the Planck constant, m_e represents the mass of the electron, and n_e indicates the electron number density in the plasma. The Saha–Eggert equation generally depicts the equilibrium between two successive ionisation levels, and considering that LIBS plasma predominantly contains neutral and singly ionised atoms, E_{ion} refers to the **first ionisation energy** of the element.

From these two equations, one can derive the equation for the photon emission rate (I) from the laser-induced plasma, which correlates to the concentration of neutral and ionised atoms ($C^{I/II}$) in the upper level of the radiative transition, the probability of spontaneous de-excitation (A_{ki}), and a geometrical factor (F) associated with the instrument setup and operational conditions:

$$I = F C^{I/II} \frac{e^{-\frac{E_k}{k_B T}}}{U^{I/II}(T)} g_k A_{ki}$$

LIBS Instrumentation

A typical LIBS system consists of four main components: the laser source, focusing optics, a light collection system, and a spectrometer equipped with a detector.

Nd:YAG lasers are the most commonly used due to their robustness and suitability for generating plasma. They are typically operated at their fundamental wavelength (1064 nm), with pulse durations in the nanoseconds range and energies of tens to hundreds millijoules, resulting in laser power of the order of megawatts. Alternative configurations include femtosecond lasers, excimer lasers, or harmonics of the Nd:YAG laser (e.g., 266 nm or 532 nm), depending on the application.

The laser beam is usually focused in a micrometric spot on the sample surface with a simple glass **lens**, achieving irradiances up to 10^{11} W/cm^2. The extreme energy density leads to rapid material removal and plasma formation. Depending on the application, focusing systems can include microscope objectives, parabolic mirrors, or telescopic optics for remote (stand-off) LIBS. The heating is strongly located on the laser spot, thus, even if extremely high temperatures are reached, the heating of the samples around the laser spot is negligible.

The emitted light is collected by optical systems such as lenses, mirrors, or **optical fibers**, which offer flexibility and high acceptance angles. Fibers facilitate coupling with modern spectrometers and allow compact, field-deployable designs.

Early LIBS systems employed Czerny–Turner monochromators with photomultipliers or photodiode arrays, covering only narrow spectral windows. Modern systems often use the so-called **echelle spectrometers** composed of intensified **CCD** or **complementary metal–oxide–semiconductor** (CMOS) detectors, enabling quick, time-resolved, broad-band spectral acquisition from 200 to 900 nm, but on the other hand, the signal needs to be enhanced by expensive **optical intensifiers** in order to obtain a good signal-to-noise ratio. The choice of spectrometer depends on the balance between spectral resolution, sensitivity, and cost.

This thesis presents measurements conducted at the *Instituto di Chimica e Composti Organometallici* (CNR-ICCOM, Pisa) using a *Modì smart LIBS* system, which is equipped with a *Zeiss Axioplan A1 microscope* and a motorised XY stage. A Nd:YAG laser (λ=1064 nm), directed onto the sample using a 10X microscope objective, served as the source for laser ablation. A ball lens gathers plasma light and transmits it via an optical fibre to an AvaSpec Dual Spectrometer, which spans a spectral range of 200 nm to 900 nm with two distinct spectral resolutions: 0.1 nm in the UV region and 0.3 nm in the VIS-IR region. A double pulse laser, with an initial pulse of 5.4 mJ and a subsequent pulse of 8.7 mJ (with a 1 μs delay between the pulses), was employed to conduct several shots at a lateral resolution of 100 μm (Figure 21).

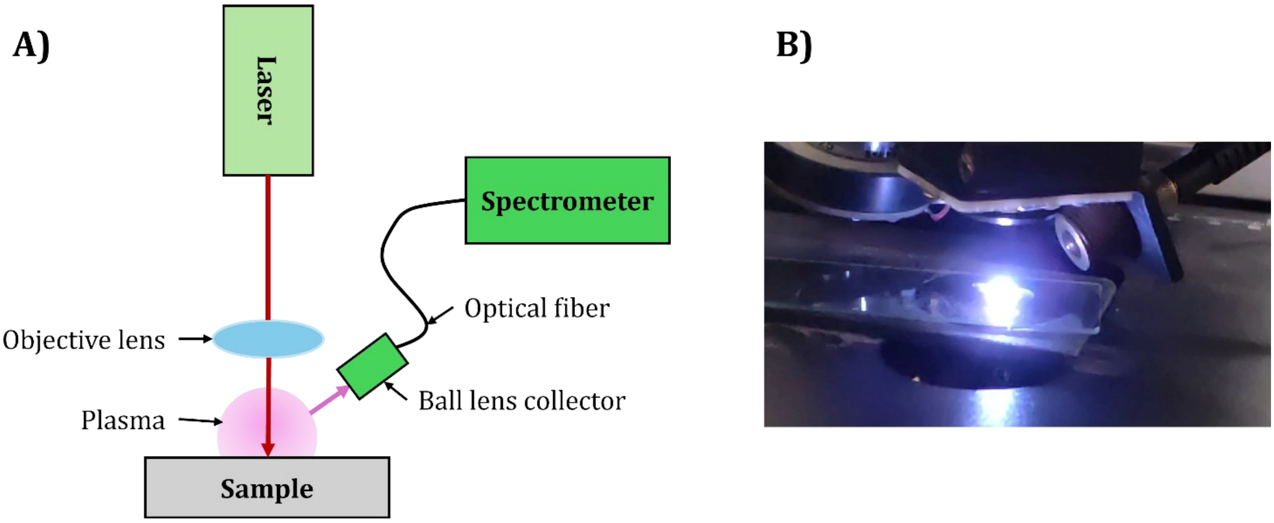

Figure 21: A) Scheme of the LIBS setup used in this work. B) Image of plasma formation and light emission on a tourmaline sample.

Quantitative Analysis In LIBS

While qualitative analysis through line identification is relatively straightforward, **quantitative LIBS** faces challenges due to matrix effects, self-absorption, and plasma variability. Traditional approaches use calibration curves built from standards of known composition. However, in many cases, suitable standards are unavailable or impractical.

The group of *Istituto di Fisica Atomica e Molecolare del CNR, Pisa,* pioneered **Calibration-Free LIBS** (CF-LIBS) in 1999[171], which uses only spectral data and fundamental spectroscopic parameters to quantify elemental concentrations. CF-LIBS eliminates the need for matrix-matched standards and compensates for plasma variability by measuring global plasma parameters directly from the spectrum.

Assuming the plasma in LTE, from the formula for the photon emission rate, considering the logarithm of each term, the equation can be written as:

$$\log\left(\frac{I}{g_k A_{ki}}\right) = \log\left(\frac{F\, C_k^{I/II}}{U(T)}\right) - \frac{E_k}{k_B T}$$

The I value can be obtained from experimental data as the integrated intensity of each peak for the k-element, whereas E_k denotes its position in the LIBS spectrum. The values of g_k and A_{ki} can be obtained from databases; in this instance, we utilised the **NIST** (National Institute of Standards and Technology) database[172]. By plotting the logarithm of the intensity of one of the ionised species of the k-element against E_k for n-lines, one may derive the value of $-\frac{1}{k_B T}$ from the slope of the linear fit, while $\log\left(\frac{F\, C_k^{I/II}}{U(T)}\right)$ appears as the intercept. It is straightforward to derive the plasma temperature (T) from the slope value, which influences the partition function U(T), obtainable from the NIST database. Consequently, the concentration of the k-element in a specific ionised state can be ascertained from the intercept (q_k) as

$$C_k^{I/II} = \frac{U(T) e^{q_k}}{F}$$

In most cases, the F geometrical factor is not known *a priori*; therefore, to ascertain the concentration of each element, it must be determined using the condition:

$$\sum\nolimits_k C_k^{I/II} = \sum\nolimits_k \frac{U(T) e^{q_k}}{F} = 100\%$$

which ensures that the total concentration of all elements equals 100%.

UV-VIS-NIR Spectroscopy

Ultraviolet–Visible–Near-Infrared (UV-VIS-NIR, or UV-VIS and VIS-NIR based on the spectral range analysed) spectroscopy is a key method in contemporary physical chemistry and materials science for investigating electronic transitions in atoms, molecules, and solids. When a material absorbs radiation in the ultraviolet, visible, or near-infrared ranges, electrons transition from lower (**ground**) states to higher (**excited**) energy states. The energy difference between these states correlates with the wavelength of absorbed light, resulting in a distinctive absorption spectrum that spans photon energies from approximately 4,000 to 50,000 cm^{-1}, equivalent to wavelengths of 200 to 2,500 nm. This spectrum encompasses a broad array of chemically relevant excitations, including **n→π* and π→π* transitions** in organic compounds, as well as d–d, **ligand-to-metal charge transfer** (LMCT), and **metal-to-ligand charge transfer** (MLCT) transitions in transition-metal complexes, thereby providing essential insights into the electronic structure, molecular composition, and both qualitative and quantitative properties of analytes. Its adaptability, economic efficiency, and user-friendliness have rendered it indispensable across various domains, including chemistry, biochemistry, pharmaceutical analysis, environmental monitoring, materials science and gemmology[173].

The intensity of light absorbed by the sample follows the **Lambert-Beer law**:

$$A = \log\frac{I_0}{I} = \varepsilon\, l\, c$$

where A is the absorbance, I_0 and I are the incident and transmitted intensities, l is the optical path length, c the molar concentration, and ε the molar extinction coefficient. For non-transparent or powdered samples, **Diffuse Reflectance Spectroscopy** (DRS) is employed, where reflectance R_∞ is converted into absorbance-like units using the **Kubelka–Munk (K–M) function**:

$$\frac{(1 - R_\infty)^2}{2R_\infty} = \frac{K(\lambda)}{S(\lambda)}$$

where K and S represent absorption and scattering coefficients, respectively. This process enables quantitative assessment of absorption in opaque catalysts and solid materials.

The selection of a suitable light source is essential for precise spectroscopic studies in the UV-VIS-NIR ranges. Common sources comprise **deuterium lamps**, utilised in the UV spectrum (150–400 nm), characterised by stability yet experiencing intensity reduction with extended usage; **tungsten-halogen lamps** for the visible and NIR spectra (340–3500 nm), recognised for their stability and intensity; and **xenon flash lamps**, which exhibit a broad spectrum encompassing UV, VIS, and NIR regions. **Monochromators** function as wavelength selectors, extracting particular wavelengths from polychromatic light. Various detector types are employed to transform transmitted or reflected light into electrical signals: **photomultiplier tubes** (PMTs) have remarkable sensitivity through electron amplification, making them suitable for low-light UV-VIS studies. **Phototubes**, less complex than PMTs, are appropriate for applications requiring moderate sensitivity, while **diode array detectors** (DADs) facilitate rapid, simultaneous spectral acquisition across an extensive wavelength range, thereby supporting high-performance liquid chromatography (HPLC) and multicomponent analysis.

UV-VIS-NIR spectra were acquired at the Laboratoire Français de Gemmologie (LFG) using a *Gemmosphere mobile instrument* (Magilabs Ltd., Helsinki, Finland) throughout the spectral range of 365 to 1000 nm, with an acquisition period of 0.05 to 0.10 seconds and 50 accumulations. It incorporates Xe-boosted halogen/UV sources and an *Ocean Optics Enhanced Sensitivity* spectrometer, ensuring a spectral resolution of 1.3 nm. The device features a PTFE integrating sphere with a diameter of 10.16 cm to optimise signal strength.

Chapter 3

Dravite And Schorl

Dravite and schorl are two of the most abundant species among the several types of tourmaline. The primary distinction in chemical composition between the end-members of these two species is found in the occupancy of the **Y-sites**: dravite possesses a higher **Mg^{2+}** content, whereas schorl contains a greater concentration of **Fe^{2+}**; thus, the end-member formulas are denoted as $NaMg_3Al_6Si_6O_{18}(BO_3)_3(OH)_3OH$ and $NaFe_3Al_6Si_6O_{18}(BO_3)_3(OH)_3OH$, respectively[3].

The two species, along with all tourmaline species, are of considerable significance in geology owing to their characteristics, notably their extensive stability range in temperature and pressure (up to 725-950°C and 7 GPa) and a low volume diffusion rate for major and trace elements within their structures[18], which allows them to preserve chemical and textural information throughout geological processes[8,15,28]. Owing to these attributes and their prevalence in various detrital sediments, tourmalines function as indicators of source rock in **provenance studies**[26,29,41,49,174]; specifically, dravite and schorl generally crystallise from intermediate igneous rocks with high Na content and intermediate Mg and Fe compositions, as well as moderately fractionated granitic rocks abundant in Fe[28].

Intermediate compositions with varying magnesium-iron ratios in Y-sites exist between the two end-member tourmalines, constituting the so-called **dravite-schorl series**, given by the general formula $Na(Mg_x,Fe_{1-x})_3Al_6(Si_6O_{18})(BO_3)_3(OH)_3OH$, where X denotes the relative magnesium-iron ratio in the Y-sites ($X = Mg/(Mg+Fe)$). The diverse compositions indicate the characteristics of the host magma where tourmaline initially crystallised; indeed, variations in magnesium and iron concentrations are associated with the conditions of crystal formation within the magma[28].

Dravite and schorl crystals can be distinguished visually by their colouration: Mg-rich tourmalines exhibit hues from pale brown to brownish-black, whereas schorl crystals display shades from bluish-black to black. However, upon analysing microscopic grains inside sediments, these characteristics are not uniformly apparent, requiring a more effective approach to distinguish the two species and get data on the relative quantities of magnesium and iron.

Raman spectroscopy behaves as a suitable tool for this objective, facilitating quick, straightforward, and non-destructive measurements with elevated spatial resolution (about micrometres) while elucidating the structure and chemical composition of the examined mineral, as the positions and relative intensities of the spectral peaks, associated with various vibrational modes, are contingent upon these sample characteristics. This section of the study concentrates on the analysis of tourmaline from the dravite-schorl series, aiming to correlate variations in the Raman spectrum with fluctuations in the relative concentrations of iron and magnesium in the Y-sites.

Raman Spectrum Of Dravite And Schorl

The Raman spectrum of dravite and schorl, like the general Raman spectrum of tourmalines, can be categorised into two primary regions: the fingerprint region, spanning 150 to 750 cm^{-1}[130,134], and the stretching region of the OH groups, ranging from 3400 to 3800 cm^{-1}[129] (Figure 22).

In the lower section of the spectrum, various subregions can be distinguished where vibrational modes linked to distinct crystallographic locations of the unit cell are observed. We concentrated specifically on two areas associated with alterations in the occupancies of Y-sites: the vibrational modes of the YO_6 octahedra, ranging from 200 to 315 cm^{-1}, characterised by three principal peaks designated as P_1, P_2, and P_3, and the vibrational modes of the ZO_6 octahedra, within the interval of 360-375 cm^{-1}, with the most intense mode identified as P_Z. The correlation between peak parameters in the first subregion and alterations in Y-sites composition is evident; nevertheless, the modifications in Z-sites-related vibrational modes may also be ascribed to variations in Y-sites composition, owing to the proximity of the Y and Z octahedra in the crystal structure, sharing oxygen atoms. Within the vibrational modes of the YO_6 octahedra, an initial indication for dravite-schorl differentiation is observed: in dravite, P_1 and P_2 are two distinct peaks of comparable intensity, whereas in schorl, P_1 just appears as a shoulder of the higher P_2 peak (Figure 22A).

Within the domain of the stretching vibrations of the OH groups, two different regions of peaks can be distinguished: those pertaining to the vibrational modes of the OH groups in the V-sites (ranging from 3400 to 3615 cm^{-1}) and those attributable to the OH groups in the W-site (spanning 3630 to 3770 cm^{-1}) (Figure 22B). The correlation with the Y-sites composition is attributed to the oxygen of the OH group being shared with the YO_6 octahedra: specifically, each V-site's OH groups share oxygen with one Y-site and two Z-sites, collectively forming three triplets, YZZ-YZZ-YZZ, whose composition influences the frequency of the ^{V}OH vibrational modes. Conversely, the OH group in the W-site shares oxygen with three Y-sites, and its vibrational frequency is also influenced by the neighbouring X-site due to the X-YYY composition. In particular, the behaviour of the ^{V}OH band, fitted with three different peaks, was already studied by Watenphul et al.[129], who derived the following formula to obtain the concentration (C) of the majority element in the Y-sites:

$$\mathrm{C}(a.p.f.u.) = \left(3I_{V_{OH_3}} + 2I_{V_{OH_2}} + I_{V_{OH_1}}\right) \Big/ I_{V_{OH_{tot}}} \qquad (1)$$

Where $I_{V_{OH_1}}$, $I_{V_{OH_2}}$ and $I_{V_{OH_3}}$ are the intensities of the three peaks utilised to model the ^{V}OH band, corresponding to the occupancy of 3 Y-sites and 6 Z-sites adjacent to the 3 V-sites within the unit cell. Specifically, $^{V}OH_1$ corresponds to the $^{Y}C^{Z}Al^{Z}Al+2\ ^{Y}Al^{Z}Al^{Z}Al$ configuration, $^{V}OH_2$ to $2^{Y}C^{Z}Al^{Z}Al+\ ^{Y}Al^{Z}Al^{Z}Al$ and $^{V}OH_3$ to $3^{Y}C^{Z}Al^{Z}Al$, where C is the predominant element at the Y-sites for the examined tourmaline species, magnesium in dravite and iron in schorl. $I_{V_{OH_{tot}}}$ denotes the cumulative intensities of the three bands.

Consequently, we examined this behaviour in the dravite-schorl samples analysed in this study while also investigating the ^{W}OH stretching modes, which provide insights on the Y-sites composition independent of the Z-sites composition.

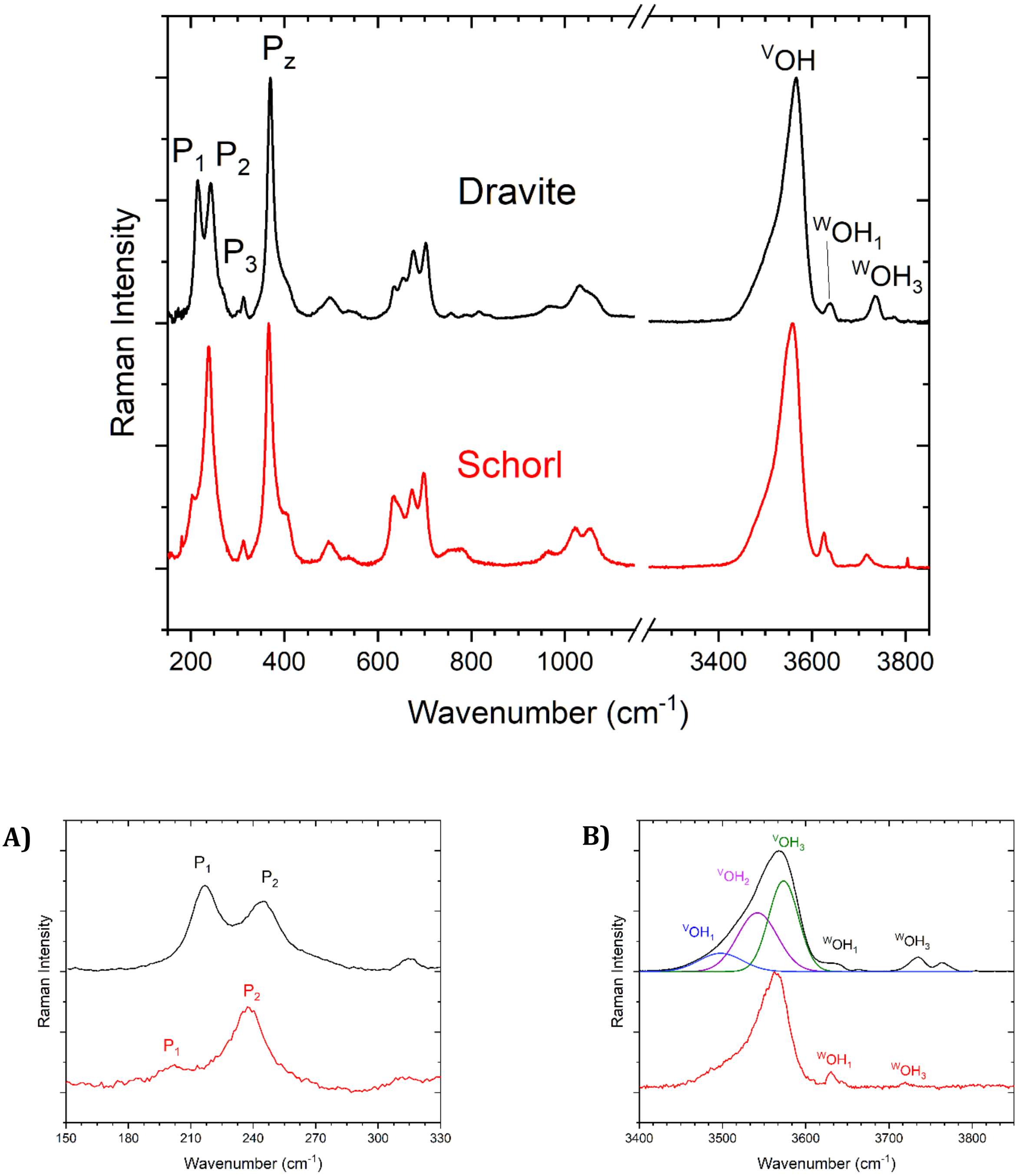

Figure 22: Comparison between dravite and schorl Raman spectra in both fingerprint and OH stretching regions with the main peaks highlighted. A) shows the behaviour of P_1 and P_2 peaks in the YO_6 octahedra vibrational modes region, while B) shows the behaviour of ^{V}OH and ^{W}OH stretching modes.

Preliminary Results On Dravite And Schorl

Fifteen tourmaline specimens from the dravite-schorl series (Figure 23), taken from different locations (Table 3), were analysed using Raman spectroscopy in the fingerprint and OH stretching regions. To augment the Raman response across each spectral region, two distinct excitation wavelengths were employed: a 632.8 nm He-Ne laser was used in the low-frequency region to minimise photoluminescence that might cover up the Raman peaks. In the OH region, a 473.1 nm, frequency-doubled Nd:YAG laser was used to enhance the signal for the analysis of low-intensity ^{W}OH modes. All samples were examined with the crystal c-axis aligned parallel to the polarisation of the incident light to eliminate the influence of crystal orientation on peak intensities, which is significant due to the polar characteristics of tourmalines (the final section of this chapter will provide a detailed discussion on the implications of crystal orientation on dravite and schorl).

Sample	Provenance	Species	Dimensions (mm)
B1	Brazil	Dravite	5x5x19
E1	Grotta d'Oggi, Elba, Italy	Schorl	2x2x4
E2	Grotta d'Oggi, Elba, Italy	Schorl	1x5x8
E3	Grotta d'Oggi, Elba, Italy	Schorl	1x2x8
E4	Grotta d'Oggi, Elba, Italy	Schorl	1x2x4
L1	Val Bodengo, Sondrio, Lombard Alps, Italy	Dravite	6x6x7
L2	Piona, Lecco, Lombard Alps, Italy	Dravite	10x10x20
L3	Piona, Lecco, Lombard Alps, Italy	Schorl	12x12x15
L4	Piona, Lecco, Lombard Alps, Italy	Schorl	7x7x20
L6	Val Bodengo, Sondrio, Lombard Alps, Italy	Dravite	10x13x16
P1	Ornavasso, Verbano-Cusio-Ossola, Piedmontese Alps, Italy	Dravite	3x4x12
P2	Ca' dei Pescatori, Biella, Piedmontese Alps, Italy	Schorl	1x1x3
P3	Ban Est, Verbano-Cusio-Ossola, Piedmontese Alps, Italy	Dravite	1x1x2
P4	Pizzo Marcio, Verbano-Cusio-Ossola, Piedmontese Alps, Italy	Schorl	1x2x2
T1	Fornovolasco, Lucca, Tuscany, Italy	Schorl	2x20x12

Table 3: Provenance and dimensions of the fifteen dravite-schorl samples.

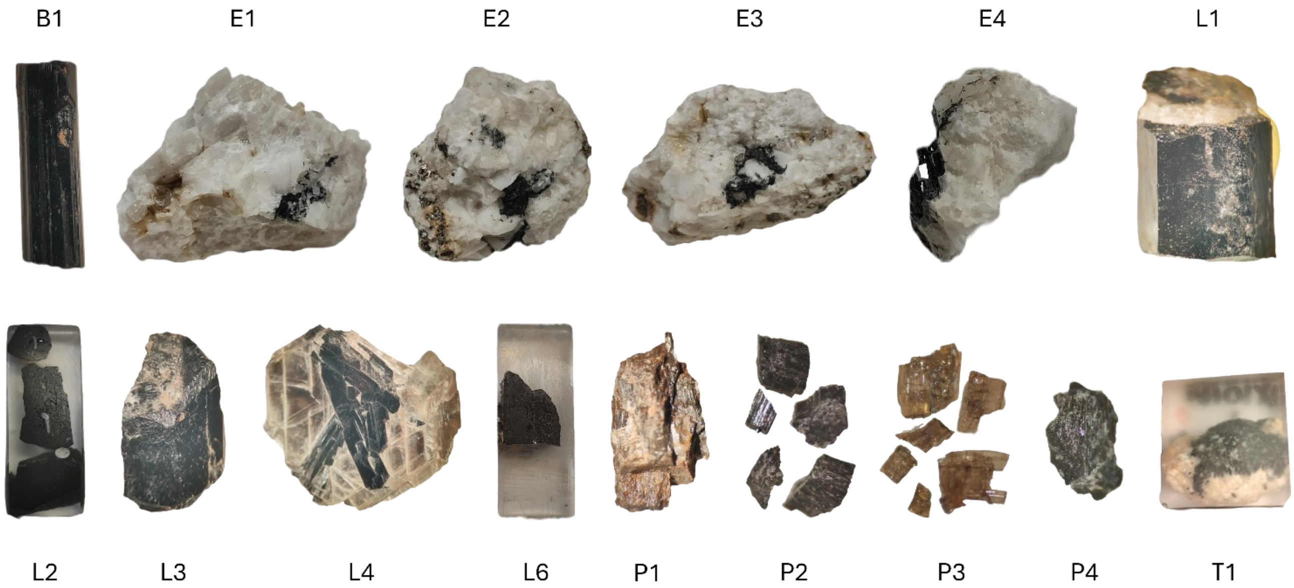

Figure 23: Photos of the fifteen tourmalines belonging to the dravite-schorl series analysed in this study.

Compositional Analyses

The composition of the fifteen dravite-schorl specimens was determined via SEM-EDS analysis, employing olivine ($(Mg, Fe)_2SiO_4$), haematite (Fe_2O_3), and kyanite ($Al_2(SiO_4)O$) as internal standards for quantifying oxide concentrations of the main component (aluminium, silicon, magnesium and iron). To assess the existence of heterogeneities within the same sample, a SEM picture was captured, and numerous points in the acquired region were evaluated using EDS, corresponding to the locations examined using Raman spectroscopy, as illustrated in Figure 24.

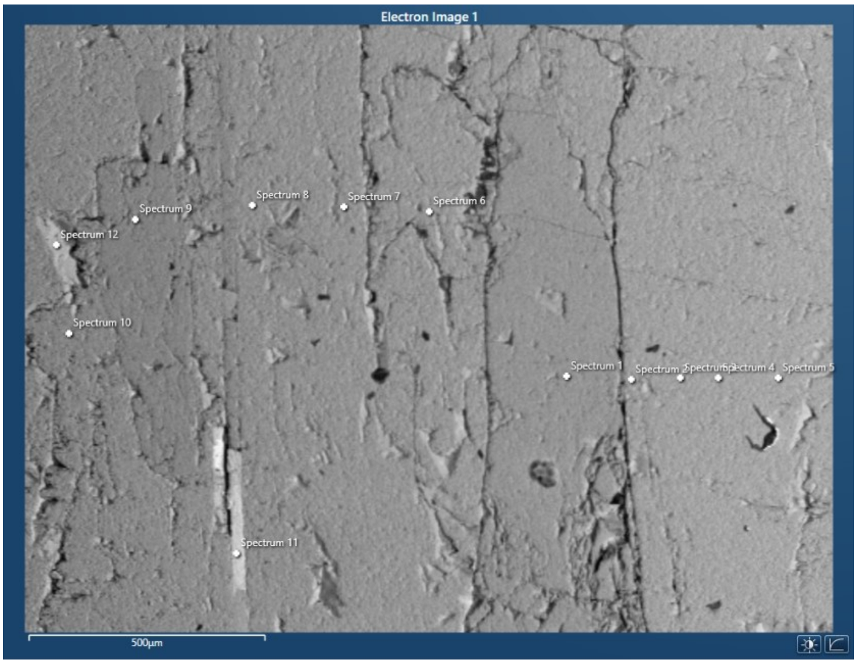

Figure 24: SEM image of sample L2 with EDS points highlighted.

Each EDS spectrum was examined using AZtecLive® software (Figure 25) to determine the oxide content of primary and trace elements usually observed in dravite-schorl tourmaline (Na_2O, MgO, Al_2O_3, SiO_2, K_2O, CaO, TiO_2, V_2O_3, Cr_2O_3, MnO, FeO, CuO, ZnO). Given that no significant heterogeneities (exceeding 1 Ox%) were detected among the various points measured on the same specimen, we can infer that the examined area in each sample is characterised by a homogeneous composition and will consider the average oxide concentration, as detailed in Table 4, for further analyses.

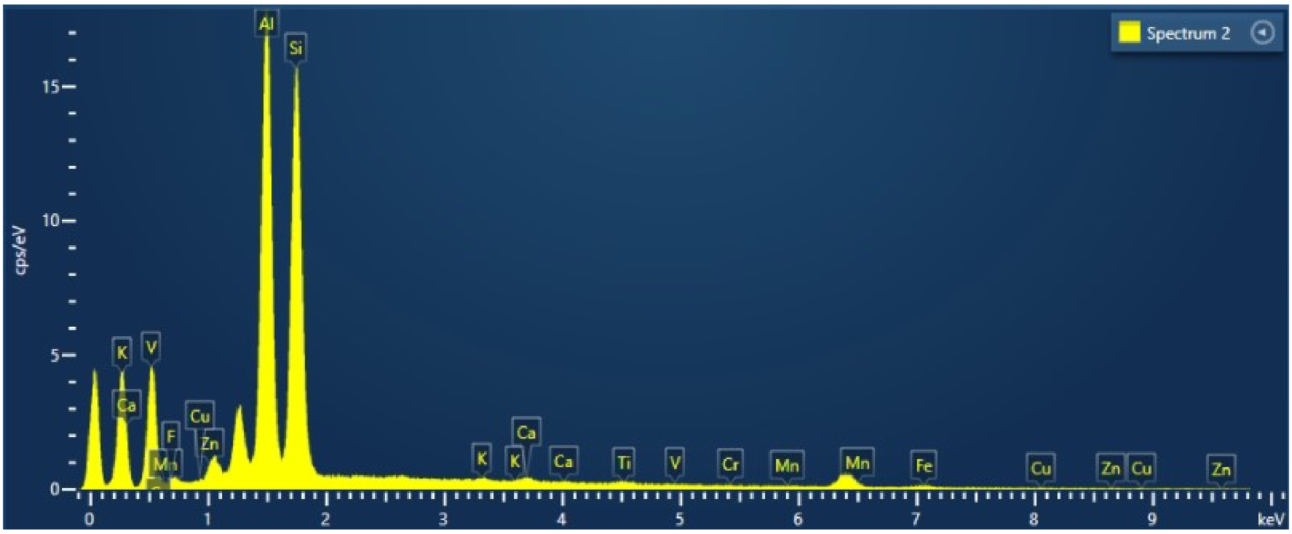

Figure 25: EDS spectrum of sample L2 visualised on AZtecLive® software.

	Na_2O	MgO	Al_2O_3	SiO_2	K_2O	CaO	TiO_2	V_2O_3	Cr_2O_3	MnO	FeO	CuO	ZnO
B1	1.45	9.37	35.62	45.18	0.09	1.46	1.31	0	0.07	0.07	5.19	0.06	0.14
E1	1.67	1.52	34.45	41.55	0.13	0.42	0.77	0	0.03	0.63	18.61	0.03	0.19
E2	1.52	3.93	34.36	42.62	0.06	0.52	0.99	0	0.01	0.32	15.55	0.09	0.03
E3	1.31	4.15	36.15	42.45	0.04	0.55	0.69	0	0.03	0.06	14.41	0.05	0.1
E4	1.72	3.07	35.59	42.86	0.05	0.2	0.62	0	0.04	0.39	15.29	0.01	0.16
L1	1.38	6.74	36.18	44.1	0.03	1.1	1.14	0.13	0.04	0.07	8.91	0.06	0.13
L2	1.71	5.02	39.2	45.74	0.17	0.52	0.55	0.05	0.04	0.08	6.87	0.06	0.01
L3	1.01	4.58	35.98	41.15	0.07	0.41	0.93	0.09	0.05	0.2	15.41	0.01	0.11
L4	1.27	3.09	35.35	41.01	0.06	0.12	0.67	0.05	0.01	0.21	18.07	0.04	0.03
L6	1.44	7.27	36.15	44.31	0.15	1.5	1.1	0.21	0.07	0.01	7.72	0.04	0.04
P1	1.98	7.68	34.73	42.9	0.04	0.35	1.08	0.1	0.02	0.28	10.49	0.16	0.21
P2	1.46	6.87	26.85	40.42	0.06	2.06	0.83	0.18	0.04	0.07	21.02	0.1	0.05
P3	1.8	10.57	36.57	46.71	0.06	1.3	0.71	0.13	0.05	0	1.97	0	0.14
P4	1.46	5.16	34.08	41.69	0.18	0.45	0.09	0.09	0.01	0.31	16.36	0.02	0.13
T1	1	6.6	32.53	41.95	0.1	2.25	2.36	0	0.05	0.07	13.07	0.01	0

Table 4: Oxide concentration in the fifteen dravite-schorl samples obtained from SEM-EDS analyses.

Nonetheless, as our attention pertains to the occupation of the Y-sites, the atomic concentration and the atoms per formula unit (a.p.f.u.) are more appropriate for our investigation. Consequently, we compute the atomic concentration of the specified elements, including boron and lithium. We fixed the boron content to 3 a.p.f.u. as suggested by Henry et al. [3], whereas the lithium concentration was determined using the methodology described by Pesquera et al.[175]:

$$Li_2O = 2.356 + 0.124\,SiO_2 - 0.121\,Al_2O_3 - 0.178\,FeO_{Tot} - 0.162\,MnO \qquad (2)$$

Still, equation (2) is applicable solely to tourmalines containing MgO < 2.0 wt%—specifically E1, E4, L4, and L5—while in tourmalines with elevated magnesium concentrations, the lithium content may be neglected due to charge balancing constraints[3,175,176]. Furthermore, only sample E4 yields a positive Li_2O concentration, whilst the remaining specimens exhibit negative values, which have been adjusted to zero. The occupation of crystal sites was obtained from the normalisation procedure 2 introduced by Henry[3], which relies on a fixed total concentration of cations in Y-, Z-, and T-sites at 15 a.p.f.u. The occupancy data presented in Table 5 was derived from this approximation.

	B1	E1	E2	E3	E4	L1	L2	L3	L4	L6	P1	P2	P3	P4	T1
X-Site															
Na	0.4	0.48	0.43	0.37	0.47	0.38	0.47	0.28	0.36	0.4	0.55	0.42	0.48	0.41	0.28
K	0.02	0.02	0.01	0.01	0.01	0.01	0.03	0.01	0.01	0.03	0.01	0.01	0.01	0.03	0.02
Ca	0.22	0.07	0.08	0.08	0.03	0.17	0.08	0.06	0.02	0.23	0.05	0.33	0.19	0.07	0.35
X-□	0.37	0.43	0.48	0.54	0.49	0.45	0.42	0.64	0.61	0.35	0.39	0.24	0.31	0.49	0.35
B-Sites															
B	3	3	3	3	3	3	3	3	3	3	3	3	3	3	3
T-Sites															
Si	6.35	6.15	6.2	6.12	6.1	6.27	6.49	5.92	5.96	6.31	6.1	6.01	6.49	6.03	6.11
Al	0	0	0	0	0	0	0	0.08	0.04	0	0	0	0	0	0
Y+Z-Sites															
Mg	1.96	0.34	0.85	0.89	0.65	1.43	1.06	0.98	0.67	1.54	1.63	1.52	2.19	1.11	1.43
Fe^{2+}	0.61	2.31	1.89	1.74	1.82	1.06	0.81	1.85	2.2	0.92	1.25	2.61	0.23	1.98	1.59
Al	5.9	6.01	5.89	6.14	5.97	6.07	6.55	6.01	6.02	6.07	5.82	4.71	5.99	5.81	5.59
Ti	0.14	0.09	0.11	0.08	0.07	0.12	0.06	0.1	0.07	0.12	0.12	0.09	0.07	0.01	0.26
V	0	0	0	0	0	0.01	0.01	0.01	0.01	0.02	0.01	0.02	0.01	0.01	0
Cr	0.01	0	0	0	0	0	0	0.01	0	0.01	0	0	0	0	0.01
Mn	0.01	0.08	0.04	0.01	0.05	0.01	0.01	0.02	0.03	0	0.03	0.01	0	0.04	0.01
Cu	0.01	0	0.01	0.02	0	0.01	0.01	0	0	0	0.02	0.01	0	0	0
Zn	0.01	0.02	0	0.01	0.02	0.01	0	0.01	0	0	0.02	0.01	0.01	0.01	0
Li	0	0	0	0	0.33	0	0	0	0	0	0	0	0	0	0

Table 5: Composition of the fifteen dravite-schorl tourmalines in a.p.f.u. with different sites occupancies obtained by normalising Y+Z+T-sites content to 15 a.p.f.u.

Based on the results in Table 5, we infer that Mg and Fe are the predominant constituents of the three Y-sites, while Al is the primary constituent in the Z-sites. The other elements at Y- and Z-sites are present in low concentrations compared to Mg, Fe, and Al, and therefore will be excluded from our study, which concentrates solely on the primary component. The relative concentrations of magnesium and iron in each dravite-schorl specimen can be determined using the formula $X = Mg/(Mg+Fe)$ (results presented in Table 6), which will be employed for comparison with variations in Raman spectral parameters in our research: from now on, all tourmalines with $X > 0.5$ will be classified as dravite, whereas specimens with $X < 0.5$ will be classified as schorl[177]. The expected disorder in the Y and Z-sites for magnesium, iron, and aluminium, attributed to charge balance discrepancies as outlined in the literature[6,9–11], will be addressed in the subsequent sections. Iron is presumed to be Fe^{2+} because SEM-EDS does not provide information on its oxidation state, and since ferrous iron predominantly resides in Y-sites, this is the most reasonable approximation based on the available data.

	Mg/(Mg+Fe)
B1	0.76±0.08
E1	0.13±0.01
E2	0.31±0.01
E3	0.34±0.01
E4	0.26±0.03
L1	0.57±0.01
L2	0.57±0.12
L3	0.35±0.02
L4	0.23±0.01
L6	0.63±0.05
P1	0.57±0.13
P2	0.37±0.08
P3	0.90±0.07
P4	0.36±0.03
T1	0.47±0.04

Table 6: Magnesium-iron relative content in all the fifteen dravite-schorl samples.

Raman Results

The Raman spectra for each sample are presented in Figure 26. The most apparent alterations, as anticipated, are observed in the P_1 and P_2 peaks associated with the vibrational modes of YO_6 octahedra, whereas modifications in the P_Z and OH stretching modes are not immediately discernible and require fitting for a comprehensive analysis of their behaviour. At first look, the configuration of the Raman spectra in the 200-315 cm^{-1} range can provide initial insight into the tourmaline species: two distinct peaks with similar height are characteristic of dravite, whereas a singular higher peak accompanied by a minor shoulder at lower wavenumbers is indicative of schorl. Nevertheless, a more precise correlation with the variations in magnesium-iron relative concentration may be achieved following a meticulous fitting of each Raman band. The results reported in the subsequent section are published in the *Journal of Raman Spectroscopy*[178].

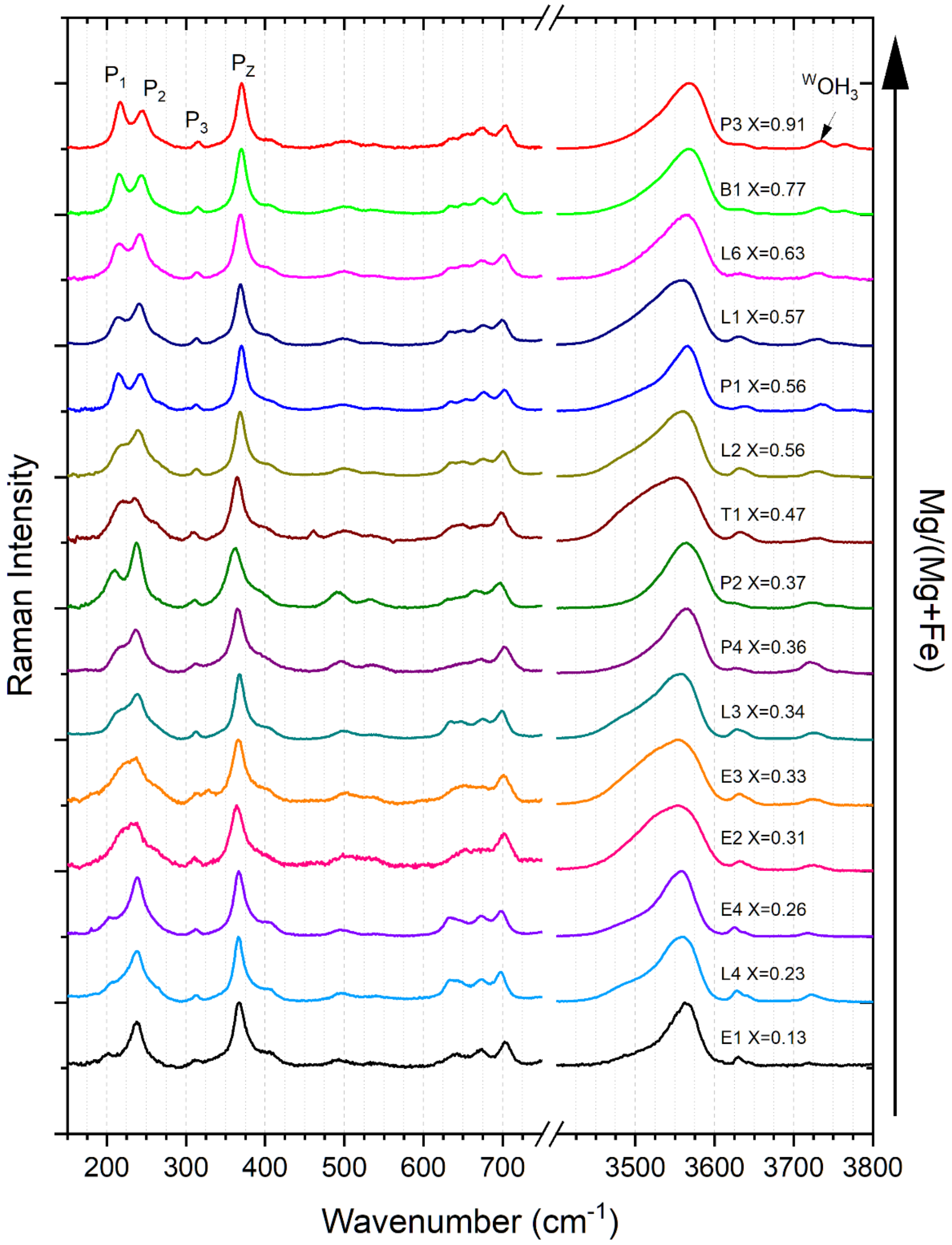

Figure 26: Normalised Raman spectra of the fifteen dravite-schorl specimens ordered by increasing X=Mg/(Mg+Fe) ratio obtained by SEM-EDS. The main peaks are indicated in the top spectrum.

To assess potential heterogeneity, 6 to 20 Raman measurements were conducted at different positions on the same sample, and the Raman spectrum parameters were averaged if no significant changes (standard deviation lower than spectral resolution) were observed within a single sample. The parameters of the Raman spectra and the compositions from SEM-EDS were averaged for each sample, as it was occasionally impossible to conduct Raman and SEM-EDS measurements at the same site due to the irregular surface of the material. Consequently, the provided numbers represent the mean of each sample.

Schorl is typically regarded as a poor Raman scatterer because of its characteristic black colour, which may lead to significant absorption of incident light[179]; however, by employing identical measurement parameters as those used for dravite and aligning the polarisation of the incident light parallel to the crystal c-axis, we obtained well-defined spectra for schorl samples as well.

YO_6 Vibrational Modes Spectral Region

As described in the previous section, P_1 and P_2 peaks represent the primary vibrational modes within the 200–315 cm^{-1} spectral range, corresponding to the vibrational modes of YO_6 octahedra. Nevertheless, the accurate fitting of these Raman bands necessitates the inclusion of several more peaks, as reported in Figure 27. In addition to P_1 and P_2, three additional peaks are required for the accurate fitting of this spectral region, along with a minor peak at 315 cm^{-1}, labelled as P_3. Among these three additional peaks, the most significant is the one situated between P_1 and P_2, designated as $P_{1/2}$, which corresponds to the saddle point between the two primary peaks.

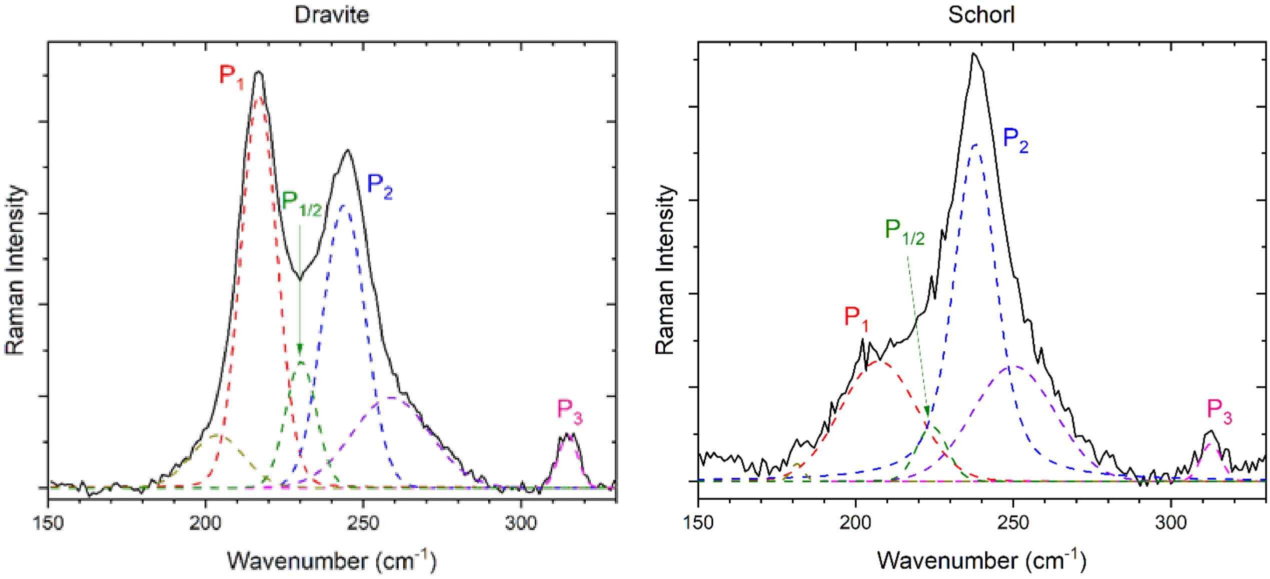

Figure 27: Example of the fitting for dravite (sample P3) and schorl (sample E4) Raman spectra in the YO_6 octahedra vibrational modes region with the main peaks highlighted.

The peak position of P_1 (Figure 28) appears to stay constant, approximately around 216 cm^{-1} for Mg/(Mg+Fe) ratios beyond 0.5 (dravite). Nonetheless, for schorl samples beneath this threshold, the behaviour of this peak gets increasingly complicated. In certain samples, it remains stable at roughly 216 cm^{-1}, comparable to dravite; however, in other instances, a red shift to about 202 cm^{-1} is noted. The observed bimodal behaviour may be attributed to the substitution of other elements for magnesium and iron at the Y-sites, despite the seeming reliance on the Mg/(Mg+Fe) ratio. Nonetheless, no additional components present at the Y-sites exhibit a link with this tendency. The presence of lithium, which cannot be directly detected with SEM-EDS, or the partial substitution of iron, magnesium, and aluminium in the Y- and Z-sites[6,9–11] are other likely explanations; the first assumption is applicable just to sample E4, which is the only sample exhibiting lithium concentration by indirect computation. However, samples E1, P2, and L4 also possess a P_1 peak at a lower wavenumber while lacking any lithium content. The latter hypothesis seems unlikely, as only sample P2 demonstrates a shift in both P_3 and P_Z peak positions (discussed in the subsequent section), aligning with literature indicating that alterations in these peaks correlate with disorder among Y- and Z-sites[130]. In contrast, other samples exhibit no significant changes.

The P_3 peak is expected to be around 315 cm^{-1}, as demonstrated in Figure 29, and a shift to lower wavenumbers can be ascribed to the presence of Fe^{3+} in the Y-sites. The shift in the P_3 peak position seen in this study is significantly less pronounced than that documented in prior research utilising tourmalines with increased Fe^{3+} concentrations at Y-sites. Sample T1 shows a shift to a lower wavenumber of approximately 5 cm^{-1} only for the P_3 peak, indicating a possible accumulation of Fe^{3+} at the Y-sites. Furthermore, sample T1 exhibits a notable quantity of quartz impurities, as evidenced by the spectrum in Figure 26, which displays the distinctive quartz peak at 465 cm^{-1}; thus, the composition of sample T1 is likely more complex than that identified by SEM-EDS.

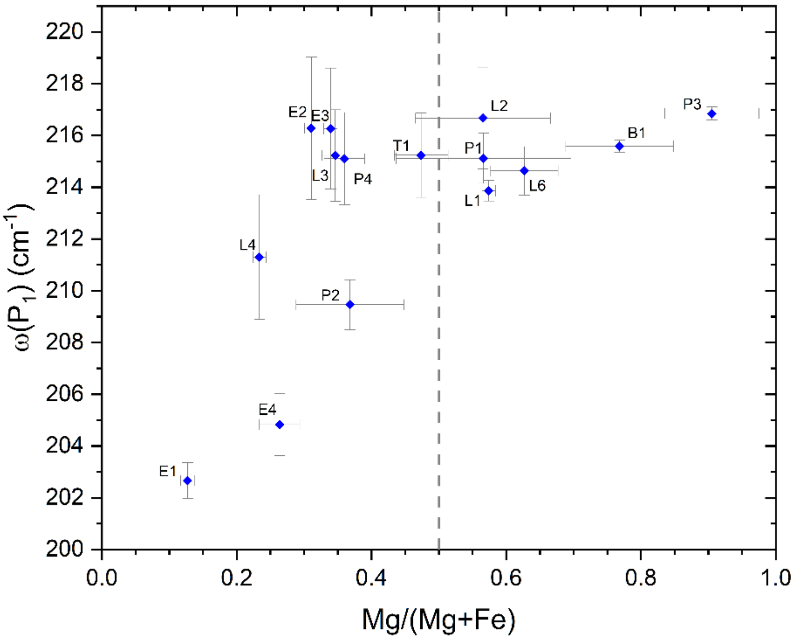

Figure 28: P_1 Raman peak position in all the fifteen dravite-schorl samples correlated to the relative content of magnesium and iron.

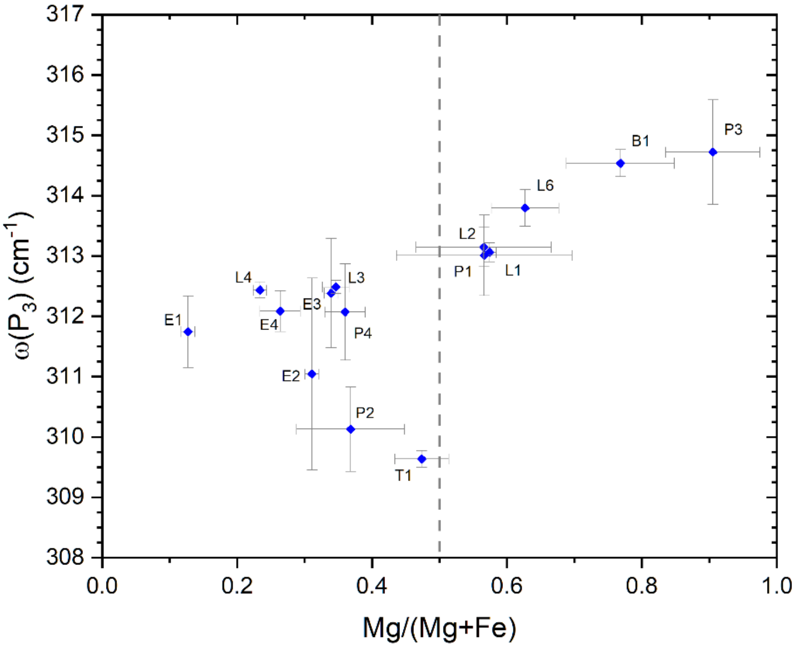

Figure 29: P_3 Raman peak position in all the fifteen dravite-schorl samples correlated to the relative content of magnesium and iron.

The location of peak P_2 exhibits a clearer pattern, as illustrated in Figure 30. In dravite samples, a linear dependence of P_2 on the Mg/(Mg+Fe) ratio is evidenced by the green line. With an increase in magnesium concentration, the P_2 peak rises to higher wavenumbers, attaining roughly 244 cm^{-1}. For Mg/(Mg+Fe) values under 0.5, the P_2 location remains more stable at approximately 237 cm^{-1}, yet with a minor shift towards higher wavenumbers as iron concentration increases, indicated by a decreasing Mg/(Mg+Fe) ratio, as illustrated by the red line in Figure 30. Generally, a notable distinction in the placements of P_2 between dravite and schorl is evident: in dravite, the peak is situated above 239 cm^{-1}, whereas in schorl, it is positioned at a lower wavenumber. Consequently, this value can serve as a criterion to differentiate between the two tourmaline species. The trends of these two lines can yield an estimation of the Mg/(Mg+Fe) ratio, but with potential imprecision. For schorl samples, we can retrieve the Mg/(Mg+Fe) ratio from the formula:

$$Mg/(Mg+Fe) = \frac{237.9 - \omega(P_2)}{2}$$

Whereas for dravite the formula became

$$Mg/(Mg+Fe) = \frac{\omega(P_2) - 234}{12}$$

The linear fitting for this parameter, as well as for all subsequent parameters, was conducted using OriginPro® software, with each point weighted according to its error as $\omega_i = \frac{1}{\sigma_i^2}$, where σ_i represents the error at the i-th point.

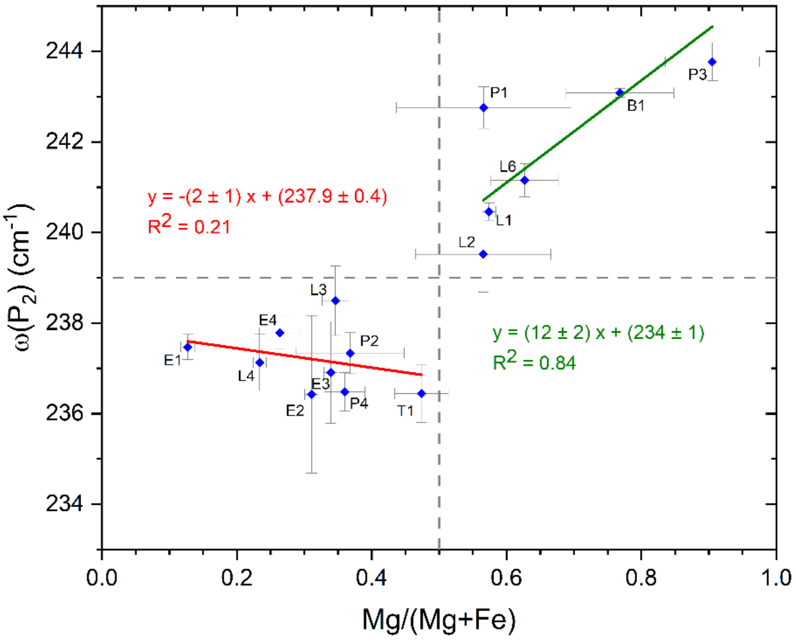

Figure 30: P_2 Raman peak position in all the fifteen dravite-schorl samples correlated to the relative content of magnesium and iron. The red line represents the linear trend for schorl samples, while the green line is the linear trend of dravite samples.

The behaviour of the peak utilised for fitting, corresponding to the saddle point between peaks P_1 and P_2, designated as $P_{1/2}$, is also noteworthy. Its position moves to higher wavenumbers with increasing magnesium concentration, varying from around 220 cm^{-1} for schorl to 230 cm^{-1} for dravite. Determining the precise location of this point is difficult because, unlike P_1 and P_2, it does not align with a discernible peak in the spectrum; instead, it represents a peak essential for achieving effective spectrum interpolation at the saddle point. Thus, particularly for schorl samples where the saddle point is less identifiable compared to dravite, the inaccuracy in ascertaining the position of $P_{1/2}$ is markedly elevated, as seen in Figure 31. In this instance, the identified linear trend can be utilised to calculate the Mg/(Mg+Fe) ratio using the formula:

$$Mg/(Mg + Fe) = \frac{\omega(P_{1/2}) - 220}{11}$$

Nevertheless, the significant error precludes the attainment of precise results.

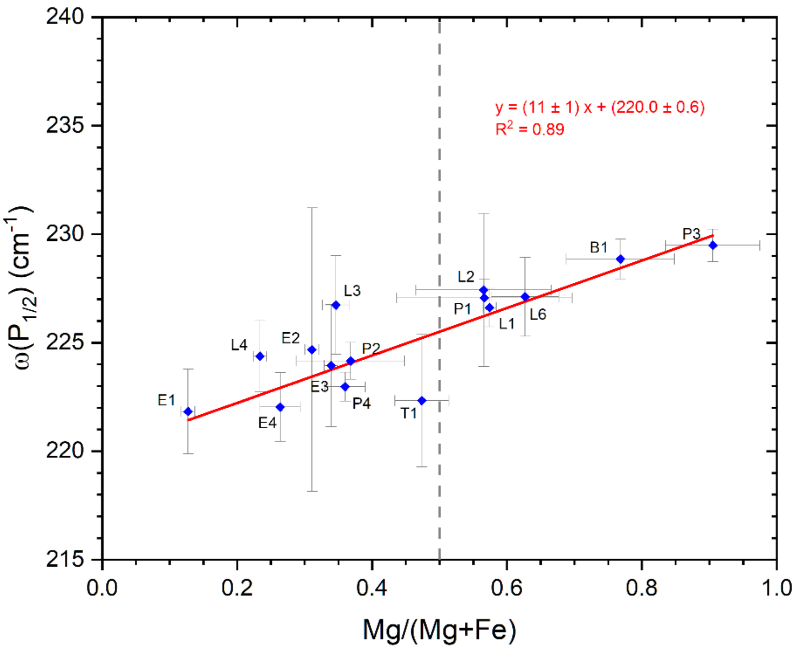

Figure 31: $P_{1/2}$ Raman peak position in all the fifteen dravite-schorl samples correlated to the relative content of magnesium and iron. The red line represents the linear trend for increasing Mg/(Mg+Fe).

It is noteworthy that the relative intensity of peaks P_1 and P_2, measured with a consistent crystal orientation across all analysed samples, is dependent on composition. Figure 26 illustrates that the intensity of P_1 increases with higher magnesium content, whereas P_2 exhibits minimal variation. The analysis of this behaviour yields the graph presented in Figure 32, which illustrates a linear increase in the ratio of the intensity of P_1 to that of P_2 as the Mg/(Mg+Fe) ratio rises. The Mg/(Mg+Fe) value can be derived by inverting the linear interpolation using the following formula:

$$\mathrm{Mg/(Mg+Fe)} = \frac{\frac{I(\mathrm{P_1})}{I(\mathrm{P_2})} - 0.03}{1.3}$$

Estimating composition based on these parameters lacks precision due to the partial overlap of the two peaks, particularly in schorl samples, which can lead to errors in the intensity evaluation of P_1 and P_2. Nonetheless, relative intensity serves as a rapid method to differentiate dravite from schorl in qualitative measurements and for *in situ* analysis: ratios equal to or greater than 1 indicate tourmalines of the first species, while ratios below 0.4 correspond to the second species. Watenphul et al.[130] previously investigated the relative intensity of the P_1 and P_2 peaks, noting an increase in this parameter with elevated Mg content in Y-sites, which aligns with our findings. However, the equation derived in this study can provide additional insights into the Mg/(Mg+Fe) ratio.

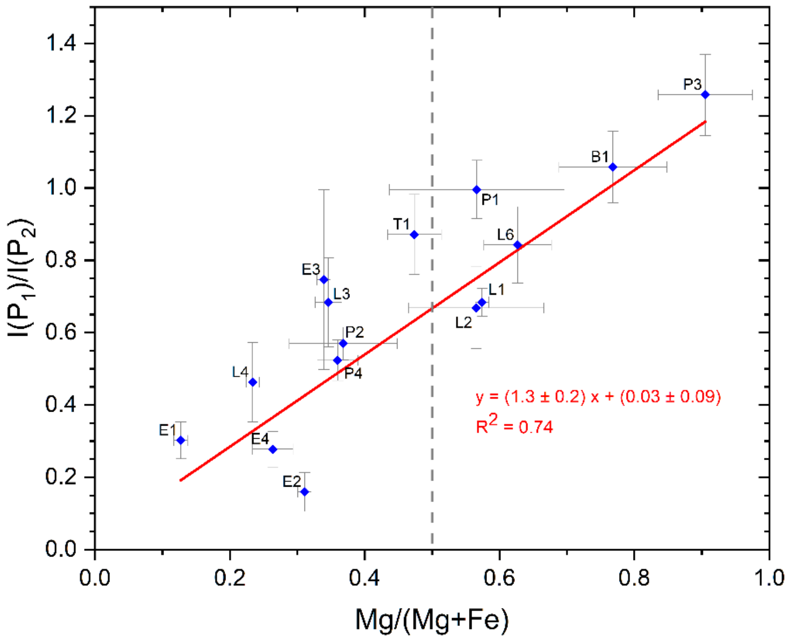

Figure 32: P_1 and P_2 Raman peak relative intensity in all fifteen dravite-schorl samples correlated to the relative content of magnesium and iron. The red line represents the linear trend for increasing Mg/(Mg+Fe).

Sample	Mg/(Mg+Fe)	ω(P_1) [cm^{-1}]	ω($P_{1/2}$) [cm^{-1}]	ω(P_2) [cm^{-1}]	I(P_1)/I(P_2)	ω(P_3) [cm^{-1}]
B1	0.76±0.08	215.6±0.2	228.9±0.9	243.1±0.1	1.1±0.1	314.5±0.2
E1	0.13±0.01	202.7±0.7	222±2	237.5±0.3	0.30±0.05	311.7±0.6
E2	0.31±0.01	216±3	225±7	237±2	0.16±0.05	311.0±1.6
E3	0.34±0.01	216±2	224±3	237±1	0.7±0.2	312.4±0.9
E4	0.26±0.03	205±1	2224±2	237.8±0.4	0.28±0.05	312.1±0.3
L1	0.57±0.01	213.9±0.4	226.6±0.9	240.5±0.2	0.68±0.04	313.1±0.2
L2	0.57±0.12	217±2	2273±4	239.5±0.8	0.7±0.1	313.1±0.3
L3	0.35±0.02	215±2	227±2	238.5±0.8	0.7±0.1	312.5±0.1
L4	0.23±0.01	211.3±2	224±2	237.1±0.6	0.5±0.1	312.4±0.1
L6	0.63±0.05	214.6±0.9	2278±2	241.2±0.4	0.8±0.1	313.8±0.3
P1	0.57±0.13	215±1	227±2	242.8±0.8	1.00±0.08	313.0±0.7
P2	0.37±0.08	209±1	224.2±0.9	237.3±0.5	0.57±0.05	310.1±0.7
P3	0.90±0.07	216.8±0.3	229.5±0.7	243.8±0.4	1.3±0.1	314.7±0.9
P4	0.36±0.03	215±2	223.0±0.7	236.5±0.4	0.52±0.06	312.1±0.8
T1	0.47±0.04	215±2	222±3	236.4±0.6	0.9±0.1	309.6±0.1

Table 7: Raman parameters in the YO_6 vibrational modes region for all the fifteen dravite-schorl samples analysed.

In summary, within the 200–315 cm^{-1} spectral range, the main characteristics are associated with the P_2 peak position and the relative intensities of P_1 and P_2, which aid in distinguishing dravite and schorl tourmaline varieties and their corresponding magnesium and iron concentrations. Additionally, the positioning of the $P_{1/2}$ peaks utilised for fitting the saddle point can provide insights into the Mg/(Mg+Fe) ratio, though with reduced accuracy. Other variables, such as P_1 and P_3 positions, may be associated with potential disorder in Y-sites; however, further work is required to evaluate this hypothesis. All Raman parameters for each sample in this region are displayed in Table 7.

ZO_6 Vibrational Modes Spectral Region

The primary peak utilised for fitting the ZO_6 vibrational modes band in the 320-450 cm^{-1} range has been defined as P_Z. While three other peaks are essential for accurately fitting this band, as depicted in Figure 33, only P_Z exhibits relevant behaviour for our analysis.

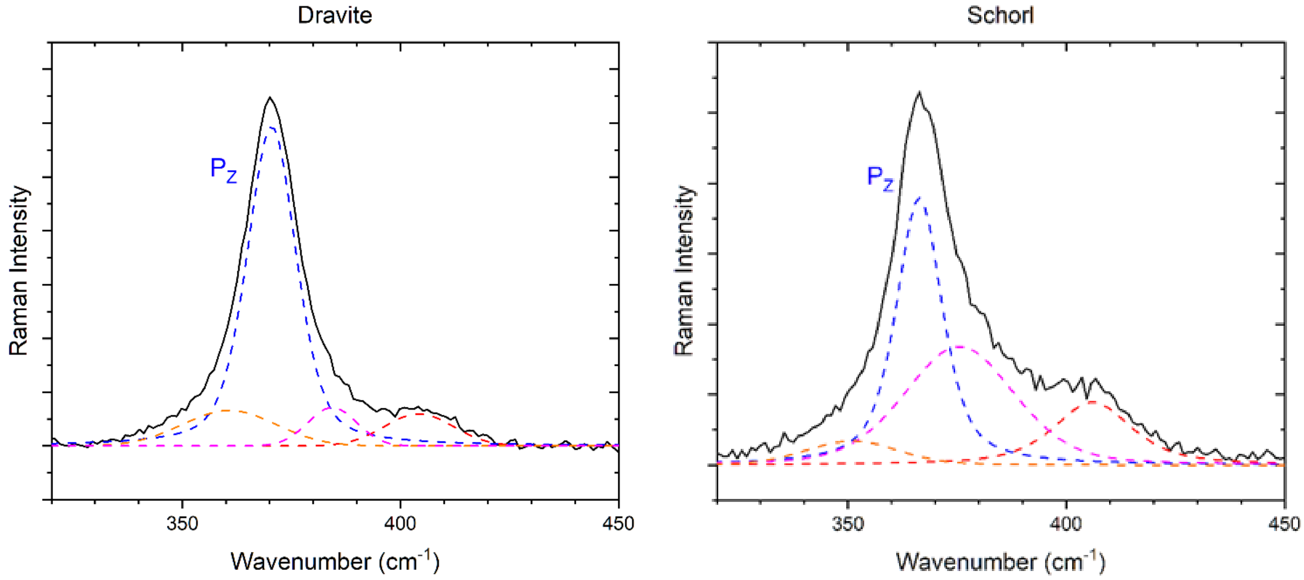

Figure 33: Example of the fitting for dravite (sample P3) and schorl (sample E4) Raman spectra in the ZO_6 octahedra vibrational modes region with the main peaks highlighted.

The replacement of Fe^{3+} for aluminium in the Z-sites may account for the displacement of the P_Z peak's wavenumber from its typical position of approximately 370 cm^{-1}[130]. Only the P2 sample exhibiting a significant shift in the P_Z peak (down to 361.7 cm^{-1}) additionally shows a corresponding shift in the P_1 peak; other samples do not exhibit both characteristics (Figure 34). Considering that sample P2 exhibits a markedly elevated iron concentration compared to the other samples and a diminished aluminium concentration, as reported in Table 5, the concurrent shifts in the P_1 and P_Z peaks may signify the presence of iron in Z-sites. Nonetheless, we cannot ascertain its oxidation status solely using SEM-EDS investigations. The P_Z mean peak positions for each dravite-schorl specimen are reported in Table 8.

	Mg/(Mg+Fe)	ω(P_Z) [cm^{-1}]
B1	0.76	369.8±0.1
E1	0.13	366.5±0.5
E2	0.31	364.0±0.2
E3	0.34	366.1±1.0
E4	0.26	366.4±0.5
L1	0.57	368.6±0.2
L2	0.57	368.1±0.4
L3	0.35	367.3±0.3
L4	0.23	366.1±0.1
L6	0.63	368.5±0.1
P1	0.57	370.1±0.7
P2	0.37	361.7±0.7
P3	0.904	370.2±0.3
P4	0.36	365.3±0.2
T1	0.47	364.5±0.5

Table 8: P_Z Raman peak position in the ZO_6 vibrational modes region for all the fifteen dravite-schorl samples analysed.

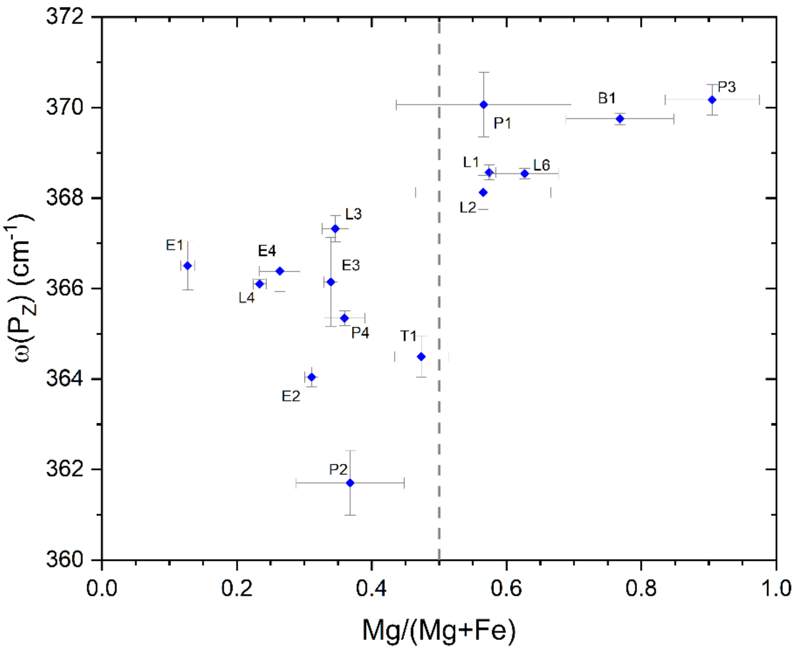

Figure 34: P_Z Raman peak position in all fifteen dravite-schorl samples correlated to the relative content of magnesium and iron.

OH Stretching Modes Spectral Region

Two different types of vibrational modes are detected within the spectral range of OH stretching: ^{V}OH in the 3400-3615 cm^{-1} range and ^{W}OH in the 3630-3770 cm^{-1} region.

We utilised equation (1) provided by Watenphul to analyse the stretching modes of OH groups in the V-sites. In our analysis, we categorised C as Mg for dravite samples and as Fe for schorl samples. In the interpolation of the ${}^{V}OH$ band, three peaks were utilised to achieve an accurate fit, as illustrated in Figure 35. To constrain the variations of these peaks during the fitting process, their positions were fixed according to the ratio X=Mg/(Mg+Fe) obtained from SEM-EDS analysis. For X=0 (schorl), the positions are 3500±3, 3545±2, and 3566±1 cm^{-1} for ${}^{V}OH_1$, ${}^{V}OH_2$, and ${}^{V}OH_3$, respectively. For X=1 (dravite), they are 3494±8, 3534±7, and 3573±4 cm^{-1} as reported in literature[129]. We subsequently linearly modified the positions of the three peaks, according to the X value, between the two end-members, as detailed in

Sample	Mg/(Mg+Fe)	ω(${}^{V}OH_1$) [cm^{-1}] (fixed)	ω(${}^{V}OH_2$) [cm^{-1}] (fixed)	ω(${}^{V}OH_3$) [cm^{-1}] (fixed)	Main element	C Calculated (a.p.f.u.)	C SEM-EDS (a.p.f.u.)
B1	0.76	3495.3	3536.4	3571.5	Mg	2.50±0.01	1.96
E1	0.13	3499.2	3543.5	3567.0	Fe	2.47±0.01	2.31
E2	0.31	3498.0	3541.3	3568.3	Fe	2.10±0.03	1.89
E3	0.34	3497.8	3541.0	3568.5	Fe	2.06±0.05	1.74
E4	0.26	3498.3	3541.9	3568.0	Fe	2.21±0.02	1.82
L1	0.57	3496.4	3538.4	3570.2	Mg	2.19±0.02	1.43
L2	0.57	3496.3	3538.2	3570.3	Mg	2.18±0.06	1.06
L3	0.35	3497.8	3540.9	3568.6	Fe	2.13±0.07	1.85
L4	0.23	3498.5	3542.2	3567.8	Fe	2.24±0.02	2.2
L6	0.63	3496.1	3537.9	3570.6	Mg	2.41±0.04	1.54
P1	0.57	3496.0	3537.6	3570.7	Mg	2.37±0.06	1.63
P2	0.37	3497.6	3540.6	3568.8	Fe	2.61±0.08	2.61
P3	0.90	3494.5	3534.9	3572.4	Mg	2.52±0.02	2.19
P4	0.36	3497.7	3540.8	3568.7	Fe	2.47±0.06	1.98
T1	0.47	3497.0	3539.5	3569.5	Fe	1.99±0.06	1.59

Table 9. Subsequently, the concentration of the primary element in Y-sites (Mg for dravite and Fe for schorl) was calculated using the aforementioned formula (1) and compared with the data obtained from SEM-EDS observations. Data reported in Figure 36 demonstrate that the values are comparable, particularly for concentrations beyond 2 a.p.f.u., although at lower concentrations, the calculated values exceed the observed ones obtained using SEM-EDS. A different approach is to suppose that Mg and Fe are the sole elements in Y-sites, thereby assuming that 3-C represents the concentration of the secondary element, Fe for dravite and Mg for schorl. After acquiring the concentrations of both magnesium and iron, the Mg/(Mg+Fe) ratio can be computed and compared to the value obtained via SEM-EDS, as seen in Figure 37. In this instance, the correspondence is better for compositions closer to the end-member, while intermediate compositions exhibit some differences; however, the similarity within calculated and measured magnesium-iron ratio is improved compared to the previous approach.

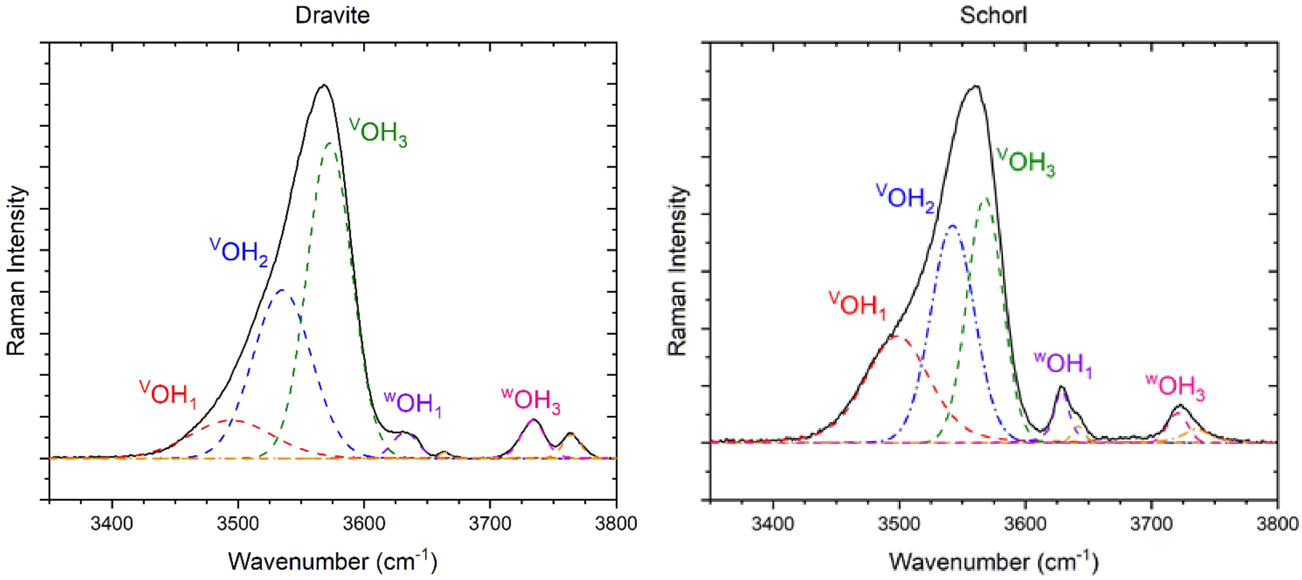

Figure 35: Example of the fitting for dravite (sample P3) and schorl (sample E4) Raman spectra in the OH stretching modes region with the main peaks highlighted for both V-sites and W-site modes.

Sample	Mg/(Mg+Fe)	$\omega(^{V}OH_1)$ [cm^{-1}] (fixed)	$\omega(^{V}OH_2)$ [cm^{-1}] (fixed)	$\omega(^{V}OH_3)$ [cm^{-1}] (fixed)	Main element	C Calculated (a.p.f.u.)	C SEM-EDS (a.p.f.u.)
B1	0.76	3495.3	3536.4	3571.5	Mg	2.50±0.01	1.96
E1	0.13	3499.2	3543.5	3567.0	Fe	2.47±0.01	2.31
E2	0.31	3498.0	3541.3	3568.3	Fe	2.10±0.03	1.89
E3	0.34	3497.8	3541.0	3568.5	Fe	2.06±0.05	1.74
E4	0.26	3498.3	3541.9	3568.0	Fe	2.21±0.02	1.82
L1	0.57	3496.4	3538.4	3570.2	Mg	2.19±0.02	1.43
L2	0.57	3496.3	3538.2	3570.3	Mg	2.18±0.06	1.06
L3	0.35	3497.8	3540.9	3568.6	Fe	2.13±0.07	1.85
L4	0.23	3498.5	3542.2	3567.8	Fe	2.24±0.02	2.2
L6	0.63	3496.1	3537.9	3570.6	Mg	2.41±0.04	1.54
P1	0.57	3496.0	3537.6	3570.7	Mg	2.37±0.06	1.63
P2	0.37	3497.6	3540.6	3568.8	Fe	2.61±0.08	2.61
P3	0.90	3494.5	3534.9	3572.4	Mg	2.52±0.02	2.19
P4	0.36	3497.7	3540.8	3568.7	Fe	2.47±0.06	1.98
T1	0.47	3497.0	3539.5	3569.5	Fe	1.99±0.06	1.59

Table 9: Fixed peak position for the three Raman bands used for the fitting of the ^{V}OH modes with comparison between the main element in Y-sites (C) calculated and obtained from SEM-EDS.

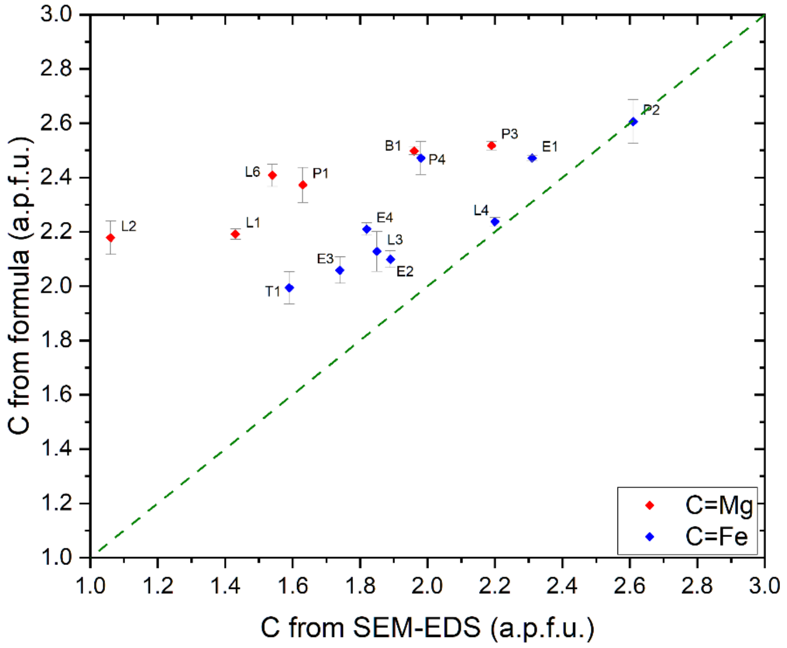

Figure 36: Comparison between the main element in the Y-sites (C) in both dravite (red points) and schorl (blue points) samples calculated from equation (1) and obtained from SEM-EDS. The green dashed line represents the 1:1 correspondence.

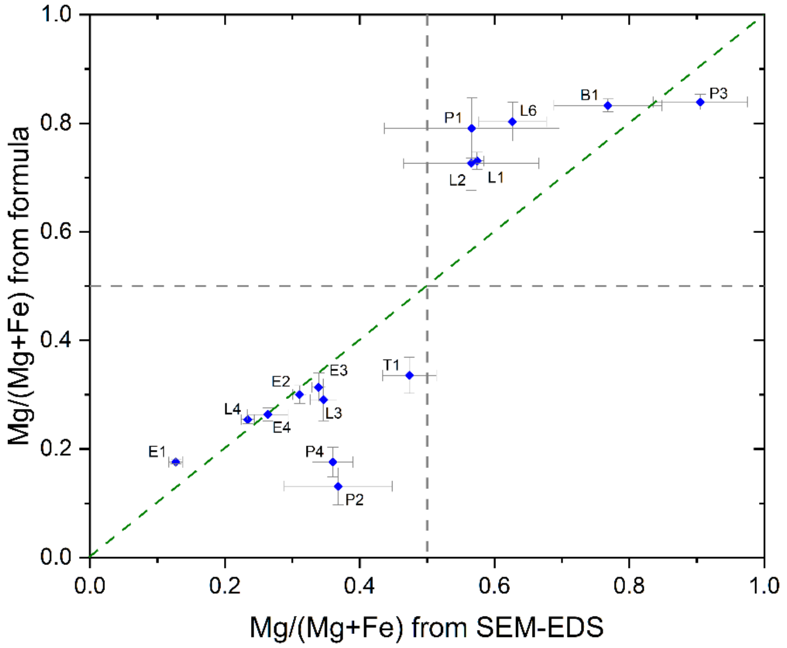

Figure 37: Comparison between the Mg/(Mg+Fe) ratio in both dravite and schorl samples calculated from equation (1) and obtained from SEM-EDS. The green dashed line represents the 1:1 correspondence.

The divergences from the green dashed line (indicative of one-to-one correspondence) can be ascribed to the Watenphul approach's consideration of aluminium as the sole element substituting the primary element at the Y-sites. In contrast, the dravite-schorl series allows for mutual substitution between magnesium and iron, potentially impacting the three triplets YZZ-YZZ-YZZ, which consequently affects the locations of the three ^{V}OH peaks. Furthermore, these inconsistencies may indicate the actual presence of aluminium at the Y-sites, substituting both magnesium and iron. Likewise, the differences may suggest that magnesium or iron is replacing aluminium in the Z-sites. The discrepancies increase significantly as the value approaches Mg/(Mg+Fe) = 0.5 or for C<2 a.p.f.u. for both Mg and Fe, suggesting that the formula yields accurate results only for compositions near the end-member; if the positions of the three peaks had not been set, these disparities would have been far more evident.

The trend of two ^{W}OH peaks throughout all spectra is particularly intriguing: $^{W}OH_1$ and $^{W}OH_3$, which are assigned to ^{Y}(Mg,Fe)^{Y}Al ^{Y}Al-^{X}□ and ^{Y}(Mg,Fe)^{Y}(Mg,Fe)^{Y}Al-^{X}Na configurations in dravite and schorl, respectively[129]. Figure 35 illustrates that two additional peaks are required for the fitting of the ^{W}OH modes; however, these peaks are not always consistently discernible. Consequently, we relied exclusively on the $^{W}OH_1$ and $^{W}OH_3$ peaks. The position of the first peak exhibits no particular correlation to the Mg/(Mg+Fe) ratio, instead ranging around 3630 cm^{-1} as visible in Figure 38.

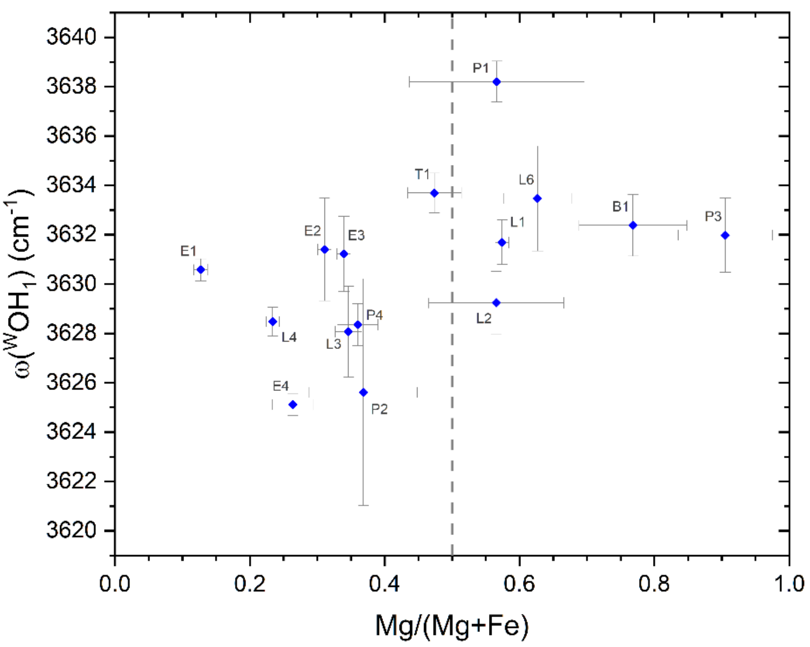

Figure 38: $^{W}OH_1$ Raman peak position in all fifteen dravite-schorl samples correlated to the relative content of magnesium and iron.

The behaviour of the $^{W}OH_3$ peak is particularly intriguing, as it shifts to higher wavenumbers with increasing magnesium concentrations, as illustrated in Figure 39. The linear relationship between position and the Mg/(Mg+Fe) ratio can be inverted to derive the subsequent equation.

$$Mg/(Mg+Fe) = \frac{\omega(\,^{W}\mathrm{OH}_3\,) - 3717.0}{20}$$

Consequently, as only sample P1 exhibits a significant deviation from this trend, this formula can be employed to derive a more accurate Mg/(Mg+Fe) ratio than that obtained using the peak parameters in the YO_6 vibrational modes region. Positions of both ${}^{W}OH_1$ and ${}^{W}OH_3$ peaks for each sample are reported below in Table 10.

Furthermore, although ${}^{W}OH$ modes exhibit significantly lower intensity compared to ${}^{V}OH$ modes, as illustrated in Figure 35, they are exclusively associated with the composition of X-YYY-sites[129]. Consequently, they remain unaffected by the composition of Z-sites, unlike ${}^{V}OH$ modes, resulting in a more direct correlation to the relative content of Mg and Fe in Y-sites, uninfluenced by potential disorder between Y- and Z-sites.

Finally, we can also obtain qualitative data regarding the total quantity of OH, as demonstrated by the intensity of the Raman bands associated with ${}^{W}OH_3$ that are unbound to vacancy sites. The hydroxyl groups preferentially occupy sites adjacent to vacancies when less than 3.3 atoms per formula unit of hydrogen are present. The detection of Raman bands within the 3710-3770 cm^{-1} range signifies a higher concentration of OH in both dravite and schorl samples, implying that our specimens are neither oxy-dravites nor oxy-schorl.

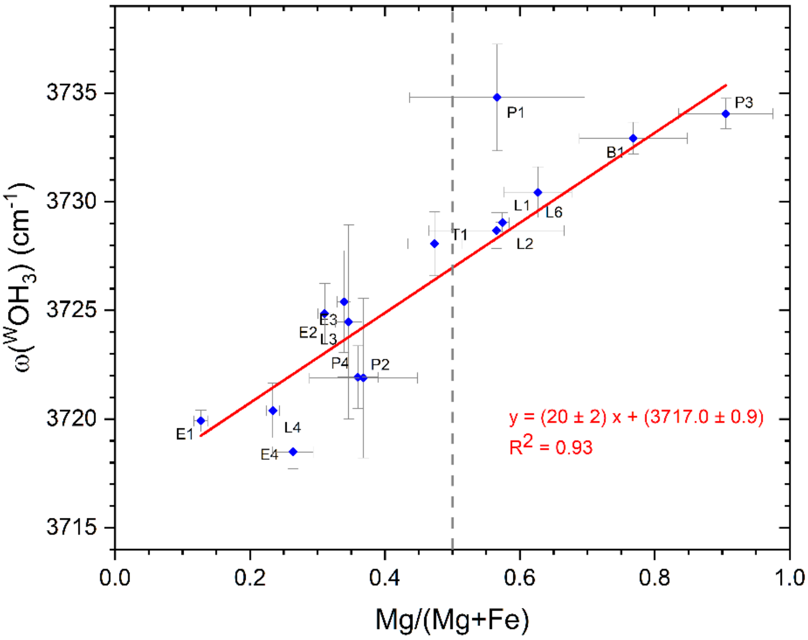

Figure 39: ${}^{W}OH_3$ Raman peak position in all fifteen dravite-schorl samples correlated to the relative content of magnesium and iron. The red line represents the linear trend for increasing Mg/(Mg+Fe).

Sample	Mg/(Mg+Fe)	ω(${}^{W}OH_1$) [cm^{-1}]	ω(${}^{W}OH_3$) [cm^{-1}]
B1	0.76	3632.4±1.2	3732.9±0.7
E1	0.13	3630.6±0.4	3719.9±0.5
E2	0.31	3631.4±2.1	3724.9±1.4
E3	0.34	3631.2±1.5	3725.4±2.3
E4	0.26	3625.1±0.4	3718.5±0.8
L1	0.57	3631.7±0.9	3729.0±0.4

L2	0.57	3629.2±1.3	3728.7±0.8
L3	0.35	3628.1±1.8	3724.5±4.5
L4	0.23	3628.5±0.6	3720.4±1.3
L6	0.63	3633.5±2.1	3730.4±1.2
P1	0.57	3638.2±0.8	3734.8±2.4
P2	0.37	3625.6±4.6	3721.9±3.7
P3	0.90	3632.0±1.5	3734.1±0.7
P4	0.36	3628.4±0.9	3721.9±1.4
T1	0.47	3633.7±0.8	3728.1±1.5

Table 10: ^{W}*OH Raman peak position in the OH stretching modes region for all the fifteen dravite-schorl samples analysed.*

Iron Oxidation State In Dravite And Schorl Through µXANES

A primary concern in our findings relates to the oxidation state of iron: SEM-EDS does not provide insights into iron speciation; consequently, we presumed that all measured iron is ferrous (Fe^{2+}), which is the predominant element in Y-sites of the end-member formula of schorl ($NaFe^{2+}{}_3Al_6Si_6O_{18}(BO_3)_3(OH)_3OH$). Nonetheless, it is established that tourmalines may include both Fe^{2+} and Fe^{3+} at the Y- and Z-sites[6,180,181]; hence, ascertaining the precise concentrations of both oxidation states of iron in our tourmaline samples can alter the oxide concentrations derived from SEM-EDS, thereby affecting the previously acquired results. Consequently, we should not disregard iron speciation.

For this reason, we conducted Fe K-edge µXANES (X-ray Absorption Near Edge Structure) spectroscopy to obtain information concerning the concentrations of the two distinct iron oxidation states in the previously examined dravite-schorl tourmalines. µXANES has been employed for the determination of Fe^{2+} and Fe^{3+} in diverse minerals exhibiting varying coordination environments for iron[151,157,182–185]. Furthermore, it has also been employed to investigate the iron oxidation status in tourmalines[186], making it an appropriate tool to address our problem. The behaviour of the pre-edge in the XANES spectrum is particularly noteworthy, as it has been directly correlated with the relative concentrations of Fe^{2+} and Fe^{3+}[157,187,188].

The research results described in the following section have been published in the *Journal of Raman Spectroscopy*[189].

µXANES Results On Dravite And Schorl

To evaluate the iron state of oxidation in the investigated specimens of dravite-schorl tourmalines, the Fe K-edge, situated between 7.110 keV and 7.130 keV, was inspected and matched with the peak locations seen in the spectra of standards, olivine and haematite, for Fe^{2+} and Fe^{3+}, respectively. Fe K-edge µXANES measures were conducted at the PUMA (Photons Utilisés pour les Matériaux Anciens) beamline (SOLEIL synchrotron, Saint-Aubin, France)[158] as part of experiment No. 20231463 titled "*Towards the Development of a Non-Destructive Compositional Tool for Tourmaline Studies: Correlation of XANES Data and Raman Parameters*".

Of the fifteen dravite-schorl samples examined in the preceding section, seven were subjected to µXANES analysis (B1, L1, L2, L3, L4, L6, and P1). The other samples were not examined due to their uneven surfaces, which precluded measurements in the 45° configuration of the instrument. However, the chosen samples encompass a broad spectrum of compositions between dravite and schorl, sufficient for our objective of determining the impact of iron's oxidation state on our prior findings.

The spectra were obtained throughout the energy range of 7.05 to 7.40 keV, with varying resolutions across different spectral segments: an energy resolution of 2 eV was employed in the regions from 7.05 to 7.10 keV and from 7.22 to 7.40 keV. The area encompassing the edge and pre-edge (from 7.10 to 7.22 keV) was analysed with enhanced energy resolution, with increments of 0.5 eV. All the µXANES spectra obtained for each sample are reported in Figure 40. The Fe K-edge profile closely resembles that of olivine, peaking at around 7.126 keV, in contrast to haematite, whose maximum is at 7.133 keV, indicating that ferrous iron predominates in our samples.

However, to obtain quantitative information on the relative content of ferric iron in our sample ($Fe^{3+}/\Sigma Fe$), the pre-edge feature located in the 7.108–7.117 keV region can be used thanks to a dependence studied in different works[157,187,188]. We utilised the methodology described by Wilke et al.[157] to deconvolute the pre-edge from the rest of the spectrum. All spectra were normalised by referencing the region prior to the pre-edge and the post-edge range: the minimum value below 7.090 keV was collected and subtracted to establish a zero baseline for each spectrum, while the mean absorption value for energies exceeding 7.200 keV was employed to normalise the post-edge region to 1. An example of the resulting XANES spectrum is reported in Figure 41.

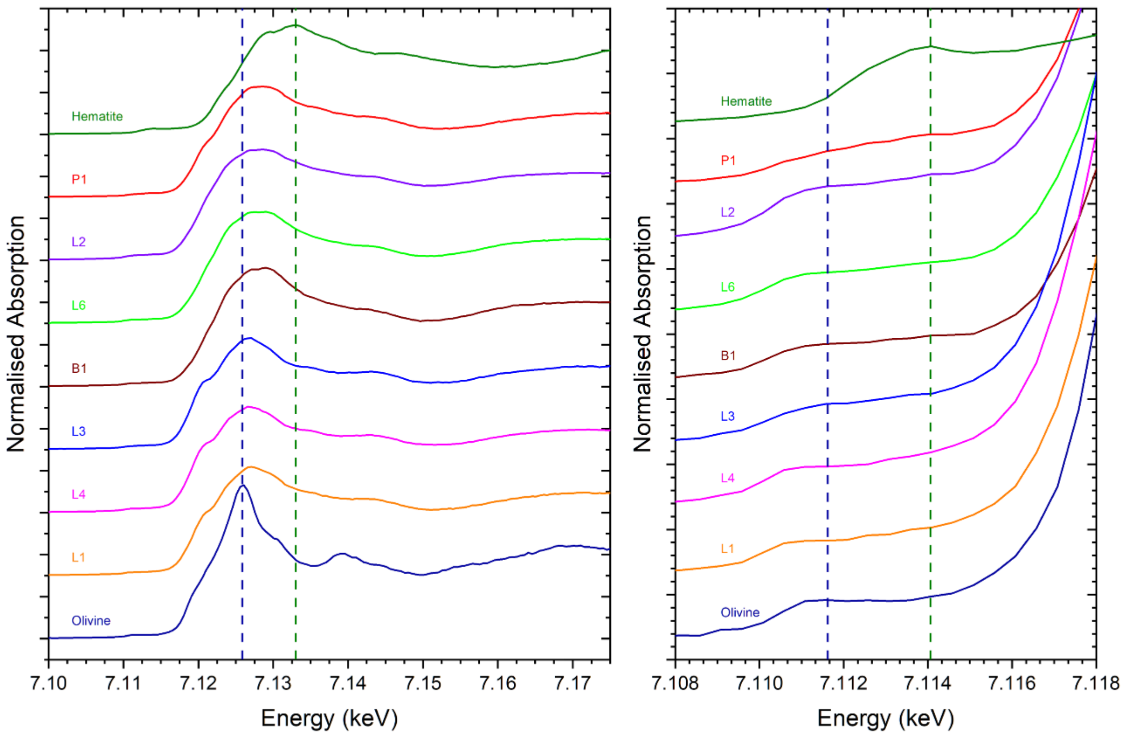

Figure 40: The image on the left shows the normalised μXANES spectra for all seven dravite-schorl samples analysed and for olivine and haematite standards. The positions of the Fe K-edge for olivine (dark blue) and haematite (dark green) are highlighted by the dashed lines. On the right image, a focus on the pre-edge region is reported with the centroid positions for olivine and haematite standards highlighted by the dashed lines.

After normalising the spectra, the pre-edge feature can be deconvoluted using baseline subtraction within the 7.100-7.118 keV region. This operation was executed in MATLAB (MathWorks®) utilising a spline function that follows the Fe K-edge in this region, as illustrated in Figure 42. Following Wilke's approach[157], the generated pre-edge has been interpolated utilising three pseudo-Voigt functions within the LabSpec5® software, employing a 50% Gaussian and 50% Lorentzian shape fraction, with the Gaussian-Lorentzian factor fixed at 0.5. The position, intensity, and FWHM (full width at half maximum) were permitted to vary until convergence was attained in the initial fitting phase. The average FWHM of the three identified peaks was subsequently calculated and established as a fixed parameter for the second interpolation phase. The outcome of the three fixed-width peaks is an interpolation that reflects the one depicted in Figure 43. The properties of the three peaks can be utilised to determine the centroid position for each pre-edge as the intensity-weighted mean position of the three peaks. This value is directly correlated with the concentration of octahedrally coordinated ferric iron relative to the total iron ($Fe^{3+}/\Sigma Fe$), as documented by Wilke[157]. Nonetheless, due to the absence of precise documentation of the slightly concave trend in the literature, we approximate it as linear, establishing the centroid positions of olivine and haematite as standards for $Fe^{3+}/\Sigma Fe=0$ and $Fe^{3+}/\Sigma Fe=1$, respectively. Linear interpolation enables the calculation of $Fe^{3+}/\Sigma Fe$ for each dravite-schorl sample based on the pre-edge centroid position, yielding the values presented in Table 11.

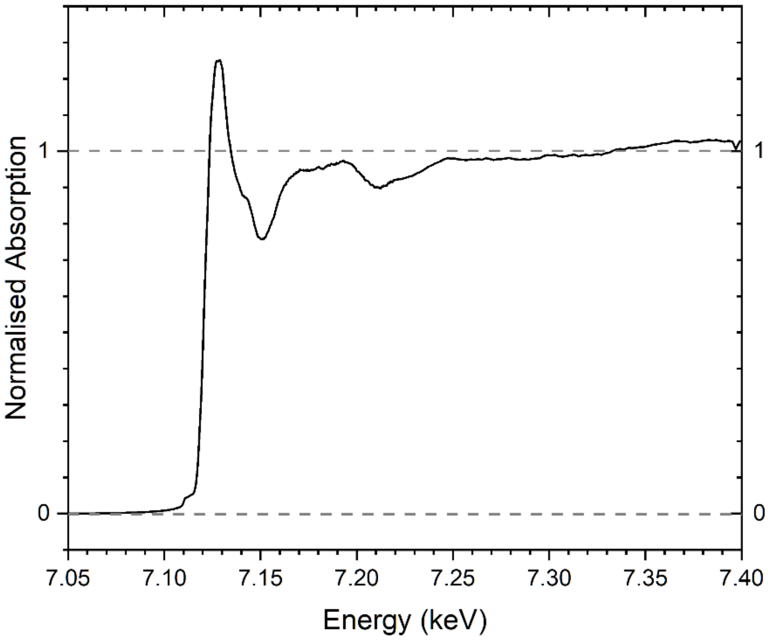

Figure 41: Example of the normalisation procedure for the XANES spectra of sample L6. The region beneath the pre-edge is normalised to 0, whereas the post-edge area is normalised to 1.

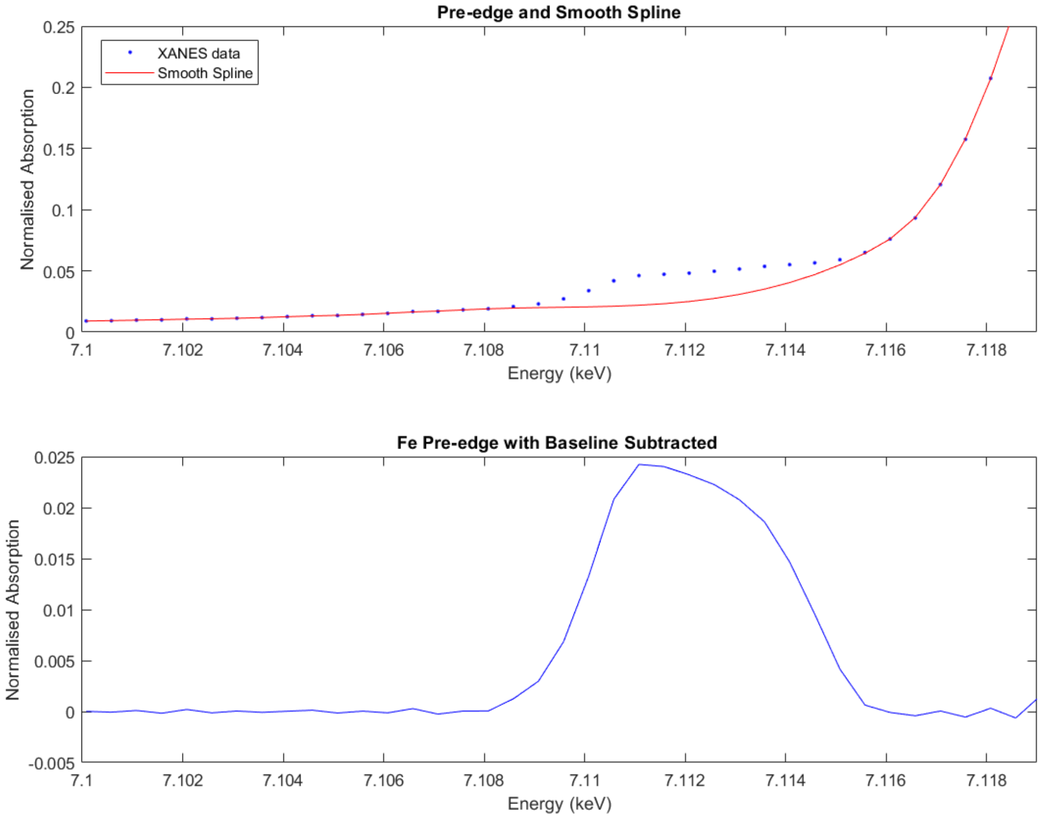

Figure 42: Representation of spline baseline subtraction and the consequent pre-edge feature for sample L6.

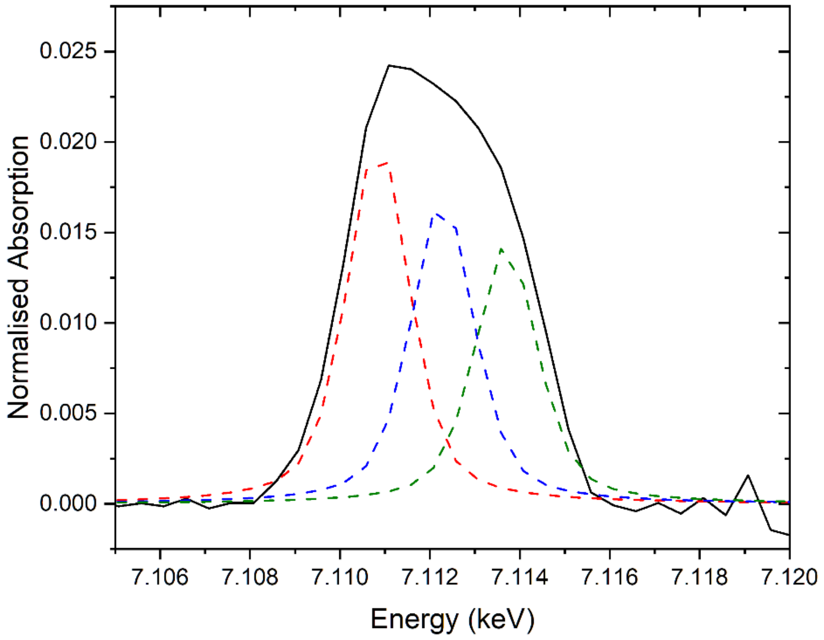

Figure 43: Illustration of pre-edge fitting utilising three width-constrained pseudo-Voigt functions on sample L6.

Sample	Centroid Position (keV)	$Fe^{3+}/\Sigma Fe$
Hematite	7.1141 (2)	1 (Fixed)
P1	7.1126 (2)	0.40 (8)
L2	7.1122 (2)	0.23 (8)
L6	7.1121 (2)	0.20 (8)
B1	7.1121 (2)	0.20 (8)
L3	7.1119 (2)	0.10 (9)
L4	7.1117 (2)	0.03 (8)
L1	7.1117 (2)	0.03 (9)
Olivine	7.1116 (2)	0 (Fixed)

Table 11: $Fe^{3+}/\Sigma Fe$ ratio obtained from the pre-edge centroids positions for each of the seven dravite-schorl samples analysed through µXANES.

Utilising the different concentrations of iron oxidation states derived by µXANES, the composition identified through SEM-EDS (Table 5) can be refined by including both FeO and Fe_2O_3 oxide concentrations, hence eliminating the prior assumption that all iron was ferrous. The newly acquired compositions, detailed in Table 12, can now be employed to recalculate the magnesium-iron ratio, taking into account solely the actual quantity of Fe^{2+}, as this represents the predominant speciation expected in Y-sites. We also attempted to incorporate the total of both Fe^{2+} and Fe^{3+} in the magnesium-iron ratio; however, this does not result in significant alterations compared to the prior scenario where all iron is assumed to be ferrous without XANES data, thereby failing to enhance the model for the behaviour of Raman parameters. The magnesium-iron ratio for each sample is presented in Table 13.

	B1	**L1**	**L2**	**L3**	**L4**	**L6**	**P1**
Na_2O	1.29	1.23	1.52	0.90	1.13	1.28	1.76
MgO	8.34	6.01	4.47	4.08	2.76	6.48	6.85
Al_2O_3	31.71	32.24	34.92	32.10	31.58	32.22	30.95
SiO_2	40.21	39.30	40.75	36.72	36.63	39.49	38.24
K_2O	0.08	0.03	0.15	0.06	0.06	0.14	0.04
CaO	1.30	0.98	0.46	0.37	0.11	1.33	0.31
TiO_2	1.16	1.02	0.49	0.83	0.60	0.98	0.96
V_2O_3	0	0.11	0.04	0.08	0.05	0.19	0.09
Cr_2O_3	0.06	0.03	0.04	0.05	0.01	0.06	0.02
MnO	0.06	0.06	0.07	0.18	0.19	0.01	0.25
FeO	3.70	7.70	4.71	12.37	15.34	5.50	5.61
Fe_2O_3	0.92	0.24	1.41	1.37	0.81	1.38	3.74
CuO	0.05	0.05	0.05	0.01	0.04	0.04	0.14
ZnO	0.12	0.12	0.01	0.10	0.02	0.04	0.18
B_2O_3	11.00	10.88	10.91	10.78	10.67	10.86	10.86
Site Occupancy							
X-Site							
Na	0.40	0.38	0.47	0.29	0.36	0.40	0.55
K	0.02	0.01	0.03	0.01	0.01	0.03	0.01
Ca	0.22	0.17	0.08	0.06	0.02	0.23	0.05
X-□	0.36	0.44	0.42	0.64	0.61	0.34	0.39
B-Sites							
B (Fixed)	3	3	3	3	3	3	3
T-Sites							
Si	6.36	6.28	6.49	5.92	5.97	6.32	6.12
Al	0	0	0	0.08	0.03	0	0
Y+Z-Sites							
Mg	1.97	1.43	1.06	0.98	0.67	1.55	1.63
Fe^{2+}	0.49	1.03	0.63	1.67	2.09	0.74	0.75
Fe^{3+}	0.11	0.03	0.17	0.17	0.10	0.17	0.45
Al	5.91	6.07	6.56	6.03	6.03	6.08	5.84
Ti	0.14	0.12	0.06	0.10	0.07	0.12	0.12
V	0	0.01	0.01	0.01	0.01	0.02	0.01
Cr	0.01	0.004	0.004	0.01	0.001	0.01	0.002
Mn	0.01	0.01	0.01	0.02	0.03	0.001	0.03
Cu	0.01	0.01	0.01	0.001	0.005	0.005	0.02
Zn	0.01	0.01	0.001	0.01	0.003	0.005	0.02

Table 12: The composition of the seven examined dravite-schorl tourmalines, analysed by µXANES, reveals varying iron oxidation states expressed in both Ox% and a.p.f.u., with distinct site occupancies achieved by normalising the Y+Z+T-sites content to 15 a.p.f.u.

Sample	Mg/(Mg+Fe) (All Fe As Fe^{2+})	Mg/(Mg+Fe^{2+}) (Only Fe^{2+} From XANES)	Mg/(Mg+Fe^{2+}+Fe^{3+}) (Both Fe^{2+} And Fe^{3+} From XANES)
B1	0.77	0.80	0.77
L1	0.57	0.58	0.57
L2	0.56	0.63	0.57
L3	0.35	0.37	0.35
L4	0.23	0.24	0.23
L6	0.63	0.68	0.63
P1	0.56	0.69	0.58

Table 13: Magnesium-iron ratio for the seven dravite-schorl specimens, considering only Fe^{2+} and both Fe^{2+} and Fe^{3+} obtained through µXANES compared to the previous Mg/(Mg+Fe) ratio obtained considering all iron as ferrous.

Improvement In The Raman Model

With the µXANES study yielding the new Mg/(Mg+Fe^{2+}) ratio, we may explore methods to improve the behaviour of Raman parameters.

We analysed the behaviour of the P_1 and P_2 peaks associated with the vibrational modes of YO_6 octahedra in the low wavenumber range (200-315 cm^{-1}). Including Fe^{2+} from µXANES in the Mg/(Mg+Fe) ratio confirms the validity of the prior correlation with the P_2 peak location. The blue points in Figure 44 indicate that the P_2 peak is below 239 cm^{-1} for schorl minerals and exceeds this value for dravite. Moreover, the equation

$$Mg/(Mg + Fe^{2+}) = \frac{\omega(P_2) - 233.9}{11}$$

indicates that these data exhibit a far more linear correlation than the prior results (black points) derived by treating all iron as Fe^{2+}. In comparison to previous data, the increased concentration of Fe^{3+} in the P1 sample leads to a substantial modification in the Mg/(Mg+Fe^{2+}) ratio, emphasising this linear relationship and significantly enhancing the data interpretation. No significant differences are observed in the P_1 peak (Figure 45), with the dravite peak consistently positioned at 216 cm^{-1}, but certain schorl samples (namely L4 in this case) exhibit a shift to lower wavenumbers. To fully comprehend this tendency, however, more samples are necessary. Regarding the $P_{1/2}$ saddle point, as shown in Figure 46, the linear trend modified to

$$Mg/(Mg + Fe^{2+}) = \frac{\omega(P_{1/2}) - 222.6}{7}$$

Nevertheless, the precision did not markedly improve compared to previous results.

The P_3 peak position doesn't show substantial changes, as visible in Figure 47, but most important is that no evident shift to lower wavenumbers is shown with respect to the concentration of Fe^{3+}: this indicates that no Fe^{3+} is present in Y-sites[130], whereas it is all located in the Z-sites, as we predicted.

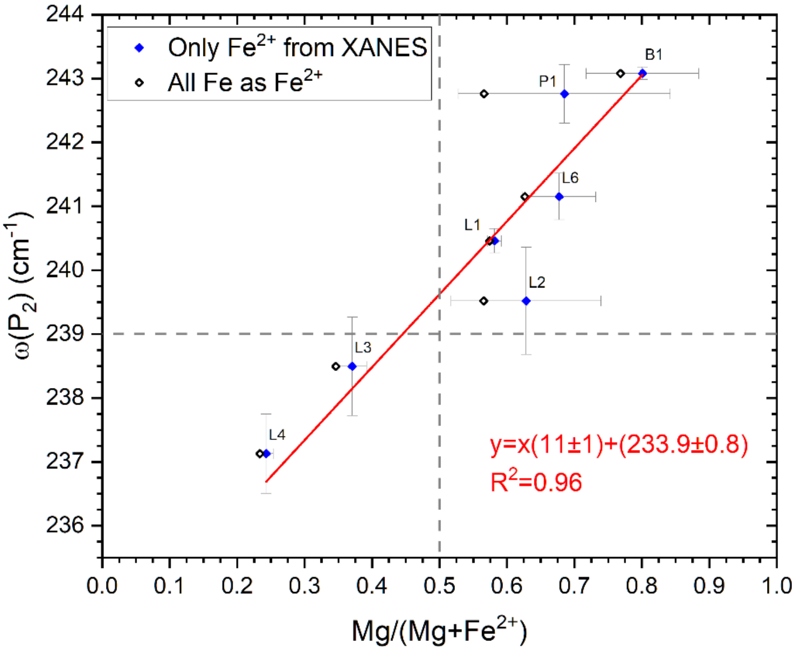

Figure 44: P_2 peak position for the seven dravite-schorl samples compared to the Mg/(Mg+Fe^{2+}) ratio obtained thanks to µXANES measurements (blue points). The black points represent the old data obtained considering all iron as Fe^{2+} in the magnesium-iron ratio. The red line represents the linear fitting of the new data.

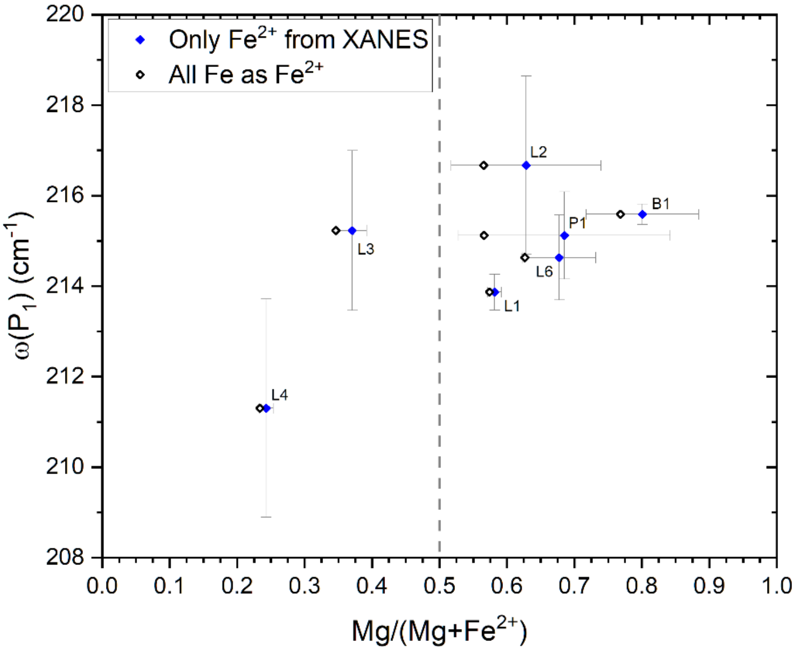

Figure 45: P_1 peak position for the seven dravite-schorl samples compared to the Mg/(Mg+Fe^{2+}) ratio obtained thanks to µXANES measurements (blue points). The black points represent the old data obtained considering all iron as Fe^{2+} in the magnesium-iron ratio.

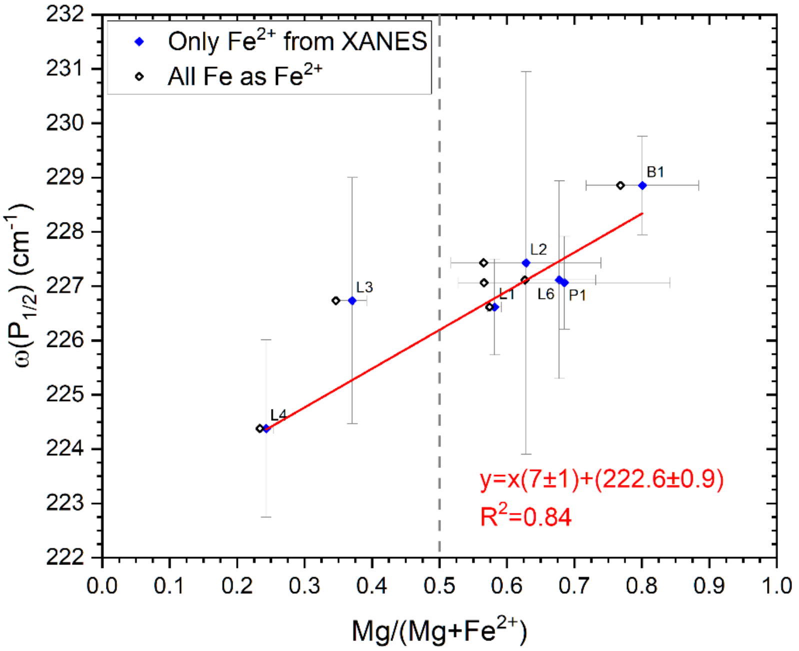

Figure 46: $P_{1/2}$ peak position for the seven dravite-schorl samples compared to the Mg/(Mg+Fe^{2+}) ratio obtained thanks to µXANES measurements (blue points). The black points represent the old data obtained considering all iron as Fe^{2+} in the magnesium-iron ratio. The red line represents the linear fitting of the new data.

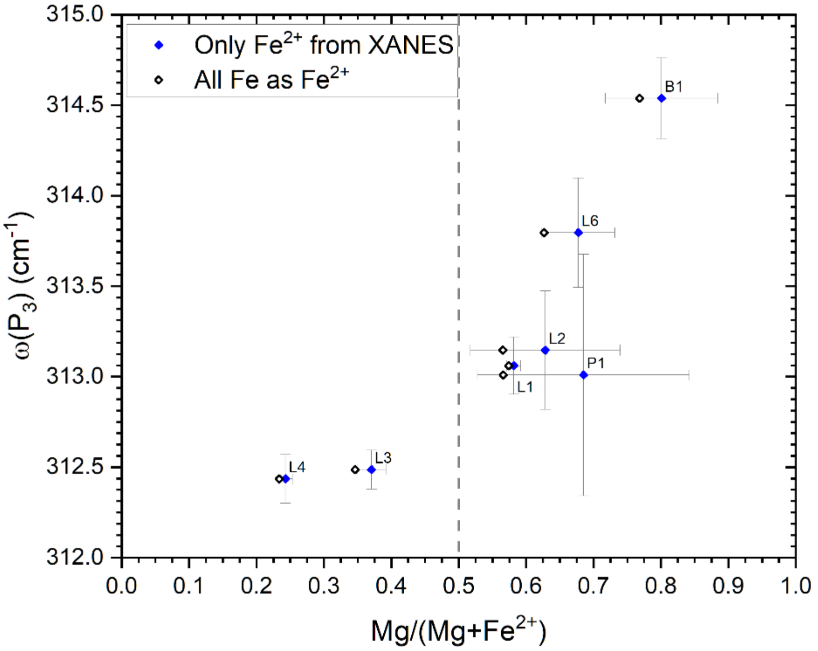

Figure 47: P_3 peak position for the seven dravite-schorl samples compared to the Mg/(Mg+Fe^{2+}) ratio obtained thanks to µXANES measurements (blue points). The black points represent the old data obtained considering all iron as Fe^{2+} in the magnesium-iron ratio.

The relative intensities of the P_1-P_2 peaks exhibit a linear correlation also when just Fe^{2+} from µXANES is considered, obtaining the new pattern shown in Figure 48. The linear trend can be used to retrieve the $Mg/(Mg+Fe^{2+})$ ratio through the formula

$$Mg/(Mg+Fe^{2+}) = \frac{I(P_1)/I(P_2) - 0.1}{1}$$

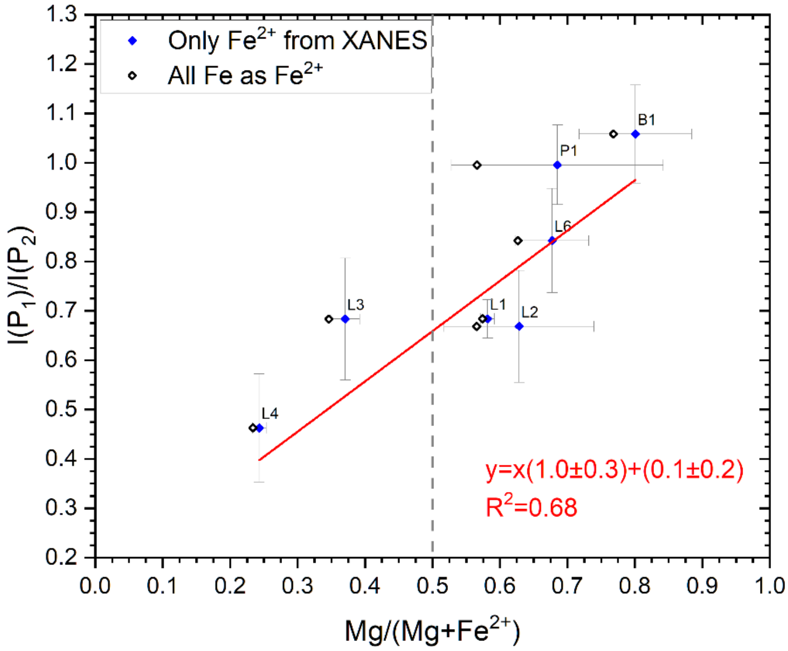

Figure 48: P_1-P_2 relative peak intensity for the seven dravite-schorl samples compared to the $Mg/(Mg+Fe^{2+})$ ratio obtained thanks to µXANES measurements (blue points). The black points represent the old data obtained considering all iron as Fe^{2+} in the magnesium-iron ratio. The red line represents the linear fitting of the new data.

The findings in the 200-315 cm^{-1} spectral range confirm that the Y-sites vibrational modes depend on the magnesium-ferrous iron ratio, predominantly found in the 6-coordinated sites of the dravite-schorl series. Utilising the P_2 peak position and the relative intensities of the P_1-P_2 peaks, we can also find information on the iron oxidation state, so enabling the calculation of the $Mg/(Mg+Fe^{2+})$ ratio.

The P_Z peak at 368 cm^{-1}, the dominant peak of ZO_6 octahedra vibrational modes, is typically independent of variations in the major Y-sites constituents. However, Figure 49 illustrates that variations in the $Mg/(Mg+Fe^{2+})$ ratio are directly correlated with the displacement of this peak position, as seen by the linear equation:

$$\omega(P_Z) = X(6.2 \pm 0.5) + (364.6 \pm 0.3) \qquad X = Mg/(Mg+Fe^{2+})$$

Prior studies have demonstrated that charge balance and bond distance refinement correlate with an actual disorder of Mg and Fe between Y and Z-sites, perhaps explaining this behaviour[10,11,177,190]. The proximity of the Z and Y-sites suggests that the vibrational modes of the ZO_6 octahedra may be influenced by the occupation of the Y-sites. Due to the lack of precise information regarding element distribution—which can only be acquired through structural refinement and the exact mean bond distance for each site—we are unable to ascertain whether this alteration is genuinely attributable to a Mg-Fe disorder between Y- and Z-sites or a neighbouring effect.

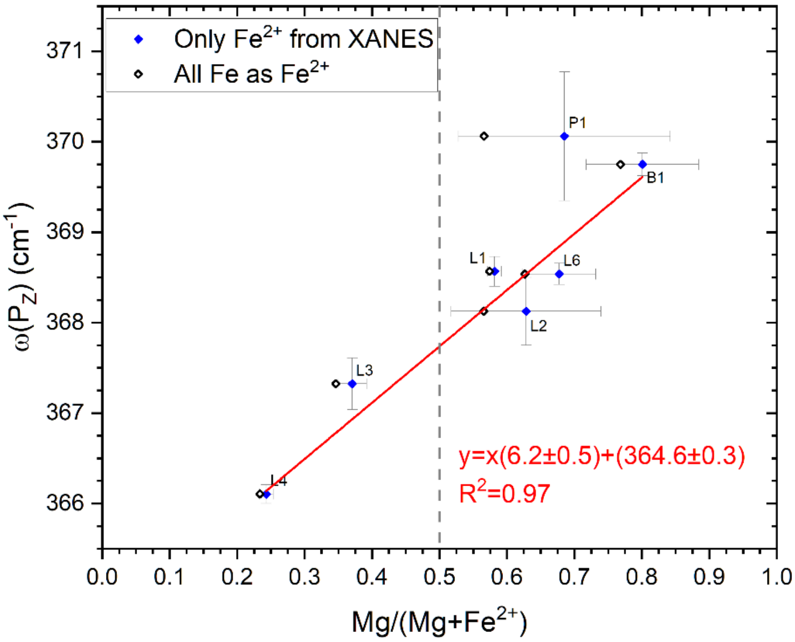

Figure 49: P_Z peak position for the seven dravite-schorl samples compared to the Mg/(Mg+Fe^{2+}) ratio obtained thanks to µXANES measurements (blue points). The black points represent the old data obtained considering all iron as Fe^{2+} in the magnesium-iron ratio. The red line represents the linear fitting of the new data.

In the OH stretching region (3450-3750 cm^{-1}), the $^{W}OH_3$ peak position, linked to the vibrational modes of the W-site, exhibits notable behaviour, adhering to the linear relationship depicted in Figure 50, now expressed by the formula

$$Mg/(Mg+Fe^{2+}) = \frac{\omega(^{W}OH_3) - 3716}{22}$$

where only the Fe^{2+} derived from XANES is factored into the magnesium-iron calculation. The proportion of Fe^{3+} in sample P1 markedly modifies the magnesium-iron ratio compared to prior data, aligning it more closely with the emerging trend. This result can be ascribed to the inherent reliance of ^{W}OH modes on the occupancy of the X and three Y-sites (X-YYY composition); thus, only iron located in Y-sites, particularly Fe^{2+} in our hypothesis, influences the $^{W}OH_3$ vibrational mode, while fluctuations in Fe^{3+} seem to have no impact on this peak.

The $^{W}OH_1$ peak in this region shows no discernible correlation with the magnesium-iron ratio, fluctuating between 3629 and 3639 cm^{-1} without a clear association to the Mg/(Mg+Fe^{2+}) ratio, as illustrated in Figure 51.

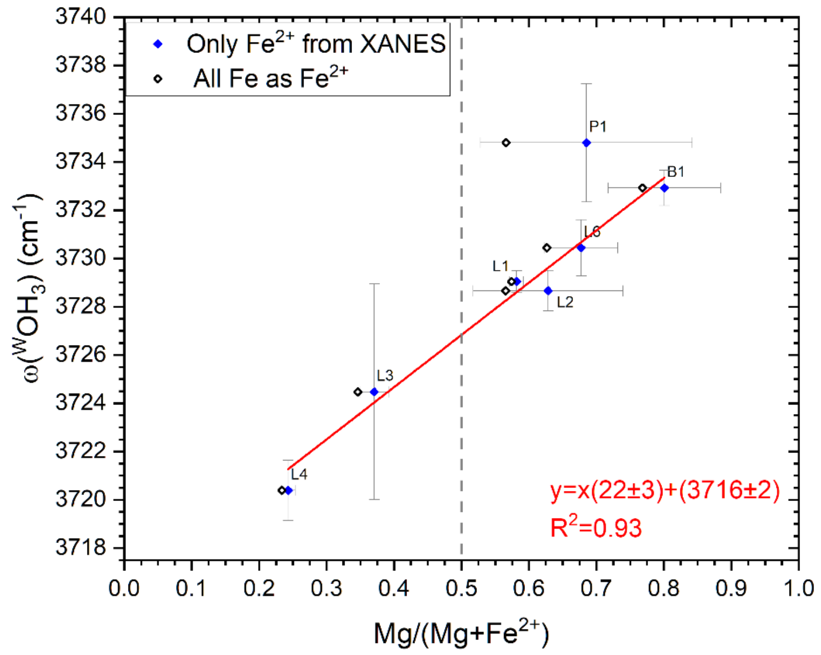

Figure 50: $^{W}OH_3$ peak position for the seven dravite-schorl samples compared to the Mg/(Mg+Fe^{2+}) ratio obtained thanks to µXANES measurements (blue points). The black points represent the old data obtained considering all iron as Fe^{2+} in the magnesium-iron ratio. The red line represents the linear fitting of the new data.

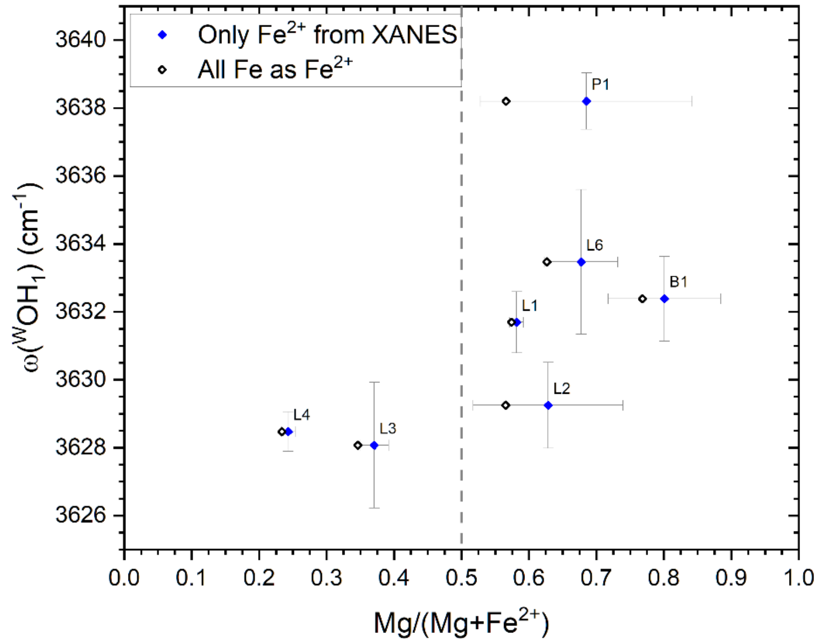

Figure 51: $^{W}OH_1$ peak position for the seven dravite-schorl samples compared to the Mg/(Mg+Fe^{2+}) ratio obtained thanks to µXANES measurements (blue points). The black points represent the old data obtained considering all iron as Fe^{2+} in the magnesium-iron ratio.

The Mg/(Mg+Fe) ratio obtained from the intensity of the ^{V}OH peaks, conversely, demonstrate in Figure 52 a superior correlation for the Mg/(Mg+Fe^{2+}) ratio, even for solid solution compositions rather than solely end-member compositions as previously found. This corroborates our hypothesis that Mg and Fe^{2+} are the principal elements in Y-sites, with any deviations from the one-to-one correlation attributed to potential disorder between Y- and Z-sites.

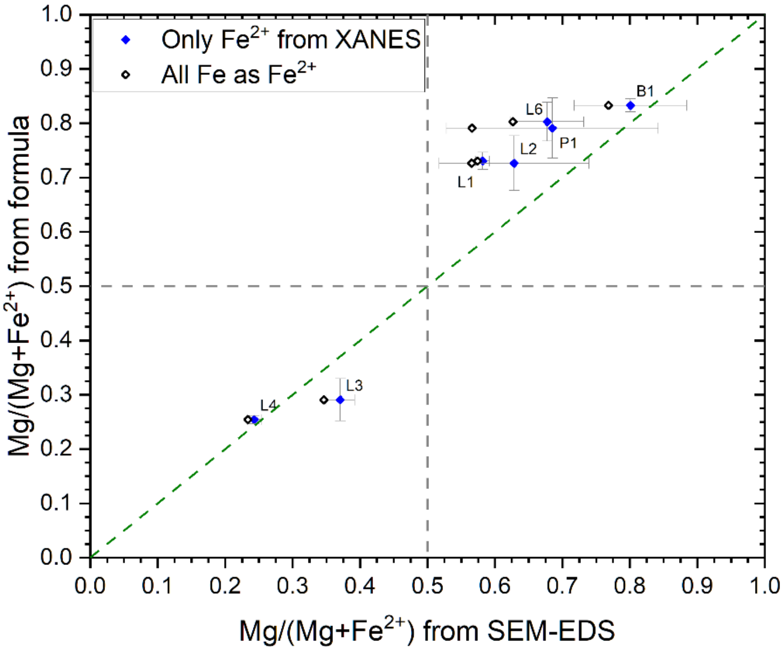

Figure 52: Comparison between the Mg/(Mg+Fe^{2+}) ratio in both dravite and schorl samples calculated from equation (1) and obtained from SEM-EDS with the Fe^{2+} concentration obtained from μXANES. The green dashed line represents the 1:1 correspondence.

The enhancement of the composition of the seven dravite-schorl samples, elucidated by the iron oxidation state data acquired through μXANES, reinforces the correlation with the Raman parameters, specifically regarding the P$_2$ position, the P$_1$-P$_2$ relative intensities, and the ^{W}OH$_3$ peak position previously identified, as well as the ^{V}OH vibrational modes intensity formula posited by Watenphul[129]. This substantiates that Fe^{2+} predominantly resides in Y-sites and should be the sole iron speciation factored into the magnesium-iron ratio calculation.

Portable Raman Results For *In Situ* Application

To assess the potential of employing results obtained for dravite and schorl by μRaman spectroscopy for *in situ* investigation, we conduct portable Raman measurements on eight of the fifteen previously examined tourmalines: B1, L1, L2, L3, L4, L6, P1, and T1. The other samples were not examined because of their small dimensions and irregular shape. Figure 53 illustrates that the low-frequency region of the Raman spectra resembles that obtained with μRaman, while the OH stretching region exhibits reduced intensity in the characteristic OH bands. This discrepancy arises from the instrument's hardware, which is inadequate for effective analysis in this region due to the use of a 532 nm excitation laser that fails to generate the same resonance effect as the 473 nm laser, coupled with a detector that is inefficient in this spectral range, as it is optimised for superior performance in the low-frequency region, despite the spectral range extending from 120 to 4000 cm^{-1}.

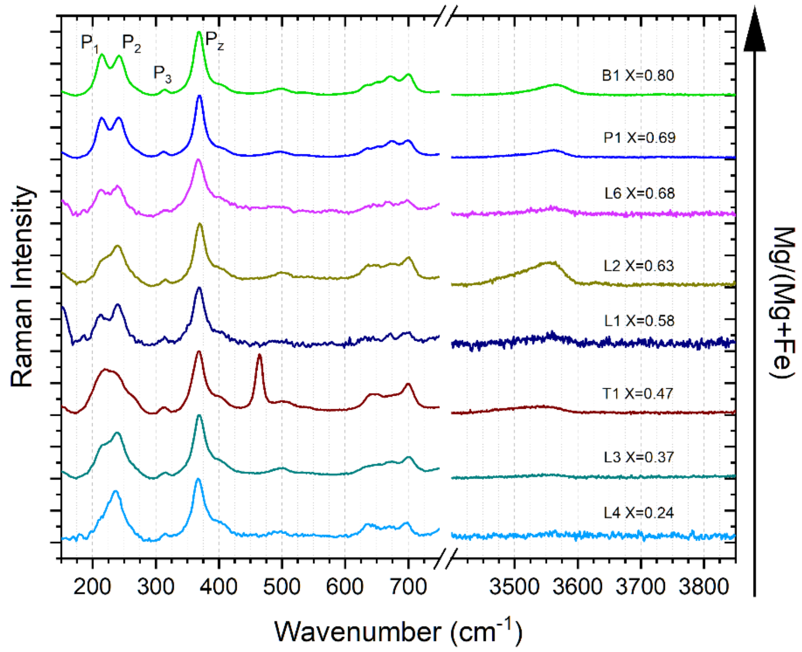

Figure 53: Raman spectra of the eight dravite-schorl samples studied with portable Raman in both low-frequency and OH stretching regions.

The values presented in Table 14 indicate that in the low-frequency band, the peaks in the Raman spectra acquired with the portable instrument are analogous to those previously obtained with the bench-top apparatus for both YO$_6$ and ZO$_6$ vibrational modes. The distinctive shape of the YO$_6$ vibrational mode peaks enables the rapid differentiation between dravite and schorl, as previously outlined. Furthermore, the P$_2$ peak position and the P$_1$-P$_2$ relative intensity enable the determination of the Mg/(Mg+Fe^{2+}) ratio using portable Raman spectroscopy, facilitating *in situ* study directly on outcrops.

Sample	**$\omega(P_1)$ [cm^{-1}]**	**$\omega(P_{1/2})$ [cm^{-1}]**	**$\omega(P_2)$ [cm^{-1}]**	**$I(P_1)/I(P_2)$**	**$\omega(P_Z)$ [cm^{-1}]**
B1	214.3	228.1	242.2	1.07	368.4
L1	213.7	231.9	240.6	0.92	367.9
L2	216.1	228.7	239.7	0.59	368.7
L3	211.6	222.9	238.2	0.65	368.6
L4	210.9	222.5	237.1	0.39	366.9
L6	212.3	224.2	240.3	0.91	367.3
P1	214.1	225.9	241.0	0.86	369.0
T1	213.8	222.4	236.5	0.98	368.3

Table 14: Raman parameters of peaks in the low-frequency region for the eight dravite-schorl samples studied with portable Raman.

Influence Of Orientation In The Raman Spectrum Of Dravite And Schorl

All dravite and schorl samples were examined in the $\bar{y}(zz)y$ configuration according to Porto's notation, with incident light polarised parallel to the crystal c-axis. This approach emphasised the A_1 vibrational modes[128,129] while also capturing the configuration with the highest intensity for the OH stretching modes, thereby facilitating the investigation of the weak ^{W}OH peaks (Figure 54). This arrangement for each measurement on the examined samples ensured that the relative intensities of the Raman peaks remained unaffected.

The determination of the c-axis orientation in dravite and schorl minerals is feasible owing to several features.

- The elongation of the crystal along the c-axis is readily observable.
- In tiny or fractured crystals, surface stripes align parallel to the c-axis.
- In semi-transparent crystals, the pronounced pleochroism of tourmaline is distinctly observable, permitting polarised light to pass just when aligned with the c-axis.

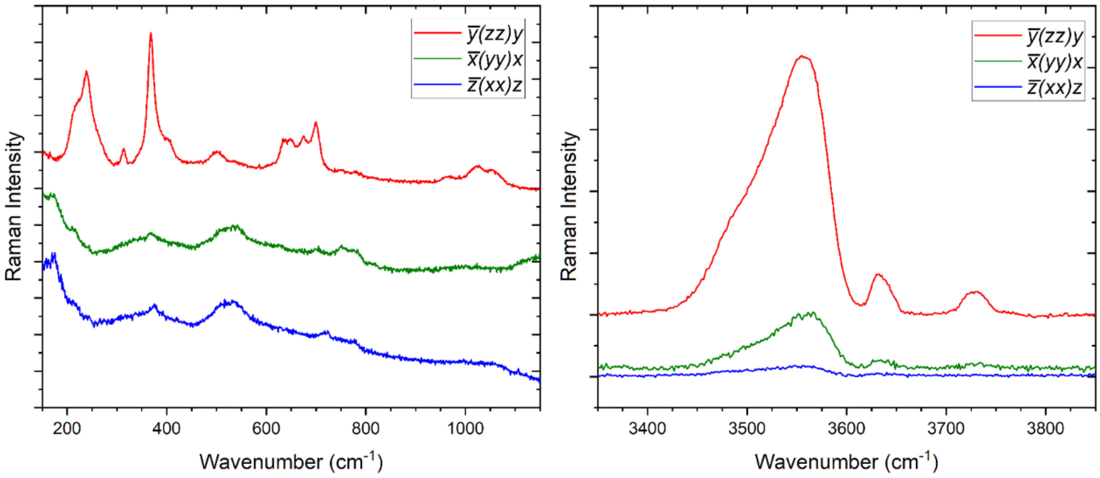

Figure 54: Polarised Raman spectra in different perpendicular configurations obtained on sample L2.

Chapter 4

Elbaite Gemstones

Elbaite, generally represented by the formula $NaLi_{1.5}Al_{1.5}Al_6Si_6O_{18}(BO_3)_3(OH)_3OH$, is a highly esteemed tourmaline species, renowned for its **extensive colour spectrum** resulting from the presence of many chromophoric components. Impurities of **transition elements**, including Fe^{2+}, Fe^{3+}, Mn^{2+}, Mn^{3+}, Ti^{4+}, Cu^{2+}, V^{3+}, and Cr^{3+}, function as **chromophores**; hence, their concentration is closely linked to the ultimate colouration of the crystal and variations within the same mineral[53]. Different varieties related to the colours, and thus the chromophores concentration, are recognised by gemmologists:

- **Achroite**, no colour, no specific chromophores.
- **Rubellite**, pink and red, Mn^{3+}.
- **Canary**, yellow to yellowish-green, Mn^{2+} or Mn^{2+} and Ti^{4+}.
- **Verdelite**, green, Fe^{2+} and Fe^{3+} or Fe^{2+} and Ti^{4+}.
- **Indicolite**, blue, Fe^{2+} or Fe^{2+} and Fe^{3+}.
- **Paraíba-type**, "neon" blue, Cu^{2+}.

Our primary attention among these varieties was on “neon” blue, green and pink elbaite, specifically the Paraíba-type, verdelite and rubellite varieties.

Colour variations are characteristic not just of distinct gemstones but may also manifest inside a single crystal. Specifically, regarding pink-green elbaite, these are referred to as **watermelon** tourmalines because of their similarity to the *Citrullus lanatus* fruit, including a pink core and a green rim. We will thus divide the discussion between the Paraíba-type variety and the pink-green watermelon elbaite. Part of the results described in this chapter, especially the ones on the Paraíba-type gemstones, are published on *Minerals*[191].

Elbaite Species Identification

Prior to examining the chromophores, it is essential to determine the tourmaline species to which the tested gems belong. A single variety of tourmaline can encompass multiple chemical species, such as **elbaite** and **liddicoatite** (another tourmaline species represented by the end-member formula $CaLi_2AlAl_6Si_6O_{18}(BO_3)_3(OH)_3OH$) plus the relative “**fluor-**” species, with fluorine substituting OH groups in W-site, in Paraíba-type tourmalines. The identification of Li-tourmaline species, along with other tourmaline varieties, is crucial for gemmologists, since it can affect the final market value of the gems. Complete characterisation can be accomplished by laser ablation inductively coupled plasma mass spectrometry (LA-ICP-MS)[73], although this method is destructive.

Consequently, Raman spectroscopy serves as an appropriate non-destructive method for the characterisation of tourmaline gemstones species[192]. The primary concern with this method pertains to **polarisation effects**[12,52,132,193]: the relative intensities of the Raman bands may vary across different crystallographic orientations, influenced by the distinct activation of the A_1 and E Raman modes based on orientation. As a result, the orientation of crystal axes with relation to the polarisation of incident light might emphasise one vibrational mode over another. Moreover, as tourmalines are polar crystals, certain Raman band positions may exhibit a minor dependence on orientation due to the longitudinal optic-transverse optic (LO-TO) splitting phenomenon[129,194]. The reliance of Raman spectrum parameters on orientation can complicate the characterisation of tourmalines, especially when mounted, as the orientation for measurement cannot be selected freely. Furthermore, in cut gemstones, the absence of the characteristic elongation of tourmaline crystals along the c-axis further complicates the determination of the axes orientation.

Because of this, we want to identify distinct tourmaline species, specifically elbaite and liddicoatite, using their Raman spectra, regardless of the orientation of the crystal axes relative to the polarisation of the input laser beam. The OH stretching modes are helpful for this aim as their positions remain unaffected by orientation.

We conducted polarised Raman measurements on an elbaite and a liddicoatite gemstone in three distinct orientations: $\boldsymbol{\bar{x}(yy)x}$, $\boldsymbol{\bar{y}(zz)y}$, and $\boldsymbol{\bar{z}(xx)z}$. As highlighted in Figure 55, the $\bar{y}(zz)y$ configuration (red spectrum) only displays the A_1 modes, whereas the other two orientations exhibit a linear combination of A_1 and E modes. In the low-frequency region, the peak position varies strongly based on orientation, with the $\bar{x}(yy)x$ and $\bar{z}(xx)z$ orientations exhibiting similarities between elbaite and liddicoatite, while the $\bar{y}(zz)y$ orientation reveals significant differences in the spectra of the two species, particularly in the 200-300 cm^{-1} range. Elbaite typically exhibits three peaks of decreasing intensities, corresponding to wavenumbers of 222, 246, and 271 cm^{-1}. Liddicoatite has two slightly overlapping peaks with comparable intensity at 227 and 242 cm^{-1}. We already know that the peaks in this region correspond to the vibrational modes of YO_6 octahedra; nevertheless, given that only a minor variation in the lithium-aluminium relative concentration is expected at the Y-sites (ranging from 0.5 in elbaite to 0.67 in liddicoatite end-members), these vibrational modes should not be substantially affected by these minor changes in Y-sites composition. In this case, the YO_6 vibrational modes may be also affected by the occupation of the X-site, with varying relative concentration of sodium and calcium between the two species.

However, these differences between elbaite and liddicoatite Raman spectra are clearly visible only in the $\bar{y}(zz)y$ orientation. The OH stretching region has an interesting behaviour: the peak positions remain unaffected by orientation, with only their relative intensities undergoing modifications. Consequently, elbaite exhibits identical OH stretching mode positions across all the three studied orientations, similar to liddicoatite; hence, the peaks positions serve as a discriminating data for the two tourmaline species. Specifically, we concentrated on the main ^{V}OH band situated approximately at 3590 cm^{-1} in elbaite and around 3610 cm^{-1} in liddicoatite; therefore, the $\mathbf{3600\ cm^{-1}}$ threshold can be employed to differentiate between elbaite and liddicoatite: tourmaline gemstones exhibiting the principal ^{V}OH band below this threshold are classified as elbaite, while those displaying it above are identified as liddicoatite.

Consequently, a single ^{V}OH Raman band enables the differentiation of elbaite and liddicoatite gemstones, even in arbitrary orientations, and this finding can be highly beneficial for the non-destructive assessment of tourmaline gemstone species.

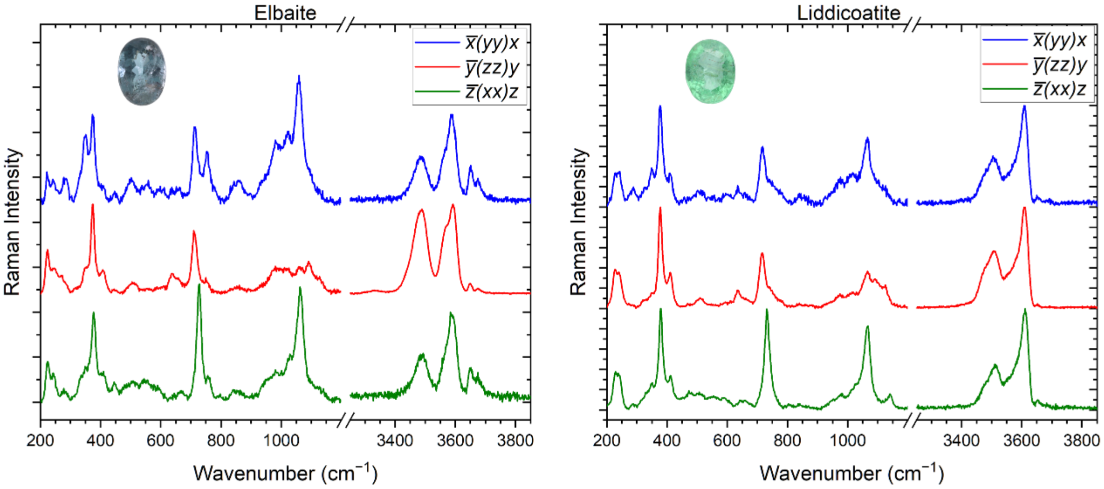

Figure 55: Normalised Raman spectra of elbaite and liddicoatite obtained in three perpendicular orientations: $\bar{x}(yy)x$, $\bar{y}(zz)y$, *and* $\bar{z}(xx)z$.

Paraíba-type Gemstones

Having distinguished various species of tourmaline gemstones, we may now concentrate on quantifying the amount of chromophores in these gems. Regarding Paraíba-type tourmalines, we want to study the **copper** concentration, which confers their characteristic "neon" blue colour, as well as the presence of **iron**, which may introduce shades of green in the specimens that can influence their market value.

Fifteen gem-quality Li-tourmalines, illustrated in Figure 56 and detailed in Table 15, from the **Laboratoire Français de Gemmologie** (LFG), were analysed using **EDXRF** to determine the chemical composition of the samples. The acquired data are presented in Table 16 as oxide percentages, and a.p.f.u. concentrations were determined using the same methodology outlined in the previous chapter for the SEM-EDS data collected from dravite and schorl samples. Since we had not the possibility to perform XANES measurements on these samples, all the quantified iron was expressed as FeO. Furthermore, B, Li, F, and water are not measurable with this method and, consequently, B_2O_3 was arbitrary set at 11%, Li_2O at 3%, H_2O at 4%, and F at 1% for each measurement. This approximation enables the identification of the principal tourmaline group for each sample with Li set up as the predominant element in Y-sites (~1.8 a.p.f.u. for each sample). We derived the X-site occupation fixing the sum Na + K + Ca + X-vacant to 1 a.p.f.u. and displayed the ternary system for the principal tourmaline group as depicted in Figure 57.

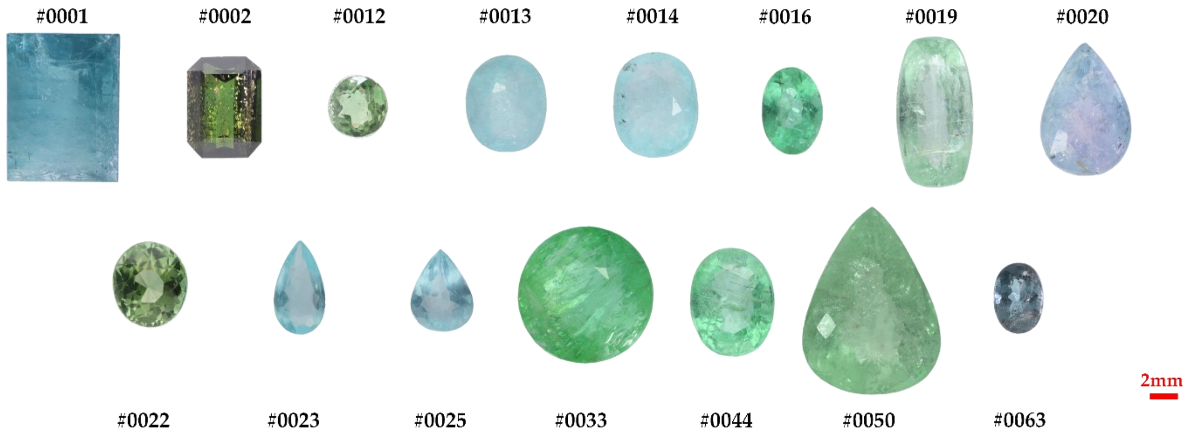

Figure 56: The fifteen blue-to-green Li-tourmaline gemstones from LFG analysed.

Sample	Provenance	Weight (ct)	Dimensions (mm)	Colour	Shape-cut
#0001	Nigeria	2.584	9.19 x 7.04 x 4.83	Greenish blue	Rectangular-step
#0002	Brazil	0.738	6.32 x 4.65 x 2.97	Dark greyish green	Rectangular corner cut-step
#0012	Nigeria	0.460	4.45 x 4.60 x 3.20	Yellowish green	Round-brillant
#0013	Nigeria	0.746	6.01 x 4.88 x 3.51	Light greenish blue	Oval-brillant
#0014	Nigeria	0.864	6.54 x 5.15 x 3.15	Light greenish blue	Oval-brillant
#0016	Mozambique	0.352	5.41 x 3.79 x 2.54	Bluish green	Oval-brillant
#0019	Mozambique	1.278	9.26 x 4.69 x 3.59	Light bluish green	Cushion-brillant
#0020	Nigeria	1.526	8.82 x 5.97 x 4.67	Light purplish blue	Pear-brillant
#0022	Nigeria	0.627	5.36 x 4.76 x 3.77	Yellowish green	Oval-brillant
#0023	Nigeria	0.190	5.82 x 3.21 x 1.62	Light greenish blue	Pear-brillant
#0025	Nigeria	0.269	5.09 x 3.89 x 2.43	Light greenish blue	Pear-brillant
#0033	Mozambique	2.618	8.38 x 8.50 x 4.11	Bluish green	Round-brillant
#0044	Mozambique	0.903	6.72 x 5.23 x 3.63	Light bluish green	Oval-brillant
#0050	Mozambique	3.424	11.63 x 8.59 x 4.11	Bluish green	Pear-brillant
#0063	Brazil	0.219	4.49 x 3.17 x 2.29	Greyish blue green	Oval-brillant

Table 15: List of the fifteen blue-to-green Li-tourmaline gemstones from LFG with general information and characteristics.

Sample	#0001	#0002	#0012	#0013	#0014	#0016	#0019	#0020	#0022	#0023	#0025	#0033	#0044	#0050	#0063
Na_2O	3.73(6)	2.20(8)	2.24(7)	2.78(10)	1.96(6)	2.76(8)	4.16(7)	3.01(6)	2.54(7)	1.42(8)	1.41(8)	3.70(7)	1.74(6)	3.92(6)	3.061(8)
MgO	0.65(2)	1.11(3)	0.81(2)	1.12(3)	0.75(2)	1.13(3)	0.62(2)	0.59(2)	0.85(2)	0.43(2)	0.45(2)	0.55(2)	0.64(2)	0.57(2)	1.06(3)
Al_2O_3	36.30(6)	34.10(7)	36.53(7)	36.46(10)	36.90(7)	34.57(7)	34.44(6)	38.84(6)	35.82(7)	33.57(8)	33.90(8)	35.38(6)	33.00(7)	36.00(6)	34.84(8)
SiO_2	36.69(8)	36.40(10)	38.73(10)	37.3(2)	38.84(9)	37.0(1)	36.36(8)	37.77(8)	38.68(10)	41.8(1)	42.4(1)	36.77(8)	37.69(10)	36.54(7)	36.4(1)
K_2O	0.014(1)	0.040(2)	0.050(2)	0.114(4)	0.040(2)	0.056(3)	0.025(1)	0.018(1)	0.089(4)	0.048(3)	0.053(3)	0.027(1)	0.074(2)	0.016(2)	0.120(4)
CaO	0.251(3)	0.328(4)	0.543(6)	0.802(9)	0.896(7)	0.613(6)	0.199(3)	0.352(4)	0.716(6)	1.30(1)	1.31(1)	0.236(3)	3.87(1)	0.051(2)	0.473(6)
TiO_2	0	0.128(3)	0.014(1)	0.008(2)	0.0015(7)	0.062(3)	0.032(2)	0	0.021(2)	0.001(1)	0	0.048(2)	0.031(2)	0.018(1)	0.023(2)
V_2O_3	0	0.003(1)	0.0015(7)	0	0	0	0.0017(8)	0	0	0	0	0.0013(8)	0	0	0.002(1)
Cr_2O_3	0	0	0	0	0	0	0	0	0	0	0	0.0014(6)	0	0	0.031(1)
MnO	0.502(5)	1.69(1)	0.336(5)	1.44(1)	1.149(7)	3.64(2)	4.94(1)	0.182(3)	0.418(5)	1.47(1)	0.675(8)	3.91(1)	3.14(1)	3.65(1)	3.17(1)
FeO	2.713(9)	3.36(1)	1.321(8)	0.012(3)	0.025(2)	0.139(5)	0	0.024(1)	1.433(8)	0.014(3)	0	0.014(3)	0.082(4)	0.025(3)	0.465(7)
CuO	0	1.440(4)	0.126(1)	0.446(3)	0.271(2)	0.762(3)	0.115(1)	0.151(1)	0.122(1)	0.547(3)	0.481(3)	0.315(2)	0.512(2)	0.158(1)	0.714(3)
ZnO	0.130(1)	0.133(1)	0.226(1)	0.309(2)	0.0042(3)	0.106(1)	0.0014(2)	0.0035(2)	0.215(1)	0.140(1)	0.0031(4)	0.0013(2)	0.0014(3)	0	0.469(2)
Ga_2O_3	0.0170(3)	0.0107(5)	0.0188(5)	0.0220(7)	0.0221(4)	0.0198(5)	0.0552(6)	0.0197(4)	0.0205(5)	0.0241(7)	0.0206(6)	0.0363(5)	0.0541(7)	0.0425(5)	0.0247(6)
PbO	0.0085(2)	0.0140(4)	0.0360(5)	0.118(1)	0.0795(6)	0.0059(3)	0.0059(3)	0.0198(4)	0.0382(5)	0.179(1)	0.202(1)	0.0034(2)	0.0530(6)	0.0012(1)	0.0101(4)
Bi_2O_3	0	0.0536(6)	0.0289(4)	0.0288(6)	0.0600(6)	0.0956(7)	0.0565(5)	0.0188(3)	0.0302(4)	0.0463(7)	0.0670(8)	0.0177(3)	0.1056(7)	0.0055(2)	0.1780(8)
X-Site															
Na	1.076	0.641	0.637	0.797	0.557	0.799	1.212	0.854	0.725	0.403	0.397	1.072	0.506	1.135	0.891
K	0.003	0.008	0.009	0.022	0.007	0.011	0.005	0.003	0.017	0.009	0.010	0.005	0.014	0.003	0.023
Ca	0.040	0.053	0.086	0.127	0.141	0.098	0.032	0.055	0.113	0.204	0.205	0.038	0.622	0.008	0.076
X-□	0	0.298	0.268	0.054	0.295	0.092	0	0.088	0.145	0.384	0.388	0	0	0	0.010
T-Site															
Si	5.463	5.484	5.692	5.527	5.696	5.542	5.470	5.524	5.703	6.128	6.187	5.497	5.652	5.454	5.460
Al	0.537	0.516	0.308	0.473	0.304	0.458	0.530	0.476	0.297	0	0	0.503	0.348	0.546	0.540
Z+Y-Sites															
Al	6.166	5.807	6.328	6.261	6.377	5.948	5.851	6.662	6.225	5.800	5.827	6.043	5.787	6.105	5.911
Li	1.796	1.818	1.773	1.786	1.769	1.805	1.815	1.765	1.779	1.768	1.759	1.803	1.809	1.801	1.811
Fe	0.338	0.423	0.162	0.001	0.003	0.017	0	0.003	0.177	0.002	0	0.002	0.010	0.003	0.058
Cu	0	0.164	0.014	0.050	0.030	0.086	0.013	0.017	0.014	0.061	0.053	0.036	0.058	0.018	0.081
Mn	0.063	0.215	0.042	0.181	0.143	0.461	0.629	0.023	0.052	0.183	0.083	0.495	0.399	0.461	0.403
Mg	0.144	0.25	0.177	0.248	0.164	0.253	0.139	0.128	0.188	0.094	0.097	0.121	0.143	0.127	0.236
Ti	0	0.015	0.002	0.001	0.001	0.007	0.004	0	0.002	0.001	0	0.005	0.003	0.002	0.003
Zn	0.014	0.015	0.025	0.034	0.001	0.012	0.001	0.001	0.023	0.015	0.001	0.001	0.001	0	0.052
V	0	0.0004	0.0002	0	0	0	0.0002	0	0	0	0	0.0001	0	0	0.0002
Cr	0	0	0	0	0	0	0	0	0	0	0	0.0001	0	0	0.004
Ga	0.00163	0.00103	0.00178	0.00209	0.00208	0.0019	0.00533	0.00184	0.00194	0.00227	0.00192	0.00348	0.00524	0.00407	0.00235
Pb	0.0003	0.0006	0.001	0.005	0.003	0.0002	0.0002	0.001	0.002	0.007	0.008	0.0001	0.002	0.0001	0.0004
Bi	0	0.002	0.001	0.001	0.002	0.004	0.002	0.0007	0.001	0.002	0.003	0.0007	0.004	0.0002	0.007
V-Site															
OH	3.000	3.000	3.000	3.000	3.000	3.000	3.000	3.000	3.000	3.000	3.000	3.000	3.000	3.000	3.000
W-Site															
OH	0.972	1.020	0.922	0.951	0.9126	0.992	1.014	0.903	0.934	0.911	0.891	0.988	1.001	0.982	1.006
F	0.256	0.259	0.252	0.254	0.2518	0.257	0.258	0.251	0.253	0.252	0.250	0.257	0.257	0.256	0.258

Table 16: Oxide concentration in the fifteen Li-tourmalines gemstone samples obtained from EDXRF analyses and calculated a.p.f.u. with different sites occupancies obtained by normalising Y+Z+T-sites content to 15 a.p.f.u.

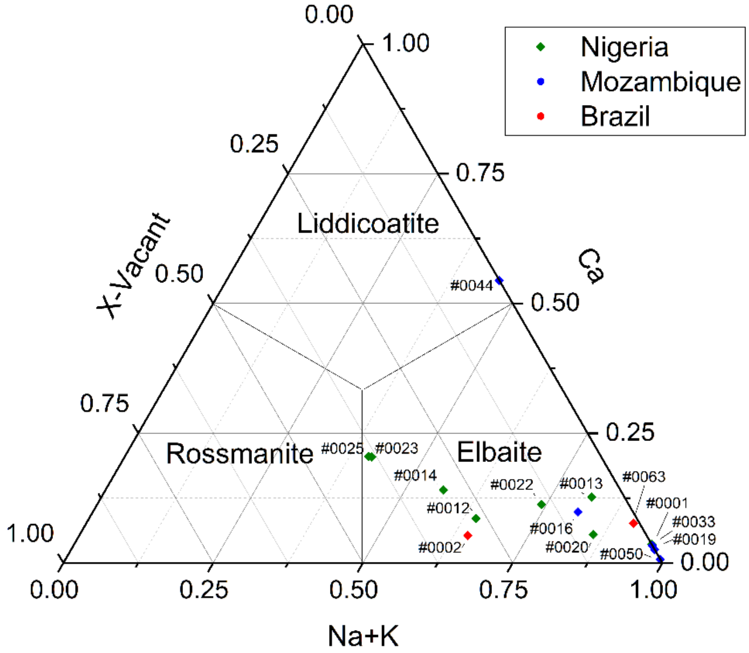

Figure 57: Ternary illustration of X-site occupancy for the fifteen Li-tourmaline gemstones. Distinct point colours denote varying geographical origins: green points represent Nigeria, blue points indicate Mozambique, and red points denote Brazil. Only one sample (#0044) is classified inside the calcic group and may therefore be identified as liddicoatite, whereas all other samples belong to the alkali group, categorising them as elbaite species.

All analysed samples, with the exception of #0044, are categorised within the **alkali group** and may be identified as elbaite. Sample #0044, instead, exhibits an elevated Ca concentration (0.6 a.p.f.u.); hence, it is classified within the **calcic group** and the liddicoatite species. EDXRF analysis is not reliable for quantifying Na; hence, these data should be interpreted with caution. Furthermore, F cannot be quantified using this technique, therefore preventing the differentiation between fluor-elbaite and elbaite, as well as between fluor-liddicoatite and liddicoatite species. The analysed samples exhibit differing copper and iron concentrations; sample #0001 has a copper content below the instrument's detection limit, whereas sample #0002 displays the highest copper content of 1.440% CuO. These two samples exhibit comparatively elevated FeO levels, whereas samples #0019 and #0025 display iron content under the detection threshold. The samples exhibit varying concentrations of trace elements such as Ti, V, Cr, Mg, Mn, Zn, Ga, Pb, and Bi (refer to Table 16).

Raman spectra were obtained from all samples in various crystallographic orientations to evaluate the possibility for differentiating elbaite from liddicoatite tourmalines in random orientations and to find correlations with the chromophore concentration. Raman spectra were studied from 200 to 1200 cm^{-1} (fingerprint region) and from 3250 to 3800 cm^{-1} (OH stretching region). Figure 58 displays a spectrum for each sample in a random orientation. Elbaite and liddicoatite can be differentiated based on the placements of the peaks in the OH stretching region, as previously established. Only the #0044 sample exhibits the characteristic peaks of liddicoatite, with the principal ^{V}OH band situated at 3610.7 cm^{-1}. In contrast, all other samples display Raman spectra characteristic of elbaite, with the main ^{V}OH band ranging from 3590 to

3595 cm^{-1}, consistent with the previously reported EDXRF results. Certain elbaite gems have an **extra band** at 3560 cm^{-1}, notably in samples #0001 and #0002. This band appears to be associated with the elevated iron concentration, as confirmed by EDXRF analysis, exhibiting a structure dominated by Fe and secondary Al in the Y-sites, along with Al in the Z-sites[129]. We investigated potential links between alterations in peak characteristics and fluctuations in the Cu/(Cu+Fe) ratio to assess the efficacy of Raman spectroscopy for identifying Paraíba-type tourmalines. Nonetheless, no clear correlations emerged with any parameter, except for the additional band at 3560 cm^{-1} in the OH region, which was present in the Fe-rich samples.

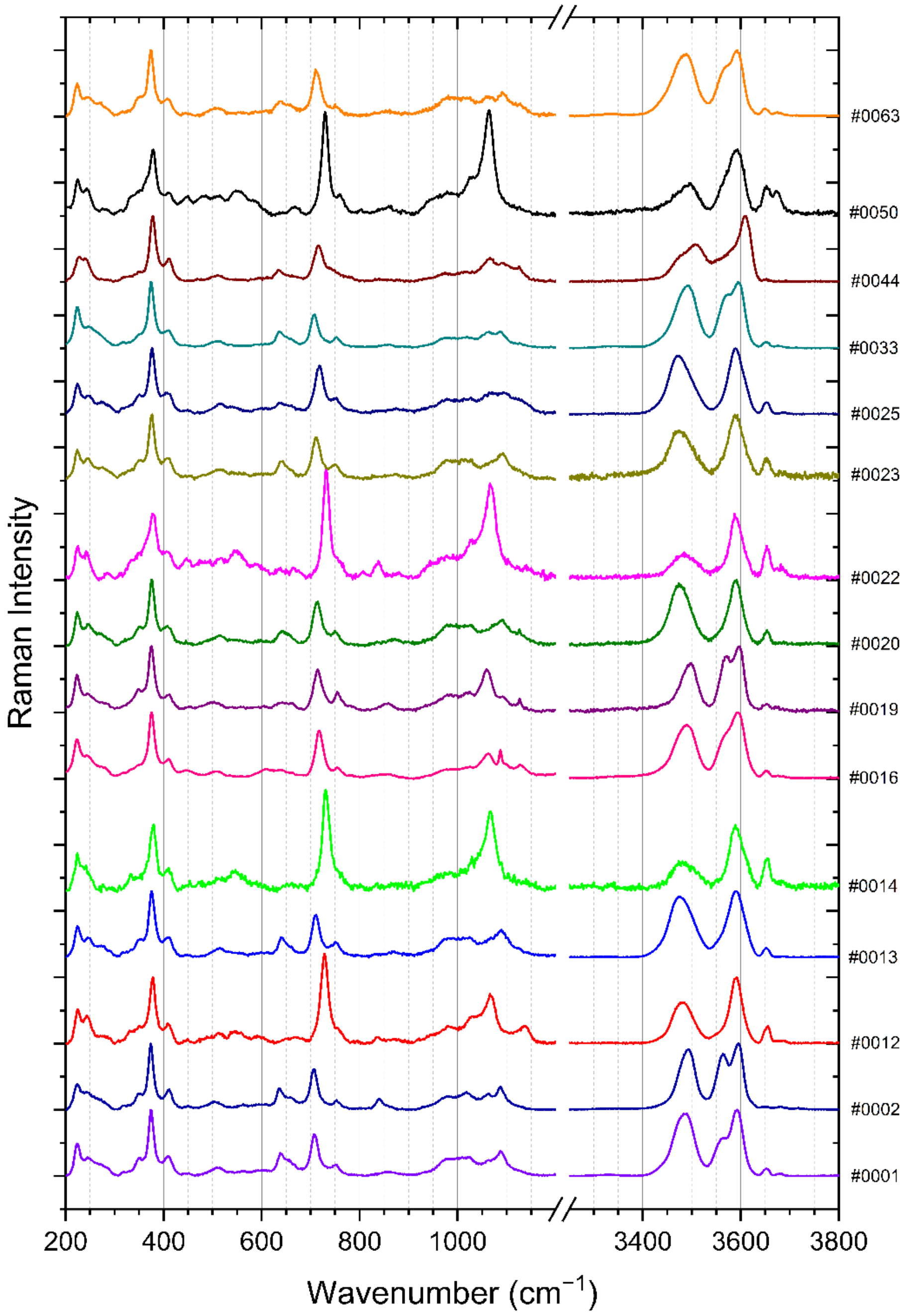

Figure 58: Normalised Raman spectra of the fifteen Li-tourmalines gemstones obtained in random orientation.

In this instance, an alternative non-destructive technique, **UV-VIS-NIR spectroscopy**, serves as an effective instrument for identifying Paraíba-type tourmalines[53,70,192]. Cu-bearing tourmalines exhibit two prominent absorption bands near **700 nm** and **900 nm**, with the latter being more pronounced due to Cu^{2+}. In contrast, Fe-rich tourmalines display a singular intense band at **720 nm** attributed to Fe^{2+}, occasionally accompanied by a broad band near 520 nm and several sharp bands around 415 nm, resulting from Mn^{3+} and Mn^{2+}, respectively[58,60]. Figure 59 illustrates the UV-VIS-NIR absorption spectra for all tourmalines examined in this study, revealing a prominent absorption band around 720 nm attributed to Fe^{2+} in four samples (#0001, #0002, #0012 and #0022). Sample #0002 exhibited the highest copper content; nevertheless, under optical microscopy, this sample displayed platelets, previously identified as native copper[59,66–68], as illustrated in Figure 56. The elevated copper level is presumably associated with the inclusions and does not contribute to the sample's colouration, which is predominantly influenced by iron, yielding the characteristic green tones. Therefore, this tourmaline cannot be classified as Paraíba-type, even with elevated copper content, as copper must serve as the primary chromophore rather than merely existing in high concentration.

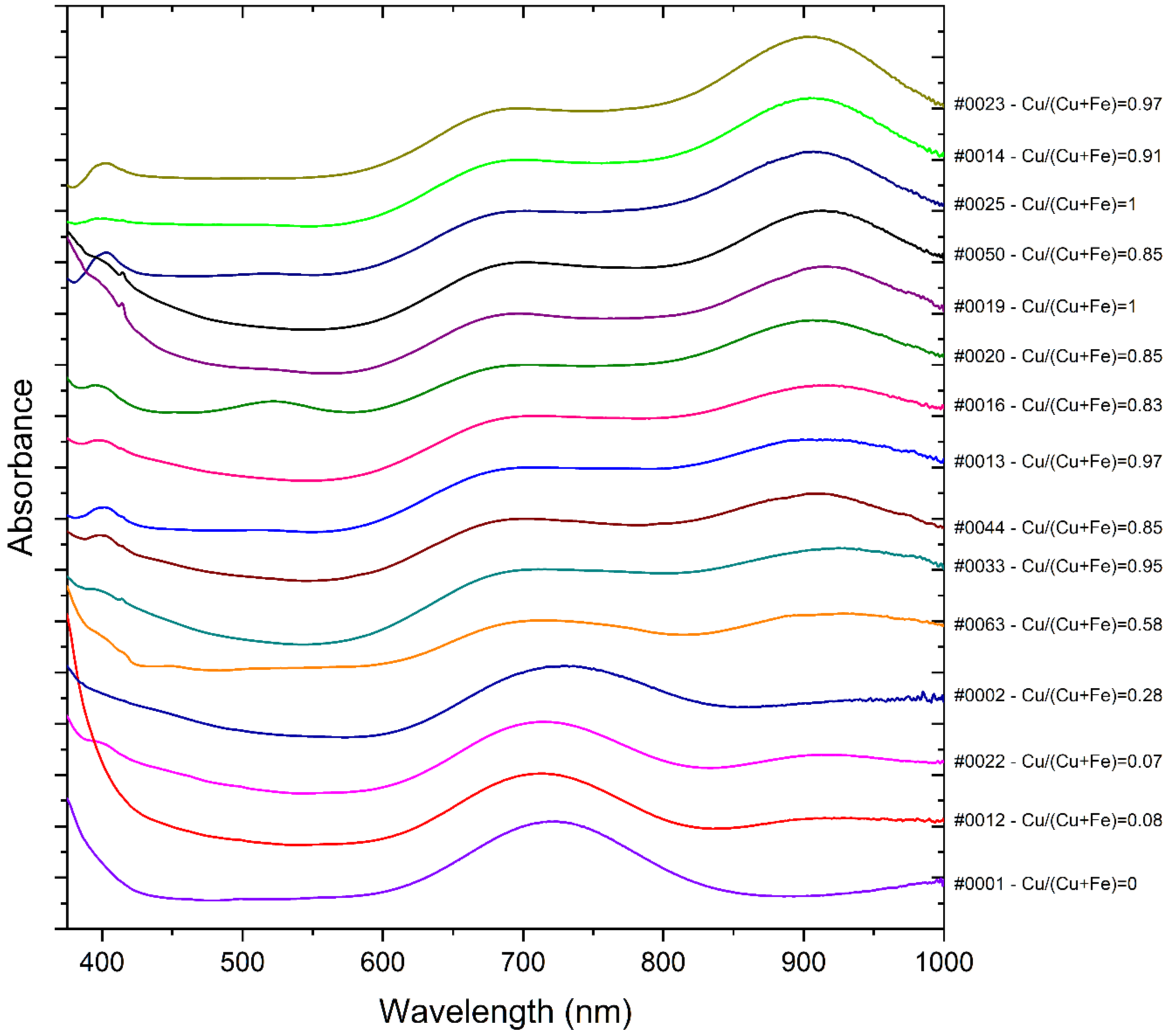

Figure 59: Normalised UV-VIS-NIR spectra for the fifteen Li-tourmaline gemstones ordered by increasing Cu/(Cu+Fe) values.

In the remaining samples, absorption bands at approximately 700 and 900 nm are detected with differing relative intensities. We examined the behaviour of the relative absorbance values at 900 nm and 700 nm (**A_{900}/A_{700}**) in randomly orientated spectra concerning the relative abundance of copper and iron (Cu/(Cu+Fe)) derived from EDXRF analysis (all the data are reported in Table 17). Figure 60 distinctly illustrates two clusters: the first comprises samples with Cu/(Cu+Fe)>0.5 and $A_{900}/A_{700}>1$, whereas the second encompasses samples with Cu/(Cu+Fe)<0.5 and $A_{900}/A_{700}<1$. This may be beneficial for distinguishing Paraíba-type tourmalines from similarly coloured tourmalines that do not qualify as Paraíba-type: in this case, the samples #0001, #0002, #0012, and #0022 cannot be classified as Paraíba-type tourmalines. A significant concern, however, is to iron-rich copper-bearing tourmaline: it has been proposed that samples exhibiting an absorption band at 700 nm, surpassing the 900 nm absorption band in the **polarised spectrum** (acquired using UV-VIS-NIR spectrometer with the incident light polarised parallel to the crystal c axis), should not be classified as Paraíba-type tourmaline[57]. In our analysis, sample #0063 exhibits absorption bands associated with Fe and Cu of comparable intensity (in orange in Figure 59). Consequently, we propose that only samples exhibiting Cu/(Cu+Fe)>0.6 and $A_{900}/A_{700}>1.1$ (in randomly orientated spectra) can be classified as Paraíba-type tourmalines.

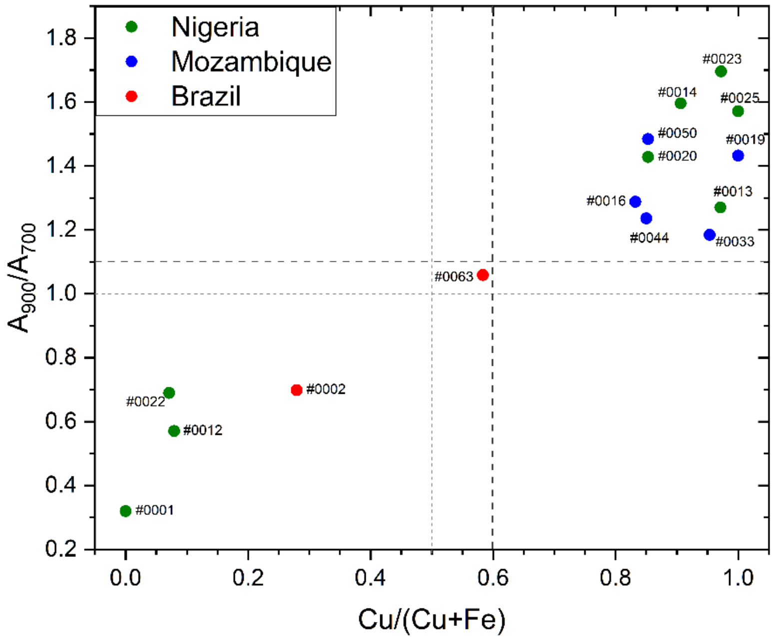

Figure 60: Relative intensities of the 900nm and 700nm absorption bands in the UV-VIS-NIR spectrum in comparison with the relative content of copper and iron (Cu/(Cu+Fe)) obtained through EDXRF. Only samples with $A_{900}/A_{700}>1.1$ has enough copper-iron relative content (higher than 0.6) to be considered Paraíba-type.

Sample	Cu/(Cu+Fe)	A_{900}/A_{700}
#0001	0	0.320
#0012	0.08	0.570
#0022	0.07	0.690
#0002	0.28	0.699
#0063	0.58	1.057
#0033	0.95	1.185
#0044	0.85	1.236
#0013	0.97	1.270
#0016	0.83	1.288
#0020	0.85	1.428
#0019	1	1.432
#0050	0.85	1.484
#0025	1	1.571
#0014	0.91	1.596
#0023	0.97	1.696

Table 17: Relative copper-iron content (Cu/(Cu+Fe)) and relative intensities of the 900 and 700nm absorption band in the UV-VIS-NIR spectrum for all the fifteen Li-tourmaline gemstones.

In conclusion, we determined that Raman spectroscopy alone is insufficient for assessing the concentration of chromophores in Paraíba-type tourmalines, specifically the Cu/(Cu+Fe) relative content. However, an alternative non-destructive technique, such as UV-VIS-NIR absorption spectroscopy, can yield quantitative results to ascertain whether a tourmaline gemstone is of Paraíba-type based on the relative intensities of the 900 and 700 nm absorption bands.

Ultimately, we tried to establish a correlation between the concentrations of **trace elements** and the alterations in the Raman or UV-VIS-NIR spectra, given that Nigerian tourmalines are rich in Ga and Pb, Brazilian specimens possess elevated levels of Mg, Zn, and Sb, while gemstones from Mozambique display higher concentrations of Be and Sc but are lacking in magnesium[70–73]. However, no association was identified between the methodologies and the trace element amounts detected by EDXRF.

Pink And Green Watermelon Tourmalines

We examined six elbaite samples of pink and green tourmalines, as illustrated in Figure 61. Two samples (B3 and GV) are entirely green, likely classifying them as the verdelite variety. The remaining four samples exhibit zoning with pink and green regions, categorising them as either rubellite or verdelite varieties, or more broadly, as watermelon-type, particularly in the case of sample EM, which features a pink core and a green rim concentric to the crystal c-axis.

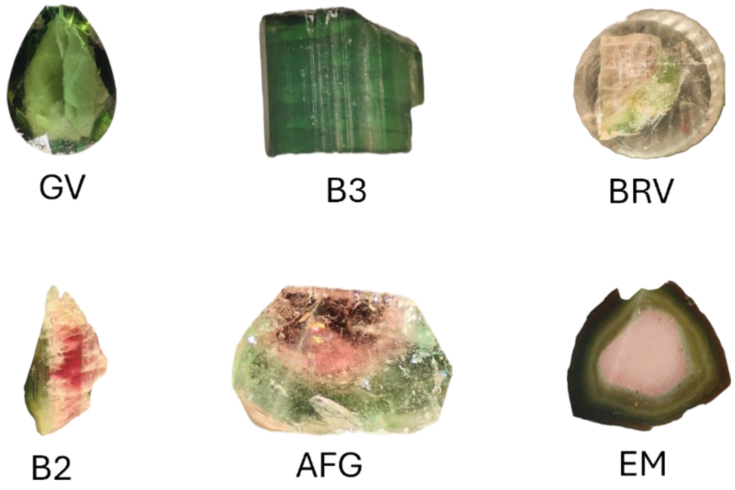

Figure 61: The six pink and green elbaite samples analysed. Samples EM show the typical watermelon zonation, with a pink core and a green rim concentric to the crystal c-axis.

The objective is to identify correlations between the Raman spectra and variations in **iron** and **manganese** concentrations, which are the chromophores responsible for the green and pink colours. Figure 62 illustrates that the Raman spectra of the two green elbaite samples exhibit an **additional band** in the ^{V}OH stretching modes region at around **3560 cm^{-1}**, consistent with the prior analysis of Paraíba-type tourmalines. Specifically, in sample E3, characterised by a dark green tone, the intensity of the additional band reaches that of the primary ^{V}OH band at 3590 cm^{-1}. Consequently, the increased band intensity seems to connect with the iron concentration, which is expected to be greater when the green shades are darker. This is also visible in the spectra performed in the pink and green parts of samples BRV, B2 and AFG, shown in Figure 63, with the extra band present only in the green part, occasionally appearing as a shoulder at lower wavenumber of the main ^{V}OH band, which is entirely absent in the pink region. Conversely, in the low-frequency band, there is no indication of any alterations between the two sections of the bi-colour samples. All these spectra were collected in the optimal $\bar{y}(zz)y$ orientation, with the crystal c-axis aligned parallel to the polarisation of the incident light. However, it is not always practicable to conduct measurements in this orientation, particularly in watermelon-type tourmalines such as EM, which are typically sliced perpendicular to the c-axis. Therefore, we must assess the existence of the additional band even in orientations perpendicular to the c-axis. Figure 64 illustrates the Raman spectra of the OH stretching region acquired from sample EM. In this instance, the lowered intensity of the OH bands, attributable to the not optimal orientation, yields a noisy spectrum. Nonetheless, across various regions of the rim, transitioning from light green to brown shades, the emergence of the additional ^{V}OH band, which is absent in the pink core, remains discernible.

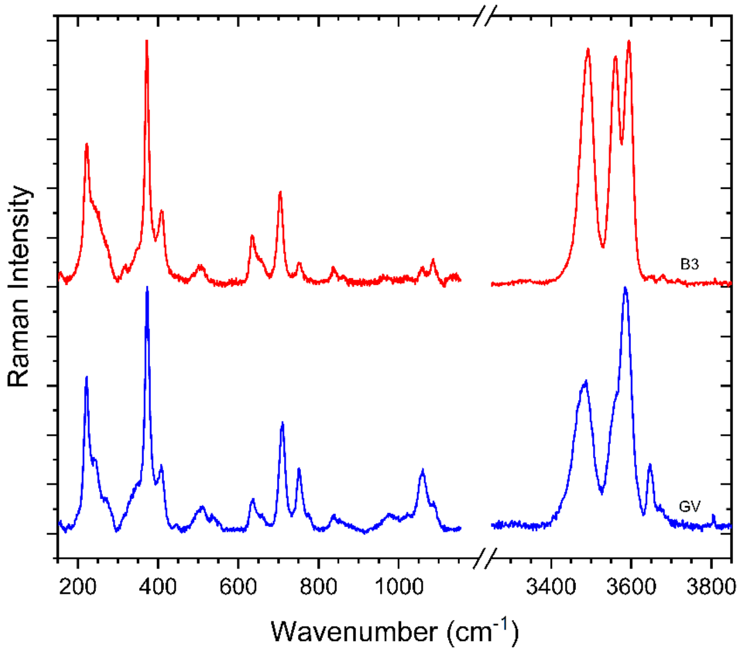

Figure 62: Normalised Raman spectra of the two green elbaite samples obtained in the $\bar{y}(zz)y$ *orientation.*

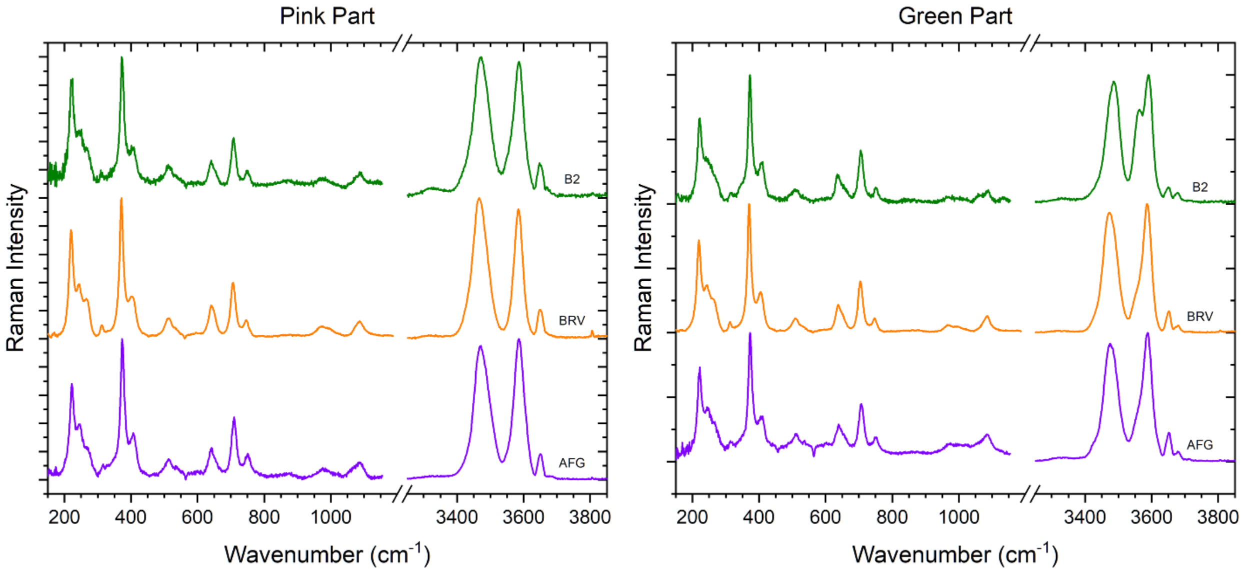

Figure 63: Comparison between the normalised Raman spectra in the pink and green parts of bi-colour elbaite samples obtained in the $\bar{y}(zz)y$ *orientation.*

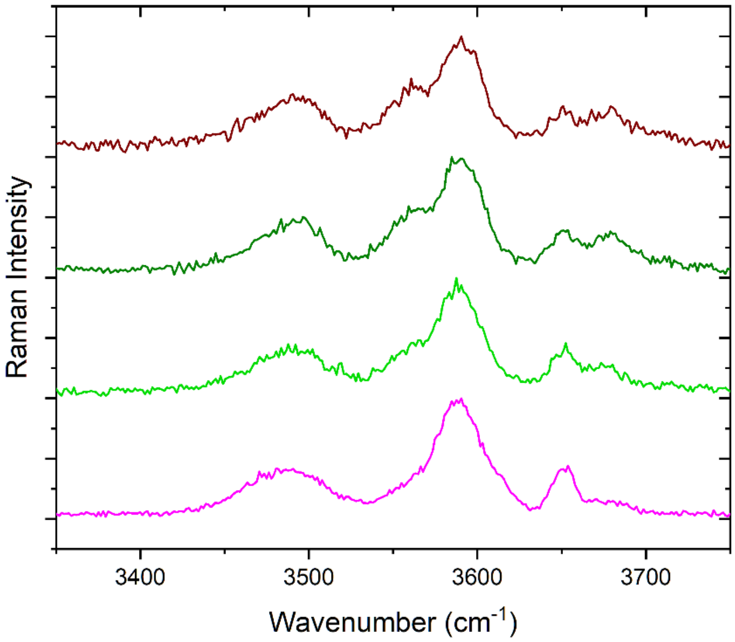

Figure 64: Normalised OH stretching region Raman spectrum of sample EM in the pink core (pink spectrum) and in the light green, dark green and brown parts of the rim. The spectra are obtained in the $\bar{z}(xx)z$ *orientation.*

Thus the additional band remains discernible regardless of orientation, and the association of its strength with iron concentration is further illustrated by linear Raman mapping conducted in the OH stretching region on the EM, BRV, and AFG samples between the pink and green areas (Figure 65). These maps clearly depict the emergence of the additional ^{V}OH band around 3560 cm^{-1} in the green zone, as well as a minor ^{W}OH peak about 3775 cm^{-1} in the same area. The two peaks are associated with the presence of iron at the Y-site; the additional ^{V}OH band corresponds to the **2^{Y}Fe^{Z}Al^{Z}Al-^{Y}Al^{Z}Al^{Z}Al** configuration near the V-sites, while the ^{W}OH peak pertains to the **^{Y}Li^{Y}(Li,Fe)^{Y}Al-^{X}□** configuration at the W-site[129]. Therefore, we aim to determine the correlation between the strength of these additional OH modes and the concentration of iron chromophore in elbaite. We will specifically focus on the ^{V}OH band, as the ^{W}OH peak is relatively weak and often not distinctly observable, particularly in orientations different from $\bar{y}(zz)y$.

Consequently, we conducted **µXRF mapping** to analyse the iron distribution in pink and green elbaite. Figure 66 illustrates that the maps obtained for samples EM and AFG exhibit elevated iron concentrations in the green regions, as expected. In particular, the EM sample shows a correlation between the varying shades of green in the rim, with the darkest green stripes containing the highest iron content, while the pink area is practically free of iron. Furthermore, the behaviour of manganese is significant, since it serves as the chromophore linked to the pink colour and therefore is expected to be more concentrated in the pink regions of the samples. However, in sample EM the distribution is uniform across the whole examined region, while in sample AFG there is a little larger concentration in the green section compared to the pink part.

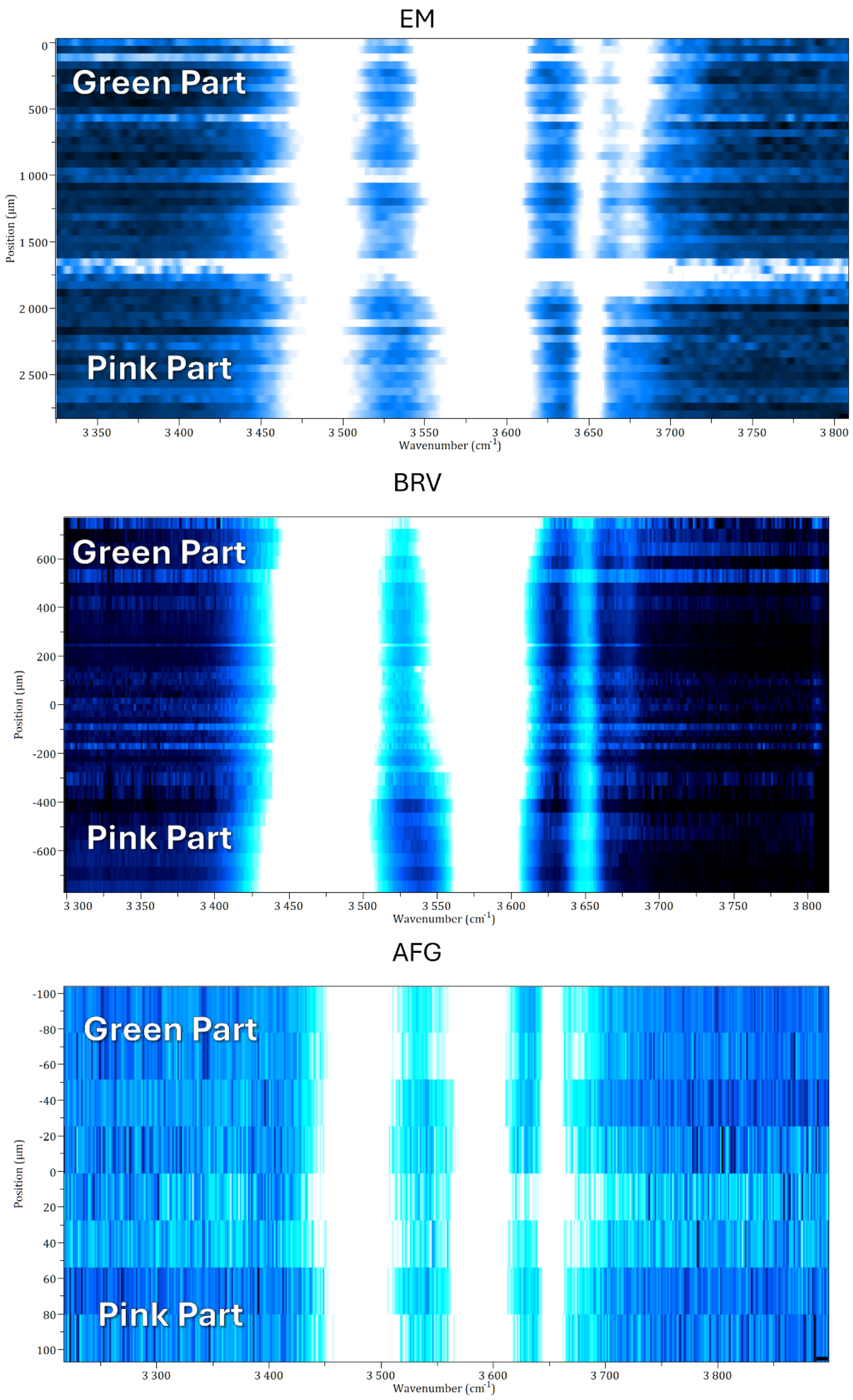

Figure 65: Linear Raman maps in the OH stretching region between the pink and green parts of three elbaite samples.

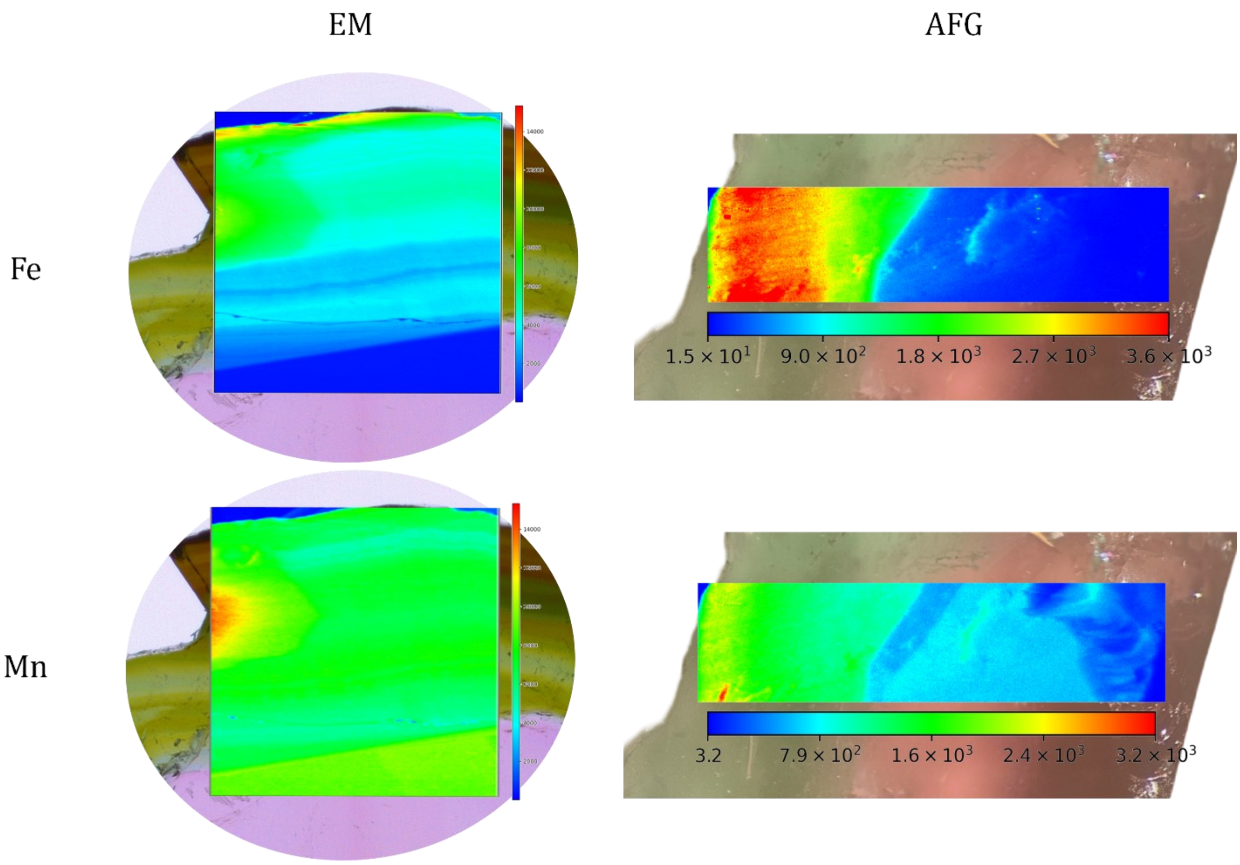

Figure 66: Normalised µXRF maps of iron and manganese distribution between the green and pink parts of samples EM and AFG. Red colour in the map represent the highest content of the element whereas the blue colour represent the minimum.

As a result, the transition between green and pink zones in those samples is likely attributable to the **presence or lack of iron**, rather than an increase in manganese amount in the pink zone.

Nevertheless, the accurate measurement of absolute iron content in Y-sites with µXRF was impracticable due to the presence of light elements, such **lithium**, undetectable by this method. The measurement of lithium in elbaite is essential as it represents a significant component in the Y-sites of this mineral species, reaching values of up to 1.5 a.p.f.u. in the end-member formula. In this context, **Laser Induced Breakdown Spectroscopy** (LIBS) serves as an effective method for quantifying all elements in tourmalines, including light elements such as lithium and boron, by directly measuring their concentrations via distinctive emission lines in the plasma. Researches on lithium measurement using LIBS have already been conducted[195–197], including on watermelon tourmalines[198]; however, they necessitated the use of **specific standards** with a matrix composition analogous to that of tourmalines. Still, standards of such nature are challenging to obtain; therefore, an alternative method may be employed to acquire quantitative data on elbaite compositions: the **Calibration-Free LIBS** (CF-LIBS) approach[171]. This method eliminates the necessity for matrix-matched standards to calibrate the instrument, deriving plasma parameters directly from the spectrum (see Chapter 2 for the description of the procedure).

LIBS point measurements were conducted on all six samples depicted in Figure 61, with analysis of both the pink and green portions of the bi-colour samples. The LIBS spectra acquired in the 2000-9000 Å range are presented in Figure 67.

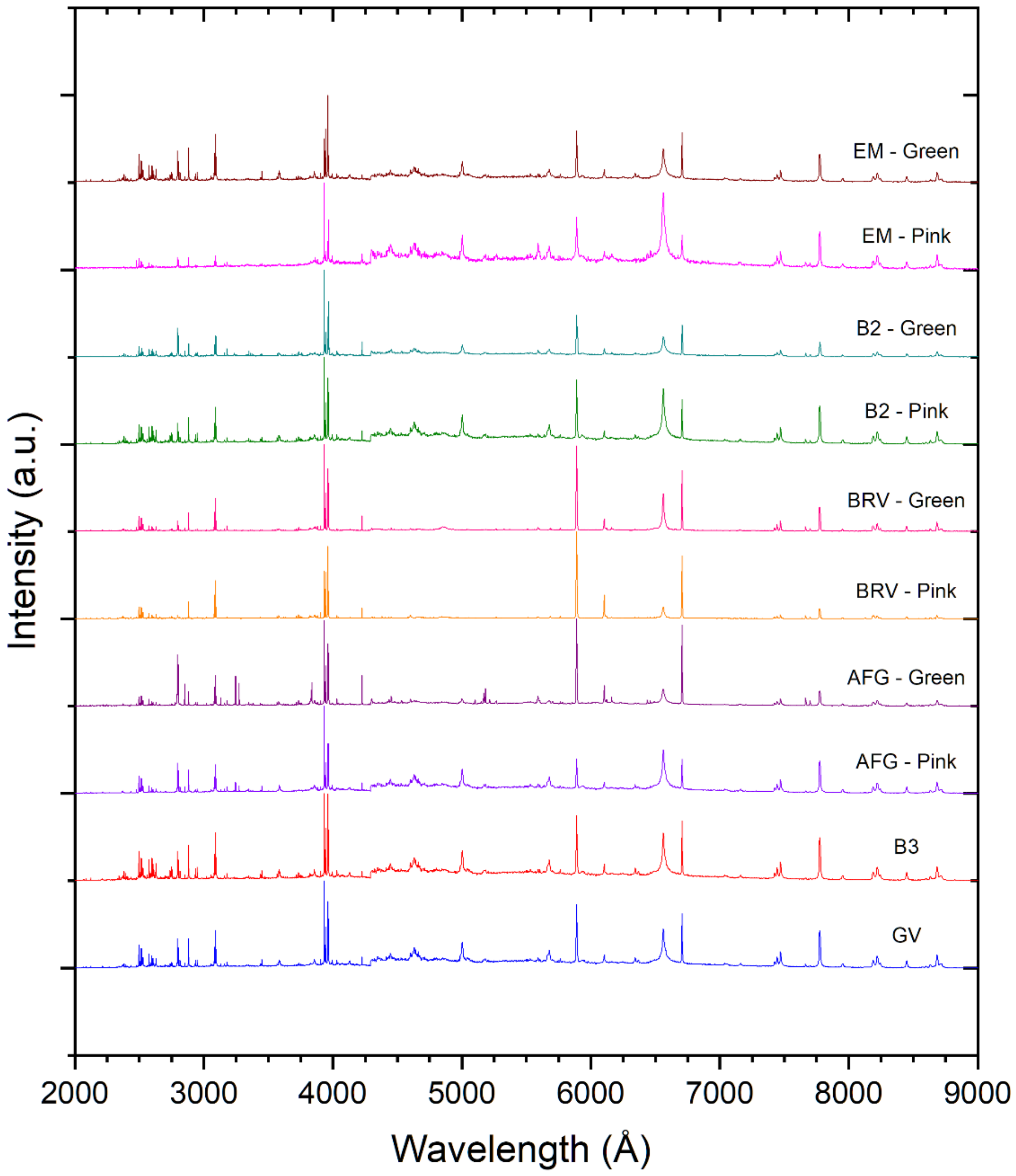

Figure 67: Normalised LIBS spectra on the six pink and green elbaite samples. Both measurements performed on pink and green regions of the bi-colour samples are reported.

The data analysis was conducted using the **LIBS++©** program, which incorporates an internal routine for all stages of the CF-LIBS procedure following the manual selection of emission lines and their assignment to the specific elements required for quantification. The obtained compositions for all samples are presented in Table 18.

Sample	AFG		B2		B3	BRV		GV	EM	
Colour	Pink	Green	Pink	Green	Green	Pink	Green	Green	Pink	Green
Na	1.64	1.71	0.88	1.59	1.41	1.35	2.92	1.43	7.61	1.80
K	0.56	1.15	0	0	0	0	0	0	0	0.22
Ca	0.82	1.68	0.19	0.47	0.32	0.29	1.00	0.48	2.44	0.16
B	13.80	16.00	20.09	23.05	6.47	12.46	9.18	10.22	9.31	6.11
Si	38.20	23.65	32.50	30.39	44.51	40.63	45.17	43.35	41.81	34.74
Al	36.22	23.25	23.51	20.39	26.76	36.32	31.59	26.56	26.76	32.72
Fe	0	9.65	10.80	15.32	13.41	6.81	7.90	11.66	0	16.88
Mn	2.82	6.23	11.90	8.58	6.89	1.83	1.84	6.09	10.49	3.44
Li	0.25	0.26	0.13	0.21	0.23	0.31	0.40	0.21	0.55	0.17
Cu	5.06	13.32	0	0	0	0	0	0	0	3.31
Mg	0.63	3.10	0	0	0	0	0	0	1.03	0.45

Table 18: Composition in Mass% of the six pink and green elbaite samples obtained through CF-LIBS measurements.

Utilising the compositions derived from CF-LIBS, we determined the relative iron content in the Y- and Z-sites as the ratio of iron concentration to the total concentration of all expected elements in these sites (Fe/(Fe+Al+Mn+Li+Mg+Cu)). This ratio was then compared to the relative intensities of the extra ^{V}OH band at 3560 cm^{-1} and the principal band at 3590 cm^{-1}, designated as $^{V}OH_3$ and $^{V}OH_4$, respectively (data are presented in Table 19).

Sample	Colour	Fe% In Y+Z-Sites	I($^{V}OH_3$)/I($^{V}OH_4$)
AFG	Pink	0	0.13
	Green	0.17	0.26
B2	Pink	0.23	0.32
	Green	0.34	0.53
B3	Green	0.28	0.99
BRV	Pink	0.15	0.24
	Green	0.19	0.41
GV	Green	0.26	0.53
EM	Pink	0	0.06
	Green	0.30	0.52

Table 19: Relative iron content in Y- and Z-sites obtained from CF-LIBS and relative intensity of the $^{V}OH_3$ and $^{V}OH_4$ Raman bands for all the analysed pink and green elbaite (in both pink and green regions for the bi-colour samples)

Figure 68 illustrates the correlation between these two values, notably indicating that samples with an **I(^{V}OH$_3$)/I(^{V}OH$_4$)** ratio over 0.5—where the additional band surpasses half of the primary ^{V}OH band—exhibit an iron concentration in the Y- and Z-sites greater than **25%**. Consequently, the strength of the extra ^{V}OH band can be correlated with the iron content, demonstrating that Raman spectroscopy can be used as quick and non-destructive technique for chromophores quantification in green tourmaline gemstones; nevertheless, we are still unable to identify the distinct elements distribution between the Y- and Z-sites.

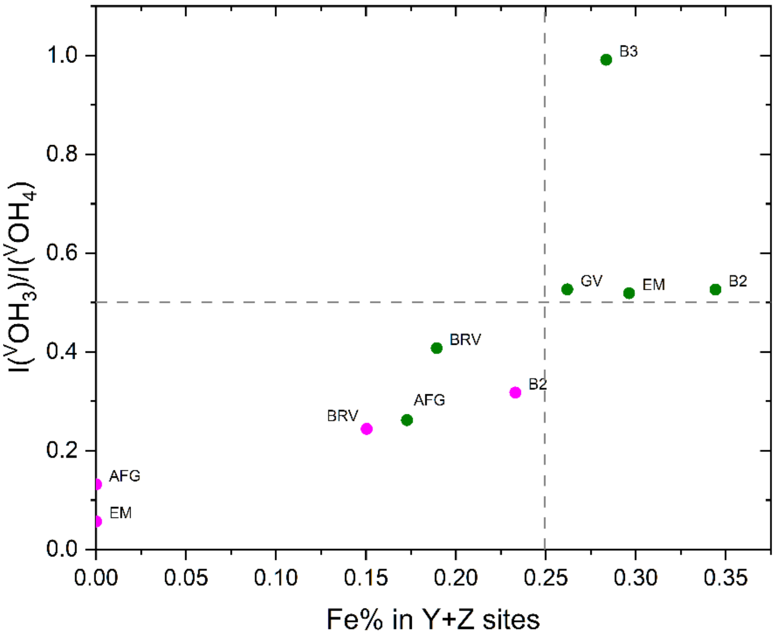

Figure 68: Correlation between the Raman I(^{V}OH$_3$)/I(^{V}OH$_4$) relative intensity and the relative content of Fe in Y- and Z-sites obtained from CF-LIBS for all the six pink and green elbaite samples. Pink points correspond to the measurements performed on the pink parts of the samples whereas green points correspond to measurements in the green parts.

Although these results are encouraging and exhibit distinct behaviour, they remain preliminary, derived from single-point measurements on a limited number of **heterogeneous** samples. Specifically, it was not feasible to conduct Raman and LIBS measurements at the exact spot; but we were able to execute both in a proximal area, potentially influencing the final results. Future analyses should concentrate on conducting **LIBS** and **Raman 2D mappings** within the same region to establish a **point-by-point correlation** between the relative iron content and the fluctuations in the I(^{V}OH$_3$)/I(^{V}OH$_4$) ratio, thereby achieving a more accurate correspondence even in heterogeneous samples such as pink and green elbaite. Additionally, the impact of the **random orientation** of crystal samples on the Raman spectrum must be considered to assess its potential influence on the relative intensity of the additional ^{V}OH band, as in most instances, particularly in watermelon tourmaline slices cut perpendicular to the crystal c-axis, the $\bar{y}(zz)y$ orientation is unattainable.

Chapter 5

Ab Initio Calculations Of Raman Vibrational Modes

The behaviours of the Raman vibrational modes observed experimentally may be influenced by **structural** and **compositional disorder**, such as the presence of Al^{3+} in the Y-sites and, conversely, Fe^{2+} and Mg^{2+} in the Z-sites, as demonstrated in the cases of dravite and schorl. Additionally, the presence of other elements, including, for example, manganese, copper, titanium, and lithium, rather than solely magnesium and iron in the Y-sites, may also play a role. All of these issues are unavoidable when doing experimental studies on natural samples. A **theoretical approach** can mitigate these concerns by providing enhanced control over the site composition within the crystal structure, permitting arbitrary variations in the relative elemental content at each site, hence facilitating a deeper understanding of the behaviour of each vibrational mode with compositional changes.

Consequently, we conducted ab initio calculations on the Raman vibrational modes utilising the **CRYSTAL23©** program[199]. However, owing to the complex crystal structure of tourmalines and the large number of atoms involved, each calculation proved to be exceedingly time-consuming; hence, we were only able to conduct calculations on the **end-member** compositions of **dravite** and **schorl**. Still, the findings remain interesting and might reveal an additional approach for the future enhancement of the dravite-schorl series Raman model.

CRYSTAL23

The CRYSTAL23 software package is a powerful and widely adopted computational tool designed for the ab initio study of the electronic structure and related properties of periodic and finite systems[200]. CRYSTAL23 enables the treatment of systems with arbitrary dimensionality, including isolated molecules (0D), polymers (1D), surfaces and slabs (2D), and fully periodic crystals (3D). The program supports a variety of electronic structure methods, notably **Hartree-Fock** and **Kohn-Sham Density Functional Theory** (DFT) and allows for extensive exploitation of system symmetry to optimize computational efficiency. The core of the CRYSTAL calculation procedure is the **linear combination of atomic orbitals** (LCAO) approximation where each **Crystalline Orbital** is defined as

$$\psi_i(\boldsymbol{r},\boldsymbol{k}) = \sum_{\mu} a_{\mu,i}(\boldsymbol{k})\phi_\mu(\boldsymbol{r},\boldsymbol{k})$$

which is the linear combination of **Bloch function**, $\phi_\mu(\boldsymbol{r},\boldsymbol{k})$, with $a_{\mu,i}(\boldsymbol{k})$ as the coefficients of the combination. The Bloch functions can be described in terms of **local functions**:

$$\phi_{\mu}(\boldsymbol{r}, \boldsymbol{k}) = \sum_{\boldsymbol{g}} \varphi_{\mu}(\boldsymbol{r} - \boldsymbol{A}_{\mu} - \boldsymbol{g})\, e^{\mathrm{i}\boldsymbol{k}\cdot\boldsymbol{g}}$$

where $\boldsymbol{A}_{\mu}$ is the coordinate related to the nucleus in the cell where the local function φ_{μ} is centred while $\boldsymbol{g}$ describes the lattice vectors, thus the sum is on the entire set. In CRYSTAL23, the local functions, also defined as **Atomic Orbitals** (AO), are the linear combination of **Gaussian-type function** (GTF) centred on the same point and normalised, expressed as:

$$\varphi_{\mu}(\boldsymbol{r} - \boldsymbol{A}_{\mu} - \boldsymbol{g}) = \sum_{j}^{n_G} d_j G(\alpha_j, \boldsymbol{r} - \boldsymbol{A}_{\mu} - \boldsymbol{g})$$

where d_j and α_j are, respectively, the coefficients and exponents of the Gaussian function fixed, together with the number of GTF (n_G), by the choice of the **basis set**.

In CRYSTAL23, the calculation of vibrational frequencies is based on a **harmonic approximation**, which is valid for small displacements of the atoms around the **equilibrium geometry**[201,202].

The procedure begins with a full **geometry optimization** to locate the minimum on the potential energy surface. Subsequently, the second derivatives of the total energy with respect to displacements of each atom are evaluated to construct the **Hessian matrix**. CRYSTAL23 offers both analytical and numerical evaluation of the Hessian, depending on the level of theory and the specific requirements of the calculation. The Hessian is then mass-weighted and diagonalized to yield the system's normal modes and their associated **vibrational frequencies**. The use of **poin**t and **space group symmetry** significantly reduces computational cost and aids in the classification of vibrational modes according to their irreducible representations.

In addition to vibrational frequencies, CRYSTAL23 is capable of computing **Raman intensities**, which are essential for the simulation and interpretation of Raman spectra. CRYSTAL23 determines these intensities by evaluating the derivatives of the polarizability tensor with respect to the normal mode displacements. This can be accomplished via analytical derivatives, when available, or through numerical differentiation using finite displacements.

The computed Raman intensities, together with the vibrational frequencies, allow for the direct simulation of Raman spectra, enabling detailed comparison with experimental data. The combined calculation of Raman and IR intensities (which are computed together) facilitates comprehensive vibrational characterization of the studied system.

Parameters For Dravite And Schorl Vibrational Modes Calculation

The initial structures of dravite and schorl end-member species used for the calculations were obtained from literature, where **single crystal XRD refinement** and **crystallographic analyses** were conducted to experimentally ascertain the position of each atom within the unit cell of both minerals[136,203]. The input geometry was subsequently completed with the tourmaline space group *R3m* (number 160 in the crystallographic tables) and the independent unit cell parameters, specifically *a* and *c*. The complete geometries for dravite and schorl are presented in Figure 69.

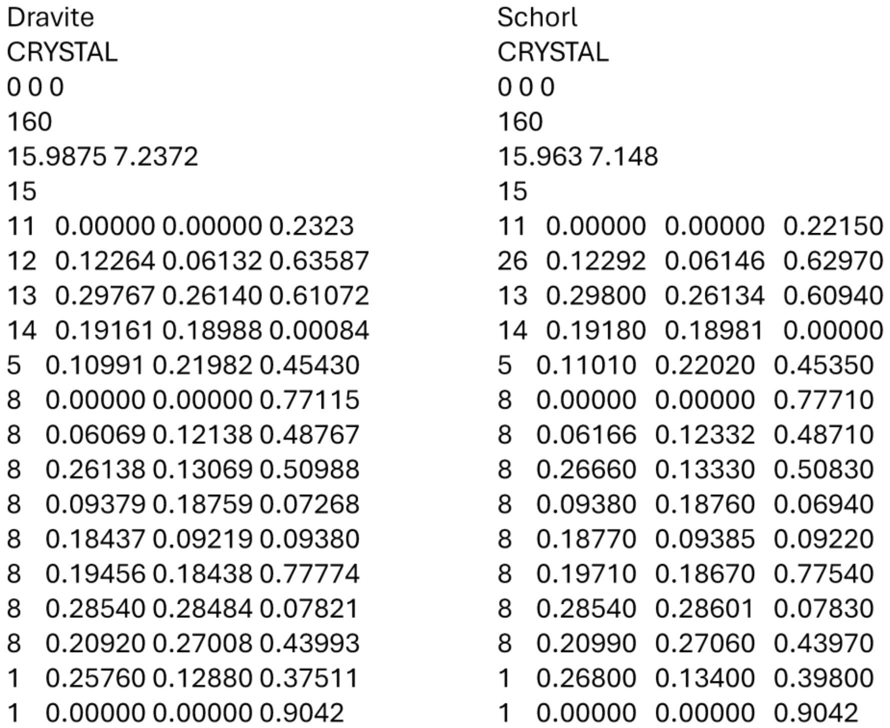

```
Dravite                                  Schorl
CRYSTAL                                  CRYSTAL
0 0 0                                    0 0 0
160                                      160
15.9875 7.2372                           15.963 7.148
15                                       15
11  0.00000 0.00000 0.2323               11  0.00000  0.00000  0.22150
12  0.12264 0.06132 0.63587              26  0.12292  0.06146  0.62970
13  0.29767 0.26140 0.61072              13  0.29800  0.26134  0.60940
14  0.19161 0.18988 0.00084              14  0.19180  0.18981  0.00000
5   0.10991 0.21982 0.45430              5   0.11010  0.22020  0.45350
8   0.00000 0.00000 0.77115              8   0.00000  0.00000  0.77710
8   0.06069 0.12138 0.48767              8   0.06166  0.12332  0.48710
8   0.26138 0.13069 0.50988              8   0.26660  0.13330  0.50830
8   0.09379 0.18759 0.07268              8   0.09380  0.18760  0.06940
8   0.18437 0.09219 0.09380              8   0.18770  0.09385  0.09220
8   0.19456 0.18438 0.77774              8   0.19710  0.18670  0.77540
8   0.28540 0.28484 0.07821              8   0.28540  0.28601  0.07830
8   0.20920 0.27008 0.43993              8   0.20990  0.27060  0.43970
1   0.25760 0.12880 0.37511              1   0.26800  0.13400  0.39800
1   0.00000 0.00000 0.9042               1   0.00000  0.00000  0.9042
```

Figure 69: Geometry inputs used for the calculation on dravite and schorl with CRYSTAL23. The position of each atom, represented by its atomic number, was obtained from literature.

After defining the geometry, it is necessary to establish a basis set that includes the coefficients and exponents of the Gaussian-type functions employed for a representation of atomic orbitals. We acquired it from the **CRYSTAL Basis Sets Library** website[204], which delineates a list of several basis sets for every element in the periodic table. The selection observed to the general principle of choosing basis sets with an unoccupied **d-shell** for each element, with the exception of oxygen, for which two unoccupied d-shells were selected. Consequently, the **electron density** may fluctuate, populating the vacant shells without restrictions pertaining to shell filling. The basis sets chosen for each element are detailed in Table 20.

Finally, the parameters for the DFT computation must be established. We specifically select the **Global Hybrid functional WC1LYP**[205] to delineate the exchange and correlation functionals, as this hybrid functional has been demonstrated to yield optimal agreement with experimental data for frequencies calculations[206]. The WC1LYP hybrid functional comprises a **WCGGA** (Generalized Gradient Approximation functional, GGA - Wu-Cohen 2006[207]) exchange potential and a **LYP** (GGA - Lee-Yang-Parr[208]) correlation potential, supplemented by a constant 16% contribution of **Hartree-Fock exchange** that corrects the electrons self-interaction error.

Prior to calculating the vibrational frequencies, a geometry optimisation of the unit cell parameters and atomic positions was conducted to ascertain the theoretical equilibrium location of each atom. To get high precision essential for accurate frequency calculations, the convergence requirements for the root mean squares of the displacement and the gradient were established at 0.00012 and 0.00003, respectively.

Element	Basis Set
H	H_5-11G*_dovesi_1984[209]
B	B_m-6-311G(d)_Heyd_2005[210,211]
O	O_m-6-311G(2d)_Heyd_2005[210,212]
Na	Na_8-511G_dovesi_1991[213,214]
Mg	Mg_m-6-311G(d)_Heyd_2005[210,211]
Al	Al_m-6-311G(d)_Heyd_2005[210,211]
Si	Si_m-6-311G(d)_Heyd_2005[210,211]
Fe	Fe_86-411d41G_towler_1992b[215,216]

Table 20: Basis sets from the CRYSTAL Basis Sets Library used for each element.

After optimising the geometry, the frequencies were computed by applying a minor displacement of 0.003 Å along the Cartesian axes from the equilibrium position for every atom, accounting for displacements in both positive and negative directions for each axis. The intensities of the Raman active vibrational modes[217,218] were computed using the **Coupled Perturbed Hartree-Fock/Kohn-Sham** (CPHF/CPKS) method[219–221] for the single-crystal spectrum with various orientations, and for the polycrystalline spectrum, which was derived by averaging all of the potential orientations[222].

Calculated Vibrational Modes For Dravite And Schorl

Figure 70 presents the results of the frequencies calculations for both dravite and schorl end-member formulas. According to group theory, there are 31 A_1, 22 A_2, and 53 E **optical modes**. The A_2 modes are inactive in both Raman and IR spectroscopy, denoted by the letter “I” in the corresponding columns, whereas A_1 and E modes are Raman and IR active, marked by the letter “A”. The intensities depicted in Figure 70 relate to the IR, while the Raman intensities are computed separately.

The computed Raman intensities for dravite and schorl **single crystals** in various orientations are presented in Figure 71, with the greatest peak (specifically the ^{V}OH band in tourmalines) normalised to 1000. Among the several directions, the most noteworthy is the **I_zz**, which corresponds to the $\bar{y}(zz)y$ examined experimentally, featuring solely the activated A_1 vibrational modes and exhibiting highest intensity in the OH stretching region. The **polycrystalline isotropic intensities** were finally estimated and presented in Figure 72, reflecting a mixed contribution from the A_1 and E modes.

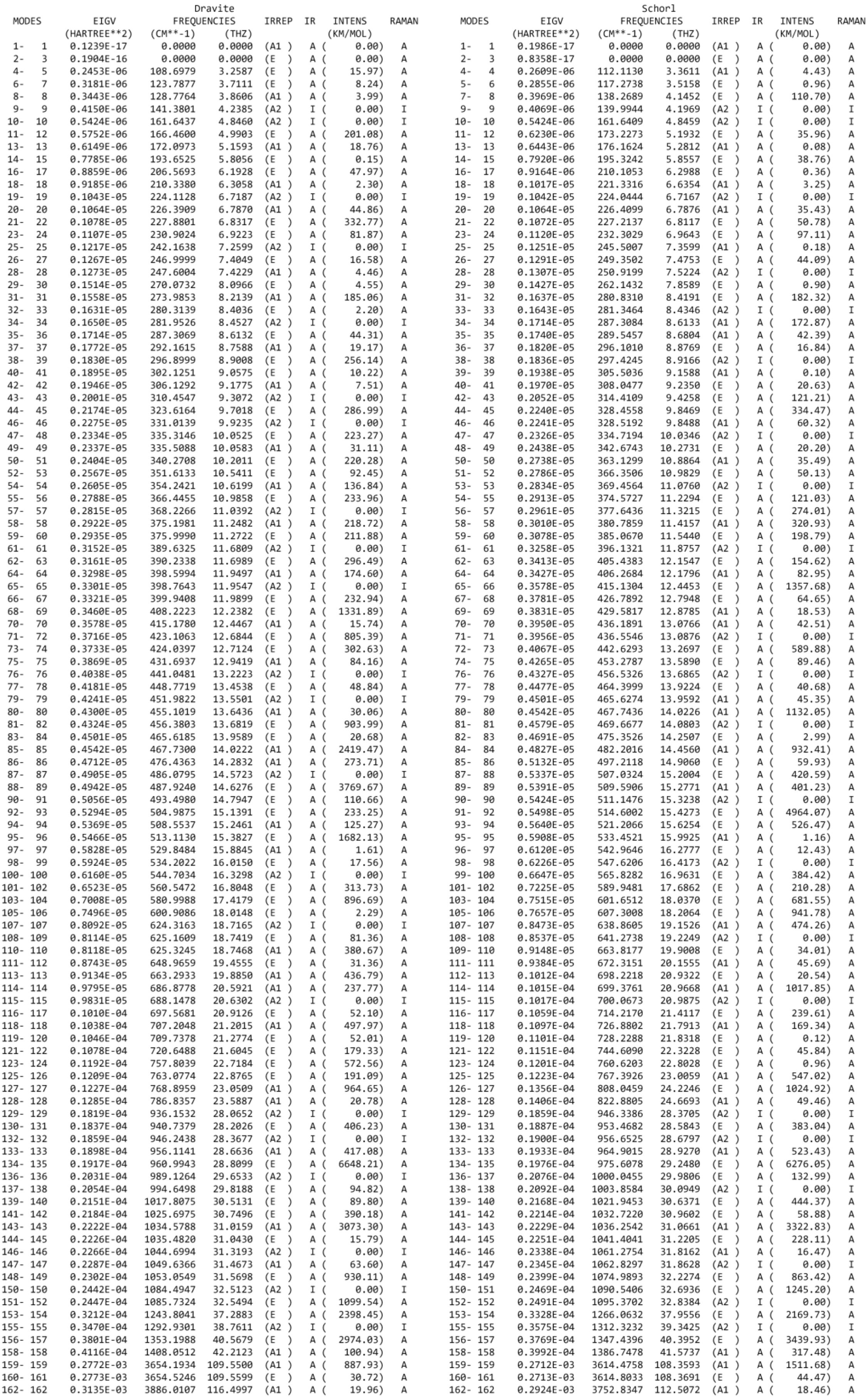

```
                            Dravite                                                              Schorl
 MODES      EIGV          FREQUENCIES       IRREP  IR    INTENS     RAMAN      MODES      EIGV          FREQUENCIES       IRREP  IR    INTENS     RAMAN
          (HARTREE**2)   (CM**-1)     (THZ)               (KM/MOL)                      (HARTREE**2)   (CM**-1)     (THZ)               (KM/MOL)
  1-   1  0.1239E-17     0.0000    0.0000  (A1 )  A (     0.00)  A        1-   1  0.1986E-17     0.0000    0.0000  (A1 )  A (     0.00)  A
  2-   3  0.1904E-16     0.0000    0.0000  (E  )  A (     0.00)  A        2-   3  0.8358E-17     0.0000    0.0000  (E  )  A (     0.00)  A
  4-   5  0.2453E-06   108.6979    3.2587  (E  )  A (    15.97)  A        4-   4  0.2609E-06   112.1130    3.3611  (A1 )  A (     4.43)  A
  6-   7  0.3181E-06   123.7877    3.7111  (E  )  A (     8.24)  A        5-   6  0.2855E-06   117.2738    3.5158  (E  )  A (     0.96)  A
  8-   8  0.3443E-06   128.7764    3.8606  (A1 )  A (     3.99)  A        7-   8  0.3969E-06   138.2689    4.1452  (E  )  A (   110.70)  A
  9-   9  0.4150E-06   141.3801    4.2385  (A2 )  I (     0.00)  I        9-   9  0.4069E-06   139.9944    4.1969  (A2 )  I (     0.00)  I
 10-  10  0.5424E-06   161.6437    4.8460  (A2 )  I (     0.00)  I       10-  10  0.5424E-06   161.6409    4.8459  (A2 )  I (     0.00)  I
 11-  12  0.5752E-06   166.4600    4.9903  (E  )  A (   201.08)  A       11-  12  0.6230E-06   173.2273    5.1932  (E  )  A (    35.96)  A
 13-  13  0.6149E-06   172.0973    5.1593  (A1 )  A (    18.76)  A       13-  13  0.6443E-06   176.1624    5.2812  (A1 )  A (     0.08)  A
 14-  15  0.7785E-06   193.6525    5.8056  (E  )  A (     0.15)  A       14-  15  0.7920E-06   195.3242    5.8557  (E  )  A (    38.76)  A
 16-  17  0.8859E-06   206.5693    6.1928  (E  )  A (    47.97)  A       16-  17  0.9164E-06   210.1053    6.2988  (E  )  A (     0.36)  A
 18-  18  0.9185E-06   210.3380    6.3058  (A1 )  A (     2.30)  A       18-  18  0.1017E-05   221.3316    6.6354  (A1 )  A (     3.25)  A
 19-  19  0.1043E-05   224.1128    6.7187  (A2 )  I (     0.00)  I       19-  19  0.1042E-05   224.0444    6.7167  (A2 )  I (     0.00)  I
 20-  20  0.1064E-05   226.3909    6.7870  (A1 )  A (    44.86)  A       20-  20  0.1064E-05   226.4099    6.7876  (A1 )  A (    35.43)  A
 21-  22  0.1078E-05   227.8801    6.8317  (E  )  A (   332.77)  A       21-  22  0.1072E-05   227.2137    6.8117  (E  )  A (    50.78)  A
 23-  24  0.1107E-05   230.9024    6.9223  (E  )  A (    81.87)  A       23-  24  0.1120E-05   232.3029    6.9643  (E  )  A (    97.11)  A
 25-  25  0.1217E-05   242.1638    7.2599  (A2 )  I (     0.00)  I       25-  25  0.1251E-05   245.5007    7.3599  (A1 )  A (     0.18)  A
 26-  27  0.1267E-05   246.9999    7.4049  (E  )  A (    16.58)  A       26-  27  0.1291E-05   249.3502    7.4753  (E  )  A (    44.09)  A
 28-  28  0.1273E-05   247.6004    7.4229  (A1 )  A (     4.46)  A       28-  28  0.1307E-05   250.9199    7.5224  (A2 )  I (     0.00)  I
 29-  30  0.1514E-05   270.0732    8.0966  (E  )  A (     4.55)  A       29-  30  0.1427E-05   262.1432    7.8589  (E  )  A (     0.90)  A
 31-  31  0.1558E-05   273.9853    8.2139  (A1 )  A (   185.06)  A       31-  32  0.1637E-05   280.8310    8.4191  (E  )  A (   182.32)  A
 32-  33  0.1631E-05   280.3139    8.4036  (E  )  A (     2.20)  A       33-  33  0.1643E-05   281.3464    8.4346  (A2 )  I (     0.00)  I
 34-  34  0.1650E-05   281.9526    8.4527  (A2 )  I (     0.00)  I       34-  34  0.1714E-05   287.3084    8.6133  (A1 )  A (   172.87)  A
 35-  36  0.1714E-05   287.3069    8.6132  (E  )  A (    44.31)  A       35-  35  0.1740E-05   289.5457    8.6804  (A1 )  A (    42.39)  A
 37-  37  0.1772E-05   292.1615    8.7588  (A1 )  A (    19.17)  A       36-  37  0.1820E-05   296.1010    8.8769  (E  )  A (    16.84)  A
 38-  39  0.1830E-05   296.8999    8.9008  (E  )  A (   256.14)  A       38-  38  0.1836E-05   297.4245    8.9166  (A2 )  I (     0.00)  I
 40-  41  0.1895E-05   302.1251    9.0575  (E  )  A (    10.22)  A       39-  39  0.1938E-05   305.5036    9.1588  (A1 )  A (     0.10)  A
 42-  42  0.1946E-05   306.1292    9.1775  (A1 )  A (     7.51)  A       40-  41  0.1970E-05   308.0477    9.2350  (E  )  A (    20.63)  A
 43-  43  0.2001E-05   310.4547    9.3072  (A2 )  I (     0.00)  I       42-  43  0.2052E-05   314.4109    9.4258  (E  )  A (   121.21)  A
 44-  45  0.2174E-05   323.6164    9.7018  (E  )  A (   286.99)  A       44-  45  0.2240E-05   328.4558    9.8469  (E  )  A (   334.47)  A
 46-  46  0.2275E-05   331.0139    9.9235  (A2 )  I (     0.00)  I       46-  46  0.2241E-05   328.5192    9.8488  (A1 )  A (    60.32)  A
 47-  48  0.2334E-05   335.3146   10.0525  (E  )  A (   223.27)  A       47-  47  0.2326E-05   334.7194   10.0346  (A2 )  I (     0.00)  I
 49-  49  0.2337E-05   335.5088   10.0583  (A1 )  A (    31.11)  A       48-  49  0.2438E-05   342.6743   10.2731  (E  )  A (    20.20)  A
 50-  51  0.2404E-05   340.2708   10.2011  (E  )  A (   220.28)  A       50-  50  0.2738E-05   363.1299   10.8864  (A1 )  A (    35.49)  A
 52-  53  0.2567E-05   351.6133   10.5411  (E  )  A (    92.45)  A       51-  52  0.2786E-05   366.3506   10.9829  (E  )  A (    50.13)  A
 54-  54  0.2605E-05   354.2421   10.6199  (A1 )  A (   136.84)  A       53-  53  0.2834E-05   369.4564   11.0760  (A2 )  I (     0.00)  I
 55-  56  0.2788E-05   366.4455   10.9858  (E  )  A (   233.96)  A       54-  55  0.2913E-05   374.5727   11.2294  (E  )  A (   121.03)  A
 57-  57  0.2815E-05   368.2266   11.0392  (A2 )  I (     0.00)  I       56-  57  0.2961E-05   377.6436   11.3215  (E  )  A (   274.01)  A
 58-  58  0.2922E-05   375.1981   11.2482  (A1 )  A (   218.72)  A       58-  58  0.3010E-05   380.7859   11.4157  (A1 )  A (   320.93)  A
 59-  60  0.2935E-05   375.9990   11.2722  (E  )  A (   211.88)  A       59-  60  0.3078E-05   385.0670   11.5440  (E  )  A (   198.79)  A
 61-  61  0.3152E-05   389.6325   11.6809  (A2 )  I (     0.00)  I       61-  61  0.3258E-05   396.1321   11.8757  (A2 )  I (     0.00)  I
 62-  63  0.3161E-05   390.2338   11.6989  (E  )  A (   296.49)  A       62-  63  0.3413E-05   405.4383   12.1547  (E  )  A (   154.62)  A
 64-  64  0.3298E-05   398.5994   11.9497  (A1 )  A (   174.60)  A       64-  64  0.3427E-05   406.2684   12.1796  (A1 )  A (    82.95)  A
 65-  65  0.3301E-05   398.7643   11.9547  (A2 )  I (     0.00)  I       65-  66  0.3578E-05   415.1304   12.4453  (E  )  A (  1357.68)  A
 66-  67  0.3321E-05   399.9408   11.9899  (E  )  A (   232.94)  A       67-  68  0.3781E-05   426.7892   12.7948  (E  )  A (    64.65)  A
 68-  69  0.3460E-05   408.2223   12.2382  (E  )  A (  1331.89)  A       69-  69  0.3831E-05   429.5817   12.8785  (A1 )  A (    18.53)  A
 70-  70  0.3578E-05   415.1780   12.4467  (A1 )  A (    15.74)  A       70-  70  0.3950E-05   436.1891   13.0766  (A1 )  A (    42.51)  A
 71-  72  0.3716E-05   423.1063   12.6844  (E  )  A (   805.39)  A       71-  71  0.3956E-05   436.5546   13.0876  (A2 )  I (     0.00)  I
 73-  74  0.3733E-05   424.0397   12.7124  (E  )  A (   302.63)  A       72-  73  0.4067E-05   442.6293   13.2697  (E  )  A (   589.88)  A
 75-  75  0.3869E-05   431.6937   12.9419  (A1 )  A (    84.16)  A       74-  75  0.4265E-05   453.2787   13.5890  (E  )  A (    89.46)  A
 76-  76  0.4038E-05   441.0481   13.2223  (A2 )  I (     0.00)  I       76-  76  0.4327E-05   456.5326   13.6865  (A2 )  I (     0.00)  I
 77-  78  0.4181E-05   448.7719   13.4538  (E  )  A (    48.84)  A       77-  78  0.4477E-05   464.3999   13.9224  (E  )  A (    40.68)  A
 79-  79  0.4241E-05   451.9822   13.5501  (A2 )  I (     0.00)  I       79-  79  0.4501E-05   465.6274   13.9592  (A1 )  A (    45.35)  A
 80-  80  0.4300E-05   455.1019   13.6436  (A1 )  A (    30.06)  A       80-  80  0.4542E-05   467.7436   14.0226  (A1 )  A (  1132.05)  A
 81-  82  0.4324E-05   456.3803   13.6819  (E  )  A (   903.99)  A       81-  81  0.4579E-05   469.6677   14.0803  (A2 )  I (     0.00)  I
 83-  84  0.4501E-05   465.6185   13.9589  (E  )  A (    20.68)  A       82-  83  0.4691E-05   475.3526   14.2507  (E  )  A (     2.99)  A
 85-  85  0.4542E-05   467.7300   14.0222  (A1 )  A (  2419.47)  A       84-  84  0.4827E-05   482.2016   14.4560  (A1 )  A (   932.41)  A
 86-  86  0.4712E-05   476.4363   14.2832  (A1 )  A (   273.71)  A       85-  86  0.5132E-05   497.2118   14.9060  (E  )  A (    59.93)  A
 87-  87  0.4905E-05   486.0795   14.5723  (A2 )  I (     0.00)  I       87-  88  0.5337E-05   507.0324   15.2004  (E  )  A (   420.59)  A
 88-  89  0.4942E-05   487.9240   14.6276  (E  )  A (  3769.67)  A       89-  89  0.5391E-05   509.5906   15.2771  (A1 )  A (   401.23)  A
 90-  91  0.5056E-05   493.4980   14.7947  (E  )  A (   110.66)  A       90-  90  0.5424E-05   511.1476   15.3238  (A2 )  I (     0.00)  I
 92-  93  0.5294E-05   504.9875   15.1391  (E  )  A (   233.25)  A       91-  92  0.5498E-05   514.6002   15.4273  (E  )  A (  4964.07)  A
 94-  94  0.5369E-05   508.5537   15.2461  (A1 )  A (   125.27)  A       93-  94  0.5640E-05   521.2066   15.6254  (E  )  A (   526.47)  A
 95-  96  0.5466E-05   513.1130   15.3827  (E  )  A (  1682.13)  A       95-  95  0.5908E-05   533.4521   15.9925  (A1 )  A (     1.16)  A
 97-  97  0.5828E-05   529.8484   15.8845  (A1 )  A (     1.61)  A       96-  97  0.6120E-05   542.9646   16.2777  (E  )  A (    12.43)  A
 98-  99  0.5924E-05   534.2022   16.0150  (E  )  A (    17.56)  A       98-  98  0.6226E-05   547.6206   16.4173  (A2 )  I (     0.00)  I
100- 100  0.6160E-05   544.7034   16.3298  (A2 )  I (     0.00)  I       99- 100  0.6647E-05   565.8282   16.9631  (E  )  A (   384.42)  A
101- 102  0.6523E-05   560.5472   16.8048  (E  )  A (   313.73)  A      101- 102  0.7225E-05   589.9481   17.6862  (E  )  A (   210.28)  A
103- 104  0.7008E-05   580.9988   17.4179  (E  )  A (   896.69)  A      103- 104  0.7515E-05   601.6512   18.0370  (E  )  A (   681.55)  A
105- 106  0.7496E-05   600.9086   18.0148  (E  )  A (     2.29)  A      105- 106  0.7657E-05   607.3008   18.2064  (E  )  A (   941.78)  A
107- 107  0.8092E-05   624.3163   18.7165  (A2 )  I (     0.00)  I      107- 107  0.8473E-05   638.8605   19.1526  (A1 )  A (   474.26)  A
108- 109  0.8114E-05   625.1609   18.7419  (E  )  A (    81.36)  A      108- 108  0.8537E-05   641.2738   19.2249  (A2 )  I (     0.00)  I
110- 110  0.8118E-05   625.3245   18.7468  (A1 )  A (   380.67)  A      109- 110  0.9148E-05   663.8177   19.9008  (E  )  A (    34.01)  A
111- 112  0.8743E-05   648.9659   19.4555  (E  )  A (    31.36)  A      111- 111  0.9384E-05   672.3151   20.1555  (A1 )  A (    45.69)  A
113- 113  0.9134E-05   663.2933   19.8850  (A1 )  A (   436.79)  A      112- 113  0.1012E-04   698.2218   20.9322  (E  )  A (    20.54)  A
114- 114  0.9795E-05   686.8778   20.5921  (A1 )  A (   237.77)  A      114- 114  0.1015E-04   699.3761   20.9668  (A1 )  A (  1017.85)  A
115- 115  0.9831E-05   688.1478   20.6302  (A2 )  I (     0.00)  I      115- 115  0.1017E-04   700.0673   20.9875  (A2 )  I (     0.00)  I
116- 117  0.1010E-04   697.5681   20.9126  (E  )  A (    52.10)  A      116- 117  0.1059E-04   714.2170   21.4117  (E  )  A (   239.61)  A
118- 118  0.1038E-04   707.2048   21.2015  (A1 )  A (   497.97)  A      118- 118  0.1097E-04   726.8802   21.7913  (A1 )  A (   169.34)  A
119- 120  0.1046E-04   709.7378   21.2774  (E  )  A (    52.01)  A      119- 120  0.1101E-04   728.2288   21.8318  (E  )  A (     0.12)  A
121- 122  0.1078E-04   720.6488   21.6045  (E  )  A (   179.33)  A      121- 122  0.1151E-04   744.6090   22.3228  (E  )  A (    45.84)  A
123- 124  0.1192E-04   757.8039   22.7184  (E  )  A (   572.56)  A      123- 124  0.1201E-04   760.6203   22.8028  (E  )  A (     0.96)  A
125- 126  0.1209E-04   763.0774   22.8765  (E  )  A (   191.09)  A      125- 125  0.1223E-04   767.3926   23.0059  (A1 )  A (   547.02)  A
127- 127  0.1227E-04   768.8959   23.0509  (A1 )  A (   964.65)  A      126- 127  0.1356E-04   808.0459   24.2246  (E  )  A (  1024.92)  A
128- 128  0.1285E-04   786.8357   23.5887  (A1 )  A (    20.78)  A      128- 128  0.1406E-04   822.8805   24.6693  (A1 )  A (    49.46)  A
129- 129  0.1819E-04   936.1532   28.0652  (A2 )  I (     0.00)  I      129- 129  0.1859E-04   946.3386   28.3705  (A2 )  I (     0.00)  I
130- 131  0.1837E-04   940.7379   28.2026  (E  )  A (   406.23)  A      130- 131  0.1887E-04   953.4682   28.5843  (E  )  A (   383.04)  A
132- 132  0.1859E-04   946.2438   28.3677  (A2 )  I (     0.00)  I      132- 132  0.1900E-04   956.6525   28.6797  (A2 )  I (     0.00)  I
133- 133  0.1898E-04   956.1141   28.6636  (A1 )  A (   417.08)  A      133- 133  0.1933E-04   964.9015   28.9270  (A1 )  A (   523.43)  A
134- 135  0.1917E-04   960.9943   28.8099  (E  )  A (  6648.21)  A      134- 135  0.1976E-04   975.6078   29.2480  (E  )  A (  6276.05)  A
136- 136  0.2031E-04   989.1264   29.6533  (A2 )  I (     0.00)  I      136- 137  0.2076E-04  1000.0455   29.9806  (E  )  A (   132.99)  A
137- 138  0.2054E-04   994.6498   29.8188  (E  )  A (    94.82)  A      138- 138  0.2092E-04  1003.8584   30.0949  (A2 )  I (     0.00)  I
139- 140  0.2151E-04  1017.8075   30.5131  (E  )  A (    89.80)  A      139- 140  0.2168E-04  1021.9453   30.6371  (E  )  A (   444.37)  A
141- 142  0.2184E-04  1025.6975   30.7496  (E  )  A (   390.18)  A      141- 142  0.2214E-04  1032.7220   30.9602  (E  )  A (    58.88)  A
143- 143  0.2222E-04  1034.5788   31.0159  (A1 )  A (  3073.30)  A      143- 143  0.2229E-04  1036.2542   31.0661  (A1 )  A (  3322.83)  A
144- 145  0.2226E-04  1035.4820   31.0430  (E  )  A (    15.79)  A      144- 145  0.2251E-04  1041.4041   31.2205  (E  )  A (   228.11)  A
146- 146  0.2266E-04  1044.6994   31.3193  (A2 )  I (     0.00)  I      146- 146  0.2338E-04  1061.2754   31.8162  (A1 )  A (    16.47)  A
147- 147  0.2287E-04  1049.6366   31.4673  (A1 )  A (    63.60)  A      147- 147  0.2345E-04  1062.8297   31.8628  (A2 )  I (     0.00)  I
148- 149  0.2302E-04  1053.0549   31.5698  (E  )  A (   930.11)  A      148- 149  0.2399E-04  1074.9893   32.2274  (E  )  A (   863.42)  A
150- 150  0.2442E-04  1084.4947   32.5123  (A2 )  I (     0.00)  I      150- 151  0.2469E-04  1090.5406   32.6936  (E  )  A (  1245.20)  A
151- 152  0.2447E-04  1085.7324   32.5494  (E  )  A (  1099.54)  A      152- 152  0.2491E-04  1095.3702   32.8384  (A2 )  I (     0.00)  I
153- 154  0.3212E-04  1243.8041   37.2883  (E  )  A (  2398.45)  A      153- 154  0.3328E-04  1266.0632   37.9556  (E  )  A (  2169.73)  A
155- 155  0.3470E-04  1292.9301   38.7611  (A2 )  I (     0.00)  I      155- 155  0.3575E-04  1312.3232   39.3425  (A2 )  I (     0.00)  I
156- 157  0.3801E-04  1353.1988   40.5679  (E  )  A (  2974.03)  A      156- 157  0.3769E-04  1347.4396   40.3952  (E  )  A (  3439.93)  A
158- 158  0.4116E-04  1408.0512   42.2123  (A1 )  A (   100.94)  A      158- 158  0.3992E-04  1386.7478   41.5737  (A1 )  A (   317.48)  A
159- 159  0.2772E-03  3654.1934  109.5500  (A1 )  A (   887.93)  A      159- 159  0.2712E-03  3614.4758  108.3593  (A1 )  A (  1511.68)  A
160- 161  0.2773E-03  3654.5246  109.5599  (E  )  A (    30.72)  A      160- 161  0.2713E-03  3614.8033  108.3691  (E  )  A (    44.47)  A
162- 162  0.3135E-03  3886.0107  116.4997  (A1 )  A (    19.96)  A      162- 162  0.2924E-03  3752.8347  112.5072  (A1 )  A (    18.46)  A
```

Figure 70: List of the computed vibrational modes frequencies for dravite and schorl.

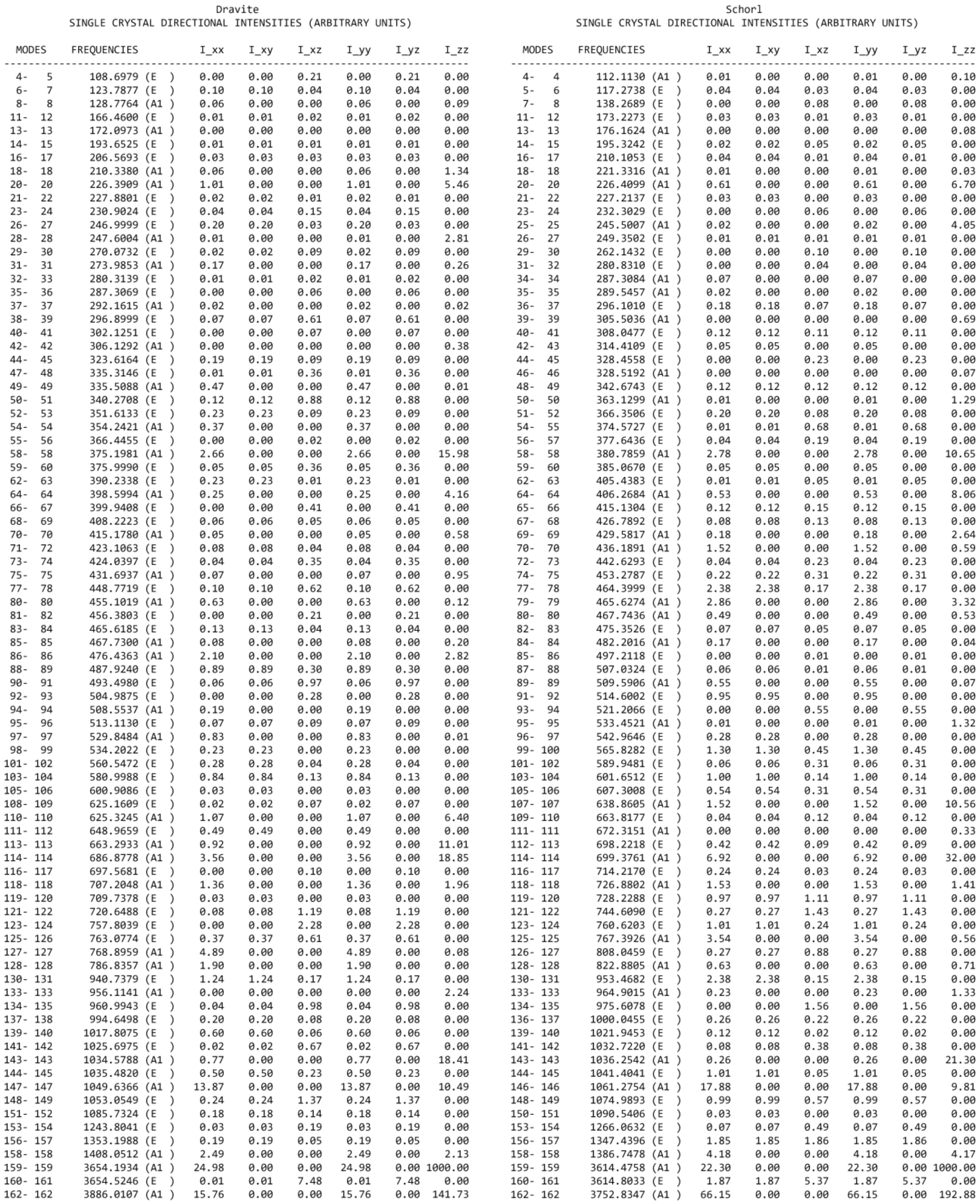

```
                                  Dravite
          SINGLE CRYSTAL DIRECTIONAL INTENSITIES (ARBITRARY UNITS)

  MODES    FREQUENCIES          I_xx    I_xy    I_xz    I_yy    I_yz    I_zz
-----------------------------------------------------------------------------
   4-   5       108.6979 (E  )    0.00    0.00    0.21    0.00    0.21    0.00
   6-   7       123.7877 (E  )    0.10    0.10    0.04    0.10    0.04    0.00
   8-   8       128.7764 (A1 )    0.06    0.00    0.00    0.06    0.00    0.09
  11-  12       166.4600 (E  )    0.01    0.01    0.02    0.01    0.02    0.00
  13-  13       172.0973 (A1 )    0.00    0.00    0.00    0.00    0.00    0.00
  14-  15       193.6525 (E  )    0.01    0.01    0.01    0.01    0.01    0.00
  16-  17       206.5693 (E  )    0.03    0.03    0.03    0.03    0.03    0.00
  18-  18       210.3380 (A1 )    0.06    0.00    0.00    0.06    0.00    1.34
  20-  20       226.3909 (A1 )    1.01    0.00    0.00    1.01    0.00    5.46
  21-  22       227.8801 (E  )    0.02    0.02    0.01    0.02    0.01    0.00
  23-  24       230.9024 (E  )    0.04    0.04    0.15    0.04    0.15    0.00
  26-  27       246.9999 (E  )    0.20    0.20    0.03    0.20    0.03    0.00
  28-  28       247.6004 (A1 )    0.01    0.00    0.00    0.01    0.00    2.81
  29-  30       270.0732 (E  )    0.02    0.02    0.09    0.02    0.09    0.00
  31-  31       273.9853 (A1 )    0.17    0.00    0.00    0.17    0.00    0.26
  32-  33       280.3139 (E  )    0.01    0.01    0.02    0.01    0.02    0.00
  35-  36       287.3069 (E  )    0.00    0.00    0.06    0.00    0.06    0.00
  37-  37       292.1615 (A1 )    0.02    0.00    0.00    0.02    0.00    0.02
  38-  39       296.8999 (E  )    0.07    0.07    0.61    0.07    0.61    0.00
  40-  41       302.1251 (E  )    0.00    0.00    0.07    0.00    0.07    0.00
  42-  42       306.1292 (A1 )    0.00    0.00    0.00    0.00    0.00    0.38
  44-  45       323.6164 (E  )    0.19    0.19    0.09    0.19    0.09    0.00
  47-  48       335.3146 (E  )    0.01    0.01    0.36    0.01    0.36    0.00
  49-  49       335.5088 (A1 )    0.47    0.00    0.00    0.47    0.00    0.01
  50-  51       340.2708 (E  )    0.12    0.12    0.88    0.12    0.88    0.00
  52-  53       351.6133 (E  )    0.23    0.23    0.09    0.23    0.09    0.00
  54-  54       354.2421 (A1 )    0.37    0.00    0.00    0.37    0.00    0.00
  55-  56       366.4455 (E  )    0.00    0.00    0.02    0.00    0.02    0.00
  58-  58       375.1981 (A1 )    2.66    0.00    0.00    2.66    0.00   15.98
  59-  60       375.9990 (E  )    0.05    0.05    0.36    0.05    0.36    0.00
  62-  63       390.2338 (E  )    0.23    0.23    0.01    0.23    0.01    0.00
  64-  64       398.5994 (A1 )    0.25    0.00    0.00    0.25    0.00    4.16
  66-  67       399.9408 (E  )    0.00    0.00    0.41    0.00    0.41    0.00
  68-  69       408.2223 (E  )    0.06    0.06    0.05    0.06    0.05    0.00
  70-  70       415.1780 (A1 )    0.05    0.00    0.00    0.05    0.00    0.58
  71-  72       423.1063 (E  )    0.08    0.08    0.04    0.08    0.04    0.00
  73-  74       424.0397 (E  )    0.04    0.04    0.35    0.04    0.35    0.00
  75-  75       431.6937 (A1 )    0.07    0.00    0.00    0.07    0.00    0.95
  77-  78       448.7719 (E  )    0.10    0.10    0.62    0.10    0.62    0.00
  80-  80       455.1019 (A1 )    0.63    0.00    0.00    0.63    0.00    0.12
  81-  82       456.3803 (E  )    0.00    0.00    0.21    0.00    0.21    0.00
  83-  84       465.6185 (E  )    0.13    0.13    0.04    0.13    0.04    0.00
  85-  85       467.7300 (A1 )    0.08    0.00    0.00    0.08    0.00    0.20
  86-  86       476.4363 (A1 )    2.10    0.00    0.00    2.10    0.00    2.82
  88-  89       487.9240 (E  )    0.89    0.89    0.30    0.89    0.30    0.00
  90-  91       493.4980 (E  )    0.06    0.06    0.97    0.06    0.97    0.00
  92-  93       504.9875 (E  )    0.00    0.00    0.28    0.00    0.28    0.00
  94-  94       508.5537 (A1 )    0.19    0.00    0.00    0.19    0.00    0.00
  95-  96       513.1130 (E  )    0.07    0.07    0.09    0.07    0.09    0.00
  97-  97       529.8484 (A1 )    0.83    0.00    0.00    0.83    0.00    0.01
  98-  99       534.2022 (E  )    0.23    0.23    0.00    0.23    0.00    0.00
 101- 102       560.5472 (E  )    0.28    0.28    0.04    0.28    0.04    0.00
 103- 104       580.9988 (E  )    0.84    0.84    0.13    0.84    0.13    0.00
 105- 106       600.9086 (E  )    0.03    0.03    0.00    0.03    0.00    0.00
 108- 109       625.1609 (E  )    0.02    0.02    0.07    0.02    0.07    0.00
 110- 110       625.3245 (A1 )    1.07    0.00    0.00    1.07    0.00    6.40
 111- 112       648.9659 (E  )    0.49    0.49    0.00    0.49    0.00    0.00
 113- 113       663.2933 (A1 )    0.92    0.00    0.00    0.92    0.00   11.01
 114- 114       686.8778 (A1 )    3.56    0.00    0.00    3.56    0.00   18.85
 116- 117       697.5681 (E  )    0.00    0.00    0.10    0.00    0.10    0.00
 118- 118       707.2048 (A1 )    1.36    0.00    0.00    1.36    0.00    1.96
 119- 120       709.7378 (E  )    0.03    0.03    0.00    0.03    0.00    0.00
 121- 122       720.6488 (E  )    0.08    0.08    1.19    0.08    1.19    0.00
 123- 124       757.8039 (E  )    0.00    0.00    2.28    0.00    2.28    0.00
 125- 126       763.0774 (E  )    0.37    0.37    0.61    0.37    0.61    0.00
 127- 127       768.8959 (A1 )    4.89    0.00    0.00    4.89    0.00    0.08
 128- 128       786.8357 (A1 )    1.90    0.00    0.00    1.90    0.00    0.00
 130- 131       940.7379 (E  )    1.24    1.24    0.17    1.24    0.17    0.00
 133- 133       956.1141 (A1 )    0.00    0.00    0.00    0.00    0.00    2.24
 134- 135       960.9943 (E  )    0.04    0.04    0.98    0.04    0.98    0.00
 137- 138       994.6498 (E  )    0.20    0.20    0.08    0.20    0.08    0.00
 139- 140      1017.8075 (E  )    0.60    0.60    0.06    0.60    0.06    0.00
 141- 142      1025.6975 (E  )    0.02    0.02    0.67    0.02    0.67    0.00
 143- 143      1034.5788 (A1 )    0.77    0.00    0.00    0.77    0.00   18.41
 144- 145      1035.4820 (E  )    0.50    0.50    0.23    0.50    0.23    0.00
 147- 147      1049.6366 (A1 )   13.87    0.00    0.00   13.87    0.00   10.49
 148- 149      1053.0549 (E  )    0.24    0.24    1.37    0.24    1.37    0.00
 151- 152      1085.7324 (E  )    0.18    0.18    0.14    0.18    0.14    0.00
 153- 154      1243.8041 (E  )    0.03    0.03    0.19    0.03    0.19    0.00
 156- 157      1353.1988 (E  )    0.19    0.19    0.05    0.19    0.05    0.00
 158- 158      1408.0512 (A1 )    2.49    0.00    0.00    2.49    0.00    2.13
 159- 159      3654.1934 (A1 )   24.98    0.00    0.00   24.98    0.00 1000.00
 160- 161      3654.5246 (E  )    0.01    0.01    7.48    0.01    7.48    0.00
 162- 162      3886.0107 (A1 )   15.76    0.00    0.00   15.76    0.00  141.73
```

```
                                  Schorl
          SINGLE CRYSTAL DIRECTIONAL INTENSITIES (ARBITRARY UNITS)

  MODES    FREQUENCIES          I_xx    I_xy    I_xz    I_yy    I_yz    I_zz
-----------------------------------------------------------------------------
   4-   4       112.1130 (A1 )    0.01    0.00    0.00    0.01    0.00    0.10
   5-   6       117.2738 (E  )    0.04    0.04    0.03    0.04    0.03    0.00
   7-   8       138.2689 (E  )    0.00    0.00    0.08    0.00    0.08    0.00
  11-  12       173.2273 (E  )    0.03    0.03    0.01    0.03    0.01    0.00
  13-  13       176.1624 (A1 )    0.00    0.00    0.00    0.00    0.00    0.08
  14-  15       195.3242 (E  )    0.02    0.02    0.05    0.02    0.05    0.00
  16-  17       210.1053 (E  )    0.04    0.04    0.01    0.04    0.01    0.00
  18-  18       221.3316 (A1 )    0.01    0.00    0.00    0.01    0.00    0.03
  20-  20       226.4099 (A1 )    0.61    0.00    0.00    0.61    0.00    6.70
  21-  22       227.2137 (E  )    0.03    0.03    0.00    0.03    0.00    0.00
  23-  24       232.3029 (E  )    0.00    0.00    0.06    0.00    0.06    0.00
  25-  25       245.5007 (A1 )    0.02    0.00    0.00    0.02    0.00    4.05
  26-  27       249.3502 (E  )    0.01    0.01    0.01    0.01    0.01    0.00
  29-  30       262.1432 (E  )    0.00    0.00    0.10    0.00    0.10    0.00
  31-  32       280.8310 (E  )    0.00    0.00    0.04    0.00    0.04    0.00
  34-  34       287.3084 (A1 )    0.07    0.00    0.00    0.07    0.00    0.00
  35-  35       289.5457 (A1 )    0.02    0.00    0.00    0.02    0.00    0.00
  36-  37       296.1010 (E  )    0.18    0.18    0.07    0.18    0.07    0.00
  39-  39       305.5036 (A1 )    0.00    0.00    0.00    0.00    0.00    0.69
  40-  41       308.0477 (E  )    0.12    0.12    0.11    0.12    0.11    0.00
  42-  43       314.4109 (E  )    0.05    0.05    0.00    0.05    0.00    0.00
  44-  45       328.4558 (E  )    0.00    0.00    0.23    0.00    0.23    0.00
  46-  46       328.5192 (A1 )    0.00    0.00    0.00    0.00    0.00    0.07
  48-  49       342.6743 (E  )    0.12    0.12    0.12    0.12    0.12    0.00
  50-  50       363.1299 (A1 )    0.01    0.00    0.00    0.01    0.00    1.29
  51-  52       366.3506 (E  )    0.20    0.20    0.08    0.20    0.08    0.00
  54-  55       374.5727 (E  )    0.01    0.01    0.68    0.01    0.68    0.00
  56-  57       377.6436 (E  )    0.04    0.04    0.19    0.04    0.19    0.00
  58-  58       380.7859 (A1 )    2.78    0.00    0.00    2.78    0.00   10.65
  59-  60       385.0670 (E  )    0.05    0.05    0.00    0.05    0.00    0.00
  62-  63       405.4383 (E  )    0.01    0.01    0.05    0.01    0.05    0.00
  64-  64       406.2684 (A1 )    0.53    0.00    0.00    0.53    0.00    8.06
  65-  66       415.1304 (E  )    0.12    0.12    0.15    0.12    0.15    0.00
  67-  68       426.7892 (E  )    0.08    0.08    0.13    0.08    0.13    0.00
  69-  69       429.5817 (A1 )    0.18    0.00    0.00    0.18    0.00    2.64
  70-  70       436.1891 (A1 )    1.52    0.00    0.00    1.52    0.00    0.59
  72-  73       442.6293 (E  )    0.04    0.04    0.23    0.04    0.23    0.00
  74-  75       453.2787 (E  )    0.22    0.22    0.31    0.22    0.31    0.00
  77-  78       464.3999 (E  )    2.38    2.38    0.17    2.38    0.17    0.00
  79-  79       465.6274 (A1 )    2.86    0.00    0.00    2.86    0.00    3.32
  80-  80       467.7436 (A1 )    0.49    0.00    0.00    0.49    0.00    0.53
  82-  83       475.3526 (E  )    0.07    0.07    0.05    0.07    0.05    0.00
  84-  84       482.2016 (A1 )    0.17    0.00    0.00    0.17    0.00    0.04
  85-  86       497.2118 (E  )    0.00    0.00    0.01    0.00    0.01    0.00
  87-  88       507.0324 (E  )    0.06    0.06    0.01    0.06    0.01    0.00
  89-  89       509.5906 (A1 )    0.55    0.00    0.00    0.55    0.00    0.07
  91-  92       514.6002 (E  )    0.95    0.95    0.00    0.95    0.00    0.00
  93-  94       521.2066 (E  )    0.00    0.00    0.55    0.00    0.55    0.00
  95-  95       533.4521 (A1 )    0.01    0.00    0.00    0.01    0.00    1.32
  96-  97       542.9646 (E  )    0.28    0.28    0.00    0.28    0.00    0.00
  99- 100       565.8282 (E  )    1.30    1.30    0.45    1.30    0.45    0.00
 101- 102       589.9481 (E  )    0.06    0.06    0.31    0.06    0.31    0.00
 103- 104       601.6512 (E  )    1.00    1.00    0.14    1.00    0.14    0.00
 105- 106       607.3008 (E  )    0.54    0.54    0.31    0.54    0.31    0.00
 107- 107       638.8605 (A1 )    1.52    0.00    0.00    1.52    0.00   10.56
 109- 110       663.8177 (E  )    0.04    0.04    0.12    0.04    0.12    0.00
 111- 111       672.3151 (A1 )    0.00    0.00    0.00    0.00    0.00    0.33
 112- 113       698.2218 (E  )    0.42    0.42    0.09    0.42    0.09    0.00
 114- 114       699.3761 (A1 )    6.92    0.00    0.00    6.92    0.00   32.00
 116- 117       714.2170 (E  )    0.24    0.24    0.03    0.24    0.03    0.00
 118- 118       726.8802 (A1 )    1.53    0.00    0.00    1.53    0.00    1.41
 119- 120       728.2288 (E  )    0.97    0.97    1.11    0.97    1.11    0.00
 121- 122       744.6090 (E  )    0.27    0.27    1.43    0.27    1.43    0.00
 123- 124       760.6203 (E  )    1.01    1.01    0.24    1.01    0.24    0.00
 125- 125       767.3926 (A1 )    3.54    0.00    0.00    3.54    0.00    0.56
 126- 127       808.0459 (E  )    0.27    0.27    0.88    0.27    0.88    0.00
 128- 128       822.8805 (A1 )    0.63    0.00    0.00    0.63    0.00    0.71
 130- 131       953.4682 (E  )    2.38    2.38    0.15    2.38    0.15    0.00
 133- 133       964.9015 (A1 )    0.23    0.00    0.00    0.23    0.00    1.33
 134- 135       975.6078 (E  )    0.00    0.00    1.56    0.00    1.56    0.00
 136- 137      1000.0455 (E  )    0.26    0.26    0.22    0.26    0.22    0.00
 139- 140      1021.9453 (E  )    0.12    0.12    0.02    0.12    0.02    0.00
 141- 142      1032.7220 (E  )    0.08    0.08    0.38    0.08    0.38    0.00
 143- 143      1036.2542 (A1 )    0.26    0.00    0.00    0.26    0.00   21.30
 144- 145      1041.4041 (E  )    1.01    1.01    0.05    1.01    0.05    0.00
 146- 146      1061.2754 (A1 )   17.88    0.00    0.00   17.88    0.00    9.81
 148- 149      1074.9893 (E  )    0.99    0.99    0.57    0.99    0.57    0.00
 150- 151      1090.5406 (E  )    0.03    0.03    0.00    0.03    0.00    0.00
 153- 154      1266.0632 (E  )    0.07    0.07    0.49    0.07    0.49    0.00
 156- 157      1347.4396 (E  )    1.85    1.85    1.86    1.85    1.86    0.00
 158- 158      1386.7478 (A1 )    4.18    0.00    0.00    4.18    0.00    4.17
 159- 159      3614.4758 (A1 )   22.30    0.00    0.00   22.30    0.00 1000.00
 160- 161      3614.8033 (E  )    1.87    1.87    5.37    1.87    5.37    0.00
 162- 162      3752.8347 (A1 )   66.15    0.00    0.00   66.15    0.00  192.88
```

Figure 71: List of the normalised Raman intensities calculated for the active modes (A1 and E) in the case of single crystal for dravite and schorl.

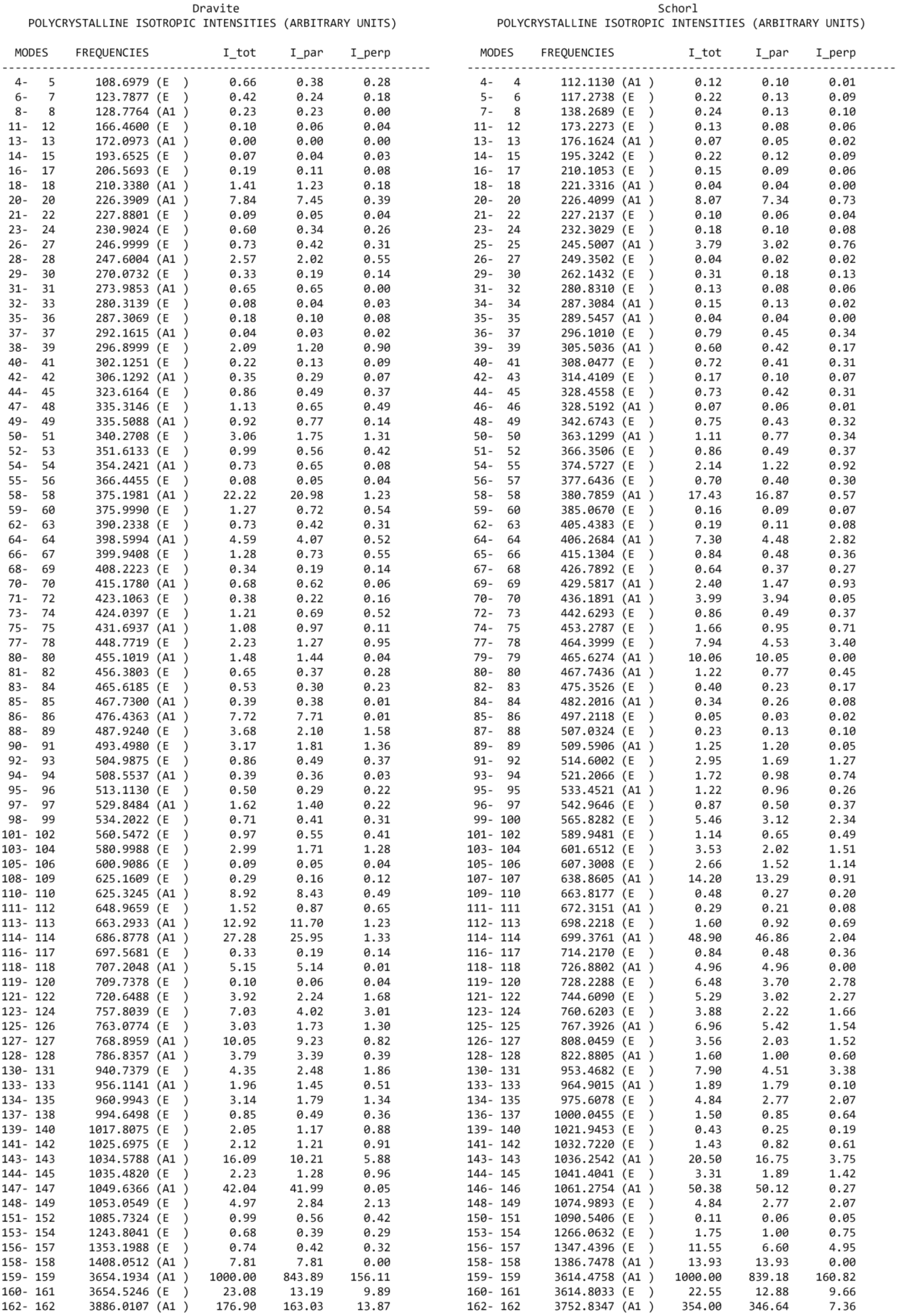

```
                              Dravite
   POLYCRYSTALLINE ISOTROPIC INTENSITIES (ARBITRARY UNITS)

  MODES    FREQUENCIES          I_tot     I_par    I_perp
----------------------------------------------------------------
  4-   5     108.6979 (E  )      0.66      0.38      0.28
  6-   7     123.7877 (E  )      0.42      0.24      0.18
  8-   8     128.7764 (A1 )      0.23      0.23      0.00
 11-  12     166.4600 (E  )      0.10      0.06      0.04
 13-  13     172.0973 (A1 )      0.00      0.00      0.00
 14-  15     193.6525 (E  )      0.07      0.04      0.03
 16-  17     206.5693 (E  )      0.19      0.11      0.08
 18-  18     210.3380 (A1 )      1.41      1.23      0.18
 20-  20     226.3909 (A1 )      7.84      7.45      0.39
 21-  22     227.8801 (E  )      0.09      0.05      0.04
 23-  24     230.9024 (E  )      0.60      0.34      0.26
 26-  27     246.9999 (E  )      0.73      0.42      0.31
 28-  28     247.6004 (A1 )      2.57      2.02      0.55
 29-  30     270.0732 (E  )      0.33      0.19      0.14
 31-  31     273.9853 (A1 )      0.65      0.65      0.00
 32-  33     280.3139 (E  )      0.08      0.04      0.03
 35-  36     287.3069 (E  )      0.18      0.10      0.08
 37-  37     292.1615 (A1 )      0.04      0.03      0.02
 38-  39     296.8999 (E  )      2.09      1.20      0.90
 40-  41     302.1251 (E  )      0.22      0.13      0.09
 42-  42     306.1292 (A1 )      0.35      0.29      0.07
 44-  45     323.6164 (E  )      0.86      0.49      0.37
 47-  48     335.3146 (E  )      1.13      0.65      0.49
 49-  49     335.5088 (A1 )      0.92      0.77      0.14
 50-  51     340.2708 (E  )      3.06      1.75      1.31
 52-  53     351.6133 (E  )      0.99      0.56      0.42
 54-  54     354.2421 (A1 )      0.73      0.65      0.08
 55-  56     366.4455 (E  )      0.08      0.05      0.04
 58-  58     375.1981 (A1 )     22.22     20.98      1.23
 59-  60     375.9990 (E  )      1.27      0.72      0.54
 62-  63     390.2338 (E  )      0.73      0.42      0.31
 64-  64     398.5994 (A1 )      4.59      4.07      0.52
 66-  67     399.9408 (E  )      1.28      0.73      0.55
 68-  69     408.2223 (E  )      0.34      0.19      0.14
 70-  70     415.1780 (A1 )      0.68      0.62      0.06
 71-  72     423.1063 (E  )      0.38      0.22      0.16
 73-  74     424.0397 (E  )      1.21      0.69      0.52
 75-  75     431.6937 (A1 )      1.08      0.97      0.11
 77-  78     448.7719 (E  )      2.23      1.27      0.95
 80-  80     455.1019 (A1 )      1.48      1.44      0.04
 81-  82     456.3803 (E  )      0.65      0.37      0.28
 83-  84     465.6185 (E  )      0.53      0.30      0.23
 85-  85     467.7300 (A1 )      0.39      0.38      0.01
 86-  86     476.4363 (A1 )      7.72      7.71      0.01
 88-  89     487.9240 (E  )      3.68      2.10      1.58
 90-  91     493.4980 (E  )      3.17      1.81      1.36
 92-  93     504.9875 (E  )      0.86      0.49      0.37
 94-  94     508.5537 (A1 )      0.39      0.36      0.03
 95-  96     513.1130 (E  )      0.50      0.29      0.22
 97-  97     529.8484 (A1 )      1.62      1.40      0.22
 98-  99     534.2022 (E  )      0.71      0.41      0.31
101- 102     560.5472 (E  )      0.97      0.55      0.41
103- 104     580.9988 (E  )      2.99      1.71      1.28
105- 106     600.9086 (E  )      0.09      0.05      0.04
108- 109     625.1609 (E  )      0.29      0.16      0.12
110- 110     625.3245 (A1 )      8.92      8.43      0.49
111- 112     648.9659 (E  )      1.52      0.87      0.65
113- 113     663.2933 (A1 )     12.92     11.70      1.23
114- 114     686.8778 (A1 )     27.28     25.95      1.33
116- 117     697.5681 (E  )      0.33      0.19      0.14
118- 118     707.2048 (A1 )      5.15      5.14      0.01
119- 120     709.7378 (E  )      0.10      0.06      0.04
121- 122     720.6488 (E  )      3.92      2.24      1.68
123- 124     757.8039 (E  )      7.03      4.02      3.01
125- 126     763.0774 (E  )      3.03      1.73      1.30
127- 127     768.8959 (A1 )     10.05      9.23      0.82
128- 128     786.8357 (A1 )      3.79      3.39      0.39
130- 131     940.7379 (E  )      4.35      2.48      1.86
133- 133     956.1141 (A1 )      1.96      1.45      0.51
134- 135     960.9943 (E  )      3.14      1.79      1.34
137- 138     994.6498 (E  )      0.85      0.49      0.36
139- 140    1017.8075 (E  )      2.05      1.17      0.88
141- 142    1025.6975 (E  )      2.12      1.21      0.91
143- 143    1034.5788 (A1 )     16.09     10.21      5.88
144- 145    1035.4820 (E  )      2.23      1.28      0.96
147- 147    1049.6366 (A1 )     42.04     41.99      0.05
148- 149    1053.0549 (E  )      4.97      2.84      2.13
151- 152    1085.7324 (E  )      0.99      0.56      0.42
153- 154    1243.8041 (E  )      0.68      0.39      0.29
156- 157    1353.1988 (E  )      0.74      0.42      0.32
158- 158    1408.0512 (A1 )      7.81      7.81      0.00
159- 159    3654.1934 (A1 )   1000.00    843.89    156.11
160- 161    3654.5246 (E  )     23.08     13.19      9.89
162- 162    3886.0107 (A1 )    176.90    163.03     13.87
```

```
                              Schorl
   POLYCRYSTALLINE ISOTROPIC INTENSITIES (ARBITRARY UNITS)

  MODES    FREQUENCIES          I_tot     I_par    I_perp
----------------------------------------------------------------
  4-   4     112.1130 (A1 )      0.12      0.10      0.01
  5-   6     117.2738 (E  )      0.22      0.13      0.09
  7-   8     138.2689 (E  )      0.24      0.13      0.10
 11-  12     173.2273 (E  )      0.13      0.08      0.06
 13-  13     176.1624 (A1 )      0.07      0.05      0.02
 14-  15     195.3242 (E  )      0.22      0.12      0.09
 16-  17     210.1053 (E  )      0.15      0.09      0.06
 18-  18     221.3316 (A1 )      0.04      0.04      0.00
 20-  20     226.4099 (A1 )      8.07      7.34      0.73
 21-  22     227.2137 (E  )      0.10      0.06      0.04
 23-  24     232.3029 (E  )      0.18      0.10      0.08
 25-  25     245.5007 (A1 )      3.79      3.02      0.76
 26-  27     249.3502 (E  )      0.04      0.02      0.02
 29-  30     262.1432 (E  )      0.31      0.18      0.13
 31-  32     280.8310 (E  )      0.13      0.08      0.06
 34-  34     287.3084 (A1 )      0.15      0.13      0.02
 35-  35     289.5457 (A1 )      0.04      0.04      0.00
 36-  37     296.1010 (E  )      0.79      0.45      0.34
 39-  39     305.5036 (A1 )      0.60      0.42      0.17
 40-  41     308.0477 (E  )      0.72      0.41      0.31
 42-  43     314.4109 (E  )      0.17      0.10      0.07
 44-  45     328.4558 (E  )      0.73      0.42      0.31
 46-  46     328.5192 (A1 )      0.07      0.06      0.01
 48-  49     342.6743 (E  )      0.75      0.43      0.32
 50-  50     363.1299 (A1 )      1.11      0.77      0.34
 51-  52     366.3506 (E  )      0.86      0.49      0.37
 54-  55     374.5727 (E  )      2.14      1.22      0.92
 56-  57     377.6436 (E  )      0.70      0.40      0.30
 58-  58     380.7859 (A1 )     17.43     16.87      0.57
 59-  60     385.0670 (E  )      0.16      0.09      0.07
 62-  63     405.4383 (E  )      0.19      0.11      0.08
 64-  64     406.2684 (A1 )      7.30      4.48      2.82
 65-  66     415.1304 (E  )      0.84      0.48      0.36
 67-  68     426.7892 (E  )      0.64      0.37      0.27
 69-  69     429.5817 (A1 )      2.40      1.47      0.93
 70-  70     436.1891 (A1 )      3.99      3.94      0.05
 72-  73     442.6293 (E  )      0.86      0.49      0.37
 74-  75     453.2787 (E  )      1.66      0.95      0.71
 77-  78     464.3999 (E  )      7.94      4.53      3.40
 79-  79     465.6274 (A1 )     10.06     10.05      0.00
 80-  80     467.7436 (A1 )      1.22      0.77      0.45
 82-  83     475.3526 (E  )      0.40      0.23      0.17
 84-  84     482.2016 (A1 )      0.34      0.26      0.08
 85-  86     497.2118 (E  )      0.05      0.03      0.02
 87-  88     507.0324 (E  )      0.23      0.13      0.10
 89-  89     509.5906 (A1 )      1.25      1.20      0.05
 91-  92     514.6002 (E  )      2.95      1.69      1.27
 93-  94     521.2066 (E  )      1.72      0.98      0.74
 95-  95     533.4521 (A1 )      1.22      0.96      0.26
 96-  97     542.9646 (E  )      0.87      0.50      0.37
 99- 100     565.8282 (E  )      5.46      3.12      2.34
101- 102     589.9481 (E  )      1.14      0.65      0.49
103- 104     601.6512 (E  )      3.53      2.02      1.51
105- 106     607.3008 (E  )      2.66      1.52      1.14
107- 107     638.8605 (A1 )     14.20     13.29      0.91
109- 110     663.8177 (E  )      0.48      0.27      0.20
111- 111     672.3151 (A1 )      0.29      0.21      0.08
112- 113     698.2218 (E  )      1.60      0.92      0.69
114- 114     699.3761 (A1 )     48.90     46.86      2.04
116- 117     714.2170 (E  )      0.84      0.48      0.36
118- 118     726.8802 (A1 )      4.96      4.96      0.00
119- 120     728.2288 (E  )      6.48      3.70      2.78
121- 122     744.6090 (E  )      5.29      3.02      2.27
123- 124     760.6203 (E  )      3.88      2.22      1.66
125- 125     767.3926 (A1 )      6.96      5.42      1.54
126- 127     808.0459 (E  )      3.56      2.03      1.52
128- 128     822.8805 (A1 )      1.60      1.00      0.60
130- 131     953.4682 (E  )      7.90      4.51      3.38
133- 133     964.9015 (A1 )      1.89      1.79      0.10
134- 135     975.6078 (E  )      4.84      2.77      2.07
136- 137    1000.0455 (E  )      1.50      0.85      0.64
139- 140    1021.9453 (E  )      0.43      0.25      0.19
141- 142    1032.7220 (E  )      1.43      0.82      0.61
143- 143    1036.2542 (A1 )     20.50     16.75      3.75
144- 145    1041.4041 (E  )      3.31      1.89      1.42
146- 146    1061.2754 (A1 )     50.38     50.12      0.27
148- 149    1074.9893 (E  )      4.84      2.77      2.07
150- 151    1090.5406 (E  )      0.11      0.06      0.05
153- 154    1266.0632 (E  )      1.75      1.00      0.75
156- 157    1347.4396 (E  )     11.55      6.60      4.95
158- 158    1386.7478 (A1 )     13.93     13.93      0.00
159- 159    3614.4758 (A1 )   1000.00    839.18    160.82
160- 161    3614.8033 (E  )     22.55     12.88      9.66
162- 162    3752.8347 (A1 )    354.00    346.64      7.36
```

Figure 72: List of the normalised Raman intensities calculated for the active modes (A1 and E) in the case of polycrystal for dravite and schorl.

This discussion will concentrate on the Raman intensities of the single crystal in the I_zz orientation to compare computational data with our prior experimental results acquired in the same orientation $(\bar{y}(zz)y)$, focusing only on the A_1 vibrational modes. However, multiple orientations of the single crystal and the polycrystalline mixed contributions from various vibrational modes may enhance future comprehension of the vibrational behaviour of tourmalines.

The calculated Raman spectra for the dravite and schorl single crystals in the I_zz orientation are presented in Figure 73. The distinct regions associated with the individual crystal sites are clearly discernible. We will initially focus on the vibrational modes associated with Y-sites, particularly in the 200-300 cm^{-1} range and then study the behaviour of the OH stretching modes.

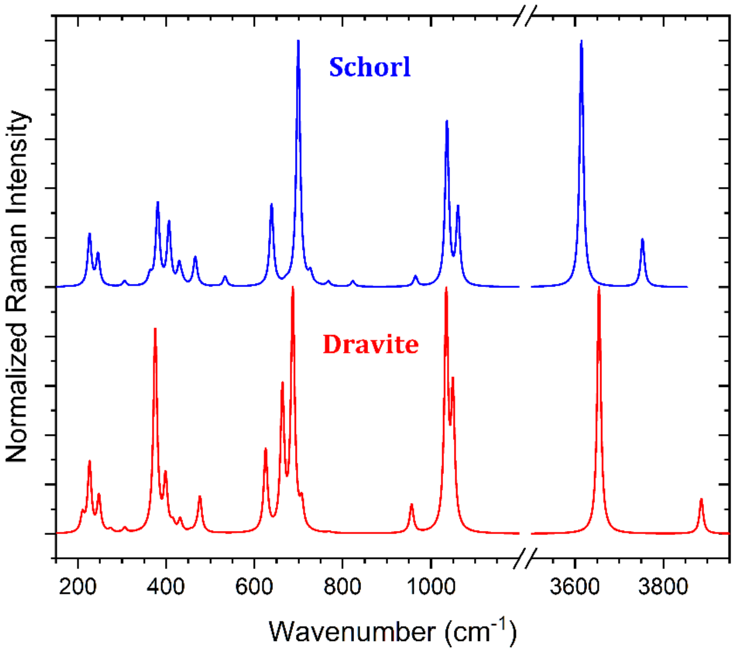

Figure 73: Computed Raman spectra of dravite and schorl in the I_zz $(\bar{y}(zz)y)$ *orientation. peak intensities in the low frequency region are normalised with respect to the* ^{V}*OH band for visualisation.*

In the 200-300 cm^{-1} range, we identify the principal peak as **P_2**, as designated in the experimental data, and the first A_1 mode at a lower wavenumber as **P_1**. This assumption implies that the peak position of P_2 remains constant between schorl (226.41 cm^{-1}) and dravite (226.39 cm^{-1}), contrary to our experimental findings. Conversely, P_1 shifts to a higher position in schorl (221.33 cm^{-1}) compared to dravite (210.34 cm^{-1}); nevertheless, experimental results indicate that it remains fixed in the same position and only shifts to lower wavenumbers in a limited number of schorl samples. The **relative intensities** of the P_1 and P_2 peaks exhibit behaviour closer to experimental observations, with P_1 increasing relative to P_2 in dravite; however, the ratio $I(P_1)/I(P_2)$ remains consistently lower than one, indicating that the intensity of P_1 never exceeds that of P_2, contrary to our empirical results. Ultimately, three further peaks are observed at elevated wavenumbers relative to P_2 within the 200-300 cm^{-1} range. The first peak is situated at approximately 246 cm^{-1}, with its intensity rising from nearly two-thirds of the P_2

peak in schorl to more than one-half in dravite. Even if one posits this peak as P_2, discrepancies from empirical data persist. The last two, within the 270-300 cm^{-1} range, exhibit minimal intensity, dropping to zero in schorl. All parameters of the five computed A_1 vibrational modes within the 200-300 cm^{-1} region are presented in Table 21

Although the reasons for the discrepancies between the calculated parameters and the experimental values remain uncertain, one potential explanation may be attributed to the lack of structural and compositional disorder in ab initio calculations. This is particularly relevant regarding the presence of elements beyond those in the dravite and schorl end-member formulas, as well as the possible disorder between Y- and Z-sites, with aluminium occupying Y-sites and magnesium and iron occupying Z-sites.

Dravite		*Schorl*	
Wavenumber (cm^{-1})	**Raman Intensity**	**Wavenumber (cm^{-1})**	**Raman Intensity**
210.34	1.34	221.33	0.03
226.39	5.46	226.41	6.7
247.60	2.81	245.50	4.05
273.99	0.26	287.31	0
292.16	0.02	289.55	0

Table 21: Positions and intensities of the computed A_1 Raman peaks (in the single crystal case with the I_zz orientation) in the 200-300cm^{-1} region for dravite and schorl. Raman intensities are normalised fixing the intensity of the A_1 ^{V}OH band to 1000.

The impact of the absence of structural and compositional disorder is significantly more evident in the computed A_1 Raman modes within the OH stretching region. In this instance, there exists only **one mode** for the **^{V}OH groups** and one for the **^{W}OH**, contrary to the numerous peaks observed experimentally, attributed to the singular atomic configuration surrounding the V- and W-sites. The single vibrational modes link to the **3^{Y}Mg^{Z}Al^{Z}Al** configuration and the **^{X}Na-^{Y}Mg^{Y}Mg^{Y}Mg** configuration for ^{V}OH and ^{W}OH in dravite, as well as the **3^{Y}Fe^{Z}Al^{Z}Al** and **^{X}Na-^{Y}Fe^{Y}Fe^{Y}Fe** configurations in schorl. The ^{V}OH A_1 modes shift from 3614.48 cm^{-1} in schorl to 3654.52 cm^{-1} in dravite, disagreeing with the literature values of 3566 cm^{-1} and 3573 cm^{-1} associated with the 3^{Y}Fe^{Z}Al^{Z}Al and 3^{Y}Mg^{Z}Al^{Z}Al configurations[129]. The difference over 50 cm^{-1} in the calculated vibrational modes is attributable to the harmonic approximation used by CRYSTAL23 for vibrational frequencies computation. Although corrections can be made by **anharmonic frequencies calculations**[223–225], fine-tuning remains unattainable. Nonetheless, the relative positioning of the two peaks aligns with the experimental findings, with the peak in dravite occurring at higher wavenumbers compared to schorl. This behaviour is supported by the ^{W}OH A_1 modes, where the peak associated with the ^{X}Na-^{Y}Fe^{Y}Fe^{Y}Fe configuration in schorl is positioned at 3752.83 cm^{-1}, and the peak corresponding to the ^{X}Na-^{Y}Mg^{Y}Mg^{Y}Mg configuration in dravite is situated at 3886.01 cm^{-1}. The significant gap with the experimental data, reaching up to 100 cm^{-1}, pertains again to the CRYSTAL23 frequency calculation methodology; nevertheless, the shift of the $^{W}OH_3$ peak to higher wavenumbers with increasing magnesium concentration found experimentally is validated.

In conclusion, ab initio calculations can elucidate the theoretical behaviour of tourmaline Raman modes as composition varies, avoiding the structural and compositional disorder present in natural samples used in the experimental approach. Nevertheless, as the results presented are merely preliminary calculations concerning the dravite and schorl end-member compositions, additional simulations will be necessary in the future, particularly on the **mixed compositions**, to enhance the understanding of how the peak parameters in the Raman spectrum change in relation to variations in the Mg/(Mg+Fe) ratio within the dravite-schorl series. To maintain symmetry, the current approach requires the use of **supercells** for the investigation of mixed compositions, which consist of various unit cells with varying chemical composition. This approach increases the atoms number for calculations, thereby lengthening computational time.

Chapter 6

Conclusions

The aim of this PhD thesis was to illustrate the efficacy of Raman spectroscopy in distinguishing between various tourmaline species and acquiring data on their chemical composition through a rapid and non-destructive technique, identifying a model that correlates deviations in these minerals' compositions with variations in the Raman spectra. The purpose was to improve existing results in literature and address unresolved questions. This was mainly intended for geological and gemmological applications, exploiting the capabilities of Raman spectroscopy to analyse tourmalines in sediments and gemstones. Nonetheless, the applications of tourmalines are extensive in several domains, enabling the results achieved to be relevant across multiple fields. We further evaluate our findings by ab initio calculations to verify their theoretical accuracy, and with portable Raman instrument to assess the usability of these results for *in situ* study.

Concerning the dravite and schorl species, distinguished by their complementary magnesium and iron content in the Y-sites, we identified a correlation between the Mg/(Mg+Fe) ratio and the fluctuations in specific peak parameters within the Raman spectrum. Notably, we concentrated on the P_1 and P_2 peaks in the 200-315 cm^{-1} range and the $^{W}OH_3$ peak in the OH stretching region, which exhibit the most intriguing behaviours. The peak position of P_2 facilitates the identification of dravite and schorl, with the first species exhibiting this peak above 239 cm^{-1} and the second one below, so enabling rapid identification of the two species, even during *in situ* analyses conducted with portable Raman instruments. To achieve quantitative data regarding the Mg/(Mg+Fe) ratio, we focused on the relative intensities of the P_1 and P_2 peaks ($I(P_1)/I(P_2)$) and the positioning of the $^{W}OH_3$ peaks, which exhibit a linear correlation with the relative concentrations of magnesium and iron. The results were further enhanced through μXANES measurements, which facilitated the identification of various oxidation states of iron (Fe^{2+} and Fe^{3+}) and established the correlation between the two Raman parameters and the $Mg/(Mg+Fe^{2+})$ ratio. This emphasises the fraction of iron present in the Y-sites, expected to be ferrous in the absence of chemical disorder between the Y- and Z-sites. The derived formula for the linear correlations of the two Raman parameters can be inverted to yield the subsequent equations for the relative concentrations of magnesium and ferrous iron in the dravite-schorl series:

$$Mg/(Mg + Fe^{2+}) = \frac{I(P_1)/I(P_2) - 0.1}{1}$$

$$Mg/(Mg + Fe^{2+}) = \frac{\omega(^{W}OH_3) - 3716}{22}$$

These equations enable the reconstruction of composition by examining a singular portion of the Raman spectrum: the low-frequency region for the first equation and the OH stretching region for the second equation. However, to achieve more accurate findings, the average Mg/(Mg+Fe^{2+}) ratio from the two regions should be considered. This may prevent systematic errors caused, for instance, by a partial overlap of P_1 and P_2 peaks, particularly in schorl where P_1 is weaker than P_2 and occasionally appears only as a shoulder, potentially impacting the assessment of their intensities, as well as the possible weaker signals of ^{W}OH modes, which can complicate the precise determination of the $^{W}OH_3$ position.

The results for the dravite-schorl series were specifically intended for provenance studies, taking advantage of the high resolution of Raman spectroscopy and the capability for rapid measurements to analyse hundreds of micrometric grains in detrital sediments. This process helps to divides them into the two species and provides information on the Mg/(Mg+Fe^{2+}) relative content, which can be employed to reconstruct their source rocks, thereby elucidating their potential geographic origins, geological history, and possible correlations with ore deposits. This is a significant advancement in the identification of tourmaline species in sediments, since dravite and schorl are not always easily distinguished by visual inspection under an optical microscope, and chemical analyses of their composition to evaluate the relative concentrations of iron and magnesium are time consuming.

Future improvements of these results should concentrate on assessing the impact of structural and chemical disorder in the tourmaline species, thereby evaluating the potential effects associated with the presence of elements beyond those predicted by the dravite and schorl end-member formulas, as well as the possible influence of occupational disorder between the Y- and Z-sites, which may lead to altered charge distribution and consequently distort the crystal structure, thereby affecting the frequencies of vibrational modes. Another strategy should involve the exclusion of disorder, which is associated with natural samples, by employing ab initio calculations to evaluate the theoretical behaviour of vibrational modes, thereby maintaining complete control over the chemical composition of the analysed samples and achieving a more accurate correlation.

Regarding the elbaite species, we focused on the presence of various chromophores responsible for distinct colour variations: copper for blue, iron for green, and manganese for pink. The objective was to assess the possibility of employing a rapid and non-destructive method such as Raman spectroscopy to determine the chromophore concentration in tourmaline gemstones and, consequently, their potential market worth.

Before investigating the chromophores, we established an accurate and univocal criterion for employing Raman spectroscopy to quickly differentiate elbaite species from liddicoatite species, even in arbitrary orientations, addressing a previously unresolved question in literature. This is significant because, in cut and mounted gemstones, it is not always feasible to select the optimal $\bar{y}(zz)y$ orientation that we previously employed for the analysis of dravite and schorl. The main ^{V}OH band helps to differentiate the two species, with elbaite exhibiting it below 3600 cm^{-1} and liddicoatite presenting it beyond that threshold. Consequently, we can immediately assess the tourmaline gemstone species, acquiring initial information regarding their composition, with elbaite exhibiting a higher sodium concentration at the X-site and liddicoatite demonstrating increased calcium levels, along with a marginally elevated lithium content in the Y-sites (ranging from 1.5 a.p.f.u. in the elbaite end-member formula to 2 a.p.f.u.

in liddicoatite). Upon identifying the tourmaline species of the gemstones, we concentrated on the amount of chromophores, specifically copper and iron in the Paraíba-type tourmalines, and iron and manganese in the pink and green watermelon tourmalines.

In the first case, we did not identify any certain correlation between alterations in the Raman spectrum and fluctuations in the Cu/(Cu+Fe) ratio; however, the UV-VIS-NIR spectrum reveals more intriguing correlations, thereby providing an alternative non-destructive method for determining the concentration of chromophores in Paraíba-type tourmalines. The respective intensities of the 900nm and 700nm absorption bands (A_{900}/A_{700}) correlate with the relative concentrations of copper and iron chromophores. Specifically, we determined those samples exhibiting A_{900}/A_{700} ratios over 1.1 include sufficient copper chromophores (Cu/(Cu+Fe)>0.6) to be classified as Paraíba-type. These results can effectively facilitate the rapid identification of chromophore concentration in a non-destructive manner, hence providing insights into the market value of tourmaline gemstones without the necessity for sample treatments required in conventional chemical analyses. Future analyses may concentrate on identifying a correlation between alterations in both Raman and UV-VIS-NIR spectra and the concentrations of trace elements such as Ga, Pb, Mg, Zn, Sb, Be, and Sc. This correlation could provide insights into the geographical provenance of Paraíba-type gemstones, thereby offering a more accurate characterisation of tourmaline gems and influencing their market value.

Concerning the pink and green watermelon elbaite, we identified a correlation between the emergence of an additional ^{V}OH band at 3560 cm^{-1} and the rising iron concentration in green-hued tourmalines. The µXRF maps indicated that the variations between pink and green colours within the same crystal are not attributable to elevated manganese levels in the pink areas, but rather to the presence or absence of iron in the green and pink regions, respectively. The concentration of iron in the green zones correlates with the increasing intensity of the additional ^{V}OH band ($^{V}OH_3$) relative to the primary Raman band at 3590 cm^{-1} ($^{V}OH_4$), resulting in the conclusion that samples with a $I(^{V}OH_3)/I(^{V}OH_4)$ ratio exceeding 0.5 possess an iron content greater than 25% between the Y- and Z-sites. Consequently, we discovered a method to ascertain the concentration of the iron chromophore in pink and green elbaite by analysing the intensity of the additional ^{V}OH band in the Raman spectrum, so avoiding the necessity for (semi-)destructive conventional chemical analyses. This result can be important in assessing the quality of pink and green tourmaline gemstones based on their iron concentration. Nevertheless, the outcomes can be enhanced by establishing a more robust correlation between Raman spectra and LIBS measurements of iron concentration, particularly through 2D mapping, which would facilitate a point-by-point correlation between the two techniques, rather than conducting measurements in close proximity that may be affected by sample heterogeneity, so future developments should concentrate on this direction.

In conclusion, we established that Raman spectroscopy serves as an effective method for distinguishing between different tourmaline species, specifically dravite from schorl and elbaite from liddicoatite, while also providing insights into their chemical makeup. We concentrated on the most prevalent species, as their samples were more readily available, to get a greater number of specimens for analysis. Nonetheless, although it is occasionally challenging to locate samples, numerous additional tourmaline species warrant investigation to establish links in their Raman spectra with variations in chemical makeup. Consequently, although these findings pertain to a limited number of tourmaline species, we have established a robust foundation for an extensive Raman model that could eventually include all recognised tourmaline species. This advancement would facilitate the rapid differentiation of these species and provide insights into their composition without necessitating any treatment, yielding valuable outcomes applicable across diverse domains, including geology, gemmology, and environmental studies

References

[1] J. Ruskin, *The Ethics of the Dust: Ten Lectures to Little Housewives on the Elements of Crystallization.*, Henry Altemus, Philadelphia, **1894**.

[2] G. E. Hamburger, M. J. Buerger, *American Mineralogist* **1948**, *33*, 532.

[3] D. J. Henry, M. Novák, F. C. Hawthorne, A. Ertl, B. L. Dutrow, P. Uher, F. Pezzotta, *Am. Mineral.* **2011**, *96*, 895.

[4] F. Bosi, *Am. Mineral.* **2018**, *103*, 298.

[5] Mindat database - Tourmaline, https://www.mindat.org/min-4003.html.

[6] F. C. Hawthorne, *Can. Mineral.* **2002**, *40*, 789.

[7] F. C. Hawthorne, D. J. Henry, *Eur. J. Mineral.* **1999**, *11*, 201.

[8] D. J. Henry, B. L. Dutrow, *J Geosci-Czech* **2018**, *63*, 77.

[9] F. C. Hawthorne, D. J. MacDonald, P. C. Burns, *Am. Mineral.* **1993**, *78*, 265.

[10] F. Bosi, *Am. Mineral.* **2008**, *93*, 1647.

[11] F. Bosi, G. B. Andreozzi, U. Hålenius, H. Skogby, *Mineral. Mag.* **2015**, *79*, 515.

[12] V. J. Van Hinsberg, D. J. Henry, H. R. Marschall, *Canadian Mineralogist* **2011**, *49*, 1.

[13] B. Celata, V. Stagno, L. S. Capizzi, F. Bosi, P. Ballirano, A. D'Arco, V. Stopponi, S. Lupi, P. Scarlato, H. Skogby, G. B. Andreozzi, *Lithos* **2023**, *438–439*, 106999.

[14] D. J. Henry, B. L. Dutrow, *Reviews in Mineralogy and Geochemistry* **1996**, *33*, 503.

[15] G. Von Goerne, G. Franz, J.-L. Robert, *Can. Mineral.* **1999**, *37*, 1025.

[16] V. J. Van Hinsberg, J. C. Schumacher, *The Canadian Mineralogist* **2011**, *49*, 177.

[17] F. C. Hawthorne, D. M. Dirlam, *Elements* **2011**, *7*, 307.

[18] B. L. Dutrow, D. J. Henry, *Elements* **2011**, *7*, 301.

[19] B. L. Dutrow, D. J. Henry, *The Canadian Mineralogist* **2000**, *38*, 131.

[20] R. V. Dietrich, *The Tourmaline Group*, Van Nostrand Reinhold Company, New York, **1985**.

[21] D. J. Henry, B. L. Dutrow, *Lithos* **2012**, *154*, 16.

[22] P. Bačík, P. Uher, A. Ertl, E. Jonsson, P. Nysten, V. Kanický, T. Vaculovič, *Canadian Mineralogist* **2012**, *50*, 825.

[23] M. Lensing-Burgdorf, A. Watenphul, J. Schlüter, B. Mihailova, *ejm* **2017**, *29*, 257.

[24] S. Farnsworth-Pinkerton, N. J. McMillan, B. L. Dutrow, D. J. Henry, *Journal of Geosciences (Czech Republic)* **2018**, *63*, 193.

[25] F. Bosi, B. Celata, H. Skogby, U. Hålenius, G. Tempesta, M. E. Ciriotti, E. Bittarello, A. Marengo, *Mineral. Mag.* **2021**, *85*, 242.

[26] K. Bónová, M. Jafarzadeh, J. Bóna, T. Mikuš, J. Anjerdi, A. Najafzadeh, R. Mahari, *J. Asian Earth Sci.* **2021**, *221*, 104943.

[27] S. Tonarini, A. Dini, F. Pezzotta, W. P. Leeman, *European Journal of Mineralogy* **1998**, *10*, 941.

[28] V. J. Van Hinsberg, D. J. Henry, B. L. Dutrow, *Elements* **2011**, *7*, 327.

[29] D. J. Henry, C. V. Guidotti, *Am. Mineral.* **1985**, *70*, 1.

[30] H. R. Marschall, S. Y. Jiang, *Elements* **2011**, *7*, 313.

[31] B. Dutrow, M. Holdaway, R. Hinton, *Contributions to Mineralogy and Petrology* **1986**, *94*, 496.

[32] J. F. Slack, R. B. Trumbull, *Elements* **2011**, *7*, 321.

[33] J. F. Slack, in *Boron: Mineralogy, Petrology, and Geochemistry*, (Eds: L. M. Anovitz, E. S. Grew), De Gruyter, **2018**, pp. 559–644.

[34] R. B. Trumbull, J. F. Slack, M.-S. Krienitz, H. E. Belkin, M. Wiedenbeck, *The Canadian Mineralogist* **2011**, *49*, 225.

[35] V. J. Van Hinsberg, J. C. Schumacher, *Contributions to Mineralogy and Petrology* **2007**, *153*, 289.

[36] T. G. Kotzer, T. K. Kyser, R. W. King, R. Kerrich, *Geochimica et Cosmochimica Acta* **1993**, *57*, 3421.

[37] R. J. Duncan, A. R. Wilde, K. Bassano, R. Maas, *Precambrian Research* **2006**, *146*, 120.

[38] A. Pesquera, J. Torres-Ruiz, P. P. Gil-Crespo, E. Roda-Robles, *American Mineralogist* **2009**, *94*, 1468.

[39] J. M. Martínez-Martínez, J. Torres-Ruiz, A. Pesquera, P. P. Gil-Crespo, *Lithos* **2010**, *119*, 238.

[40] E. Wethered, *Quarterly Journal of the Geological Society of London* **1888**, *44*, 186.

[41] L. S. Brown, *Am. Mineral.* **1929**, *14*, 238.

[42] A. C. Morton, A. G. Whitham, C. M. Fanning, *Sedimentary Geology* **2005**, *182*, 3.

[43] D. Henry, B. Dutrow, *Contributions to Mineralogy and Petrology* **1992**, *112*, 203.

[44] John F. Hubert, *SEPM Journal of Sedimentary Research* **1962**, *32*, 440.

[45] A. Brammall, *Proceedings of the Geologists' Association* **1926**, *37*, 251.

[46] P. D. Krynine, *The Journal of Geology* **1946**, *54*, 65.

[47] S. Andò, E. Garzanti, M. Padoan, M. Limonta, *Sedimentary Geology* **2012**, *280*, 165.

[48] V. J. Van Hinsberg, G. Franz, B. J. Wood, *Geochem. Persp. Let.* **2017**, 160.

[49] S. Andò, E. Garzanti, *J. Geol. Soc. London* **2014**, *386*, 395.

[50] I. M. Reinitz, G. R. Rossman, *American Mineralogist* **1988**, *73*, 822.

[51] G. R. Rossman, Mineral Spectroscopy Server, https://doi.org/10.7907/jywr-qq57.

[52] F. C. Hawthorne, D. M. Dirlam, *Elements* **2011**, *7*, 307.

[53] F. Pezzotta, B. M. Laurs, *Elements* **2011**, *7*, 333.

[54] E. Fritsch, J. E. Shigley, G. R. Rossman, M. E. Mercer, S. M. Muhlmeister, M. Moon, *Gems & Gemology* **1990**, 189.

[55] H. Beurlen, O. J. M. De Moura, D. R. Soares, M. R. R. Da Silva, D. Rhede, *The Canadian Mineralogist* **2011**, *49*, 277.

[56] S. Karampelas, L. Klemm, *Gems & Gemology* **2010**, *46*, 323.

[57] G. R. Rossman, E. Fritsch, J. E. Shigley, *American Mineralogist* **1991**, *76*, 1479.

[58] B. M. Laurs, J. C. (Hanco) Zwaan, C. M. Breeding, W. B. (Skip) Simmons, D. Beaton, K. F. Rijsdijk, R. Befi, A. U. Falster, *Gems & Gemology* **2008**, 294.

[59] M. S. Krzemnicki, H. A. O. Wang, *The Journal of Gemmology* **2022**, *38*, 20.

[60] P. B. Merkel, C. M. Breeding, *Gems & Gemology* **2009**, *45*, 112.

[61] C. Castañeda, S. G. Eeckhout, G. M. da Costa, N. F. Botelho, E. De Grave, *Phys Chem Minerals* **2006**, *33*, 207.

[62] J. I. Koivula, R. C. Kammerling, *Gems & Gemology* **1990**, *26*, 103.

[63] A. Abduriyim, H. Kitawaki, M. Furuya, D. Schwarz, *Gems & Gemology* **2006**, *42*, 4.

[64] A. Ertl, G. Giester, U. Schüssler, H. Brätz, M. Okrusch, E. Tillmanns, H. Bank, *Mineralogy and Petrology* **2013**, *107*, 265.

[65] J. E. Shigley, B. C. Cook, B. M. Laurs, M. de Oliveira Bernardes, *Gems & Gemology* **2001**, 260.

[66] H. A. O. Wang, D. Grolimund, L. Franz, D. Mathys, R. Schultz-Güttler, M. S. Krzemnicki, *The Journal of Gemmology* **2023**, *38*, 427.

[67] A. Hartley, *The Journal of Gemmology* **2018**, *36*, 203.

[68] F. Brandstatter, G. Niedermayr, *Gems & Gemology* **1994**, *30*, 178.

[69] LMHC Standardised Gemmological Report Wording, LMHC Information Sheet # 6.

[70] Y. Katsurada, Z. Sun, C. M. Breeding, B. L. Dutrow, *Gems and Gemology* **2019**, *55*, 648.

[71] Y. Katsurada, Z. Sun, *Gems & Gemology* **2017**, 1.

[72] M. Okrusch, A. Ertl, U. Schüssler, E. Tillmanns, H. Brätz, H. Bank, *Journal of Gemmology* **2016**, *35*, 120.

[73] Z. Sun, A. C. Palke, C. M. Breeding, B. Dutrow, *Gems & Gemology* **2019**, 2.

[74] L. Natkaniec-Nowak, M. Dumańska-Słowik, A. Ertl, *Neues Jahrbuch für Mineralogie - Abhandlungen* **2009**, 185.

[75] F. Bosi, B. Celata, H. Skogby, U. Hålenius, G. Tempesta, M. E. Ciriotti, E. Bittarello, A. Marengo, *Mineralogical Magazine* **2021**, *85*, 242.
[76] M. Akizuki, T. Kuribayashi, T. Nagase, A. Kitakaze, *American Mineralogist* **2001**, *86*, 364.
[77] R. B. Cook, *Rocks & Minerals* **2013**, *88*, 346.
[78] G. Agrosì, F. Bosi, S. Lucchesi, G. Melchiorre, E. Scandale, *American Mineralogist* **2006**, *91*, 944.
[79] D. M. Dirlam, B. M. Laurs, F. Pezzotta, W. B. (Skip) Simmons, *Gems & Gemology* **2002**, *38*, 28.
[80] A. J. Lussier, F. C. Hawthorne, *The Canadian Mineralogist* **2011**, *49*, 89.
[81] Y. Liang, X. Tang, Q. Zhu, J. Han, C. Wang, *Chemosphere* **2021**, *281*, 130780.
[82] K. Wang, Y. Sun, J. Tang, J. He, H. Sun, *Chemosphere* **2020**, *241*, 125044.
[83] Y. Chen, S. Wang, Y. Li, Y. Liu, Y. Chen, Y. Wu, J. Zhang, H. Li, Z. Peng, R. Xu, Z. Zeng, *Journal of Colloid and Interface Science* **2020**, *575*, 367.
[84] M. Prasad, S. Saxena, S. S. Amritphale, *Ind. Eng. Chem. Res.* **2002**, *41*, 105.
[85] R. Apiratikul, P. Pavasant, *Chemical Engineering Journal* **2008**, *144*, 245.
[86] C. Wang, J. Liu, Z. Zhang, B. Wang, H. Sun, *Ind. Eng. Chem. Res.* **2012**, *51*, 4397.
[87] C. P. Wang, J. Z. Wu, H. W. Sun, T. Wang, H. B. Liu, Y. Chang, *Ind. Eng. Chem. Res.* **2011**, *50*, 8515.
[88] M. Zhang, J. Pu, *Journal of Environmental Sciences* **2011**, *23*, 607.
[89] A. Lu, J. Wang, X. Qin, K. Wang, P. Han, S. Zhang, *Science of The Total Environment* **2012**, *425*, 66.
[90] R. A. Wuana, F. E. Okieimen, *International Scholarly Research Notices* **2011**, *2011*, 402647.
[91] F.-J. Zhao, Y. Ma, Y.-G. Zhu, Z. Tang, S. P. McGrath, *Environ. Sci. Technol.* **2015**, *49*, 750.
[92] T. Nakamura, T. Kubo, *Ferroelectrics* **1992**, *137*, 13.
[93] C. Wang, B. Wang, J. Liu, L. Yu, H. Sun, J. Wu, *Chin. Sci. Bull.* **2012**, *57*, 3218.
[94] H. Liu, C. Wang, J. Liu, B. Wang, H. Sun, *Journal of Environmental Management* **2013**, *128*, 727.
[95] C. Wang, Y. Zhang, L. Yu, Z. Zhang, H. Sun, *Journal of Hazardous Materials* **2013**, *260*, 851.
[96] X. Tan, Y. Liu, Y. Gu, G. Zeng, X. Wang, X. Hu, Z. Sun, Z. Yang, *Environ Sci Pollut Res* **2015**, *22*, 12597.
[97] B. Wang, C. Wang, J. Li, H. Sun, Z. Xu, *Journal of Environmental Chemical Engineering* **2014**, *2*, 1281.
[98] X. Li, Q. Zhang, B. Yang, *Chemosphere* **2020**, *239*, 124660.
[99] W. Jia, B. Wang, C. Wang, H. Sun, *Journal of Environmental Chemical Engineering* **2017**, *5*, 2107.
[100] H. Xu, M. Prasad, X. He, L. Shan, S. Qi, *Sci. China Ser. E-Technol. Sci.* **2009**, *52*, 3054.
[101] H. Xu, M. Prasad, Y. Liu, *Journal of Hazardous Materials* **2009**, *165*, 1186.
[102] Y. Zhang, J. Shi, Z. Xu, Y. Chen, D. Song, *Chemosphere* **2018**, *202*, 661.
[103] L. Yu, C. Wang, X. Ren, H. Sun, *Chemical Engineering Journal* **2014**, *252*, 346.
[104] M. Muruganandham, J.-S. Yang, J. J. Wu, *Ind. Eng. Chem. Res.* **2007**, *46*, 691.
[105] L. Hou, L. Wang, S. Royer, H. Zhang, *Journal of Hazardous Materials* **2016**, *302*, 458.
[106] M. Tokumura, H. Tawfeek Znad, Y. Kawase, *Chemical Engineering Science* **2006**, *61*, 6361.
[107] D. Zhao, J. Zhou, N. Liu, *Materials Science and Engineering: A* **2006**, *431*, 256.
[108] J. Yu, Q. Xiang, M. Zhou, *Applied Catalysis B: Environmental* **2009**, *90*, 595.
[109] F. Huang, Y. Guo, S. Wang, S. Zhang, M. Cui, *Solid State Sciences* **2017**, *64*, 62.
[110] J. Meng, J. Liang, G. Liang, J. Yu, Y. Pan, *Transactions of Nonferrous Metals Society of China* **2006**, *16*, s547.
[111] H. Zhang, A. Lv, J. Liang, J. Meng, *RSC Adv.* **2015**, *5*, 55704.
[112] L. Yu, C. Wang, F. Chen, J. Zhang, Y. Ruan, J. Xu, *Journal of Molecular Catalysis A: Chemical* **2016**, *411*, 1.

[113] C. Yu, M. Wen, S. Li, Z. Tong, Y. Yin, X. Liu, Y. Li, Z. Wu, D. D. Dionysiou, *Journal of Hazardous Materials* **2020**, *398*, 122932.

[114] B. Niu, N. Wang, Y. Chen, M. Yu, Z. Hou, Z. Li, Y. Zheng, *Separation and Purification Technology* **2021**, *257*, 117893.

[115] D. Wang, X. Luo, S. Yang, G. Xue, *Journal of Environmental Chemical Engineering* **2021**, *9*, 105221.

[116] M.-S. Xia, C.-H. Hu, H.-M. Zhang, *Process Biochemistry* **2006**, *41*, 221.

[117] J. Li, C. Wang, D. Wang, Z. Zhou, H. Sun, S. Zhai, *Chemical Engineering Journal* **2016**, *296*, 319.

[118] C. Wang, L. Yu, Z. Zhang, B. Wang, H. Sun, *Journal of Hazardous Materials* **2014**, *264*, 439.

[119] Z. Zhang, C. Wang, J. Li, B. Wang, J. Wu, Y. Jiang, H. Sun, *Environ Sci Pollut Res* **2014**, *21*, 14037.

[120] D. A. Keys, *The London, Edinburgh, and Dublin Philosophical Magazine and Journal of Science* **1921**, *42*, 473.

[121] D. A. Keys, *The London, Edinburgh, and Dublin Philosophical Magazine and Journal of Science* **1923**, *46*, 999.

[122] C. Frondel, *American Mineralogist* **1948**, *33*, 1.

[123] J. F. Tressler, S. Alkoy, R. E. Newnham, *Journal of Electroceramics* **1998**, *2*, 257.

[124] H. Zu, H. Wu, Q.-M. Wang, *IEEE Transactions on Ultrasonics, Ferroelectrics, and Frequency Control* **2016**, *63*, 486.

[125] A. M. Taylor, B. C. Terrell, *Journal of Crystal Growth* **1967**, *1*, 238.

[126] C. Frondel, R. L. Collette, *American Mineralogist* **1957**, *42*, 754.

[127] T. Tomisaka, *Mineralogical Journal* **1968**, *5*, 355.

[128] E. Kroumova, M. I. Aroyo, J. M. Perez-Mato, A. Kirov, C. Capillas, S. Ivantchev, H. Wondratschek, *Phase Transitions* **2003**, *76*, 155.

[129] A. Watenphul, M. Burgdorf, J. Schlüter, I. Horn, T. Malcherek, B. Mihailova, *Am. Mineral.* **2016**, *101*, 970.

[130] A. Watenphul, J. Schlüter, F. Bosi, H. Skogby, T. Malcherek, B. Mihailova, *Am. Mineral.* **2016**, *101*, 2554.

[131] D. A. McKeown, *Physics and Chemistry of Minerals* **2008**, *35*, 259.

[132] A. V. Korsakov, O. V. Rezvukhina, D. I. Rezvukhin, E. D. Greshnyakov, V. Y. Shur, *Journal of Raman Spectroscopy* **2020**, *51*, 1839.

[133] E. J. Berryman, B. Wunder, A. Ertl, M. Koch-Müller, D. Rhede, K. Scheidl, G. Giester, W. Heinrich, *Physics and Chemistry of Minerals* **2016**, *43*, 83.

[134] B. Gasharova, B. Mihailova, L. Konstantinov, *Eur. J. Mineral* **1997**, *9*, 935.

[135] C. Fantini, M. C. Tavares, K. Krambrock, R. L. Moreira, A. Righi, *Phys. Chem. Miner.* **2014**, *41*, 247.

[136] G. D. Gatta, F. Bosi, G. J. McIntyre, H. Skogby, *Mineral. Mag.* **2014**, *78*, 681.

[137] B. Mihailova, B. Gasharova, L. Konstantinov, *Journal of Raman Spectroscopy* **1996**, *27*, 829.

[138] L. H. Hoang, N. T. M. Hien, X. B. Chen, N. V. Minh, I. S. Yang, *Journal of Raman Spectroscopy* **2011**, *42*, 1442.

[139] T. Gonzalez-Carreño, M. Fernández, J. Sanz, *Phys Chem Minerals* **1988**, *15*, 452.

[140] C. V. Raman, K. S. Krishnan, *Nature* **1928**, *121*, 501.

[141] G. Keresztury, in *Handbook of Vibrational Spectroscopy*, (Eds: J. M. Chalmers, P. R. Griffiths), Wiley, 1st edn., **2001**.

[142] D. A. Long, R. J. H. Clark, *Raman spectroscopy*, McGraw-Hill, New York, **1977**.

[143] D. P. Strommen, K. Nakamoto, *J. Chem. Educ.* **1977**, *54*, 474.

[144] A. Kudelski, *Talanta* **2008**, *76*, 1.

[145] B. Robert, *Photosynth Res* **2009**, *101*, 147.

[146] J. Jehlička, A. Culka, D. Bersani, P. Vandenabeele, *J Raman Spectroscopy* **2017**, *48*, 1289.

[147] D. E. Newbury, N. W. M. Ritchie, *Scanning* **2013**, *35*, 141.
[148] J. J. Rehr, A. L. Ankudinov, *Coordination Chemistry Reviews* **2005**, *249*, 131.
[149] K. Okada, T. Uoaumi, A. Kotani, *Journal of the Physical Society of Japan* **1994**, *63*, 3176.
[150] G. S. Henderson, F. M. F. De Groot, B. J. A. Moulton, *Reviews in Mineralogy and Geochemistry* **2014**, *78*, 75.
[151] G. A. Waychunas, M. J. Apted, G. E. Brown, *Phys. Chem. Miner.* **1983**, *10*, 1.
[152] G. Dräger, R. Frahm, G. Materlik, O. Brümmer, *physica status solidi (b)* **1988**, *146*, 287.
[153] T. E. Westre, P. Kennepohl, J. G. DeWitt, B. Hedman, K. O. Hodgson, E. I. Solomon, *J. Am. Chem. Soc.* **1997**, *119*, 6297.
[154] D. Heumann, G. Dräger, S. Bocharov, *J. Phys. IV France* **1997**, *7*, C2.
[155] E. W. White, H. A. McKinstry, *Advances in X-Ray Analysis* **1965**, *9*, 376.
[156] U. C. Srivastava, H. L. Nigam, *Coordination Chemistry Reviews* **1973**, *9*, 275.
[157] M. Wilke, F. Farges, P.-E. Petit, G. E. Brown, F. Martin, *Am. Mineral.* **2001**, *86*, 714.
[158] S. Schöder, K. Müller, L. Tranchant, A. Rouquié, P. Gueriau, M. Thoury, E. Bérard, T. Okbinoglu, F. Berenguer, C. Iacconi, L. Robbiola, T. Moreno, S. X. Cohen, L. Bertrand, *Appl. Phys. A* **2024**, *130*, 848.
[159] B. Beckhoff, B. Kanngießer, N. Langhoff, R. Wedell, H. Wolff, *Handbook of Practical X-Ray Fluorescence Analysis*, Springer Science & Business Media, **2007**.
[160] P. Brouwer, *Theory of XRF: getting acquainted with the principles*, PANalytical BV, Almelo, **2003**.
[161] P. Acquafredda, *Physical Sciences Reviews*.
[162] W. Xu, Z. Du, S. Liu, Y. Zhu, C. Xiao, A. Marcelli, *Condensed Matter* **2018**, *3*, 29.
[163] J. A. Bearden, *Rev. Mod. Phys.* **1967**, *39*, 78.
[164] W. Heitler, *The Quantum Theory of Radiation*, Courier Corporation, **1984**.
[165] B. L. Henke, E. M. Gullikson, J. C. Davis, *Atomic Data and Nuclear Data Tables* **1993**, *54*, 181.
[166] J. H. Scofield, L. (USA) L. L. L. California Univ., *Theoretical photoionization cross sections from 1 to 1500 keV*, California Univ., Livermore (USA). Lawrence Livermore Lab, **1973**.
[167] L. J. Radziemski, T. R. Loree, *Plasma Chem Plasma Process* **1981**, *1*, 281.
[168] T. R. Loree, L. J. Radziemski, *Plasma Chem Plasma Process* **1981**, *1*, 271.
[169] G. Cristoforetti, S. Legnaioli, V. Palleschi, E. Tognoni, P. A. Benedetti, *J. Anal. At. Spectrom.* **2008**, *23*, 1518.
[170] V. Palleschi, *ChemTexts* **2020**, *6*, 18.
[171] A. Ciucci, M. Corsi, V. Palleschi, S. Rastelli, A. Salvetti, E. Tognoni, *Appl. Spectrosc., AS* **1999**, *53*, 960.
[172] NIST (National Institute od Standards and Technology), https://physics.nist.gov/PhysRefData/ASD/lines_form.html.
[173] M. Bols, J. Ma, F. Rammal, D. Plessers, X. Wu, S. Navarro-Jaén, A. J. Heyer, B. Sels, E. Solomon, R. Schoonheydt, *Chem Rev* **2024**, *124*, 2352.
[174] D. J. Henry, B. L. Dutrow, in *Boron - Mineralogy, Petrology, and Geochemistry*, De Gruyter, **1996**, vol. 33, pp. 503–558.
[175] A. Pesquera, P. P. Gil-Crespo, F. Torres-Ruiz, J. Torres-Ruiz, E. Roda-Robles, *Mineral. mag.* **2016**, *80*, 1129.
[176] A. G. Tindle, F. W. Breaks, J. B. Selway, *Can. Mineral.* **2002**, *40*, 753.
[177] F. Bosi, S. Lucchesi, *Eur. J. Mineral.* **2004**, *16*, 335.
[178] L. Pasetti, L. Fornasini, L. Mantovani, S. Andò, S. Raneri, V. Palleschi, D. Bersani, *J. Raman Spectrosc.* **2024**, *55*, 276.
[179] A. Ertl, U. Kolitsch, M. D. Dyar, H.-P. Meyer, G. R. Rossman, D. J. Henry, M. Prem, T. Ludwig, L. Nasdala, C. L. Lengauer, E. Tillmanns, G. Niedermayr, *ejm* **2016**, *28*, 163.
[180] S. M. Mattson, G. R. Rossman, *Phys. Chem. Miner.* **1987**, *14*, 163.

[181] J. Filip, F. Bosi, M. Novák, H. Skogby, J. Tuček, J. Čuda, M. Wildner, *Geochimica et Cosmochimica Acta* **2012**, *86*, 239.
[182] F. Farges, S. Rossano, Y. Lefrre, M. Wilke, G. E. B. Jr., *Phys. Scr.* **2005**, 957.
[183] P.-E. Petit, F. Farges, M. Wilke, V. A. Solé, *J Synchrotron Rad* **2001**, *8*, 952.
[184] A. J. Berry, H. St. C. O'Neill, K. D. Jayasuriya, S. J. Campbell, G. J. Foran, *Am. Mineral.* **2003**, *88*, 967.
[185] S. Bajt, S. R. Sutton, J. S. Delaney, *Geochim. Cosmochim. Acta* **1994**, *58*, 5209.
[186] E. A. Levy, D. J. Henry, A. Roy, B. L. Dutrow, *Jour. Geosci.* **2018**, *63*, 167.
[187] G. Calas, J. Petiau, *Solid State Commun.* **1983**, *48*, 625.
[188] L. Galoisy, G. Calas, M. A. Arrio, *Chem. Geol.* **2001**, *174*, 307.
[189] L. Pasetti, S. Raneri, A. Gianoncelli, L. Tranchant, S. Schöder, L. Mantovani, D. Bersani, in *J. Raman Spectrosc.*, **2025**.
[190] J. D. Grice, T. S. Ercit, *Neues Jahrb. Mineral. Abh.* **1993**, *165*, 245.
[191] L. Pasetti, L. Borromeo, D. Bersani, S. Andò, J. Schnellrath, U. Hennebois, S. Karampelas, *Minerals* **2023**, *14*, 44.
[192] U. Hennebois, A. Delaunay, S. Karampelas, *The journal of gemmology* **2022**, *38*, 317.
[193] K. A. Musiyachenko, A. V. Korsakov, R. Shimizu, P. S. Zelenovskiy, V. Y. Shur, *Journal of Raman Spectroscopy* **2020**, *51*, 1415.
[194] M. A. Alvarez, R. Coy-Yll, *Spectrochim. Acta* **1978**, *34*, 899.
[195] M. T. Sweetapple, S. Tassios, *American Mineralogist* **2015**, *100*, 2141.
[196] C. Fabre, M.-C. Boiron, J. Dubessy, A. Chabiron, B. Charoy, T. Martin Crespo, *Geochimica et Cosmochimica Acta* **2002**, *66*, 1401.
[197] K. Rifai, M. Constantin, A. Yilmaz, L. Ç. Özcan, F. R. Doucet, N. Azami, *Minerals* **2022**, *12*, 253.
[198] F. Rizzo, F. Bosi, G. Tempesta, G. Agrosì, *Crystals* **2023**, *13*, 1290.
[199] CRYSTAL, https://www.crystal.unito.it/.
[200] A. Erba, J. K. Desmarais, S. Casassa, B. Civalleri, L. Donà, I. J. Bush, B. Searle, L. Maschio, L. Edith-Daga, A. Cossard, C. Ribaldone, E. Ascrizzi, N. L. Marana, J.-P. Flament, B. Kirtman, *J. Chem. Theory Comput.* **2023**, *19*, 6891.
[201] F. Pascale, C. M. Zicovich-Wilson, F. López Gejo, B. Civalleri, R. Orlando, R. Dovesi, *Journal of Computational Chemistry* **2004**, *25*, 888.
[202] C. M. Zicovich-Wilson, F. Pascale, C. Roetti, V. R. Saunders, R. Orlando, R. Dovesi, *Journal of Computational Chemistry* **2004**, *25*, 1873.
[203] F. F. Foit, *American Mineralogist* **1989**, *74*, 422.
[204] CRYSTAL Basis Sets Library, https://www.crystal.unito.it/basis_sets.html.
[205] R. Demichelis, B. Civalleri, M. Ferrabone, R. Dovesi, *International Journal of Quantum Chemistry* **2010**, *110*, 406.
[206] M. Prencipe, *Rend. Fis. Acc. Lincei* **2019**, *30*, 239.
[207] Z. Wu, R. E. Cohen, *Phys. Rev. B* **2006**, *73*, 235116.
[208] C. Lee, W. Yang, R. G. Parr, *Phys. Rev. B* **1988**, *37*, 785.
[209] R. Dovesi, C. Ermondi, E. Ferrero, C. Pisani, C. Roetti, *Phys. Rev. B* **1984**, *29*, 3591.
[210] J. Heyd, J. E. Peralta, G. E. Scuseria, R. L. Martin, *J. Chem. Phys.* **2005**, *123*, 174101.
[211] P. Pernot, B. Civalleri, D. Presti, A. Savin, *J. Phys. Chem. A* **2015**, *119*, 5288.
[212] B. Civalleri, D. Presti, R. Dovesi, A. Savin, *Chem. Modell* **2012**, *9*, 168.
[213] R. Dovesi, C. Roetti, C. Freyria-Fava, M. Prencipe, V. R. Saunders, *Chemical Physics* **1991**, *156*, 11.
[214] B. Civalleri, A. M. Ferrari, M. Llunell, R. Orlando, M. Mérawa, P. Ugliengo, *Chem. Mater.* **2003**, *15*, 3996.
[215] G. Valerio, M. Catti, R. Dovesi, R. Orlando, *Phys. Rev. B* **1995**, *52*, 2422.

[216] I. de P. R. Moreira, R. Dovesi, C. Roetti, V. R. Saunders, R. Orlando, *Phys. Rev. B* **2000**, *62*, 7816.
[217] L. Maschio, B. Kirtman, M. Rérat, R. Orlando, R. Dovesi, *J. Chem. Phys.* **2013**, *139*, 164101.
[218] L. Maschio, B. Kirtman, M. Rérat, R. Orlando, R. Dovesi, *J. Chem. Phys.* **2013**, *139*, 164102.
[219] M. Ferrero, M. Rérat, R. Orlando, R. Dovesi, *Journal of Computational Chemistry* **2008**, *29*, 1450.
[220] M. Ferrero, M. Rérat, R. Orlando, R. Dovesi, *J. Chem. Phys.* **2008**, *128*, 014110.
[221] M. Ferrero, M. Rérat, B. Kirtman, R. Dovesi, *J. Chem. Phys.* **2008**, *129*, 244110.
[222] S. A. Prosandeev, U. Waghmare, I. Levin, J. Maslar, *Phys. Rev. B* **2005**, *71*, 214307.
[223] F. Pascale, S. Tosoni, C. Zicovich-Wilson, P. Ugliengo, R. Orlando, R. Dovesi, *Chemical Physics Letters* **2004**, *396*, 308.
[224] B. Lindberg, *J. Chem. Phys.* **1988**, *88*, 3805.
[225] P. Ugliengo, in *University of Torino, Torino, Italy*, **1989**.